Philipp Thaler, Dipl. Ing.

Buildup and Characterization of an Apparatus for the Synthesis of Metallic Nanoparticles Inside Helium Droplets

DOCTORAL THESIS

to achieve the university degree of

Doktor der technischen Wissenschaften

submitted to

Graz University of Technology

Supervisor

Univ.-Prof. Mag. Dr.rer.nat Wolfgang E. Ernst

Institute of Experimental Physics

Graz, September 2015

AFFIDAVIT

I declare that I have authored this thesis independently, that I have not used other than the declared sources/resources, and that I have explicitly indicated all material which has been quoted either literally or by content from the sources used. The text document uploaded to TUGRAZonline is identical to the present doctoral thesis.

Date

Signature

Abstract

Nanoparticles are an exciting field of research as their properties are governed by their size, shape and composition and can differ from those of the corresponding bulk material. Because of their smallness, concepts of classical physics do no longer fully apply and quantum physics becomes essential, which makes it difficult to predict their behavior. As metal nanoparticles promise to show interesting new effects which can be useful in future applications in the fields of *e.g.* optics, magnetism or catalysis, experimental investigations of these systems are essential.

In order to synthesize metal nanoparticles, multiple methods can be applied - one of them is the helium droplet technique which is a novel approach that has been presented first in 2007. The helium droplet technique distinguishes itself from other methods by the extraordinarily cold environment provided by the superfluid matrix as well as by the exceptionally clean production process which guarantees virtually no contamination. Additionally, the He-environment is completely inert, and no solvents, additives, ligands or templates are required for the nanoparticle synthesis, in contrast to many other synthesis methods. The growth process can be well controlled by varying the droplet size and the pickup conditions which allows, in principle, the creation of nanoparticles tailored for a given purpose.

In the course of this thesis, a new apparatus applying the helium droplet technique was designed and built. In numerous experiments, the new machine was characterized and the capabilities of the helium droplet approach were explored. Special focus was placed on the creation of bi-metallic core-shell structures as well as the utilization of quantized vortices as volatile templates for the synthesis of nanowires. The data collected during the experiments provides new insights into the nanoparticle formation mechanism inside helium droplets and allows the formulation of a growth model, depending on the size of the utilized helium droplets. Furthermore, it shows the applicability and the limitations of the helium droplet technique. The experiments conducted within this thesis build the foundation for future experiments, in which tailored clusters will be produced in order to investigate their special properties.

Kurzfassung

Nanopartikel stellen ein spannendes Forschungsgebiet dar, da sich ihre Eigenschaften von jenen des entsprechenden Festkörper-Materials unterscheiden können und stark durch deren Größe, Form und Zusammensetzung beeinflusst werden. Aufgrund ihrer Kleinheit können die Eigenschaften dieser Partikel nicht mehr vollständig mit den Gesetzmäßigkeiten der klassischen Physik beschrieben werden und ihre quantenphysikalischen Eigenschaften treten in den Vordergrund, was eine Vorhersage ihrer Eigenschaften sehr schwierig gestaltet. Da jedoch speziell von metallischen Nanopartikeln erwartet wird, dass diese neuartige Effekte z.B. in den Bereichen Optik, Magnetismus und Katalyse zeigen, die für zukünftige Anwendungen interessant wären, sind experimentelle Untersuchungen an diesen Systemen sehr wichtig.

Zur Herstellung von Nanopartikeln gibt es viele Methoden, eine von ihnen ist die Heliumtropfenmethode, welche einen neuartigen Ansatz darstellt, der erstmals 2007 präsentiert wurde. Diese Methode unterscheidet sich von anderen Techniken durch die extrem kalten Temperaturen, die von der superfluiden Heliummatrix zur Verfügung gestellt werden, sowie durch die außergewöhnliche Reinheit des gesamten Produktionsprozesses, der quasi verschmutzungsfreie Nanopartikel garantiert. Außerdem findet der Syntheseprozess in einer komplett inerten He-Umgebung statt und benötigt, im Gegensatz zu manch anderen Syntheseverfahren, keine Lösungsmittel, Additive, Stabilisatoren oder Formen. Über die Anpassung der Heliumtropfengröße sowie der Dotierungsbedingungen kann der Wachstumsprozess der Nanopartikel gut kontrolliert werden. Dies erlaubt im Prinzip die Erzeugung maßgeschneiderter Nanopartikel für vorgegebene Zwecke.

Im Rahmen dieser Doktorarbeit wurde eine neue Heliumtropfenanlage entworfen und aufgebaut. In einer Vielzahl an Experimenten wurde die neue Maschine charakterisiert und die Möglichkeiten der Heliumtropfenmethode erkundet. Dabei wurde ein spezieller Fokus auf die Synthese bi-metallischer Schalen-Strukturen gelegt sowie auf die Ausnutzung von quantisierten Wirbeln als flüchtige Formen für die Bildung von Nanodrähten. Die während der Experimente aufgenommenen Daten geben neue Einblicke in den Wachstumsmechanismus von Nanopartikeln in Heliumtropfen und erlauben die Aufstellung eines Wachstumsmodelles in Abhängigkeit von der auftretenden Heliumtropfengröße. Außerdem zeigen die Experimente die möglichen Anwendungen sowie die Grenzen der Anwendbarkeit der Heliumtropfenmethode. Damit bilden die während dieser Doktorarbeit durchgeführten Versuche die Grundlage für zukünftige Experimente, bei denen die speziellen Eigenschaften von maßgeschneiderten Nanopartikeln untersucht werden können.

Articles Related to this Work

1. **High resolution electron microscopy of Ag-clusters in crystalline and noncrystalline morphologies grown inside superfluid helium nanodroplets**
   Alexander Volk, **Philipp Thaler**, Markus Koch, Evelin Fisslthaler, Werner Grogger and Wolfgang E. Ernst
   J. Chem. Phys., **138**, 214312 (2013)

2. **Molecular dynamics simulation of the deposition process of cold Ag-clusters under different landing conditions**
   Philipp Thaler, Alexander Volk, Martin Ratschek, Markus Koch and Wolfgang E. Ernst
   J. Chem. Phys., **140**, 044326 (2014)

3. **Formation of bimetallic core-shell nanowires along vortices in superfluid He nanodroplets**
   Philipp Thaler, Alexander Volk, Florian Lackner, Johannes Steurer, Daniel Knez, Werner Grogger, Ferdinand Hofer, and Wolfgang E. Ernst
   Phys. Rev. B, **90**, 155442 (2014)

4. **Atomic collisions in suprafluid helium-nanodroplets: timescales for metal-cluster formation derived from He-density functional theory**
   Andreas W. Hauser, Alexander Volk , **Philipp Thaler** and Wolfgang E. Ernst
   Phys. Chem. Chem. Phys., **17**, 10805-10812 (2015)

5. **Formation of bimetallic clusters in superfluid helium nanodroplets analyzed by atomic resolution electron tomography**
   Georg Haberfehlner, **Philipp Thaler**, Daniel Knez, Alexander Volk, Ferdinand Hofer, Wolfgang E. Ernst and Gerald Kothleitner
   Accepted: Nat. Commun., September 2015

6. **Thermal instabilities and Rayleigh breakup of ultrathin Ag nanowires grown in He droplets**
   Alexander Volk, Daniel Knez, **Philipp Thaler**, Andreas W. Hauser, Werner Grogger, Ferdinand Hofer and Wolfgang E. Ernst
   Phys. Chem. Chem. Phys., **17**, 24570-24575 (2015)

7. **Synthesis of nanoparticles in helium droplets - a characterization comparing mass-spectra and electron microscopy data**
   Philipp Thaler, Alexander Volk, Daniel Knez, Florian Lackner, Georg Haberfehlner, Johannes Steurer, Martin Schnedlitz and Wolfgang E. Ernst
   Accepted: J. Chem. Phys., **143**, (2015)

8. **Electron induced Kirkendall effect at atomic resolution**
   Daniel Knez, **Philipp Thaler**, Alexander Volk, Wolfgang E. Ernst and Ferdinand Hofer
   in preparation, 2015

Note: The articles (2), (3), (5) and (7) are part of this work.

Contents

Chapter 1

Introduction

Already more than 50 years ago Richard P. Feynman discussed the potential of miniaturization in the famous lecture "There's Plenty of Room at the Bottom" [41]. He stated that (by that time futuristic) miniaturized applications do not violate any known physics and that, in principle, there is no reason why they couldn't be manufactured. Some of the ideas presented in the lecture are omnipresent nowadays, as for example the storage of extensive amounts of information on very small devices, the miniaturization of computers in general or minimally invasive surgery. In order to find examples for nanotechnology one does not have to limit the search to man-made products though - there are also many examples in nature, such as nanometric "data storage" in DNA, the "sticky" feet of Geckos or the self-cleaning leafs of the Lotus flower. However, the development of new applications or the utilization of new effects based on the already known laws of physics is not straight forward. Especially when entering the size regime where concepts of classical physics do no longer fully apply and quantum physics becomes essential (system dimensions of a few nanometers), interpretations based on everyday experience or common sense are no longer adequate. One way to gain insight into such systems are computer simulations, but despite the performance of today's computers and the quality of available simulation tools, the exact quantum-mechanical treatment of systems containing more than a few dozen atoms seems out of reach. A possible way to study particles with a size where a full quantum treatment would be desirable, but is computationally too demanding, is by experiment, as it will be presented in this work.

Within this thesis, helium droplets (He_N) are utilized as nano-reactors to synthesize nanoparticles with diameters of less than 10 nanometers. Using the He_N-technique for the production and surface deposition of metal nanoparticles is a novel approach which has been presented first in 2007 [112]. Building on the experience on He_N-beam machines for matrix isolation spectroscopy at the institute, a new machine was built in the course of this thesis, particularly designed for the synthesis of metal nanoparticles. Whereas the actual realization of this technique is quite delicate, its underlying principle is very simple: If an atom or molecule collides with a He_N, it is deposited inside the droplet. Using a suitable setup, hundreds of dopant atoms or molecules can be added to the same droplet, where they can aggregate. Thereby, the particle growth process can be well controlled by varying the droplet size and the pickup conditions. This allows, in principle, the creation of nanoparticles tailored for a given purpose.

The He_N-method distinguishes itself from other nanoparticle synthesis methods by the extraordinarily cold environment provided by the superfluid matrix and enables interesting possibilities such as the formation of core-shell structures by employing sequential pickup schemes or the generation of wire-structures by exploiting quantized vortices (see chapters 6 and 7). The whole production process takes place in high- or ultra-high-vacuum, which makes the procedure exceptionally clean. Additionally, the He-environment is completely inert, and no solvents, additives, ligands or templates are required for nanoparticle synthesis, in contrast to many other synthesis methods. The ability to produce and understand pristine samples is an important first step towards designing and understanding more complex structures.

1.1 Structure of this Thesis

This work is designed as a cumulative thesis, which means that the main scientific results are presented in the form they were published in peer-reviewed journals. Each of the publications is arranged in a separate chapter (chapters 5-8), containing a list describing the contributions of every author.

Besides research on nanoparticles, one of the main aspects of this thesis was the construction and characterization of a new apparatus for the synthesis of metal nanoparticles in micron-sized helium droplets. The basic concepts behind this machine are covered in chapter 2. For the purpose of keeping this thesis succinct, detailed technical aspects of the experiment as well as operating instructions are covered in a manual attached to this thesis. This manual also includes engineering drawings and typical settings of the different devices.

In order to help the reader to understand typical experiments with the new apparatus as well as the associated problems, some exemplary experiments and their results are presented and discussed in chapter 3.

Computer simulations modeling the growth- and surface-deposition-process of nanoparticles in helium droplets are discussed in chapter 4.

The journal articles published during this thesis are presented in a content-oriented order rather than a chronological one. Chapter 5 deals with computer simulations of the landing process of the synthesized particles in deposition experiments. These simulations elucidate the occurrence of unexpected morphologies [155] as well as the influence of particle-substrate-interaction on the final shape of the nanoparticle.

The article in chapter 6 focuses on electron tomographic investigations of the particles produced in the new apparatus. Three dimensional reconstructions of our particles confirm their expected lenticular shape. Furthermore, the utilization of two different dopants in a sequential pickup scheme, combined with element sensitive detection techniques, provides insight into the core-shell growth mechanism of bimetallic nanoparticles.

Quantized vortices, a feature of very large He_N, are exploited in the publication in chapter 7 to synthesize nanowires. The utilization of a sequential doping scheme in this experiment leads to the formation of a core-shell structure. Reversing the doping sequence results in a reversed core-shell order, confirming that the order of the constituents is indeed defined by the sequence of the doping cells.

Finally, chapter 8 contains an article characterizing the apparatus built during this thesis. Special attention was paid to the comparison of *in-situ* particle analysis with mass spectrometry and *ex-situ* particle analysis with electron microscopy. It was shown that in a certain particle size range, both methods can be applied and yield the same results. Proving the reliability of our *in-situ* diagnostics and the theoretical predictions allows us to go without elaborate microscopic investigations for the characterization of nanoparticles created in future experiments.

1.2 Helium, Helium Droplets and Vortices

Helium is the second most abundant element in the universe and occurs in two stable isotopes, ^{3}He and ^{4}He. On earth, however, ^{4}He is rare (5 ppm of the atmosphere) and was mostly created through radioactive decay, *i.e.* emission of alpha-particles. ^{3}He occurs even less frequently (only about one in a million He-atoms is ^{3}He) and is extremely expensive. Hence, for this work, the properties of ^{4}He are paramount. Helium has the highest ionization energy (24.6 eV) as well as the lowest boiling point (4.2 K) of all elements and is the only element that cannot be solidified under ambient pressure. Below the boiling point, ^{4}He acts as a normal liquid, but as it is cooled down below 2.17 K (the so-called lambda-point of ^{4}He), it enters a new phase, the superfluid phase. In this state, the thermal de Broglie wavelength of ^{4}He becomes larger than the interatomic spacing, the ^{4}He-atoms loose their identity and the bosonic condensate can be described by a macroscopic wave function. In this macroscopic quantum state the viscosity of the fluid vanishes, the thermal conductivity approaches infinity and other unusual phenomena such as fountains or creep-flow occur [34, 151].

If liquid helium droplets are brought into vacuum, they cool themselves by evaporation and reach a temperature (≈ 0.4 K) below the transition temperature to the superfluid state (2.17 K) [23]. Despite being superfluid, the droplets have the capability to pickup any foreign species upon collision with a high probability (pickup cross-section $\approx$ geometrical cross-section of the droplet). The position of the dopant, which can be inside or on the surface of the droplet, depends on the strength of the He-dopant interaction and is characterized by the so-called Ancilotto-parameter [6]. While alkaline or alkaline-earth atoms usually adopt a position in a dimple on the surface of the droplet, other elements, molecules or clusters in general take a position inside the droplet. In a helium droplet beam experiment, where the He_N are sent through a volume containing the desired dopant in the gaseous phase, the droplets can pick up tens, hundreds or even thousands of atoms along their trajectory. In the superfluid, the dopants are able to move, which means they eventually collide and coagulate inside the droplet [64], whereby the binding energy is dissipated by the helium matrix. Thus, doping of helium droplets, which provide confinement and cooling, leads to the efficient formation of clusters which makes helium droplets an interesting means for nanoparticle synthesis.

Helmholtz's theorems describe circulating flows and vortices in fluids. These laws state that vortex lines cannot start or end inside of fluids - they either form a ring or end at the boundary surface of the respective fluid. Additionally, they state that vorticity ($\omega = \nabla \times \vec{v}$) cannot be created and cannot decay inside a fluid, but can only be introduced or dissipated at the boundary surface of the fluid (also valid for viscous fluids)[57]. This means, that vorticity transferred to the fluid during the expansion though the nozzle is conserved until the droplet hits a surface. As the droplets turn superfluid the viscosity of the liquid helium vanishes, which prevents the appearance of shear forces and hence, makes the fluid irrotational ($\nabla \times \vec{v} = 0$) [1]. The consequences are irrotational vortices (also guaranteeing conservation of angular momentum) where

$v \propto \frac{1}{r}$ and $\omega = 0$ everywhere, except for the vortex core. Furthermore, the quantum nature of the superfluid requires the quantization of the angular momentum. Since a doubly quantized vortex would have four times the energy of a singly quantized line [34], doubly or multiply quantized vortices are very unlikely to occur - instead, a larger angular momentum is realized by multiple singly quantized vortices [34]. Vortices in the bulk superfluid have been known for quite some time and have been visualized exploiting the pressure gradient of the superfluid towards the vortex centers, which drives foreign species to locate along the vortex lines [34, 108, 138]. In droplets, however, evidence for vortices was only found very recently [49]. In terms of nanoparticle synthesis, this adds the interesting option of generating elongated structures such as nano-rods or nano-wires.

1.3 Nanoparticles

In the past decades particles not larger than a few nanometers in diameter have been studied with great interest. Because of their small size, these particles no longer behave like the bulk material but neither like the bare atoms. Reasons for this can be *e.g.* the comparatively high amount of surface atoms or quantum size effects. Especially their unusual optical, magnetic or catalytic properties can be of great interest for future applications. Since the actual physical and chemical characteristics of such nanoparticles strongly depend on their size, shape and composition, synthesis methods controlling these features are required. Within this thesis, the controlled synthesis of bare and bimetallic nanoparticles using helium droplets as micro-reactors was studied and characterized.

To start with, model systems such as Ag- and Au-nanoparticles were implemented, as they are experimentally easy to handle because of their relative chemical inertness and the moderate evaporation conditions required. Furthermore, in binary systems, their very similar crystal lattice is beneficial. Later, Ni and Cr were chosen as constituents because of their magnetic properties, which have been a topic of interest in our group for several years.

Remark: *Within this thesis, the terms "nanoparticle" and "cluster" are often used interchangeably. In the text, the actual size of the discussed particles is either specifically stated or becomes evident from the context. In general, the term "cluster" is more frequently used with smaller compounds, while particles containing a thousand atoms or more are rather denominated "nanoparticle".*

1.4 Surface Deposition of Nanoparticles

For applications or in order to be able to use *ex-situ* diagnostics, the synthesized nanoparticles have to be deposited on a suitable substrate on which they can be remove from the apparatus. It is therefore necessary to know about the deposition conditions and how they might influence the produced nanoparticles. The impact of a particle on a surface can be characterized in two regimes, low- and high-energy impacts. In the former, often called "soft landing", the kinetic energy per atom of the particle lies below the binding energy of the constituents and the impact typically does not lead to fragmentation of the particle [123]. Nevertheless, the particles can undergo plastic deformations. In the high-energy impact regime, on the other hand, the kinetic energy per atom exceeds the binding energy, which leads to significant deformation, fragmentation or even implantation of the particle into the substrate [123] . In the soft landing regime, the choice of the substrate is the most critical parameter. Molecular dynamics simulations *e.g.* show that deposition of clusters on metal surfaces, even with negligible kinetic energy, may lead to substantial deformation of the deposited particles [116, 120].

During the course of this work, nanoparticles of different sizes and materials were deposited mainly on very thin commercial amorphous carbon (a-c) substrates. The a-c substrates proved to be a good compromise between particle deformation and fixing the particles position on the surface, which is essential for subsequent *ex-situ* microscopic investigations. Using other substrates such as *e.g.* Au(111) or HOPG (highly ordered pyrolytic graphite) for scanning probe microscopy experiments turned out to be problematic. While metal clusters seem to melt on Au(111) due to the large binding energy (which prevents their detection), metal clusters are very mobile on HOPG, which leads to the aggregation of many clusters into ramified structures.

In the most recent experiments it was found that surface diffusion (along the surface of the nanoparticles) after deposition plays an important role for the morphology observed in the microscope. Especially in the case of silver, extensive restructuring occurred already at temperatures well below room temperature [154]. This effect has not been considered in the first experiments on this machine. Beforehand, effects related to the impact, which happen on a nanosecond time scale, and diffusion processes happening during the few hours it takes to transfer the sample and to get the first microscopy images cannot be distinguished. Working with cooled substrates can suppress diffusion, but makes electron microscopy much more difficult.

Chapter 2

Experimental Setup and Experimental Methods

In the course of this thesis, a helium beam scattering machine, donated by Prof. Christof Wöll (Universität Bochum), was cannibalized in order to build a new apparatus for nanoparticle synthesis in helium droplets - HelENA (Helium Environment for Nanoparticle Assembly). The construction-phase started in September 2011 with the preparation of the lab and the transfer of the machine, and lasted about two years, but also afterwards several new features were added. At this time, the most prominent feature of the machine is a specialized time-of-flight mass spectrometer (TOFMS) for the *in-situ* characterization of the produced nanoparticles. After depositing the synthesized nanoparticles on suitable substrates, the samples can be analyzed *ex-situ* using *e.g.* electron microscopy or scanning probe microscopy. As improvement and extension of the machine are ongoing processes, the following chapter describes the current status of the machine. Naturally, several people besides the author were involved in the setup and improvement of HelENA, most importantly Alexander Volk and Johannes Steurer whose theses (AV: doctoral thesis [153], JS: diploma thesis [142]) include their own contributions, while this thesis focuses the contributions of the author.

2.1 General Structure of the Laboratory and the Apparatus

Based on the know-how about helium droplet beam machines for spectroscopy, HelENA was designed in a typical three vacuum chamber setup (Fig. 2.1). Thereby, the first chamber contains the nozzle to produce the beam of He_N (source chamber, SC), the second chamber houses the facilities for doping the droplets (pickup chamber, PC) and the last chamber contains the diagnostics (diagnostics chamber, DC).

Electrical wiring and cooling-water supplies were newly installed in the lab, fitting the requirements of the new machine. Additionally, two air-conditioning units and a gas locker were newly set up (see Ref. [153] and the attached manual).

In order to reduce the noise level in the lab, the fore-pumps for the vacuum system are located in the adjacent room. A home-made electronic control-unit enables operating the fore-pumps and reading the attached pressure sensors from the lab. As foundation

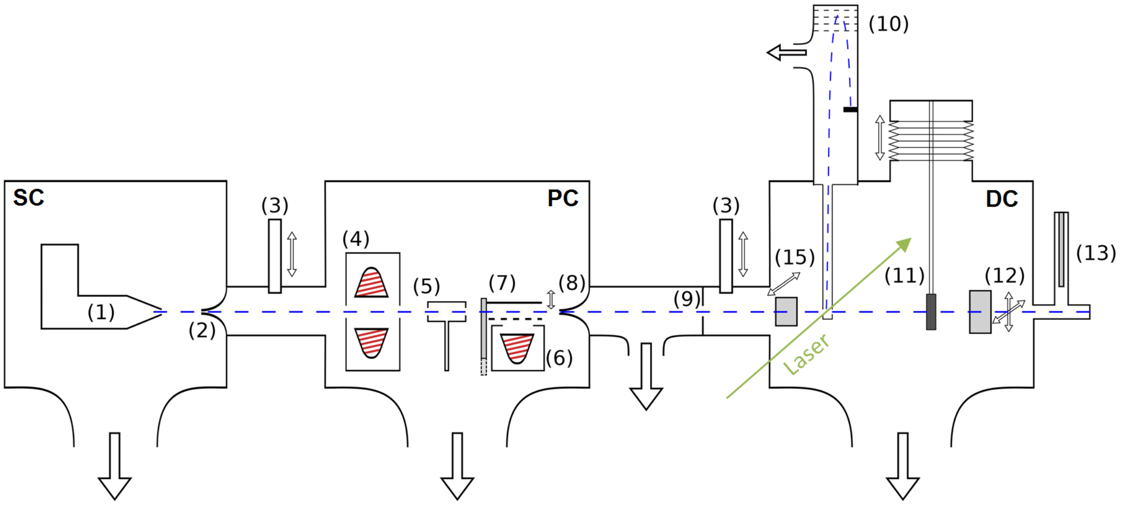

Figure 2.1: Schematics of the three chamber setup (SC, PC, DC) of the He_N beam machine used for the experiments in this thesis. The droplet beam produced by the cooled nozzle (1) is shaped by the skimmers (2, 8) and an aperture (9). The droplets can be sequentially doped using different sources (4, 5, 6). As diagnostic tools a TOFMS (10), substrates for *ex-situ* TEM investigations (11) and a quartz crystal microbalance (12) are available on axis, as well as an off-axis QMS (13). The TOFMS is equipped with an electron gun for electron impact ionization (not shown) but also enables photo-ionization using an external laser. A UHV-transfer system (15) enables the transport of surface deposited samples to external diagnostics without breaking the vacuum.

for the machine a robust metal frame with steel-rails on top is used. The three before mentioned vacuum chambers, which constitute the main structure of the apparatus, are mounted on the steel-rails using linear bearings, which allows easy repositioning of the single components and therefore maximum flexibility. For the assembly of heavy parts a crane was installed on the ceiling above the machine.

In our three chamber setup the SC as well as the vacuum system for the SC were adopted from the previous machine, the old scattering chamber was retrofitted to serve as DC and the PC was built from scratch. The vacuum system was designed to yield subsequently decreasing pressure, reaching ultra high vacuum (UHV) in the last chamber (DC), while the pumps of the first chamber still manage the high gas load stemming from the jet expansion producing the He_N. In order to be able to shut down the different parts of the apparatus individually, gate valves were installed between the chambers.

The diagnostics mainly rely on *in-situ* mass spectrometry and *ex-situ* transmission electron microscopy (TEM) - for a comparison of the two methods see chapter 8. The former is conducted using a TOFMS with reflectron (Stefan Kaesdorf, RFT50), specifically designed for the detection of large masses, which allows electron impact ionization as well as laser-ionization of the constituents in the doped helium droplet beam. The latter takes place at the Institute for Electron Microscopy and Nanoanalysis located in the neighboring building, which provides transmission electron microscopes capable of achieving atomic resolution and containing detectors for chemical analysis. Complementary, a quartz crystal microbalace (QCM) and a quadrupole mass spectrometer (QMS) are used for measuring the dopant mass flow and the gas composition in the DC, respectively. Recently, a UHV-transfer system (UHV-Suitcase, Ferrovac GmbH) was added which allows us to remove and transport surface deposited samples to external diagnostics without breaking the vacuum. This transfer system is designed to run solely on battery power for three days, which enables the transfer of samples to any facility all over the world.

The following sections present a more detailed description of the parts contributed by the author.

2.2 Helium Droplet Beam

In the SC, helium droplets can be created by expanding pressurized ($p_0 = 10$ - 100 bar) high purity He (99.9999%) through a nozzle ($d_0 \approx 5\,\mu$m diameter) cooled to cryogenic temperatures ($T_0 < 20$ K). Especially for the generation of very large droplets, the lowest possible nozzle temperature is required. A skimmer (diameter $400\,\mu$m) that shapes the beam is placed shortly after the nozzle and the beam is then guided through the subsequent chambers. Only a fraction of the helium flow through the nozzle contributes to the beam. Consequently, the excess-helium, which does not pass the skimmer, has to be efficiently removed from the SC which requires a huge throughput of the vacuum system. For this purpose, an oil diffusion pump with a nominal throughput of 12000 l/s is installed on this machine.

In the first setup, the nozzle design by Markus Koch [79] was adopted on our machine, albeit using a more powerful cold head (Sumitomo RDK-408D2). This closed cycle refrigerator is able to provide a cooling power of 1 W at 4 K. Following the same estimations as in Ref. [79], this design in combination with the better cold head should have been sufficient to meet the objectives for our machine ($T_0 < 5$ K). However, in the experiments no temperatures lower than 6.5 K were reached. Most likely, this discrepancy was caused by the thermal resistance of the copper cord connecting the end-plate of the cold head with the nozzle ((3) in Fig. 2.2). Furthermore, the heat flow over the wires of the temperature sensing diode and the heating resistor for the temperature control were underestimated, as copper has a strongly increased thermal conductivity at cryogenic temperatures [157].

As a consequence, a new design, developed by the author of this thesis, was realized, significantly reducing the thermal resistance between the nozzle body and the end-plate of the cold head ((3) in Fig. 2.2). Additionally, all copper wires were replaced by Manganin wires, a copper-nickel-manganese-alloy exhibiting a low thermal conductivity, even at cryogenic temperatures. In the previous design, cold head and nozzle were connected *via* flexible copper cords, because of concerns that the cold head might pass on vibrations to the nozzle. In the new design, nozzle and cold head are no longer mechanically decoupled, but this turned out not to be an issue. The direct connection of the nozzle to the cold head in the new design required the whole setup to sit on a manipulator. There, a low cost approach using nuts on three threaded rods as an adjustable tripod for the cold head flange turned out to provide sufficiently precise and stable positioning (Fig. 2.3).

With the new design, an ultimate temperature of $T_0 = 3.8$ K was reached in operation with $p_0 = 20$ bar stagnation pressure, allowing to access the Rayleigh-breakup regime which yields the largest droplet sizes (Fig. 2.4).

Characterizations of helium droplet sources similar to the one used in this work have already been presented elsewhere [48, 79, 84, 142, 151]. The data given in these refer-

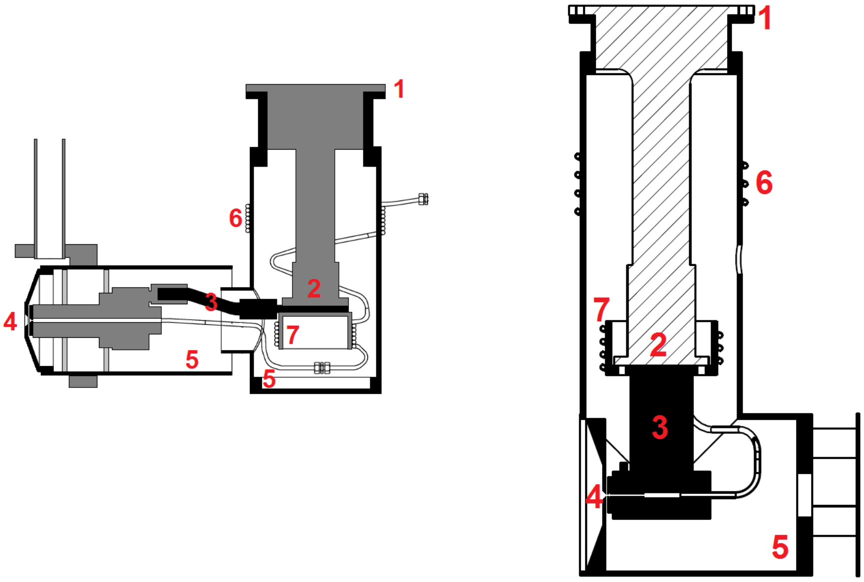

Figure 2.2: Schematics of the old (left) and new (right) nozzle design. (1) coldhead, 1st stage; (2) coldhead, 2nd stage; (3) thermal connection to nozzle; (4) nozzle; (5) radiation shield; (6) 1st helium precooling; (7) 2nd helium precooling

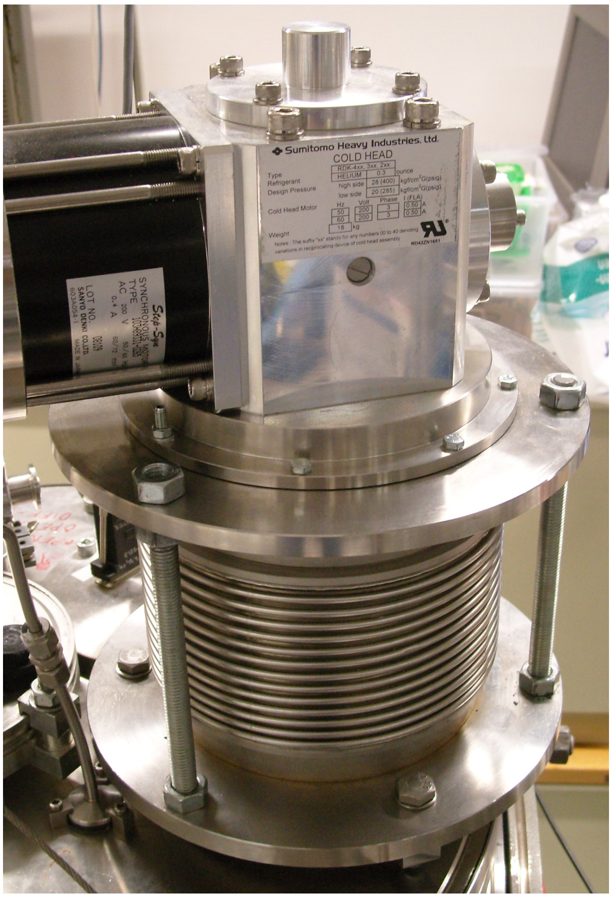

Figure 2.3: Adjustable tripod for the positioning of the nozzle.

ences corresponds very well to the results obtained with our apparatus. Figure 2.4 gives an overview of the mean droplet sizes as well as the corresponding formation mechanism depending on the nozzle temperature and the stagnation pressure. Thereby, the droplet size distributions are reported to have a lognormal (higher T_0) or exponential (lower T_0) shape, which means that they are rather broad [150]. Besides the size, also the velocity of the droplets as well as the total He-flux depend on the source conditions [48, 142].

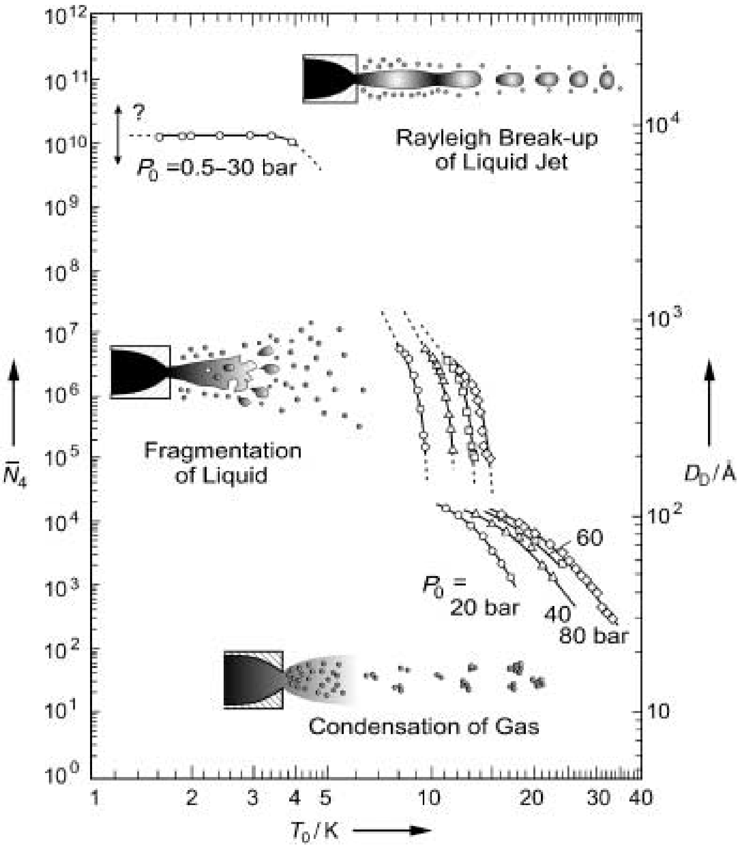

Figure 2.4: Mean He-droplet size (number of atoms $\bar{N}$, diameter D_D) depending on the stagnation conditions (stagnation pressure p_0, nozzle temperature T_0) for a nozzle with 5 μm diameter. This graph is reprinted with permission from Ref. [151], Copyright (c) 2004 Wiley-VCH Verlag GmbH & Co. KGaA.

2.3 Droplet Doping

After creating a droplet beam, the second step in our experiment is the doping of the droplets, which happens by passing the He_N-beam though different cells containing the desired dopant in the gas phase. These doping cells are located in a separate vacuum chamber, the pickup chamber, which was newly designed in the course of this thesis.

Design of the Vacuum Chamber

A 6-way cross (flange size ISO DN250) serves as PC. Front and back flange of this chamber are reserved for the lead through of the helium droplet beam that has to pass a second skimmer (diameter 3 mm) at the exit of the PC. On the bottom and top flange, a large turbo pump (Oerlikon Turbovac 1000C, 1000 l/s) and a cryo-trap are mounted, respectively. In order to be able to service the pickup-cell inside the chamber comfortably, one of the side flanges was left blank, while all necessary feed-throughs where mounted on the other side flange. All these flanges are mounted using Viton-O-rings as seals. Inside the chamber a frame consisting of aluminum profile rails was set up to mount the pickup cells on. Again, the rail system guarantees maximum flexibility in terms of positioning as well as a quick exchange of doping cells. As the pickup-cells require regular maintenance the PC needs to be vented frequently. In order to reach a sufficiently low base pressure within a short period of time, a bake-out system using commercial light bulbs as heating elements inside the vacuum chamber was employed. In contrast to heating tapes, this system heats up the inside of the chamber faster and the light bulbs can be pointed selectively towards critical positions.

Design of the Pickup Cells

In order to dope helium droplets with a desired species, this species has to be brought into the gas phase. For metals, this means that the solid sample has to be heated until a sufficiently high vapor pressure builds up inside the doping cell. For the synthesis of nanoparticles, usually temperatures shortly above the melting temperature of the respective metal are needed. For the current experiments, high electrical currents and the connected magnetic fields are no concern. Therefore, simple resistively heated crucibles (Ted Pella, alumina coated tungsten wire basket, style 6) can be used to heat up the dopants. In order not to damage other elements inside the chamber, the crucibles are housed in water cooled radiation shields.

Within this work, two different designs of metal doping cells were employed (see Fig. 2.5). In the first design (Fig. 2.5, left image), the crucible is covered with a tantalum-sheet with a slit-shaped aperture, which is placed below the beam. This way, a beam of dopant atoms can be created, which crosses the helium droplet beam. Thereby, the cover of the crucible reduces the loss of dopant atoms as well as heat radiation

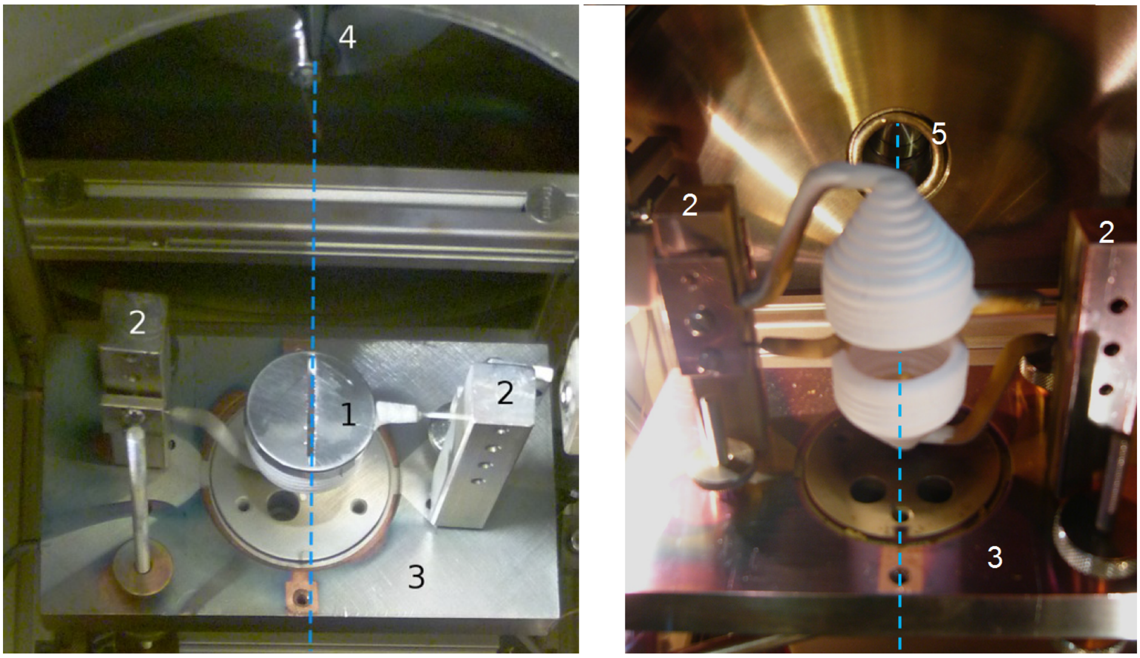

Figure 2.5: Two different doping cell designs, photographed without the cooling shields. The dashed line indicates the position of the helium droplet beam. The numbers indicate the Ta-aperture (1), the Cu-electrodes which hold the crucible(s) in position and provide the heating current (2), the water-cooled base-plate (3), the skimmer at the exit of the chamber (4) as well as the inlet of the He_N-beam (5).

losses. When doping the droplets heavily with this doping source design, conservation of momentum leads to a deflection of the He_N beam, and the beam no longer passes the skimmer before the DC. To overcome this problem, the tantalum sheet was removed and a second crucible was placed above the first, mirrored around the beam axis (see Fig. 2.5, right image). With the beam passing between the two crucibles the dopant atoms can hit the beam coming from different directions, so that the overall momentum transfer to the droplet beam can be neglected.

A stable and reproducible measurement of the dopant temperature is a crucial aspect in the experiments, because temperature changes as small as 2 % can have a large influence on the dopant vapor pressure and hence the pickup conditions. During the operation of the doping cells, it turned out to be difficult to conduct reliable and reproducible measurements of the crucible temperature. Placing an unprotected thermocouple inside the crucible is not an option as the metal dopant species is molten during the doping process, which contacts the wires and therefore corrupts the measurement. When using a protective husk for the thermocouple, buoyancy leads to repositioning of the thermocouple upon melting and therefore the measurements are not reproducible. When clamping the protective husk to prevent repositioning, a comparatively large heat-flow from the melt to the clamps occurs. In this case significantly more heating power is required, which means that the maximum reachable temperature decreases. Furthermore, the husk is cooler than the melt and the measured temperature can no longer be related to the dopant temperature, especially during heatup or cooldown.

A solution to this problem is to measure the electrical resistance of the heating wire of the crucible, which is temperature dependent.

$$R_T = R_{20} \cdot [1 + \alpha \cdot (T - 20)] \qquad \text{with} \qquad \alpha_{tungsten} = 0.0044\,K^{-1} \tag{2.1}$$

The wiring from the power supply to the crucibles is realized using $> 25\,\mathrm{mm}^2$ cross-section copper wires which contribute only a small fraction of the total resistance. Hence, the voltage and current measurement provided by the power supply is sufficiently accurate with respect to the overall uncertainty of this method to determine the temperature. Naturally, the electrical connections of the crucibles are not at dopant temperature, which leads to an offset between the actual temperature and the temperature calculated from the resistance. However, this measurement is reproducible and can be calibrated by observing melting plateaus. Being able to use the output signals of the power supply (EA-PS 9080-100) for the automated temperature control has the additional advantage that the control software is easy to program and less prone to errors.

In the current layout three different doping cells can be placed on the rail system at most (regularly two) and the resistively heated designs are limited to temperatures $\leq 2000\,\mathrm{K}$. If higher temperatures are required an electron bombardment heating system [124], tested on a different machine in the institute, can be retrofitted, reusing many parts of the current design.

Additionally, a pickup-cell for gaseous dopant species is employed in the PC, but has not been used within the experiments relevant for this thesis.

2.4 Diagnostics

Layout of the Diagnostics Chamber

An existing vacuum chamber equipped with many access-ports was adapted to house the diagnostics. A previously installed Mu-metal shield was removed and two additional view-ports (gray in Fig. 2.7), enabling laser-ionization in the TOFMS, were welded onto the chamber in the university workshop.

Following the flight path of the droplet beam, the features of the DC are (see Fig. 2.6):

- UHV-Transfer-System
- Time-of-flight mass spectrometer
- Substrates for transmission electron microscopy
- Quartz crystal microbalance
- Quadrupole mass spectrometer

These tools are described in more detail in the following paragraphs.

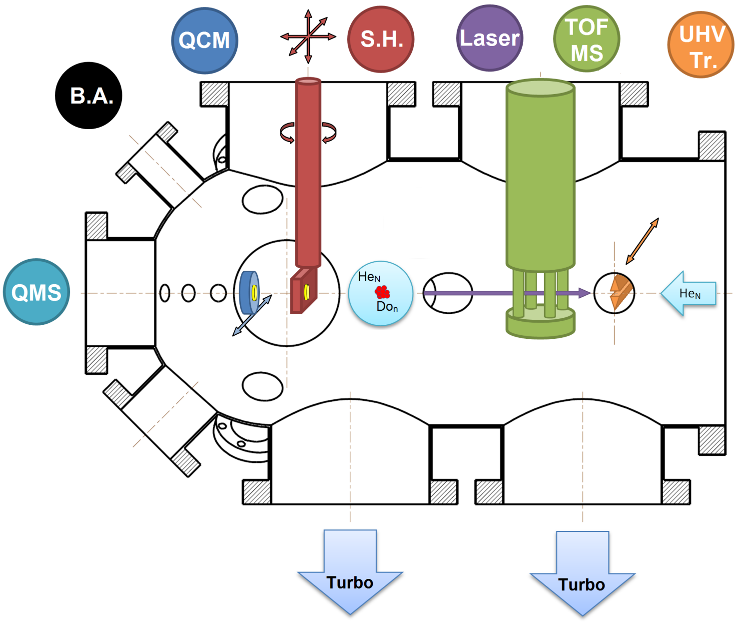

Figure 2.6: Scheme showing the positions of the instruments in the diagnostics chamber. The He$_N$-beam enters the chamber from the right side. QMS ... quadrupole mass spectrometer, B.A. ... Bayard-Alpert pressure gauge, QCM ... quartz crystal microbalace, S.H. ... sample holder, TOFMS ... time of flight mass spectrometer, UHV Tr. ... UHV transfer system

Vacuum Transfer System

Experiments with reactive substances such as *e.g.* chromium showed that it is crucial to be able to transfer the produced nanoparticles to external diagnostics without exposure to ambient conditions. For highly reactive species, UHV conditions are required at all times in order to keep the nanoparticles in a pre-reactive state. For this purpose, a commercial transfer system (UHV-Suitcase, Ferrovac GmbH) was purchased, which allows the introduction of suitable substrates into the droplet beam using a wobblestick with calipers. After depositing nanoparticles on the substrate, the sample can be removed from the beam and stored inside the suitcase along with other samples in a storage shelf. Using a lock-system, the suitcase can be disconnected from the DC without breaking the vacuum in either of them. The suitcase is designed to be able to run on battery power for three days and to maintain UHV-conditions during that time, which enables transport to external diagnostics all over the world.

Time-of-Flight Mass Spectrometer

The TOFMS with reflectron installed on this machine (Stefan Kaesdorf RFT50) was customized to support a steeper angle (55°) of the ionizing laser beam. Using the regular setup (45°) was prevented by the geometry of our vacuum chamber (Fig. 2.7).

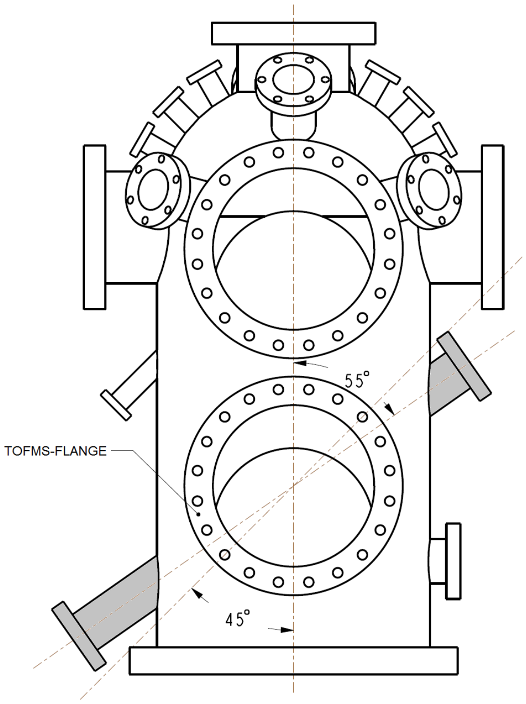

Figure 2.7: Vacuum vessel housing the diagnostics. The flanges marked in gray were added to the existing chamber, to enable laser ionization in the TOFMS.

This TOFMS was especially designed for the detection of heavy particles ($m \geq 20000\,\mathrm{amu}$) and serves as control instrument to monitor the nanoparticle synthesis. For this purpose, the He_N - dopant-particle system is ionized by a pulsed electron- or laser-beam. During the ionization and extraction phase the ionized dopants usually leave the He_N - host and the bare dopant particles are detected. Thereby, the flight time of a particle until it impacts on the detector is a characteristic for its mass, hence a time-resolved measurement of the ion-current yields a mass spectrum. Chapter 8 provides a detailed discussion of mass spectrometry on metal nanoparticles using electron impact ionization.
Additionally, performing resonance enhanced multi-photon ionization (REMPI) spectroscopy with tuneable lasers enables to gain electronic spectra of dopant atoms, molecules and clusters in helium nanodroplets. Mass spectra obtained by photo-ionization complement electron impact ionization spectra and reveal additional insight into the cluster formation process and cluster properties. So far, laser ionization has only been applied for demonstration purposes, the implementation of further laser systems as well as systematic experiments will be the topic of future projects.

Surface Deposition Unit

The substrates for surface depositioning are mounted on a six-axis manipulator, which is a functional overkill but this specific manipulator was recovered from the cannibalized previous machine and overhauled, and was therefore available. In our experiments, the manipulator is used to adjust the sample position in x-,y- and z-direction and to swivel (around the vertical axis) the samples in and out of the He_N beam. Thereby, the option to swivel the whole setup is advantageous in terms of quickness, it takes less than a second to move the substrates into deposition position as well as to unblock the beam. Furthermore, the option to face the samples towards a side flange enables the implementation of a simple home-made quick release sample holder, which allows to place and remove the samples though the side flange. By venting the chamber with dry nitrogen and using the quick release sample holder, the exposure time of the samples to ambient conditions (especially oxygen) can be minimized.

In most experiments it is advantageous to produce more than one sample. Therefore, the home-made holder for the TEM substrates is designed to hold two or more substrates, and switching between the different substrates is realized by rotating the holder around the manipulator axis parallel to the He_N-beam (see Fig. 2.8).

In addition to providing the positioning, the sample holder is connected to a cooling finger *via* a flexible stranded copper wire. By filling the finger with liquid nitrogen, the sample holder can be cooled down to $\approx 120\,\mathrm{K}$ (heat conduction losses). On the other hand, by placing a small commercial light bulb as heating element on the bottom of the finger, the sample holder can be heated to $\approx 420\,\mathrm{K}$. The ability to heat the substrate before deposition turned out to be advantageous in order to reduce contamination on the substrate and the option to deposit nanoparticles on cooled substrates (suppressing

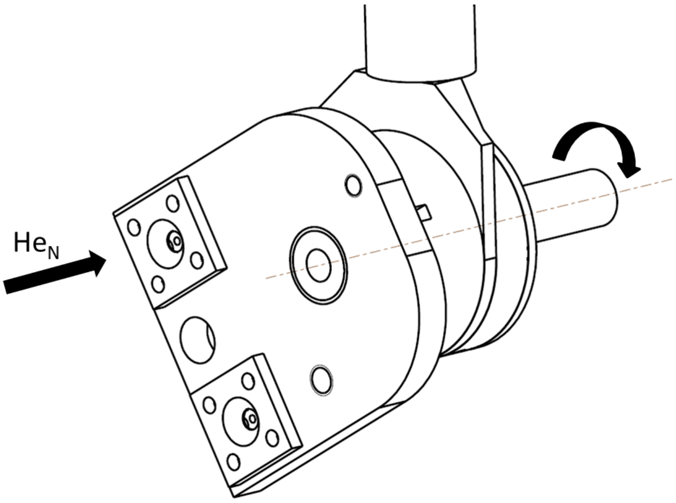

Figure 2.8: Sample holder for two TEM-substrates and lead through for the He$_N$-beam. The switching between the two substrates is realized by rotating the holder around the manipulator axis parallel to the He$_N$-beam.

diffusion effects) led to new insights into the thermal stability of nanowires [154].

Quartz Crystal Microbalance (QCM)

In order to determine the deposition time necessary to reach the desired surface coverage for subsequent microscopic studies, the mass flow of nanoparticles carried by the He$_N$ beam has to be measured. Typically, this mass flow is very low (between 10^{-6} and 10^{-3} μg/cm^{2}s), and therefore measuring it is challenging. A device that is sensitive enough to measure such small mass flows is the quartz crystal microbalance. Its measurement principle is based on the measurement of the resonance frequency of the shear-oscillations of a piezo-quartz. As mass is deposited on the quartz crystal, the resonance frequency f of the oscillation system changes by Δf and allows a very precise measurement of the deposited mass m using the Sauerbrey-equation:

$$\Delta f \approx -\frac{2f^2}{Z}m \tag{2.2}$$

with Z being a constant, depending on the density and shear modulus of the quartz. In the measurements with the QCM a constant temperature not only of the quartz crystal itself (linear thermal expansion changes the resonance frequency of the crystal) but also of the electronics, which is essentially an LC-resonator, is absolutely crucial. Temperature changes as small as 0.05 K/min can yield virtual mass changes of the same order as the signals. To resolve the temperature issue, the crystal as well as the electronics are temperature stabilized using Eurotherm controllers, and the coaxial cable between the electronics and the feed-through of the vacuum chamber is thermally isolated using foam plastics. In addition to controlling the temperature, the measurement is conducted under UHV-conditions, with a prior bakeout of the QCM and the vacuum chamber, in order to avoid adsorption and desorption effects. With these measures, the displayed mass of the QCM stays for hours within ±2 digits ($\hat{=} \pm 0.002\,\mu\mathrm{g/cm^2 s}$) in the idle state. With basically no drift, the long measurements needed for determining very low flow rates still yield reliable data.

Using the QCM, not only the nanoparticle mass deposition rate, but also mass gain or loss due to chemical reactions can be measured. For this purpose, nanoparticles are deposited on the QCM while the base pressure in the vacuum chamber is in the UHV-range. Then a precision leak valve is used to dose the desired reactant into the chamber. Upon chemical reaction the mass of the deposited particles changes, which is detected time resolved. This way chemical reaction rates can be determined. For future experiments it is intended to implement heating and cooling options in order to be able to measure reaction rates at different temperatures.

Quadrupole Mass Spectrometer (QMS)

The QMS installed on the machine is applicable for masses between 0 and 200 amu, which limits the device basically to residual gas analysis. While similar machines often use an on-axis QMS to detect helium droplet fragments He_x with $x \geq 2$, the TOFMS is used for this task here. Therefore, an off-axis position was chosen for the QMS, which means that the total helium flux in the beam is represented by the signal at 4 amu, "integrating" over all helium droplet sizes. Comparisons between the TOFMS-signal at 8 amu and the QMS-signal at 4 amu showed good correspondence which makes both signals a good measure for the helium droplet flux in the beam. During experiments, monitoring the time-dependent He-signal (4 amu), or rather the quotient of the He-intensities with and without doping [102], gives us an additional parameter to control the doping intensity (evaporation of He upon doping). This is of special importance when producing nanoparticles that are too large to be detected by the TOFMS.

Chapter 3

Exemplary Results

The presentation of the experimental results of this work, in the form of peer reviewed journal articles (chapters 6-8), is rather concise. Interpretations and conclusions presented in these chapters are based on the interplay of all diagnostic tools available on the machine. In order to give an introduction for readers not familiar with the helium droplet technique, this chapter includes a discussion of exemplary results of the individual diagnostic techniques separately.

3.1 Mass Spectrometry

Undoped Helium Droplets

When measuring the undoped droplet beam with the TOFMS, the results are somewhat counter-intuitive and shall therefore be discussed briefly. In mass spectrometric measurements, the helium droplet beam is visible as a long series of peaks, separated by 4 atomic mass units (helium comb). In the TOFMS measurements (at $T_0 = 13\,\mathrm{K}$ and $p_0 = 20\,\mathrm{bar}$) around thousand adjacent peaks are visible (see Fig. 3.1). If the nozzle temperature is reduced and hence the droplet size increases, peaks at higher masses start to vanish until only the first 100 peaks of the comb remain (at $T_0 \leq 8\,\mathrm{K}$ and $p_0 = 20\,\mathrm{bar}$).

To understand this behavior, the abundance and stability of the droplets have to be considered. For an efficient ionization of the droplets in the beam, an electron beam with an energy of 89 eV is used. Thereby, the large amount of excess energy in combination with the very weak binding energy between the helium atoms can lead to fragmentation of the droplets. As the nozzle is cooled down, the droplet size shifts towards larger droplets, but the total intensity is distributed among many more mass channels, which means that the intensity at a specific mass is very low. Consequently, at higher temperatures (*e.g.* $T_0 = 13\,\mathrm{K}$ and mean droplet size of ≈ 2000 He atoms), the concentration of the intensity on fewer mass channels enables the detection of larger droplets or fragments. In contrast, at $T_0 \leq 9\,\mathrm{K}$, which yields mean droplet sizes of more than 10^6 helium atoms, only frequently occurring small fragments yield enough signal to be visible in the mass spectra.

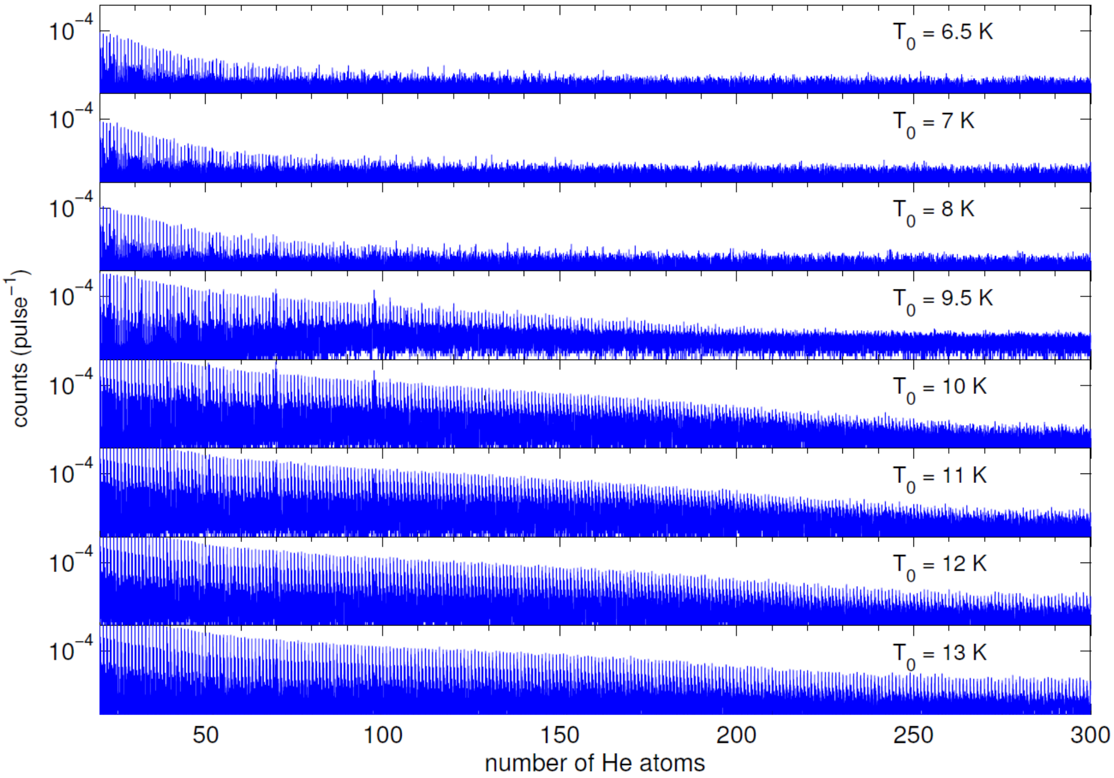

Figure 3.1: Mass spectra of the He droplet beam for different nozzle temperatures T_0 at constant stagnation pressure $p_0 = 20\,\mathrm{bar}$.

Doped Helium Droplets

The difficulty discussed above also applies for the detection of heavy dopant clusters. Additionally, the decreasing sensitivity of the detector for higher masses plays a role for the detection of large metal clusters. Just like the helium droplets, dopant clusters also follow a certain size distribution, which gets wider the larger the clusters get. Wider size distributions consequently mean less intensity for a specific mass channel, and hence a lower probability for detection. Furthermore, most elements have more than one stable isotope, which means that clusters with the same number of atoms can correspond to different masses; the intensity of the corresponding peaks in the mass spectrum follows a multinomial distribution. In the mass spectra of polyisotopic dopants, the peaks stemming from two clusters (Do_n) with $n_1 = x$ and $n_2 = x + 1$ start to overlap at sufficiently large x. In this case an assignment of the peaks in the mass spectrum to certain cluster sizes becomes impossible.

The following Figs. 3.2 and 3.3 show typical mass spectra obtained from doped helium droplets. In addition to the peaks corresponding to the bare clusters, also peaks corresponding to pure helium droplets as well as $\mathrm{Do}_n\mathrm{X}_m$ compounds are visible, where the X either stands for He or residual gas (mostly H_2O) picked up along the doplet trajectory.

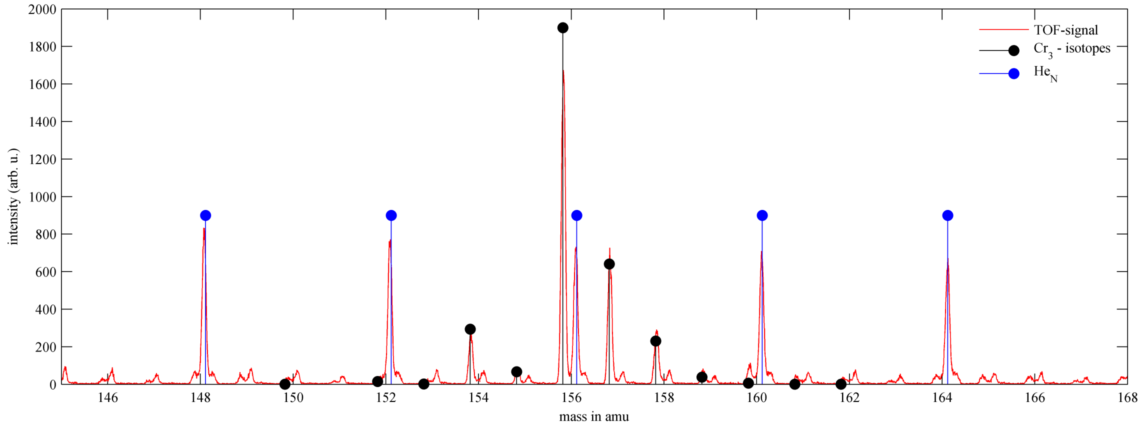

Figure 3.2: Multinomial intensity distribution of the Cr_3-cluster in the mass spectrum. The mass resolution is sufficient to see the peaks stemming from pure He_N separately due to the mass defect (*e.g.* double peak at 156 amu).

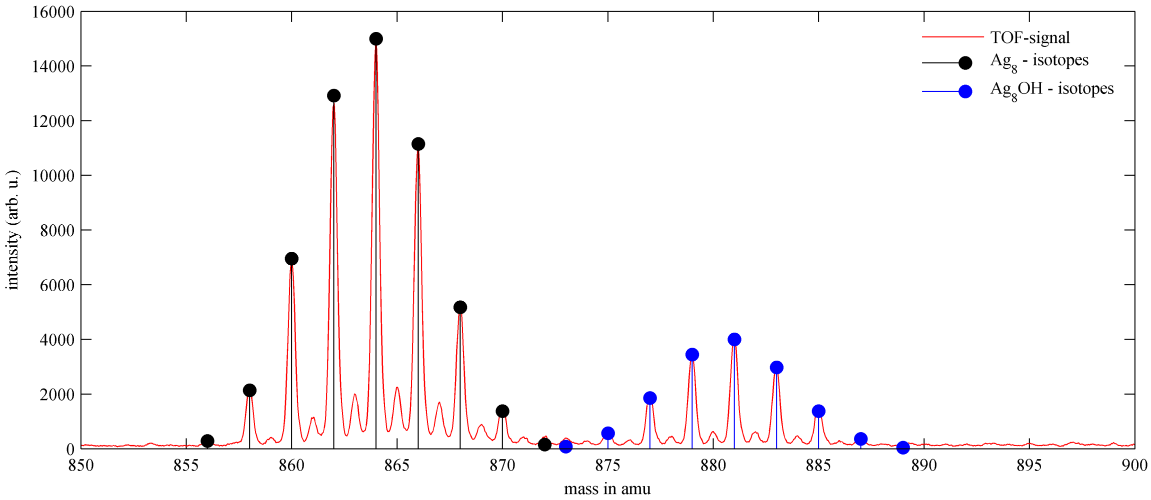

Figure 3.3: Multinomial intensity distribution of the bare Ag_8-cluster in the mass spectrum followed by Ag_8-clusters with an attached OH-molecule.

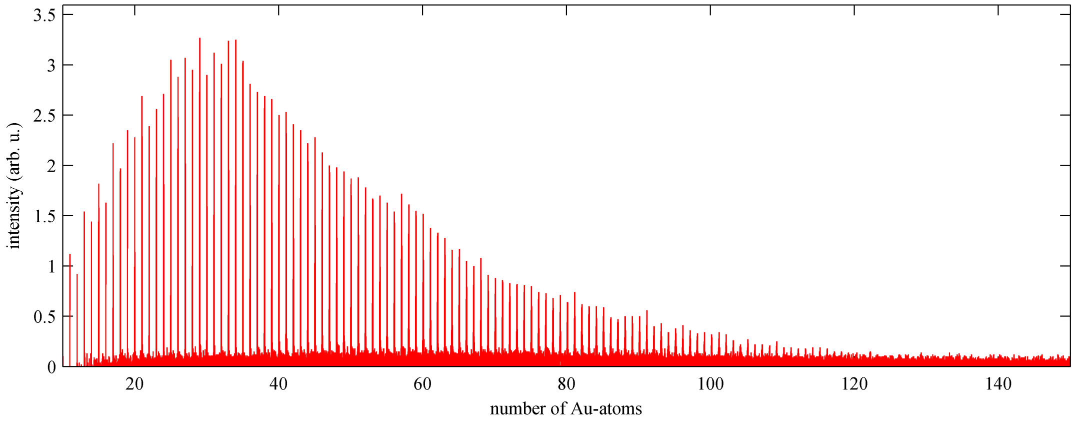

Figure 3.4: Intensity distribution of differently sized Au-Clusters (experimental conditions: $T_0 = 9\,\mathrm{K}$, $p_0 = 20\,\mathrm{bar}$, $T_{Au} = 1100\,°\mathrm{C}$)

3.2 Pickup Characteristics

Another educative experiment is the observation of the intensity of certain mass peaks in the TOF-spectrum as a function of the doping cell temperature. An increased cell temperature yields a higher vapor pressure of the dopant and hence more pickup. Because of the initial droplet size distribution and the fact that the pickup process is a statistical process, helium droplet experiments will always result in a certain dopant cluster size distribution. At lower doping cell temperatures, small clusters dominate, while at higher temperatures, the intensity of larger clusters increases at the expense of the intensity of the smaller ones. The absolute intensity seen in the graph (Fig. 3.5) depends on the specified mass region to sum over. The set summation limits exclude the intensity in possibly present Au_nX_m-peaks, which would lead to a lower signal at the mass of the bare cluster. In addition to the masses of the Au-clusters, the signal at 8 amu (corresponding to He_2) was logged, which originates solely from He-droplets, in contrast to the 4 amu signal, which might also stem from already evaporated He atoms. The binding energy released by the formation of larger clusters at higher temperatures leads to the shrinking of the droplets and hence a decreased He_2-signal. In a strongly simplified picture, neglecting the helium droplet size distribution, the mean He-droplet size ($6.4 \cdot 10^4$ helium atoms [48] at the experimental conditions of Fig. 3.5) and the amount of beam attenuation (*e.g.* $\approx 20\,\%$ at 1100 °C in Fig. 3.5) can be taken to calculate the size of the produced clusters. Knowing the amount of energy carried away by

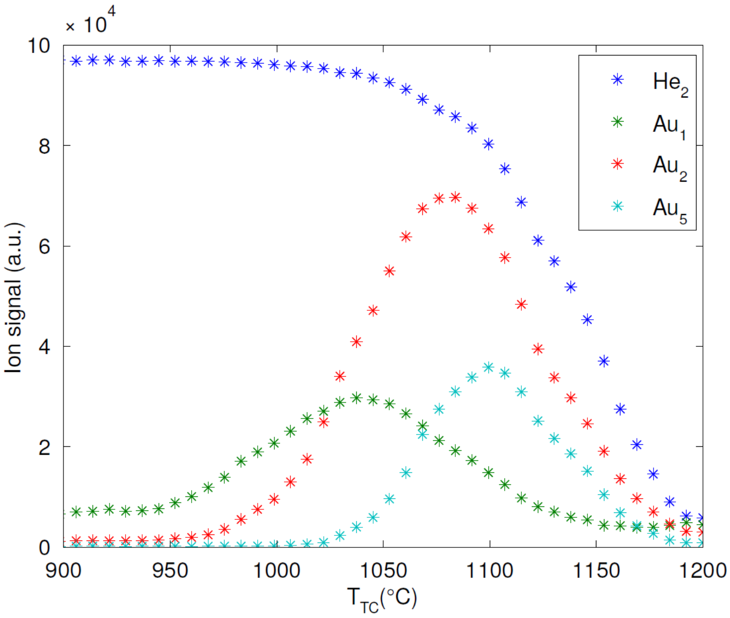

Figure 3.5: Intensities of different Au-clusters (Au_1, Au_2 and Au_5) and the helium droplet beam (measured at 8 amu) as a function of the doping cell temperature. The nozzle temperature and the stagnation pressure were held constant at $T_0 = 10\,\mathrm{K}$ and $p_0 = 20\,\mathrm{bar}$ during the whole experiment.

the evaporated helium atoms (He-loss ≈ 1600 atoms / eV) leads to the conclusion that ≈ 8 eV of binding energy have been deposited into the droplets in the given example. Using the following formula [60],

$$E_b = \phi + 2^{\frac{1}{3}} \cdot (\frac{De}{2} - \phi) \cdot n_{\mathrm{Au}}^{-\frac{1}{3}} \tag{3.1}$$

the amount of binding energy (E_b) of a Au_5-cluster can be estimated (using the bulk cohesive energy ϕ and the dimer binding energy De) to be ≈ 9 eV. This means that the mean clusters size in the discussed experiment (at 1100 °C) should be approximately 5 Au atoms. The actual He_N size distribution of course leads to a broad dopant cluster size distribution containing significantly smaller (as seen by the intensities of Au_1 and Au_2 in Fig. 3.5) and significantly larger clusters.

3.3 Nanoparticle Deposition

A short introduction into surface deposition of nanoparticles embedded in helium droplets has already been given in section 1.4. In the current configuration, nanoparticles can be deposited on three different solid surfaces, namely the substrates introduced by the wobblestick of the UHV-suitcase, the quick-release sample holder and the quartz crystal microbalance. All of these elements can be moved in and out of the droplet beam. Thereby, their position can be checked with a telescope, which is positioned on the beam axis and faces at the back end of the apparatus.

Using the wobblestick, previously prepared substrates, which can be stored inside the suitcase, can be introduced into the droplet beam. After the experiment, the deposited nanoparticles can be stored in the UHV-suitcase and transported to external diagnostics while remaining under UHV-conditions. So far, this device has only been used to transfer samples to a scanning probe microscope (group of L. Grill) at the University of Graz. One exemplary image of these investigations is shown below (Fig. 3.6).

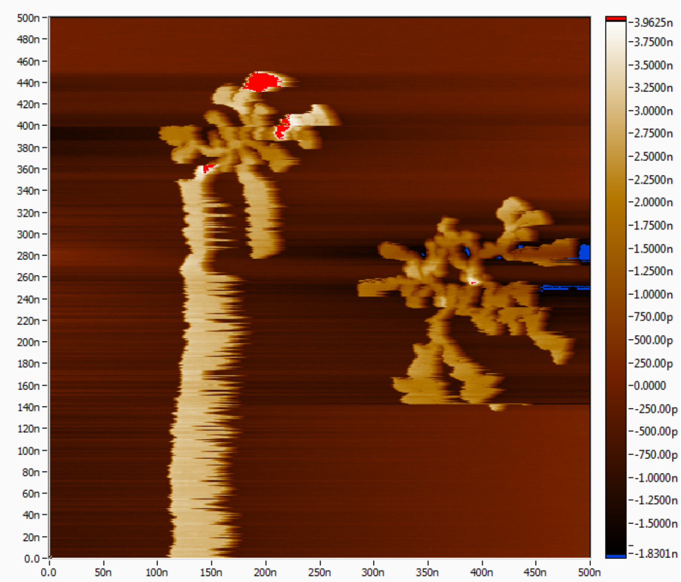

Figure 3.6: STM image of Au-clusters on an HOPG surface. The high mobility of the clusters on the surface leads to the formation of ramified structures. Experiments done by C. Nacci and L. Grill (Physical Chemistry Department, University of Graz), unpublished data.

While the samples produced for electron microscopic investigations are usually transported in a vacuum-vessel, they are briefly exposed to ambient conditions during the extraction from the analysis chamber and during the introduction into the microscope. Due to their high surface to volume ratio, nanoparticles are in general much more reactive than their bulk counterparts. Even short exposure to oxygen can lead to a complete oxidation of the entire particle, which may change all of the particles' properties. In order to avoid problems caused by oxidation, among other reasons, the first experiments on the machine were carried out using Ag and Au as dopants. Characteristic images of nanoparticles produced under different experimental conditions are shown below (Fig. 3.7).

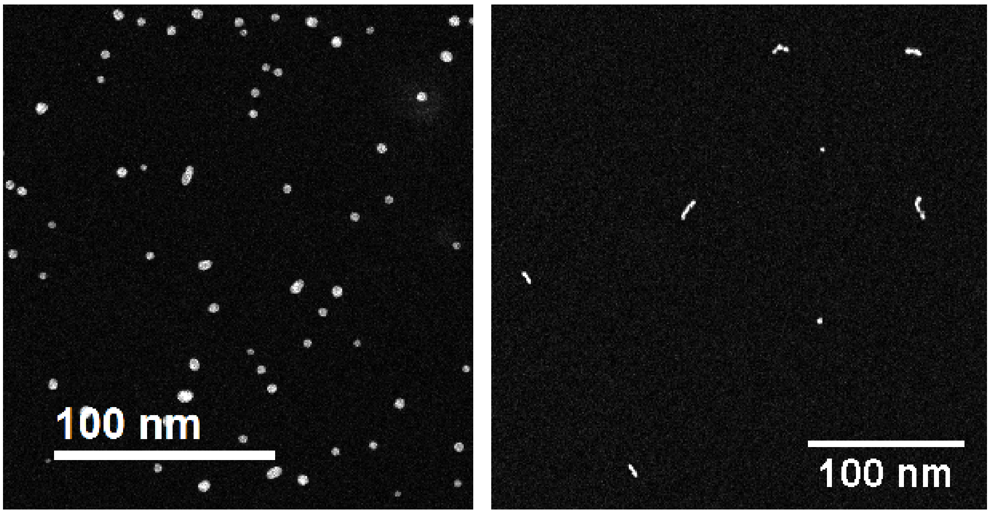

Figure 3.7: Typical HAADF-STEM images of spherical (left) and elongated (right) Au-nanoparticles on an a-c TEM substrate. The change from spherical to elongated particles occurs between $T_0 = 8\,\mathrm{K}$ and $T_0 = 7\,\mathrm{K}$ at a stagnation pressure of $p_0 = 20\,\mathrm{bar}$.

In order to be able to investigate nanoparticles made of more reactive substances in their pre-reactive state in the transmission electron microscope, a vacuum transfer holder is available at the Institute for Electron Microscopy and Nanoanalysis. A suitable docking port for this holder will be added to our machine in the near future.

In order to get the desired surface coverage in deposition experiments, the deposition rate can be measured using the quartz crystal microbalance (see section 2.4). A typical experiment consists of three steps: At first the mass is monitored without deposition to see if there is any drift. The biggest source for drift, which is the temperature of the crystal and the electronics is efficiently suppressed by the employed temperature control. Then, nanoparticles are deposited onto the crystal, whereby the Au-coating of the crystal leads to a sticking coefficient very close to unity. As can be seen in Fig. 3.8, the deposition rate is usually very smooth, *i.e.* the production process is very stable. Finally, the deposition is turned off and the mass is monitored again for a couple of minutes to check for drift. In the absence of drift, as in Fig. 3.8, even very small deposition rates can be measured by extending the measuring time. With the knowledge of the deposition rate, the time to reach a certain surface coverage on the substrates can be calculated.

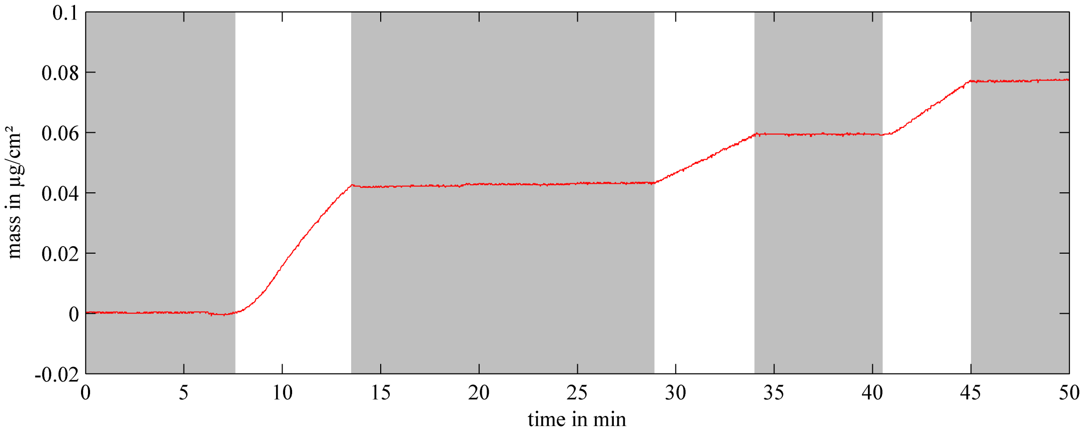

Figure 3.8: Typical measurement of the deposition rate. In the shaded areas the gate valves were closed and hence no mass was deposited - possible mass changes are mostly related to drift. The constant slope during the deposition phases (white background) shows that the synthesis process is a very steady process.

Besides the purpose discussed above, the microbalance can also be used to monitor chemical reactions of the deposited nanoparticles. Since the microbalance is operated in a UHV-environment and the crystal is covered by a chemically inert gold layer, adsorption and desorption effects as well as chemical reactions of the residual gas with the surface are not expected to play any role. Once nanoparticles are deposited on the microbalance, a desired reactant can be dosed into the chamber *via* a leak valve. If a chemical reaction between the deposites and the reactant takes place, the mass on the microbalance changes. When knowing the partial pressure of the reactant in the chamber, a reaction rate can be determined by fitting the time evolution of the mass-graph. The graph below shows an exemplary experiment where chromium nanowires are at first deposited and then oxidized (Fig. 3.9). In order to avoid additional reactions of the reactant gas with the substrate during step IV in Fig. 3.9, the reactant is dosed into the chamber prior to the experiment until the mass measured by the microbalance no longer changes. Afterwards, the leak valve is closed again and the experiment can be started as soon as the reactant no longer appears in the mass spectrum of the residual gas. Possible desorption effects during nanoparticle deposition can also be monitored by looking at the mass spectrum of the residual gas. By utilizing the heating element of the temperature stabilization of the crystal, such experiments may be repeated at different substrate temperatures in order to determine temperature dependent reaction rates.

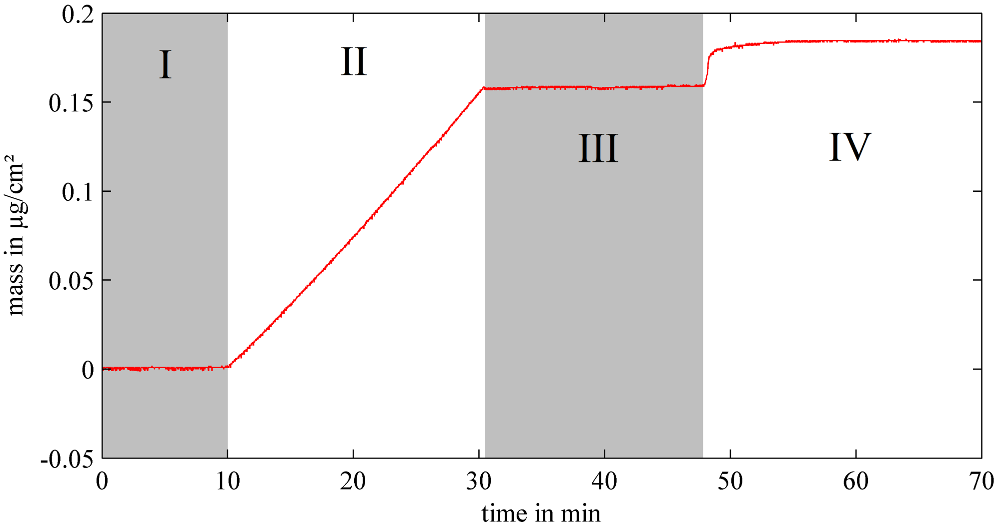

Figure 3.9: Typical measurement showing the mass gain due to chemical reactions (step IV). During steps I and III no mass was deposited, the constant mass confirms the absence of drift. In step II chromium nanowires were deposited onto the microbalance and in step IV oxygen is dosed into the chamber (oxygen partial pressure $= 5 \cdot 10^{-6}$ mbar).

Chapter 4

Computer Simulations

4.1 Model Calculation of the Droplet Doping Process

As stated earlier, the actual size distribution of larger He_N created in our machine cannot be measured with the installed diagnostics. Still, in order to obtain the desired experimental results, it is necessary to know how to set the experimental parameters to get a certain size distribution. Fortunately, several other groups dealt with this problem and their results can be applied [48, 61, 66, 89]. Furthermore, it is necessary to know how high to heat the pickup cells in order to obtain the right amount of doping and, prior to the experiments, to choose the right doping source.

The whole doping process can be modeled in a very simple way. As the droplets are rather slow compared to the atoms of the vapor they pass through, the collision rate is determined by the area impingement rate of the dopant atoms. The density of droplets in the beam is rather low, so that shadowing effects do not play a role. Despite being an open system where dopant atoms are lost due to condensation on the cooling shield, the dopant vapor density can be estimated by the equilibrium vapor pressure at the doping cell temperature. Almost every collision between dopant atoms and droplets leads to the pickup of the dopant which then aggregates with other dopants inside the droplet. There, the dopant atoms are cooled to droplet temperature and, upon aggregation, binding energy is released, which leads to the evaporation of He-atoms off the droplet ($\approx$ 1600 He-atoms / eV [23, 151]). When producing nanoparticles, the droplets are usually heavily doped, which means that a significant amount of the He in the droplets evaporates, leading to a decreasing pickup cross-section during the doping procedure. When using the crossed beam doping cell (Fig. 2.5, left image) heavy doping can lead to the deflection of the beam (conservation of momentum) so that the produced nanoparticles no longer reach the diagnostics chamber [142]. The symmetric doping cell design largely improves this issue, nevertheless, also with this design the deposition rates measured with the QCM are strongly reduced if all the He in the droplets is evaporated.

A pseudocode of the applied algorithm is stated on the next page. Using only the helium droplet source conditions as well as the dopant cell temperature as input parameters, the final nanoparticle size distribution, which should be present on the substrate after deposition can be calculated. Furthermore, the loss of He in the beam due to

Algorithm 1 Droplet Doping Simulation

```
input experimental conditions (droplet source parameters, doping cell parameters)

create sample of droplets (→ sizes depending on the experimental conditions)

for all doping conditions of interest do
    calculate the vapor pressure (→ dopant density and impingement rate)

    for all droplets in the sample do

        while droplet inside pickup cell do
            get flight distance until next pickup event
            (drawn from exponential distribution)

            if cumulated flight distance > pickup cell length then
                exit while, next droplet in sample
            else
                pickup atom (dopant size = dopant size + 1)
                calculate energy release → shrink the droplet
            end if

        end while

    end for

end for
```

doping is calculated and can be compared to the value measured with the QMS. The algorithm described in this section is applied in chapter 8 to compare results found using two different experimental methods with the underlying theoretical concepts. Chapter 8 shows that theory and both experiments yield very similar results in a certain particle size region, which proves the quality of the theoretical model.

4.2 Model Calculation of the Growth Process

While it is computationally feasible to simulate the nucleation behavior of two dopant atoms in a droplet on quantum-chemistry level [64], the time-scale (milliseconds) and the number of dopant atoms (up to $> 10^5$) in our experiments are out of reach. Based on the complex simulation of the simple system by Hauser *et. al.* [64], a simple model for the growth of large particles in He_N was developed.

The formation of nanoparticles in He_N involves the pickup of single atoms by passing the droplets through a vapor of the desired dopant material and the aggregation into particles inside the droplets. The binding energy released upon nucleation is dissipated by the evaporation of helium from the droplet, which means that large He_N ($N > 10^7$ atoms) are required to grow nanometer sized dopant clusters. A comparison of the doping frequency (given by the beam velocity and the size of the pickup cell) and the two-particle nucleation time (calculated in Ref. [64]) shows that the two processes happen at the same time scale and cannot be treated independently [101]. In the model calculation, dopant atoms are added to the droplet with a certain frequency, where they are spawned with a certain velocity v_0 and they are confined to the volume of the droplet. The number of dopant-atoms added to a droplet, and hence the doping frequency, depends on the droplet size. For simplicity, the doping frequency is held constant during the simulation, neglecting the shrinking of the droplet, which changes the pickup behavior only slightly.

Already during the doping process, the initially separated atoms aggregate and form clusters, depending on the dopant-density inside the droplet. The time it takes for two atoms to form a dimer $\mathit{\Delta} t_a(2)$ is taken from Ref. [64]. As more and more dopant-atoms are added to the droplet, the nucleation rate will increase until equilibrium conditions are reached. In this model, the nucleation frequency ($\frac{1}{\mathit{\Delta} t(j)}$) increases like the number of pairs that can be formed with j particles in the droplet:

$$\mathit{\Delta} t_a(j) = \frac{2 \cdot \mathit{\Delta} t_a(2)}{j^2 - j} \tag{4.1}$$

During the doping and nucleation process, the droplets shrink (evaporation to dissipate the kinetic and binding energy) which leads to a decrease of nucleation time $\mathit{\Delta} t_a(2)$. On the other hand, assuming inelastic collisions, the velocity of particles containing n atoms decreases with larger n because of conservation of momentum,

$$v(n) = v_\lambda \cdot \sqrt{\frac{2}{3\pi n}} \tag{4.2}$$

leading to an increase of $\mathit{\Delta} t_a(2)$ proportional to $\frac{v_0}{v(n)}$.

In the model calculation, every particle is connected to a timer which is adjusted as soon as the conditions (droplet size, number of dopants in the droplet, size/velocity of the particle) change. When the timer of a particle expires, it is merged with another particle. The simulations of Hauser *et. al.* [64] show that particle-particle interactions only have a minor influence on the time it takes for two particles to nucleate. More important are particle mass effects which lead to lower nucleation rates of heavier particles. Hence, the second particle for a merger is chosen among the other particles with a probability based on the velocity of the second particle (*i.e.* mergers with smaller / faster particles are preferred as they sample a larger volume of the droplet). After the merger, the resulting particle is larger and has a lower velocity (affecting its timer) and the initial particles are deleted. This algorithm yields a time evolution of the particle size distribution.

While the addition of atoms or small clusters to an existing particle yields a new spherical particle, the collision of two large clusters may not lead to a complete restructuring of the two collision partners. Therefore, the new particle can exhibit an elongated shape. Whether or not two colliding particles will restructure depends on their temperature during collision, hence, on their size (*i.e.* binding energy released vs. heat capacity) and their temperature prior to the collision. For this reason, the temperature of each particle is calculated classically and tracked during the simulation - particles are heated up due to aggregation and are cooled by the surrounding He-matrix whereby the cooling rate is determined by the surface area of the particle. If the two colliding particles are not heated above a certain temperature, they are considered to form an elongated particle. Of course, a classical calculation can only give an estimation for systems as small as the ones considered here. Without external forces, large particles consisting of smaller beads will assume a ramified form [3]. In the presence of vortices inside the droplets, which exert a guiding force, the resulting particles will be nanowires [49, 50, 87, 145].

The algorithm on the following page shows the working principle of the described model calculation.

The simplifications made in this simulation lead to a linear dependence of the timescales on the starting velocity v_0. In a superfluid particles usually do not experience friction below the so-called Landau-velocity, which is about $50\,\frac{m}{s}$. However, the aggregation process of metal clusters is strongly exothermic and it is not clear if the He-matrix stays in the superfluid state at all times. This or other neglected effects may introduce additional friction and an overall slower aggregation behavior. Taking the starting velocity as a parameter, best correspondence between experiment and simulation was attained when setting $v_0 \approx 10\,\frac{m}{s}$.

As described in chapter 6, this model calculation manages to describe the occurrence of single core and multi core structures, as observed in the experiments, very well: Using a sequential pickup scheme and large enough droplets, two or more separated clusters can survive inside a single droplet until it reaches the second pickup cell, giving rise to separated cores of the first dopant embedded in the second dopant material. Furthermore, also the transition from spherical particles to elongated structures at large

Algorithm 2 Particle Growth Simulation

```
input: experimental parameters
(droplet size and velocity, doping cell length and doping rate)

for run number $j = 1$ to $n_{max}$ (for statistics) do
    initiate timers

    while simulation time < specified end time do
        calculate current 2-particle nucleation time

        if doping timer expires then
            add new particle to the droplet
            reset doping timer
        else if nucleation timer of any particle expires then
            merge the particle with expired timer with another particle
            (faster particles are chosen more likely for a merger)
            reset nucleation timer
        end if

        update the size of the dopant(s)
        update nucleation timers
        progress in time
    end while

end for
```

droplet sizes is described reasonably well.

4.3 Molecular Dynamics Simulation

In order to calculate the time evolution of a system, a set of differential equations has to be solved. Finding a solution for such a problem becomes difficult already for very small systems. A different approach is finding a solution numerically, using molecular dynamics (MD). In MD one divides the time into certain time steps Δt and sets the velocity and the acting forces (acceleration) within these time steps as constant. The forces, particle positions and velocities for a single time step are calculated from the situation in the previous time step(s). In this thesis the "Velocity Verlet Algorithm" is applied. The basic idea of this algorithm is to do a Taylor-expansion of the particle coordinates at $\mathrm{t} = \mathrm{t}_0$ and, using this, calculate the new positions at $\mathrm{t} = \mathrm{t}_0 + \Delta\mathrm{t}$, neglecting higher order terms. The "Velocity Verlet Algorithm" is a two step algorithm where at first the new particle positions for the current time step are calculated by:

$$\vec{x}(t_0 + \Delta t) = \vec{x}(t_0) + \vec{v}(t_0) \cdot \Delta t + \frac{\vec{F}(t_0)}{2m} \cdot \Delta t^2 \tag{4.3}$$

then, using the new positions, the acting forces $\vec{F}(t_0 + \Delta t)$ are calculated, and finally the new velocities of the particles are determined:

$$\vec{v}(t_0 + \Delta t) = \vec{v}(t_0) + \frac{\vec{F}(t_0) + \vec{F}(t_0 + \Delta t)}{2m} \cdot \Delta t \tag{4.4}$$

The respective computer program works according to the following scheme:

Algorithm 3 Simulation of the Landing Process

```
input: parameters and initial condition

for $t = 0$ to $t_{max}$ do
    calculate new atomic positions

    calculate distance matrix $\Delta r$

    calculate forces between the atoms in the particle (depending on $\Delta r$)
    calculate forces exerted by the substrate potential

    calculate new velocities of the atoms

    apply thermostat
end for
```

In the case of infinitely small time steps, this method depicts the actual physical process. For increasing time steps, the deviation from the actual physical situation increases. For suitably small time steps the system still evolves physically correct, which means that energy and momentum are conserved. If the time steps are chosen too long, the simulation can diverge and the obtained results will be worthless. With MD, the size of the systems which can be simulated is only limited by the available computing power.

In order to keep the computational effort reasonable, a potential which only depends on pairwise distances (Δr) is desired for the calculation of the acting forces. In the literature there are several semi-empirical effective pair potentials available, which account for two-body interactions and three- or more-body interactions but only need pairwise distances [27, 39, 129, 143]. Still, the computationally most expensive part is the calculation of the pairwise distances which scales quadratically with the size of the simulated system. In some cases, however, long range interactions can be neglected *i.e.* in the simulation there won't be any interactions between atoms further apart than a certain cutoff radius. Even if this is not the case, small position changes are only critical for neighboring atoms, but the relative positions Δr and therefore the forces between distant atoms stay very much the same over many time steps. This opens the possibility to update only the pairwise distances and forces of close atoms every time step while assuming the forces of distant atoms to be constant. Implementing these considerations by applying a clever indexing scheme can reduce the computational effort enormously, especially in systems containing a hundred atoms or more, without losing much accuracy. The improved computer program may look like the following scheme:

Algorithm 4 Optimized Simulation of the Landing Process

```
input: parameters and initial condition

calculate nearest neighbors for fast indexing

for $t = 0$ to $t_{max}$ do
    calculate new atomic positions

    calculate distance matrix $\Delta r$ (full calculation only every $N$ runs)
    update fast indexing (only every $N$ runs)

    calculate forces between particles
    (forces between close particles are updated every run, others every $N$ runs)
    calculate forces exerted by the substrate potential

    calculate new velocities of the atoms

    apply thermostat
end for
```

Within this thesis, an MD simulation was conducted to determine the changes in morphology of the deposited nanoparticles caused by the landing process (see chapter 5).

Chapter 5

Molecular Dynamics Simulation of the Landing Process

This chapter corresponds to the publication
"Molecular Dynamics Simulation of the Deposition Process of Cold Ag-Clusters Under Different Landing Conditions"
by **Philipp Thaler**, Alexander Volk, Martin Ratschek, Markus Koch and Wolfgang E. Ernst in *The Journal of Chemical Physics*, **140**, 044326 (2014),
which was written by the author of this thesis.

The author of this thesis was responsible for:

- development of the computer simulation program
- interpretation of the results
- author of the publication

The contributions of the co-authors are listed below:

- A. Volk: assistance in interpreting the results
- M. Ratschek: implementation of the computer program in FORTRAN for better performance
- M. Koch: supervision, editing
- W.E. Ernst: supervision, editing, funding

Abstract

We present a series of molecular dynamics simulations on the surface deposition process of initially free silver clusters ($\mathrm{Ag_n}$) with different sizes ($n = 100 - 2000$) and morphologies. During the whole deposition process the morphology of the clusters was studied as a function of the landing conditions. These conditions include variations of the depth and range of the substrate potential as well as the thermal coupling to the surface and a variation of the impact velocity of the free clusters. Depending on the applied conditions the clusters' final form ranges from spread out fragments via deformed and restructured heaps to quasi unchanged spherical clusters sitting at the surface. Under certain landing conditions larger clusters retain their initial multiply twinned morphology upon deposition, while smaller ones undergo structural transitions to form single domain particles. Furthermore, the occurrence of a structural transition depends on the initial structure - initially decahedral clusters tend to conserve their morphology better than icosahedral ones. The same behavior can also be observed in our experiments, where silver clusters were grown in helium nanodroplets and subsequently deposited on amorphous carbon substrates.

5.1 Introduction

In the age of nanotechnology, metal clusters containing a few hundred or thousand atoms are of particular interest. They are bridging the gap between isolated atoms and the bulk material but differ from both in their physical and chemical properties. Additionally the properties of clusters of the same material can change with the cluster sizes and/or the cluster morphology.[11, 29] In that sense, clusters of a certain size and morphology can be viewed as a new separate material. Possible applications lie in the fields of catalysis,[65] optics[95] and magnetism.[16] The knowledge of the atomic structure of a cluster is the starting point to understand its characteristics.[12] It is well known that free nanometer sized clusters can occur in crystalline (i.e. single domain) and non-crystalline (i.e. multiply twinned but highly symmetric) morphologies.[10, 105] The non-crystalline morphologies are common especially at small sizes and often clusters take the form of icosahedrons (Ih) or truncated decahedrons (Dh) which are highly symmetric arrangements with six or one fivefold symmetric axes, respectively.[106] It has been observed with various analytical methods that for noble metal clusters produced with different beam techniques, these non-crystalline morphologies are not limited to small cluster sizes (few hundred atoms) but also occur in clusters of a few nanometers diameter (several thousands of atoms).[81, 126, 155] In this size range the bulk structure, which is face centered cubic (fcc), should be energetically preferred, suggesting that the growth kinetics play an important role in the creation of these non-crystalline structures.[11]
The unique experimental environment provided by helium nanodroplets ($\mathrm{He_N}$) makes them particularly interesting for studying the influence of growth kinetics.[23, 150, 151, 155] Note that in this paper the capital N denotes the number of helium atoms in a droplet while the lower case n denotes the number of silver atoms in a cluster. With a

temperature of only 0.37 K [62] and cooling rates as high as 10^{14} K/s, [94, 133] $\mathrm{He_N}$ are exploited as nano-cryostats which offer the possibility of sequential single atom pickup for cluster growth.[150, 151] Very recently clusters grown inside $\mathrm{He_N}$ were deposited on surfaces with various deposition rates and surface coverages.[20, 37, 38, 49, 102, 112, 155, 158] Subsequent high resolution transmission electron microscopy (HRTEM) images reveal information about their structure. [20, 155] It has been stated that $\mathrm{He_N}$ lead to very special landing conditions.[2, 102, 123] With an impact velocity between 200 and 300 m/s the kinetic energy per cluster atom lies way below the binding energy, furthermore the $\mathrm{He_N}$ around the cluster may act as a cushion which softens the landing.[2] This is fortified by calculations which predict shells or pockets around the cluster with a helium density higher than the one of bulk liquid helium.[68, 150]

In a previous HRTEM study of $\mathrm{Ag_n}$ synthesized and deposited in $\mathrm{He_N}$ we found a large abundance of fcc clusters in a size range where the non-crystalline structures should be preferred. To explain this effect it seems important to take into account the cluster's interactions with the substrate as these may influence the final structure.[155]

The motivation for the present theoretical study was to explain this behavior and investigate the cluster substrate interaction in general, as for technical application it is important to know how the structures of supported clusters are influenced by the deposition conditions as well as the choice of the substrate. Numerous theoretical studies on cluster deposition processes can be found in literature, but can not be discussed here in detail (see eg. Ref. [123] and references therein, especially [25, 28]). Our simulation focuses on the morphology evolution of clusters with different initial sizes and/or morphologies during the deposition process for a variety of different landing conditions, in contrast to most of these publications. It should be noted that with most beam techniques it is difficult or even impossible to create neutral clusters with a single morphology and a narrow size distribution. Furthermore, not only during the growth process but also during the deposition process kinetics are important, leading to different final structures even if the initial conditions are identical. Thus an interpretation of the final results without knowing the path of getting there can be very complicated.[26] Computer simulations can overcome these experimental limitations and shine light on the kinetics by analyzing the cluster at any time during the deposition process. This makes computer simulations an essential component of structural studies.[26]

We report the results of molecular dynamics simulations of the deposition process of $\mathrm{Ag_n}$ with different sizes and different initial morphologies for a variety of landing conditions, the influence of the $\mathrm{He_N}$ was incorporated indirectly by the choice of the initial temperature and the landing conditions. The sweeps of the different parameters defining the landing conditions were centered around the values we expected to be present in our experiment. [155] The simulations show that there is a set of conditions where the clusters stick to the substrate and larger clusters retain their initial morphology while smaller ones undergo structural transitions, as it is seen in the experiment. The influence of several parameters on the final morphology is discussed. We show that besides the depth and range of the substrate potential the orientation in which the cluster approaches the substrate as well as the random thermalization events influence the final form of the deposited cluster.

5.2 Model and Methods

The simulations in this article follow a sequence of three steps: At first a geometrically ideal cluster with the desired size and either Ih, Dh or fcc morphology is created by adding correspondingly ordered shells around the center atom. The formed cluster is then relaxed to find the interatomic distances preferred by the underlying potential and thermalized to 0.37 K as provided by the helium environment in the experiment. For computational reasons the further influence of the $\mathrm{He_N}$ on the cluster is only taken into account by a reduced impact velocity. This seems to be justified by the fact that $\mathrm{He_N}$ is only weakly interacting with dopants in general and is expected to evaporate upon surface impact. Finally the cluster approaches the substrate where it interacts with the surface potential and the thermostat algorithm.
For the simulations atom-atom interaction, atom-surface interaction and a thermostat function were implemented in a Velocity Verlet algorithm with variable time steps (length of a timestep is set in a way that the spatial step of every atom is smaller than a certain threshold). It should be noted that neither of these interactions are treated with quantum-chemical methods, which would be computationally too demanding for a system of $> 10^3$ Ag atoms on an amorphous carbon substrate. To evaluate structural changes during the whole simulation process a common neighbor analysis (CNA) was conducted,[40] as well as a calculation of the local bond order parameters (BOP). [141] All these points are treated in more detail in the following sections.

Interactions inside the cluster

It is well known that many properties of metals cannot be modeled by using only two body interactions. Therefore, a lot of (semi-) empirical many-body potentials have been introduced for the simulation of metal clusters.[27, 39, 129, 143] In a work by Shao et al.[139] the minimum energy structures obtained by using the two similar many-body potentials out of Refs. [129, 143] (both based on the second moment approximation to the tight binding model) are compared. The minimum energy structures computed with the Sutton-Chen (SC) potential for different cluster sizes are generally less strained and more ordered. A difference between the methods is no surprise, considering the diverse local minima in the potential energy which are of nearly the same depth. In our survey we apply the SC-potential (eq. (5.1)) to calculate the atomic interactions inside the cluster since our HRTEM observations show ordered structures.[155] Parameters of this potential for some transition metals are given in Ref. [143].

$$U_{\mathrm{SC}} = \epsilon \left[\sum_{\mathrm{ij}} \left(\frac{a}{r_{\mathrm{ij}}} \right)^{\nu} - C \sum_{\mathrm{i}} \sqrt{ \sum_{\mathrm{j}} \left(\frac{a}{r_{\mathrm{ij}}} \right)^{\mu} } \right] \tag{5.1}$$

The parameters ϵ, a and C are determined fitting the model to the experimental values of the bulk cohesive energy and the crystal lattice parameter. The exponents ν and μ are limited to integer values for computational reasons. This limitation leads to minor deviations of the calculated bulk modulus from the experimental value.[143]

Interactions with the substrate

We are interested in situations where there is an attractive force between the substrate and the atoms of the cluster. Cluster-substrate interactions, especially with amorphous carbon substrates as used in our experiment are difficult to model. Therefore, we take a simplified approach and use a Morse-potential with various sets of parameters to calculate the forces which the substrate exerts on the different atoms of the cluster.

$$U_{\mathrm{Morse}}(r) = D_{\mathrm{M}} \cdot \left(\left(1 - e^{-a_{\mathrm{M}} \cdot (r - R_{\mathrm{M}})}\right)^2 - 1 \right) \tag{5.2}$$

Here r is the distance of a cluster atom to the surface of the substrate, D_{M} controls the depth of the surface potential, a_{M} controls the stiffness of the surface potential and R_{M} controls the position of the potential minimum. The a_{M} and D_{M} are varied in different simulation runs, the position of the potential minimum R_{M} is kept constant since it does not change the shape of the potential. Changing the position of the minimum would lead to the same situation for the clusters only at different absolute distances to the surface. Hence the substrate is modeled as rigid, flat and homogenous all over its surface. As a basis, the parameters of the Morse potential are chosen to correspond to the data given in Ref. [9] (see TABLE 5.1) for silver on a carbon surface.

Thermostat algorithm

During the deposition, the cluster's kinetic energy and the binding energy of the cluster to the substrate will be dissipated. In the final state the cluster will assume the substrate temperature, which was set to 300 K. To achieve this, atoms in proximity to the surface are thermalized by means of a modified Andersen thermostat.[7] The original Andersen thermostat picks random cluster atoms at a chosen frequency, erases their velocity vector and generates a new one, randomly drawn from a Boltzmann distribution at a given temperature. With a non-zero collision frequency the Andersen thermostat leads to a canonical distribution of microstates.[72]

In the present work the interatomic distances are very small and the motion of neighboring atoms are strongly correlated. In this case, randomly reassigning the velocity of a single atom in the center of the cluster means a big perturbation. Our modified algorithm generates thermostat particles which collide elastically with selected atoms of the cluster. As the cluster approaches the surface, cluster atoms closer to the surface than a certain distance threshold are selected randomly with a fixed rate. This surface-distance threshold is fixed at the position where the surface potential reaches 10% of it's minimum value at the far end. The collision rate in our experiments was estimated to be in the order of 10^{12} collisions per second for each atom in contact with the substrate. In our simulations three different rates in this range were considered. High collision rates will lead to a fast dissipation of the impact energy thus hampering morphology transitions. If a cluster atom is selected for thermalization, a thermostat particle is spawned for elastic collision. The thermostat particle's velocity vector orientation is uniformly distributed within a half-sphere pointing away from the substrate surface. The length of the vector is based on the most probable velocity of the Maxwell-Boltzmann distribution at the preset thermostat temperature and varied by a factor uniformly distributed between 0.5 and 1.5. This algorithm models the contact with the heat bath more gently, thereby not perturbing the system as much as an Anderson thermostat in its original form would.

Determination of the cluster morphology

During the whole simulation process the (local) structure of the cluster is monitored by the common neighbor analysis (CNA)[40] as well as by calculating the local bond order parameters (BOP).[141] These two methods are based on different ideas. The CNA method analyzes the environment of a bond between nearest neighbors while the BOP describe the environment of an atom. The results of both methods are in qualitative agreement (as shown later, in FIG. 5.2) and give the same picture of the cluster's structure.

The CNA gives a 3-tuple of integer values (a,b,c) for every pair of nearest neighbor atoms, where a is the number of common nearest neighbors, b is the number of bonds between these neighbors and c is the length of the longest chain found within these bonds. For example when looking at the bond between two atoms on a fivefold symmetry axis one finds this bond surrounded by a ring of five atoms, which, together with the two atoms on the axis, form a pentagonal bipyramid. In this case there are **5** common nearest neighbors (the ring of five atoms) to the two atoms in the tips. Between these five atoms there are **5** nearest neighbor bonds and the length of the longest chain found within these bonds is once around the ring, i.e. **5**, leading to a (5,5,5)-signature. For the characterization of the global structure the relative occurrence of tuples (5,5,5), (4,2,1) and (4,2,2) are calculated, which are related to fivefold symmetry axes (FFA), hexagonal close packed (hcp) local symmetry and fcc local symmetry respectively. In the case of free clusters the relative occurrence of these three signatures is sufficient to distinguish between Ih, Dh, fcc and amorphous morphologies.[15] In our simulations it is a measure for how much of the structure is preserved upon impact and moreover it gives an idea which structure is adopted after the impact, in case a structural rearrangement takes place.

The BOP method associates a set of spherical harmonics with each pair of nearest neighbors. With spherical harmonics it is possible to construct parameters q_{l} which describe the local order and are independent of the choice of the coordinate system:[141]

$$q_{\mathrm{l}}(i) = \left(\frac{4\pi}{2l+1} \sum_{\mathrm{m=-l}}^{\mathrm{l}} |q_{\mathrm{lm}}(i)|^2 \right)^{\frac{1}{2}} \tag{5.3}$$

where

$$q_{\mathrm{lm}}(i) = \frac{1}{N_{\mathrm{n}}} \sum_{\mathrm{j=1}}^{N_{\mathrm{n}}} Y_{\mathrm{lm}}(\theta_{\mathrm{ij}},\phi_{\mathrm{ij}}) \tag{5.4}$$

with N_{n} the number of nearest neighbors, j the index of the nearest neighbors of atom i and $Y_{\mathrm{lm}}(\theta_{\mathrm{ij}},\phi_{\mathrm{ij}})$ the spherical harmonic associated to the pair (i,j).

A set of three parameters (q_4,q_6,q_8) can be used to distinguish between different local structures.[26] Certain areas of the space spanned by these three parameters can be attributed to fivefold axes (FFA) and fcc or hcp local structure likewise.[73] FIG. 5.1 shows a projection of the (q_4,q_6,q_8) - space onto the (q_6,q_8)-plane for a Dh prior to the deposition. The contour lines represent the occurrence of the respective parameter couple with the light color corresponding to low occurrence and the dark color corresponding to high occurrence. The areas attributed to the respective local structures are labeled. The relative abundances of the different local structures are used as a measure for the global morphology. Further, the q_6 parameter is used as a color coordinate in FIG. 5.3 in order to make the morphology more apparent.

To get a simple and unbiased view on the final structure the q_8 parameter defined

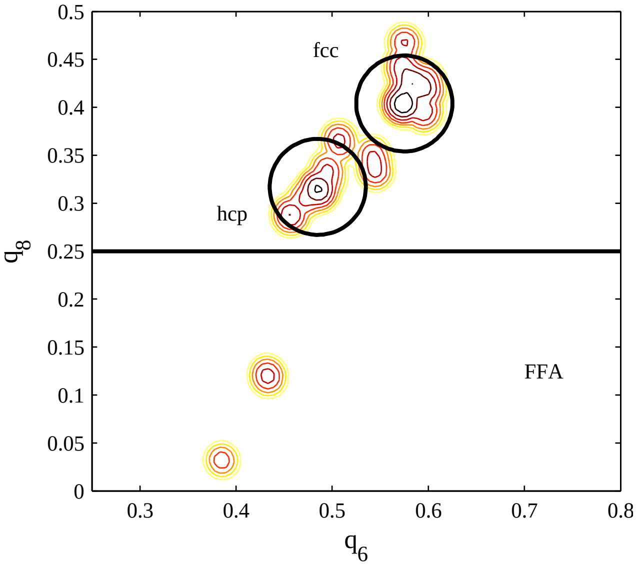

Figure 5.1: (Color online) Projection of the (q_4,q_6,q_8) - space onto the (q_6,q_8)-plane shows the structural information gained from the BOP analysis of a perfect, relaxed Dh prior to the deposition. The contour lines represent the occurrence of the respective parameter couple with the light color corresponding to low occurrence and the dark color corresponding to high occurrence. The contours below the $q_8 = 0.25$ line can be attributed to atoms with a local fivefold symmetry, the fcc and hcp regions are marked with circles. Contours outside the circles do not correspond to FFA, hcp or fcc, but are related to surface atoms or strongly strained points in the structure. Note that the small fraction of atoms with fivefold local symmetry contains most of the structural information.

in equation 5.3 was used. As displayed in FIG. 5.1, this parameter is lower than 0.25 if the local structure is fivefold symmetric and higher than 0.25 for fcc and hcp local environment. With this we define an order parameter

$$O_{\text{mean}} = \frac{\langle p_{\text{final}}(q_8 < 0.25)\rangle}{p_{\text{initial}}(q_8 < 0.25)} \tag{5.5}$$

where $p_{\text{final}}(q_8 < 0.25)$ and $p_{\text{initial}}(q_8 < 0.25)$ denote the percentage of atoms with q_8 smaller than 0.25, thus with local fivefold symmetry, in the structure prior to the deposition and after the deposition respectively. The angle brackets in the numerator symbolize the average taken over the 10 simulation runs with different random orientations for a certain set of parameters.
The normalized standard deviation

$$O_{\text{std}} = \frac{std\,(p_{\text{final}}(q_8 < 0.25))}{p_{\text{initial}}(q_8 < 0.25)} \tag{5.6}$$

indicates the influence of the cluster orientation in the moment of impact. If the final morphology is very susceptible to the initial orientation, the normalized variance will be large and vice versa.
Aside from the non-crystalline structures, fivefold local order only occurs at lattice defects. In our simulations, the formation of such a lattice defect during the impact of an fcc cluster, which creates a noticeable amount of atoms with fivefold local structure, was only observed in very few cases. In general, the percentage of atoms remaining in a fivefold local order after the impact is a good characterization for how well the non-crystalline structure is conserved.
For the characterization of fcc-clusters an order parameter based on fivefold local order, on the other hand, makes no sense. However, when looking on the projection of the (q_4,q_6,q_8) - space onto the (q_4,q_6)-plane (not shown in FIG. 5.1) one sees a much clearer separation between the fcc and hcp region. Therefore, the idea from above still can be used by replacing the ($q_8 < 0.25$) by ($q_4 > 0.15$) which then characterizes atoms with a local fcc structure.

5.3 Results and Discussion

In this section the qualitative influence of several parameters on the morphology of the deposited cluster will be discussed. In the impact energy range considered here (corresponding to the described soft landing conditions in the experiments of Refs. [102] and [155]) no material exchange with the substrate will take place.[123] However, the atoms of the deposited cluster can completely rearrange during the impact. The final morphology of a deposited cluster not only depends on its velocity prior to the collision and the substrate potential, but also on the size of the cluster, its structure prior to deposition, the orientation of its structure with respect to the substrate, the substrate temperature, the thermal coupling to the substrate (thermalization frequency) and other parameters which go beyond the scope of this article.
In this article we do not attempt to cover the whole parameter space mentioned before, but focus on the qualitative effect of some of the parameters: In our simulations we consider 3 different cluster sizes (diameter ≈ 2 / 3 / 4 nm, corresponding to

n ≈ 300 / 700 / 2000 respectively), for each size all three main morphologies (Ih, Dh, fcc), each in ten different random orientations with respect to the substrate. Thus there are 90 different size/geometry situations. Further, we choose three different depths and three different widths of the potential, as well as three different starting velocities and three different thermalization frequencies for our simulations, leading to 81 different environmental conditions. In the following the width of the potential w denotes the width at half of the minimal depth. For the smallest cluster size (2 nm), all environmental conditions were simulated (2430 simulation runs) while due to limitations in computation time, a reduced parameter space was scanned for the bigger clusters. TABLE 5.1 lists the varied energy parameters.

Table 5.1: Energy parameters considered in the sweep. See text for further explanation.

Parameter	values		
Potential depth D_M in K	2500	5000	10000
Potential width w in Å	3.5	1.4	0.7
therm. frequency c in THz	0.4	1.3	3.9
Starting velocity in ms^{-1}	25	100	300

Further on, the landing conditions will be specified by a 4-tuple of numbers $L(klmn)$ where k-n stand for the parameters (rows) in TABLE 5.1 and the numbers themselves denote the column from which the respective parameter is taken. E.g. $L(3112)$ has the potential depth taken from the right column, potential width and thermalization frequency taken from the left column and the starting velocity taken from the center column.

As an example for how to read the results of our simulations, the time evolution of the (local) structure of two clusters approaching the surface with different orientations and different random thermalization pathways but otherwise identical conditions is shown in FIG. 5.2 by plotting the fractions of the three most prominent local structures over time. Note that not all of the bonds/atoms can be assigned to one of the three structures. Therefore the sum of the three fractions in each graph is not equal to unity and neither stays constant over time. This figure contains a lot of information. Firstly it shows the qualitative agreement of the two used structure evaluation techniques (BOP and CNA). Although the graphs with the same gray scale are related to the same local structure (e.g. (5,5,5) and FFA) the calculation method is different and therefore the absolute fractions differ between the methods. Nevertheless, both analyzing methods show the same trend. Secondly it gives an example of how to read the results of the structure evaluation: right at the impact the overall order drops, which can be attributed to an elevated temperature of the cluster. As the cluster is cooled to substrate temperature the overall order increases again. In FIG. 5.2d a migration of fcc atoms towards hcp

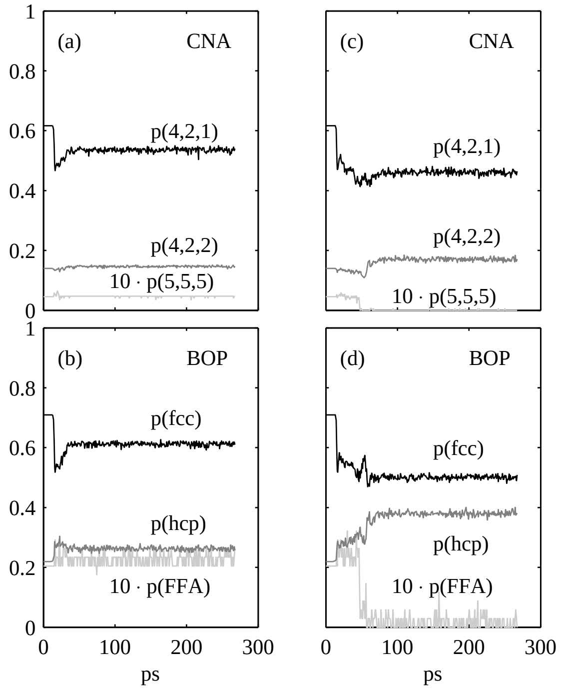

Figure 5.2: Time evolution of two $n = 684$ Dhs (2 columns) with different random orientation with respect to the substrate / random thermalization pathways but otherwise using the same conditions ($L(2222)$). The graphs show the fractions of bonds (CNA) and atoms (BOP) in a certain local order. For a better visibility the p(5,5,5) and the p(FFA) are 10 times magnified. The Dh in the left column keeps its structure while the one in the right column completely looses its fivefold axis. The first kink in the graphs corresponds to the moment of impact on the substrate surface which takes place at about 15 ps.

local structure can be seen, which marks the displacement of a lattice plane in an fcc sub-domain (stacking fault). This also leads to the - in terms of lattice strain - unfavorable fivefold axis being pushed out of the cluster, the FFA fraction basically goes to zero. Thirdly the timescale and the dynamics of the deposition process can be seen. The impact takes place at about 15 ps and in this case the new structures are stable after about 100 ps. One of the clusters (left column) retains most of its initial structure while the other one (right column) undergoes a structural transition upon impact as it can be seen by looking at the fivefold symmetric part. Finally the figure points out the susceptibility of the final structure to the orientation of the cluster in the moment of impact and/or to the random kinetics during the landing process, leading to the conservation of the original fivefold symmetric structure in the one case (left column) and a restructuring into a close packed configuration in the second case (right column).

Final structures: an overview

In the simple model used here, the cluster-substrate binding energy increases proportionally with the width of the potential, in contrast to a diatomic potential. Of the three potential widths considered in this survey, the narrowest only acts on the atomic layer next to the substrate surface, while the widest yields significant attractive forces as far as to the fifth fcc-stacked layer above the surface. In the case of a wide potential, the upper layers press on the layers closer to the surface, which can lead to the collapse of the initial spherical structure into a pancake-like shape (e.g. $L(1111)$). In the case of a narrow and shallow potential, combined with a low starting velocity, the clusters rebound from the surface (e.g. $L(1331)$). Although, in the real experiment the helium droplet surrounding the cluster should prevent rebounding. When going to the other extreme of a wide and deep potential, the clusters get very hot, which can lead to the evaporation of silver atoms. The evaporation / escape of single atoms was observed in some simulation runs (e.g. $L(3113)$), but might also be suppressed by surrounding helium droplet in the real experiment. Also in the parameter space between the extreme cases mentioned above a variety of different final structures is possible. An overview over the resulting structures can be seen in FIG. 5.3.

Interaction with the substrate

An average of simulation results is depicted in FIG. 5.4a which shows the order parameter for the different cluster sizes, averaged over all landing conditions. Applying landing condition $L(3222)$, which we expect to be present in our experiment,[155] we find that small clusters ($n < 300$) undergo a structural transition towards a close packed structure (mixture of fcc and hcp, FIG. 5.3e) while larger clusters are quasi spherical and conserve parts of their initial structure, depending on the random collisions with the thermostat particles and their orientation with respect to the substrate in the moment of the impact. We argue that the reason for this characteristic is the smaller curvature of bigger clusters which enables them to establish a large contact area to the substrate by deforming the existing structure instead of undergoing a structural transition. Hence bigger clusters tend to preserve their initial structure better than smaller ones. Furthermore, large fcc domains are very stable, making larger clusters more stable than smaller ones and Dhs more stable than Ihs. This behavior, where bigger clusters (4 nm, $n \approx 2000$) tend to conserve their structure better than smaller ones and Dhs conserve their structure better than Ihs, can be seen in our simulation runs. However, the deformation of the original spherical shape, defined by the distance of the deposited clusters' the center of mass to the surface of the substrate, normalized by the initial cluster radius, stays nearly constant, independent of size and morphology.

An increase of the depth of the surface potential D_{M} leads to higher impact energies and therefore to temporarily higher temperatures which favor structural rearrangements (FIG. 5.4b). Even more important in the view of changes in the cluster morphology is the width of the substrate potential w (FIG. 5.4c) as it controls the number of atoms influenced by the substrate. The thermal coupling to the surface (described by the

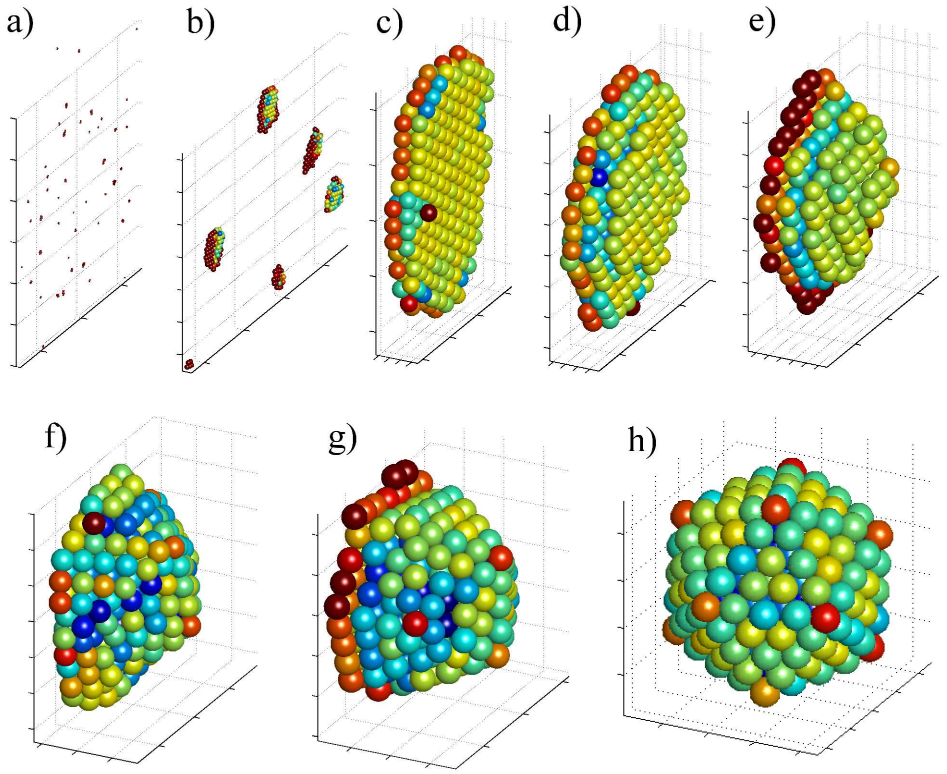

Figure 5.3: Different simulated final morphologies of the initial $n = 309$ Ih. The colors represent the local order given by the q_6 parameter, defined in equation 5.3. Here yellow corresponds to fcc local order, light blue corresponds to hcp local order and dark blue corresponds to the fivefold axes, the other colors are for intermediate states or not classified surface states. All spheres representing the atoms of the clusters shown here have a radius of 1.5 Angstroms, corresponding to the covalent radius. The final structures vary from fragments (a,b / $L(3111)$, $L(3121)$), fcc or hcp stacked mono-, double- (c / $L(1111)$) or multilayer (d,e / $L(1131)$, $L(3222)$) structures to half spherical (f / $L(2213)$), quasi-spherical (g / $L(2233)$) or even spherical (h/ $L(1232)$ and $L(3333)$) clusters, partially or completely retaining their initial morphology. Using the order parameter defined in equation 5.5 the morphologies in e) - h) correspond to order-values of 0.00, 0.35, 0.47 and 0.86 respectively.

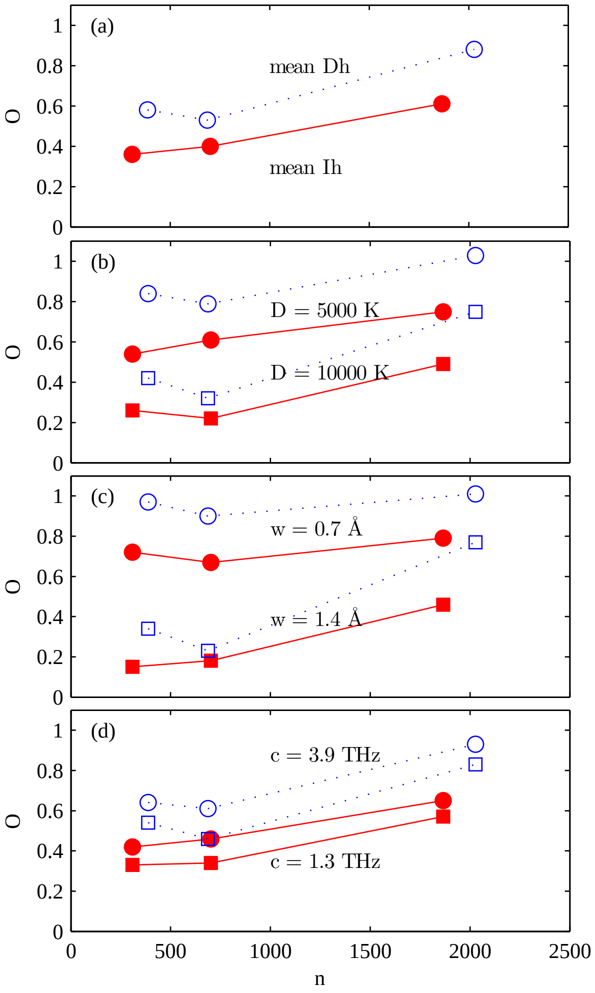

Figure 5.4: (Color online) Size dependence of the order parameter defined in equation 5.5. In all graphs the solid lines stand for the Ihs and the dotted lines stand for the Dhs; the lines are just a guide to the eye. Graph (a) shows the average taken over all simulations conducted, hence only general trends are pictured. In the graphs (b-d) averages over sub-groups of simulations are shown, where only one parameter is picked (indicated by circles and squares) and the others are averaged. For a discussion see section 5.3.

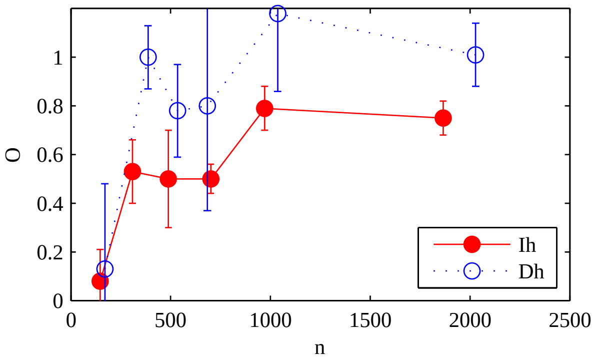

Figure 5.5: (Color online) Size dependence of the order parameter defined in equation 5.5, the landing conditions ($L(3332)$) are kept constant. The uncertainty bars depict the normalized standard deviation of the order parameter, defined in equation 5.6 and show the susceptibility to the orientation in the moment of the impact. The solid line stands for Ih and the dotted line stands for Dh; the lines are just a guide to the eye.

thermalization frequency c) only shows a minor effect within the observed range (FIG. 5.4d). What can be stated is that the better the coupling the faster the energy will be dissipated and the less likely are morphology transitions.

To find an explanation for the kink seen in FIG. 5.4 at the medium cluster size, additional simulations for intermediate cluster sizes were performed using only one set of landing conditions. The results are displayed in FIG. 5.5. As it was reported in Refs. [139] and [14] the stability of clusters depends on the number of atoms in the cluster. Closed shell configurations corresponding to magic numbers show the highest stability. Our cluster creation method produces clusters with a certain radius, meaning that the cluster is symmetric but the shells are not necessarily filled, there might be missing atoms at the tips and/or additional atoms at the faces. Thus it is not surprising that the order parameter defined in equation 5.5 does not increase monotonically with the cluster size. Nevertheless, the trend that bigger clusters better conserve their initial morphology is obvious.

Orientation of the cluster

Our simulations show that the random collisions with the thermostat particles as well as the orientation of the cluster with respect to the surface of the substrate plays an important role, as shown in FIG. 5.2. This figure depicts the time evolution of two identical clusters deposited under identical landing conditions, differing in their orientation with respect to the surface and the random interactions with the thermostat algorithm (note that the average interaction with the thermostat, i.e. collision frequency, etc. is the same in both runs!). One of the clusters retains most of its original morphology while the other undergoes a structural transition. This susceptibility to the orientation and/or kinetic effects is depicted by the uncertainty bars in FIG. 5.5 which are calculated using equation 5.6. In general it can be stated that the impact scenario differs a lot if a cluster approaches the surface with a tip or with a facet. Therefore, for each set of parameters 10 different random orientations were simulated. Given the high symmetry of the clusters, 10 orientations give a good overview of the possible outcomes.

Cluster velocity

Within a large area of the parameter space covered in this article, the starting velocity has very little influence on the outcome of the simulation. As the clusters fall into the surface potential they speed up to velocities much larger than the starting velocities, making the starting velocity irrelevant. The kinetic energy of each atom stemming from the starting velocity in our simulations is much lower than the binding energy of the atoms. Nevertheless, for growing clusters the total kinetic energy grows faster than the number of surface atoms which absorb the collision energy. Eventually this must become an issue, even with the low starting velocities considered here.

Temperature distribution

As described in section 5.2, the cluster temperature was initially set to 0.37 K, the temperature of the helium droplet. Upon impact, the cluster temperature rises to levels above or below the substrate temperature, depending on the landing conditions. Finally the cluster is thermalized to the substrate temperature, which was set to 300 K.

FIG. 5.6 depicts the temperature distribution of the 309 Ih shown in FIG. 5.3 e at different moments during the deposition process. Besides the surface potential, an elevated cluster temperature during the landing process is the main reason for structural rearrangements. The high temperature enables a cluster, which was previously frozen in a multiply twinned configuration, to get out of this local energy minimum and to restructure into the bulk morphology.

As displayed in FIG. 5.6 the temperature on both ends of a cluster can be very different during the deposition process. When averaging the temperature over the whole cluster the information about the hot contact region gets lost. Only looking at the temperature average in the contact region is also misleading. For the graphs in FIG. 5.7 the clusters were cut in quarters and the average temperature of the second quarter next to the substrate was plotted, which seemed to be a good compromise. FIG. 5.7 a shows the temperature progression over time for the cluster in FIG. 5.3 e ($L(3222)$), as well as the clusters in FIG. 5.3 g and h which were deposited under softer landing conditions ($L(2233)$ and $L(1232)$). While in the first case (e) the whole cluster heats up to temperatures above the melting temperature and restructures into an fcc structure, the temperature in the latter cases (g,h) stays far beyond the melting temperature and the clusters retain their morphology. The same conditions as in FIG. 5.3 e were applied to larger clusters (FIG. 5.7 b). These graphs reflect the characteristics which can be seen in the order parameter - while the Ihs with n = 309 and 701 atoms exhibit the same temperature corresponding to about the same value of the order parameter, the Ih with

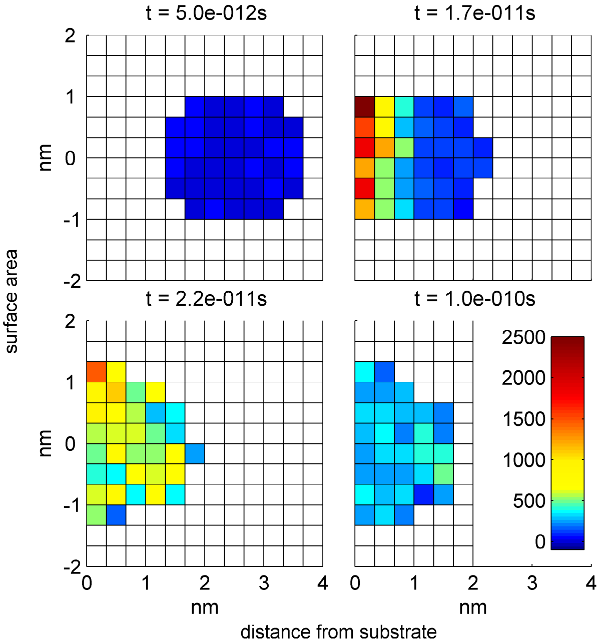

Figure 5.6: Temperature distribution at specific moments during the deposition process (prior to deposition, after the impact, during the structural reorganization, after thermalization) of the cluster shown in FIG. 5.3 e. The temperature scale is in Kelvin.

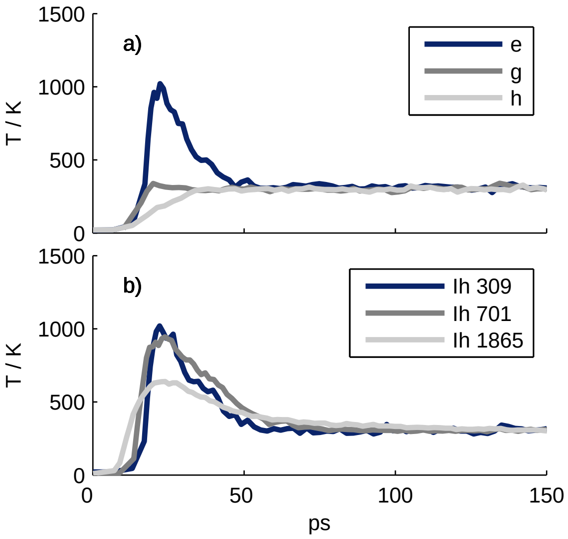

Figure 5.7: Cluster temperature progress during the deposition process a) for a n = 309 Ih under different landing conditions (labels refer to FIG. 5.3) and b) for different sized clusters under the same landing conditions ($L(3222)$).

n = 1865 atoms exhibits a lower temperature, corresponding to a higher value of the order parameter.

Time dependence

As already mentioned when discussing FIG. 5.2 a drop in the overall order can be seen right at the impact which can be attributed to an elevated temperature of the cluster. Depending on the thermal coupling to the substrate the overall order increases again over 50-100 ps following the impact, as the cluster is cooled to substrate temperature. In most simulations the structure then stays stable over the rest of the simulation time. In some cases, however, transitions from fcc local structure to hcp local structure and vice versa were observed. This marks the displacement of a lattice plane in a sub-domain (stacking fault) and may additionally lead to the reduction of the FFA fraction by pushing out the - in terms of lattice strain - unfavorable fivefold axis. Due to limitations in computation time, time dependent effects in the nanosecond range were not investigated. Still, as we observe Ih and Dh morphologies in our experiment, which are also the final morphologies in our simulation when applying $L(3222)$, we are confident that most of the dynamics happening after the impact are covered by our simulations.

Comparison with experimental results

In our experiments, where we use the helium droplet method for synthesizing and depositing $\mathrm{Ag_n}$, [155] as well as in experiments using inert gas aggregation sources a large abundance of big Ih and Dh silver clusters can be found.[11, 126] This is unexpected from a purely energetic point of view but can be explained taking kinetics into account.[13, 14, 15] Additionally, smaller clusters ($n < 700$) mostly adopt an fcc morphology in our experiments. In our last article, we argued that this must be due to interactions with the substrate.[155] In this article we show that there is in fact a set of landing conditions where small clusters undergo structural transitions towards close packed morphologies while larger clusters keep their morphology. All morphology changes seen in our simulations took place from non-crystalline structures (Ih, Dh) to the bulk structure, transitions from fcc clusters to either of the non-crystalline structures were not observed. This also confirms our model that clusters with Ih and Dh morphology actually grow inside the droplet and are not subject to surface effects.

5.4 Conclusions

Motivated by our previous work,[155] which shows an unexpected abundance of small fcc ordered clusters in a deposition experiment, a theoretical survey on the dependence of the cluster morphology of deposited clusters on the landing conditions was conducted. For this purpose geometrically ideal Ag clusters were constructed in different morphologies (Ih, Dh, face centered cubic) and different sizes corresponding to spherically symmetric arrangements. The interactions of the cluster atoms among each other were modeled with the Sutton-Chen-potential (which is a many-body-potential), the interactions of each cluster atom with the substrate were modeled by a Morse-potential whose parameters were altered to scan over different conditions. In the MD simulation the clusters first were relaxed to obtain the interatomic distances preferred by the underlying SC-potential at the initial temperature, which was set to 0.37 K, the temperature of the clusters in our experiment. Then, the clusters approach the substrate (modeled as flat and rigid plane), where they interact with the surface as a function of different landing conditions. Further a modified Andersen thermostat was applied to thermalize the landed cluster to the substrate temperature.

For a wide range in the parameter space the impact velocity (in the observed range) plays only a minor role since the cluster is accelerated to much higher velocities when falling into the potential well. The width and depth of the surface potential are very critical parameters. In case of a narrow potential, where the attractive force decreases significantly within a very short distance from the surface, atoms further away from the surface will not be influenced by the substrate. In case of a wide potential, on the other hand, atoms a few atomic layers away from the substrate also feel a significant attractive force, which can lead to the collapse of the initial spherical structure and the formation of a pancake-like structure. A stronger thermal coupling to the substrate leads to a faster dissipation of the impact energy, thus hampering morphology transitions.

The simulations show that there is a set of landing conditions where large clusters are likely to maintain their initial morphology, except for the atomic layers right next to the substrate surface while smaller clusters restructure into a single domain close-packed morphology.

In our previous work we took HRTEM micrographs of silver clusters, synthesized and deposited in helium nanodroplets, revealing their size- and morphology distribution. Deposited clusters with diameters smaller than 3 nm ($\approx$ 700 atoms) exhibit mostly a single domain close packed morphology while larger clusters are almost exceptionally found in non-crystalline morphologies (Ih, Dh).[155] This behavior is in very good agreement with the simulation results for the parameter set shown in FIG. 5.5.

In many applications of nanoparticles, their behavior close to a surface is of fundamental interest, especially since their properties might be shifted. In order to conduct more sophisticated simulations a closer investigation of the surface-interactions and their dependence on the ambient conditions are necessary.

5.5 Additional Remarks

Experiments [154] more recent than the article above show that diffusion processes on the surface of deposited Ag-nanoparticles play an important role for their final shape, which is observed in the microscope. In the cited article, Ag-nanowires break up into a chain of spherical nanoparticles already below room temperature, similar to Rayleigh-breakup of liquids. Obviously, if nanoparticles change their shape during the time between deposition and imaging in the microscope, they can as well alter their structure within this time.

This offers an alternative explanation for the highly symmetric icosahedral and decahedral nanoparticles found in Ref. [155]. Instead of a shell by shell growth mechanism around a five-fold symmetric seed cluster inside the droplet, which seems to be rather unlikely in the more current picture of cluster-cluster-growth [59], the highly symmetric structure might evolve after deposition by surface diffusion starting from a five-fold symmetric core.

However, even if the starting conditions of the simulations (highly symmetric morphology) in the article above may not correspond to the real experimental situation (supposedly partially chaotic structure, containing smaller five-fold symmetric regions), the statements made in this article remain valid. The simulations only cover a timespan of a few hundred picoseconds, which means they only model effects directly linked to the impact of the nanoparticle on the substrate. They highlight that the choice of the substrate is the crucial parameter which determines the shape (deformation) and structure (single domain, decahedral, icosahedral) of the deposited particles. Furthermore, the simulations show that the internal structure of larger particles is less influenced by the impact than in smaller ones. Starting from a partially chaotic structure this could mean that if a five-fold symmetric core survives the landing process, subsequent surface diffusion leads to the outwards-propagation of the core structure and hence to the highly symmetric morphologies seen in the microscope. Additionally, when modeling the cluster-substrate interactions more accurately using an otherwise very similar code, the simulation predicts the deformation of the nanoparticles during the landing process very well.[59]

Although Ag exhibits a very high surface diffusion coefficient in comparison to other metals, similar restructuring effects cannot be excluded for nanoparticles consisting of other materials.

Chapter 6

Bimetallic Clusters Analyzed by Atomic Resolution Electron Tomography

This chapter corresponds to the publication
"Formation of bimetallic clusters in superfluid helium nanodroplets analyzed by atomic resolution electron tomography"
by Georg Haberfehlner, **Philipp Thaler**, Daniel Knez, Alexander Volk, Ferdinand Hofer, Wolfgang E. Ernst and Gerald Kothleitner; *Submitted July 2015.*

The author of this thesis was responsible for:

- performing of the nanoparticle synthesis
- development of the computer simulation of the growth- and the deposition process
- interpreting the results concerning the growth- and the deposition process
- editing the manuscript paragraphs on particle synthesis and computer simulations

The contributions of the leading author and the co-authors are listed below:

- G. Haberfehlner: performing the electron microscopic investigations, data processing and tomographic reconstruction, authorship of the article
- D. Knez: adaptation of the computer simulation of the landing process, preliminary microscopic investigations
- A. Volk: preliminary experiments
- F. Hofer: supervision (microscopy), editing the manuscript
- W.E. Ernst: supervision(particle synthesis), editing the manuscript
- G. Kothleitner: supervision (microscopy), editing the manuscript

6.1 Main Article

Structure, shape and composition are the basic parameters responsible for properties of nanoscale materials, distinguishing them from their bulk counterparts [11]. To reveal these parameters in three dimensions (3D) at the nanoscale electron tomography is a powerful tool [8, 17, 58, 109, 118]. Advancing electron tomography to atomic resolution in an aberration-corrected transmission electron microscope (TEM) remains challenging though and has been demonstrated only few times for monocrystalline nanoparticles using strong constraints [54, 55, 152], or for single-metallic polycrystalline particles employing extensive filtering [24, 137]. Here we demonstrate atomic resolution electron tomography on Ag/Au core/shell nanoclusters grown in superfluid helium nanodroplets. We reveal 3D morphology and composition of a cluster identifying Au- and Ag-rich regions and we estimate atomic positions without using any prior information and with minimal filtering. The ability to get full 3D information down to the atomic scale allows understanding the growth and deposition process of the nanoclusters and demonstrates an approach which is generally applicable to all types of nanoscale materials.

Metallic nanoparticles consisting of a few thousand atoms are of large interest for potential applications in different fields such as optics [95], catalysis [65] or magnetism [16]. Superfluid helium droplets represent a versatile, novel tool for designing such nanoparticles, allowing fine-tuned synthesis of pure or composite clusters for a wide range of materials [20, 112, 145]. Using ultra-high vacuum (UHV) conditions and getting on without solvents or additives compared to chemical synthesis, the method delivers high purity materials, which can be well controlled in terms of size and composition. In this Letter we investigate core-shell nanoparticles produced using the He-droplet technique. We analyze their structure, composition and morphology at the atomic level by advancing electron tomographic methods to better understand and optimize their unique properties.

Despite significant recent progress in 3D electron tomographic imaging [8, 17, 58, 109, 118], the ultimate goal of resolving position and type of each single atom inside a material remains elusive. The first reconstructions at atomic resolution were demonstrated for monocrystalline particles from few images taken along high-index crystallographic orientations, applying strong constraints in the reconstruction algorithms [54, 55, 152]. For polycrystalline or amorphous materials such approaches are not applicable and a full tomographic tilt series needs to be carried out. Near-atomic resolution of single-metallic polycrystalline particles has been first demonstrated on gold nanoparticles [137], and more recently Chen et al. [24] have mapped 3D dislocations in platinum nanoparticles at atomic resolution using very strong filtering in the Fourier domain. This approach has been used to some success, but has also lead to some controversy [128] and moreover proves unnecessary when careful considerations in the reconstruction are applied to low-noise experimental data. Extending atomic resolution electron tomography to composite materials such as bimetallic polycrystalline nanoparticle, by locating (structure) as well as identifying (composition) atoms in all three dimensions, however, is even more challenging. For this, we adapted the image acquisition scheme to obtain high-resolution projections with improved signal to noise ratio and minimal distortions. Without any prior assumption about the structure, no particular tilt scheme or special filtering, we continue to reconstruct the nanoparticle applying rather standard reconstruction algorithms. Demonstrated for a Au/Ag bimetallic system, we reveal Au- and Ag-rich regions and we estimate atomic positions. We then use this information to answer fundamental questions about the growth of nanoclusters in superfluid helium droplets.

A beam of superfluid helium droplets (T = 0.4 K) [23] is guided through two doping cells containing vapors of the desired dopants (Fig. 6.2a). By passing through the vapor, the He droplets pick up foreign atoms. When adding Ag to the droplet first and Au second in sequential doping cells, a Ag-Au core-shell structure of the cluster is achieved . For TEM observation, the droplet beam is terminated on an amorphous carbon TEM grid, where the helium evaporates while the dopant is adsorbed. The low impact velocity of ≈ 200 m/s as well as the helium, acting as a cushion, ensure so-called soft landing, avoiding structural modification during deposition. The size distribution of the clusters was ranging between 2 nm and 8 nm (Fig. 6.1).

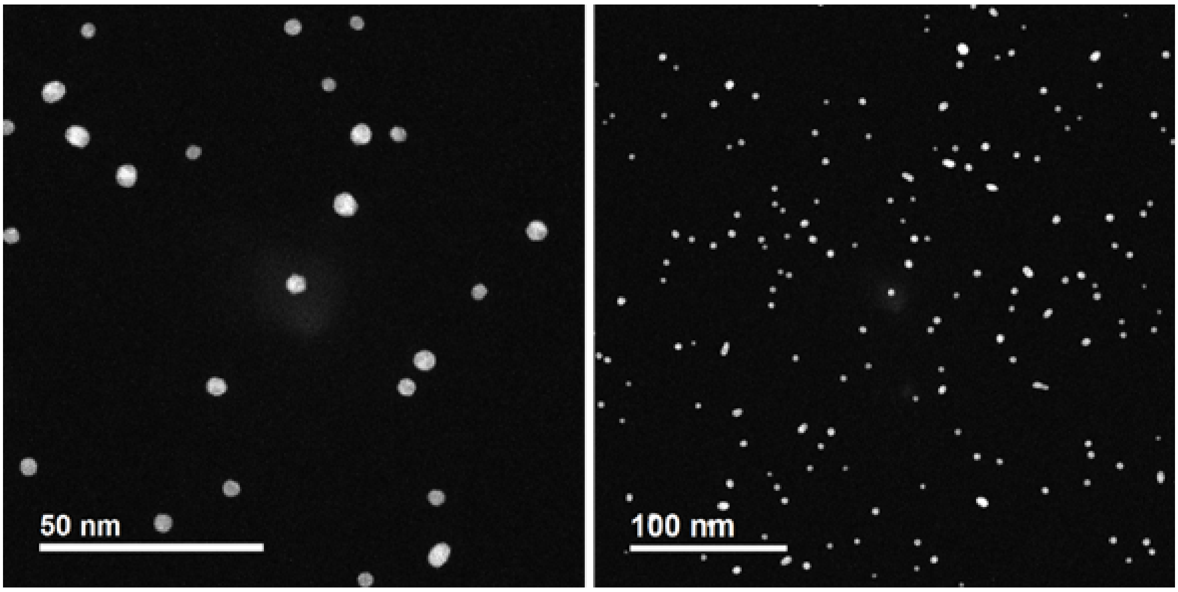

Figure 6.1: HAADF STEM overview images showing the distribution of clusters on the grid.

Analytical TEM investigations reveal smaller clusters mainly consisting of a single silver core, surrounded by a gold shell, while larger clusters contain two or more silver grains embedded in a gold matrix (Fig. 6.2b&c and Fig. 6.3). The largest diameters of single core clusters were measured to be 5 nm, whereas the smallest double core clusters amounted to 7 nm. With the transition threshold between a single and double core set between these numbers, a cluster size of approximately 5000 atoms or an initial droplet

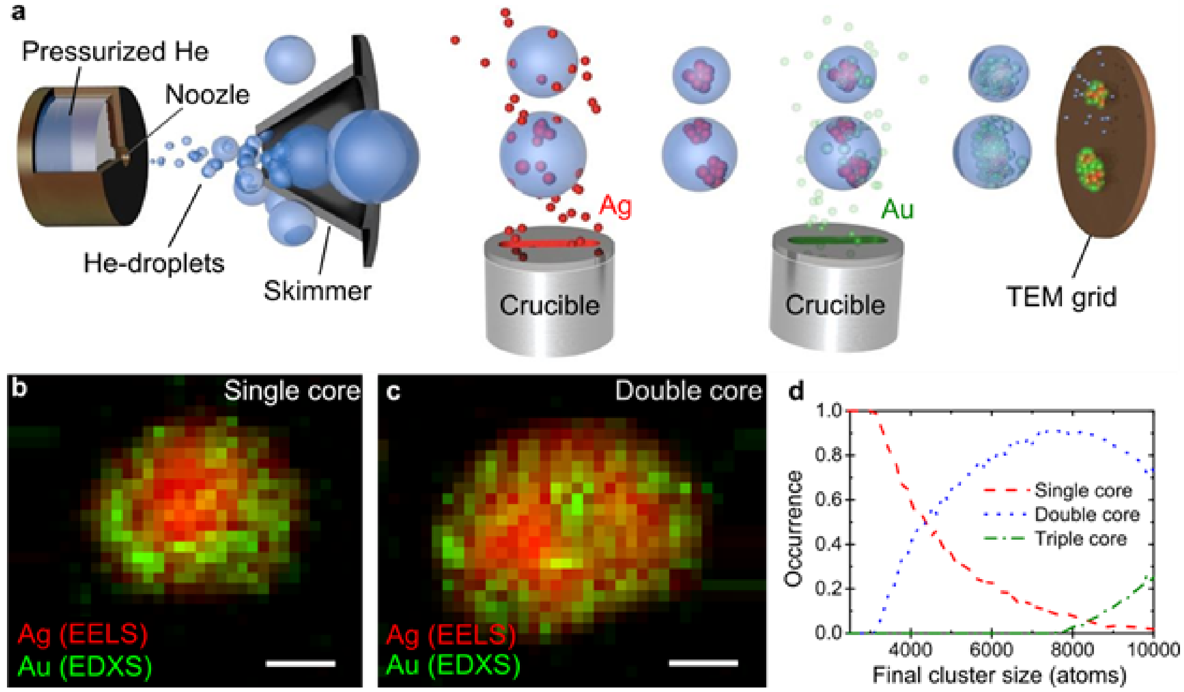

Figure 6.2: Synthesis and characterization of single and multi-core nanoclusters. (a) Schematic of the experimental setup for cluster synthesis: Superfluid He-droplets are guided through two doping cells and terminated on a TEM grid. (b-c) Elemental maps of a single-core/shell Ag-Au cluster (b), and of a dual-core/shell cluster (c). The Ag elemental maps are extracted from the EELS signal of the Ag M-edge, the Au elemental maps from the Au L-lines in the EDXS signal. (d) Calculated occurrence probability of single, double and triple core clusters as a function of final cluster size. Scale bars are 2 nm.

size of $5 \cdot 10^7$ He atoms can be obtained as a crossover value. Based on a simple estimation of the recombination time for two atoms inside a helium droplet [102], a transition from single center growth to multi center growth has been predicted at an initial droplet size of $5 \cdot 10^5$ He atoms. Applying more elaborate ab-initio simulation data [64] as a model, one can calculate the entire growth behavior of clusters inside a droplet (Methods). Thereby newly added dopant atoms aggregate very fast, keeping the total number of clusters inside the droplet low. At the droplet size where multi center aggregation starts ($5 \cdot 10^5$ He atoms), initially separated clusters will aggregate very shortly after they leave the first pickup cell. In sufficiently large droplets, however, two or more separated clusters of the first species can survive until they arrive at the second pickup cell. Using our experimental parameters in this model (Fig. 6.2d) we find the crossover between single- and double-core clusters at 4000-5000 atoms (initial droplet size: $4 - 5 \cdot 10^7$ He atoms), matching well with the experimental value and supporting our model for multi-center aggregation. The experimental parameters and setup can be tuned to switch between single or multi core clustering and thereby customize the clusters properties, such as their optical response [102].

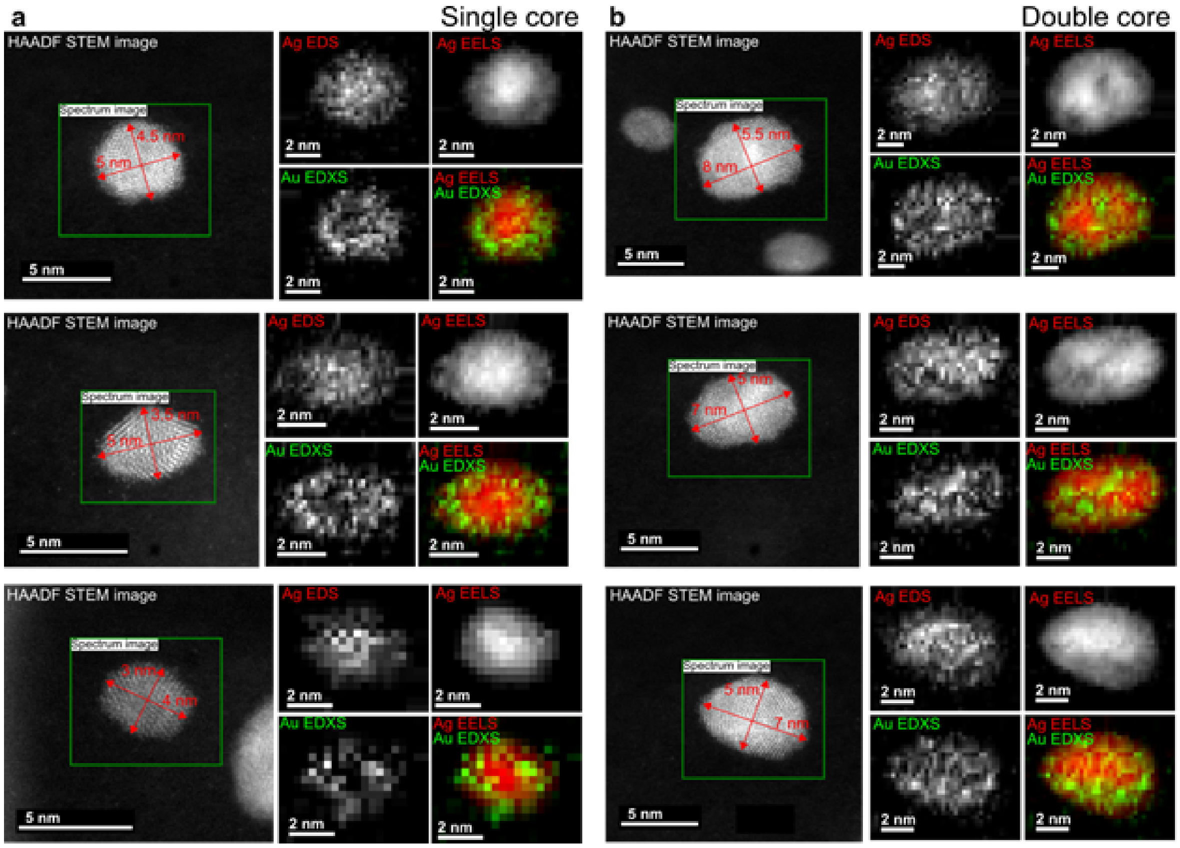

Figure 6.3: EELS and EDXS elemental maps of different (a) single and (b) double-core nanoclusters taken at a tilt angle of 65°. In the HAADF STEM image the region, where the elemental map are taken is indicated and the size of the clusters is measured. The extracted elemental maps show the EDXS signal from the Ag L-lines and the Au L-lines, the EELS signal from the Ag M-edge as well as an overlay of the Ag EELS signal and the Au EDXS signal.

A single cluster was analyzed three-dimensionally for its atomic structure, shape and composition. 31 high-angle annular dark field (HAADF) STEM projections were taken between −72° and +70°, optimized for signal-to-noise, by adding up 15 drift-corrected, fast-scan images at each tilt (Methods & Fig. 6.4). The tilt series, aligned with a center of mass approach, was then subject to both a multiplicative SIRT [45] (simultaneous iterative reconstruction technique) and a TV [58, 91] (total-variation) minimization algorithm. In the SIRT reconstruction (Fig. 6.6a and Suppl. Movie 1) five-fold symmetry centers are notable together with darker and brighter regions, which can be attributed to silver- or gold-rich regions. This comes out even clearer in the TV reconstructed model, where only composition information is kept (Fig. 6.6b and Suppl. Movie 2). As expected for this cluster size, two silver cores are visible as darker regions, separated by gold layer with a minimal thickness of 2-3 atomic layers. This double core structure was also confirmed by 2D EELS measurements on the same particle (Fig. 6.5).

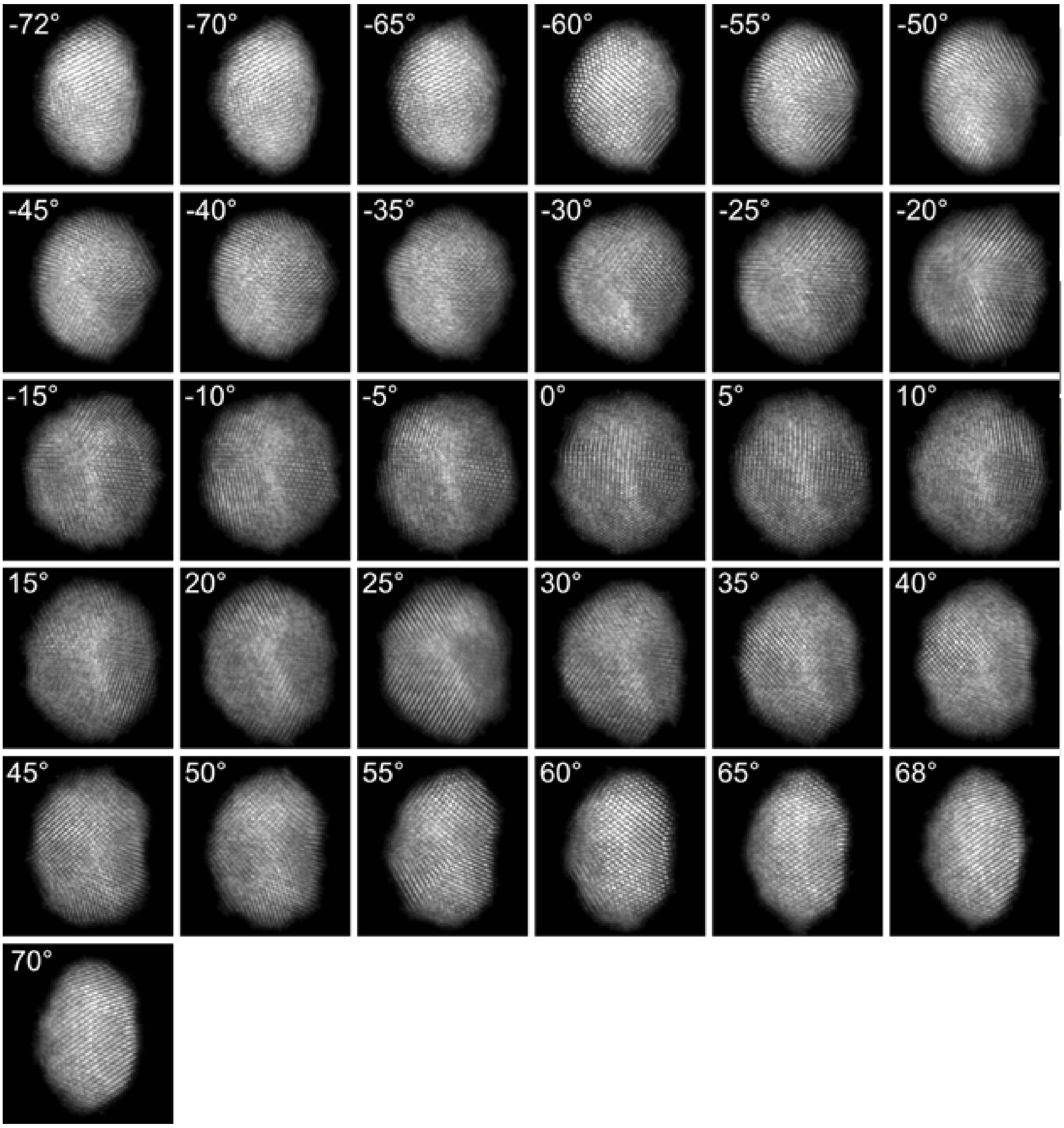

Figure 6.4: All projections acquired in the tilt series. Each projection is the sum of 15 drift-corrected aligned HAADF STEM images.

By searching for confined maxima in the SIRT reconstruction (Methods & Fig. 6.7), 7150 Au atomic positions can be localized within the cluster volume. Measured to be 119 nm^3, the 4.08^3 $Å^3$ unit cell in the fcc lattice of Au would correspond to 7050 atoms, matching approximately the experimental value. The cluster appears in a highly symmetric multiply twinned structure (overlaid with the compositional reconstruction,

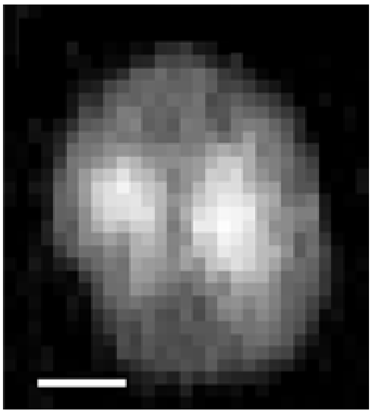

Figure 6.5: Ag M-edge EELS map of investigated nanoparticle at 0° viewing angle. Scale bar is 2 nm.

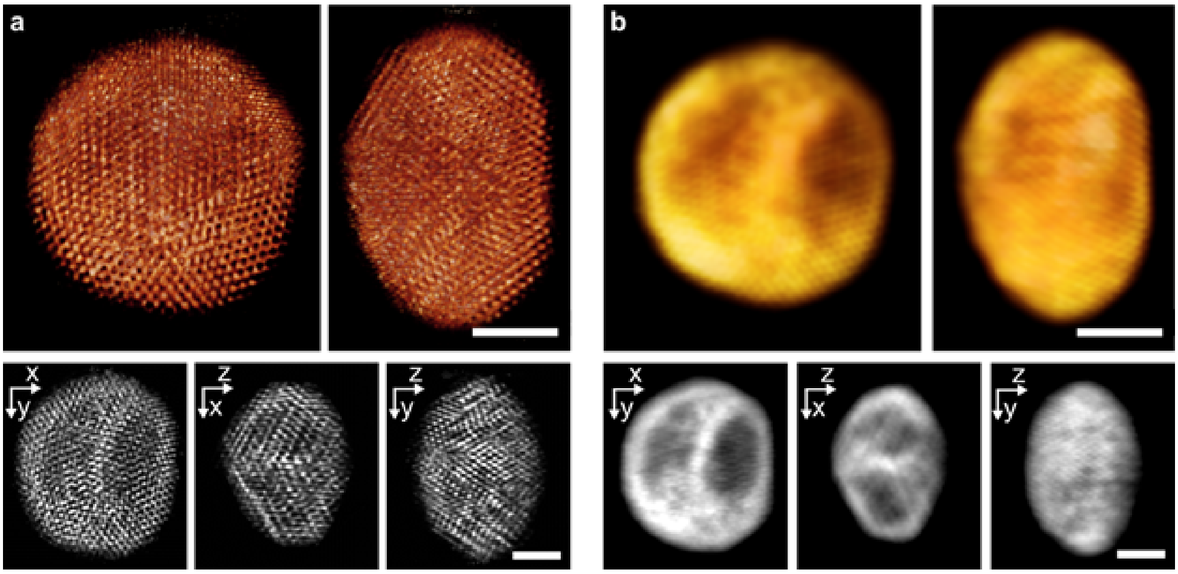

Figure 6.6: 3D reconstructions of a Ag-Au nanoclusters. Reconstruction showing structure (a) and composition (b) of the cluster. For each reconstruction a volume-rendered 3D view and 3 orthogonal 0.23 Åthick slices through the reconstruction are shown. Scale bars are 2 nm.

Fig. 6.9 and Suppl. Movie 3), shaped roughly as an icosahedron, which is structurally modified due to binding of the cluster to the surface. In the figure both a model of a modified icosahedron (Fig. 6.9a) and the reconstruction (Fig. 6.9b) are tilted in the same way to center different five-fold symmetry axes (cf. Fig. 6.8).

3D information from the final state of the cluster on the substrate can now be linked to the growth and deposition process. From simulations [146] and considerations of the binding energy [51], it is known that high temperatures or even partial melting during cluster-cluster collisions within the helium droplet and deposition on the substrate can

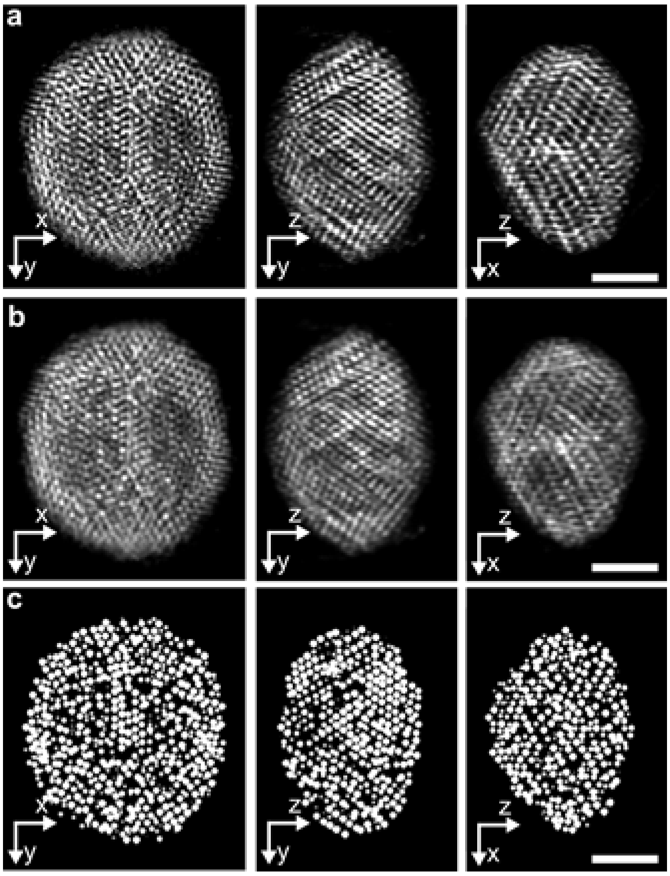

Figure 6.7: Detection of atomic positions: Slices through the original volume (a), which is smoothed by convolution with a Gaussian kernel (b). A local maximum search in the smoothed volume is used to estimate atomic positions, displayed as spheres in (c). Scale bars are 2 nm.

occur on a very short timescale (few picoseconds). The fact however, that the double core structure survives aggregation and deposition, and does not form an alloy as expected in a melt [96], implies efficient cooling by the matrix and restricts melting processes to the contact region. Furthermore a molten cluster of this size would cool from the outside and will not adopt this highly symmetric multiply twinned form [67]. Efficient cooling is guaranteed if the He remains liquid around the clusters and does not form a gaseous layer which would reduce heat dissipation. This condition is still fulfilled for the present cluster size but this could change for even larger clusters [51]. We can also observe that the structure of the nanoparticle does not change significantly between Au-rich and Ag-rich regions. This indicates that due to the similar lattice constants of Ag and Au the different types of atoms arrange themselves on a common lattice and that the different phases do not affect the structure of the cluster.

Considering the last steps of the aggregation process (cluster-cluster aggregation) one would expect rather irregular cluster shapes at the time of landing. The tomographic

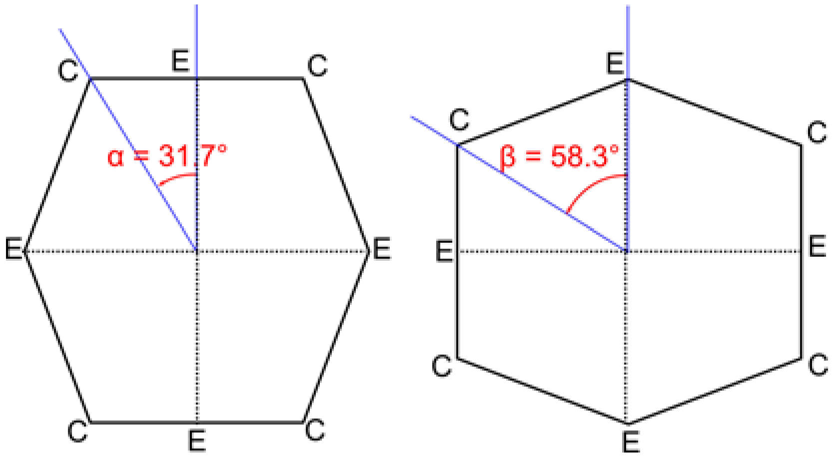

Figure 6.8: Rotation angles for centering five-fold symmetry axes as calculated based on the geometry of an ideal icosahedron. Corners (C) and edges (E) are indicated.

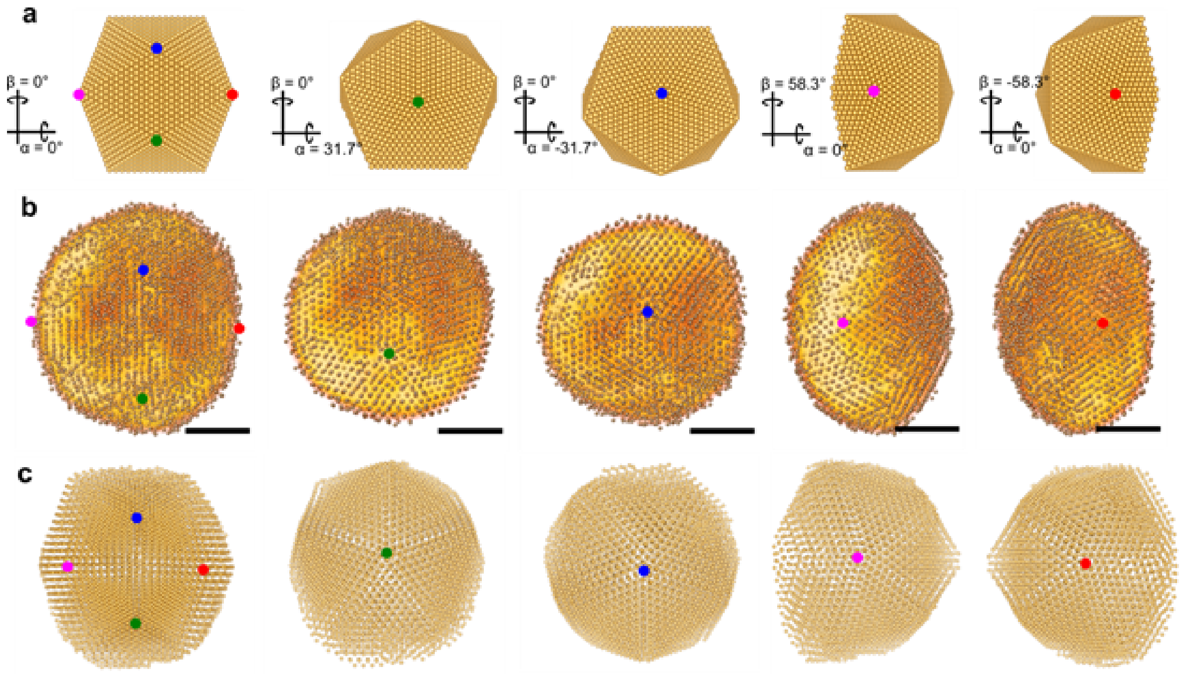

Figure 6.9: Model, reconstruction and simulation of atomic positions in the nanocluster. (a) Model of a modified icosahedron (lower part cut off) seen from the top and along 4 different five-fold symmetry axes. (b) Reconstruction of atomic positions seen along the same directions. (c) Result of molecular-dynamics simulation of a soft-landed cluster on a carbon film seen along the same directions. Five-fold symmetry centers are indicated in all images. Scale bars are 2 nm.

reconstruction shows a smooth lenticular shape of the cluster though. Its size is about 8 nm x 7 nm x 5 nm, with the smallest dimension being in the direction perpendicular to the substrate. Given a significant amount of time (few hours) passed between deposition of the clusters and the imaging, the smooth shape of the cluster likely stems from surface diffusion; a mechanism which preserves the inner structure but relaxes the outer shape of the cluster.

Simulations for smaller clusters predict a lenticular shape due to binding of the cluster to the surface [146]. Following this approach, the landing of an icosahedral cluster on an amorphous carbon substrate was simulated using molecular dynamics (see Suppl. Movie 4) and the final shape of the cluster has been compared with the reconstruction (Fig. 6.9c). Even though we do not expect an ideal icosahedral shape as starting condition the deformation of the cluster due to binding to the substrate and the impact of landing on its inner structure can be explored; for these two parameters (aspect ratio & inner structure) we observe good agreement between experiment and simulation. The exterior cluster shape comes out differently though, which is anticipated due to the small amount of time, framing the simulation. The simulation stops few nanoseconds after landing of the cluster, while relaxation to the equilibrium shape due to surface diffusion may take minutes or even hours [67]. Even though multiply twinned clusters do not represent the minimum energy configuration for clusters larger than a few hundred atoms [11], five-fold symmetric substructures are not rare when growing clusters. Still, the high symmetry of the icosahedral structure in such a large cluster would be very surprising without relaxation effects, supporting the interpretation that surface diffusion leads to the relaxation of the outer shell of the soft-landed cluster, which then adopts the symmetry of the inner region. In conclusion we have estimated atomic positions within nanoparticles in 3D without any prior information, while getting at the same time information about the local elemental composition. This approach was used to get insights into the growth and deposition process of composite nanoclusters created in superfluid helium droplets, revealing the mechanisms responsible for particle structure and for single or multi core particle formation. This understanding will allow fine-tuning of process parameters to optimize materials properties of nanoclusters for applications in optics, catalysis and other fields. This work establishes electron tomography as a singularly powerful tool for analyzing complex nanostructures at 3D atomic resolution, from composite nanoparticles to nanowires or quantum dots. Furthermore there is potential to approach true elemental identification at the atomic level using EELS or EDXS tomography.

6.2 Methods

Particle Synthesis

The experimental setup used to produce the core-shell clusters for this investigation consists of three vacuum chambers with subsequently decreasing baseline pressure (p_0). In the first chamber a beam of helium droplets (He_N) is produced by expanding pressurized ($p_0 = 20\,\mathrm{bar}$) high purity He (99.9999 %) through a 5 μm nozzle cooled to cryogenic temperatures ($T_0 < 10\,\mathrm{K}$) into high vacuum ($p = 10^{-5}\,\mathrm{mbar}$). During this free jet expansion, the He cools down even further and superfluid droplets are formed, which maintain a temperature of $\approx 0.4\,\mathrm{K}$ by evaporative cooling [23]. A few millimeters after the nozzle, a skimmer is placed in order to shape the droplet beam. The beam continues in the second chamber ($p = 10^{-7}\,\mathrm{mbar}$), where it is guided through two metal vapor cells. In these cells, resistively heated crucibles generate a vapor of the desired dopant materials and the vapor pressure is adjustable by tuning the temperature. As the beam passes through the cells, droplets colliding with dopant atoms pick up the foreign species with a probability close to unity. This way, up to several thousand atoms are picked up along the trajectory of a droplet. Inside the He_N the dopant atoms agglomerate and form clusters. Employing a sequential pickup scheme, Ag-Au core-shell clusters can be formed [145]. The binding energy released during the cluster formation process is dissipated by the droplet and leads to the evaporation of roughly 1600 He atoms per electron-volt binding energy. In the case of large metal clusters, approximately 5000 He atoms are evaporated per dopant atom, leading to a significant shrinking of the droplet. The relative decrease of He in the beam can be taken as a measure to adjust the composition of the clusters. After the doping in the second chamber, the droplet beam passes through another skimmer and enters the last chamber ($p = 10^{-10}$ mbar) where the beam is terminated on a commercial TEM substrate (Ted Pella Inc.) consisting of an ultra-thin amorphous carbon (a-C) film with a thickness smaller than 3 nm, backed with a holey carbon support film and a 400 mesh copper grid. During the landing process, the He evaporates, cushioning the impact. This and the low velocity of the beam ($\approx 200\,\mathrm{m/s}$) lead to so-called soft landing, which guarantees no major structural changes upon deposition. For the transport to the microscope, the samples were shortly exposed to ambient conditions ($\approx 1\,\mathrm{min}$).

Simulation of Cluster Growth

Since a detailed simulation of the aggregation process inside the droplets is computationally very costly, a simplified calculation was conducted to get insight into the process. From experiments, we know the size and velocity of the helium droplets as well as the size of the clusters produced for a specific droplet size. Using this information and the geometry of our pickup-source, we can calculate the rate at which dopant atoms are added to the droplet and compare it to the timescales for aggregation. The doping process is modeled by spawning single atoms with thermal velocity (8 m/s at 0.4 K for Ag-atoms) with the known doping frequency. It is assumed that every 2-particle collision leads to the formation of a cluster, containing all atoms of the colliding particles. The time it takes for 2 atoms to collide was taken from Hauser et al. [64]. For the collision of clusters, the collision times were corrected based on the lower velocity of the aggregates, considering conservation of momentum. If more than two particles are present in the droplet, the probability of a collision grows as the number of pairs between these particles. The binding energy released upon aggregation is dissipated by the surrounding He-matrix, leading to a shrinking of the droplet, which reduces the accessible volume and therefore the time between collisions. In this model, only a small number (few tens) of clusters are present in a droplet at any time. During the whole doping process, faster (smaller) clusters aggregate after a very short period of time. Larger clusters inside the droplet, on the other hand, can survive for a significant period of time, even after the droplet leaves the doping cell. In our experiment, where a sequential pickup scheme is employed, large droplets can contain more than one cluster of the first species as they arrive at the second pickup-cell. Employing our experimental parameters, we run calculations for several cluster sizes up to 10000 atoms. The crossover between single core and double core configurations occurs at 4000-5000 atoms, where half of the particles have one core and the second half have two cores, when reaching the second doping cell.

Simulation of Cluster Landing

To simulate landing of a cluster on an amorphous carbon substrate molecular dynamics simulation of the cluster deposition process and the substrate interaction were done. For the cluster a model with icosahedral morphology comprised of 6525 gold atoms was used. The integration of Newton's equations of motion was performed by using a Velocity Verlet algorithm. For temperature control we used an Andersen thermostat with a collision frequency of 2 THz. In order to reduce perturbation of the system only atoms next to the substrate were considered by the thermostat. The interatomic forces were calculated by using a semi-empirical many-body potential proposed by Sutton and Chen [143]. For the interaction with the amorphous carbon support a parameterized Lennard-Jones 6-12 potential obtained from ab-initio calculations [156] was applied. Initially the cluster was thermalized at 0.4 K. During the landing process the time step was set to 5 fs and increased after 50 ps to 10 fs, during thermalization to the substrate temperature of 300 K. After 250 ps the system is fully thermalized and finally evolved for 1 ns with a time step of 20 fs.

Experimental Crossover Between Single and Double-Core Growth

For an estimation of the crossover between single and double center aggregation from experimental data we analyzed the elemental maps shown in Fig. 6.3, where we see that the largest single core clusters we analyzed have a size of 5 nm in the direction parallel to the substrate and 4.5 nm in the vertical image direction (under 65° tilt angle). The smallest double core clusters we recorded have a diameter of 7 nm parallel to the substrate and 5 nm in the vertical image direction. Putting the cross-over in between these values we calculate the volume for an ellipsoid with a size of 6 nm for two prinicipal axes and 4.5 nm for the third principal axis, which gives a volume of 85 nm^3 corresponding to 5000 atoms in an fcc-lattice with a unit cell size of 4.08^3 Å^3 .

STEM EELS and EDXS

For all TEM experiments a probe-corrected FEI Titan3 60-300 microscope was used equipped with a Gatan Imaging Filter (GIF) Quantum and a four-quadrant FEI Super-X EDX detector. The microscope was operated in scanning mode at 300 kV with the electron beam set to a current of approximately 130 pA and a convergence semi-angle of 19.6 mrad. EDXS spectra and dual-EELS spectra were acquired in parallel using the DigiScan engine in the Gatan Microscopy Suite. EDXS spectra were acquired with a pixel time of 50 ms/pixel. EELS spectra were acquired with a collection semi-angle of 20.5 mrad, using a dispersion of 0.25 eV/pixel. Low-loss spectra were acquired with a pixel time of 50 μs over a range of -50 eV to 450 eV and core-loss spectra with a pixel time of 50 ms over a range of 150 eV to 650 eV. All analytical data except for Fig. 6.7 was recorded at a tilt angle of 65° to minimize shadowing of the x-ray detectors from the sample holder (Fischione 2020 Advanced Tomography Holder).

Spectrum images are drift-corrected after acquisition assuming a linear drift model. This is illustrated in Fig. 6.10. The survey image, which is taken before acquisition of the spectrum image with a short dwell time is taken as reference to be compared with the signal from the same detector recorded during spectrum image acquisition. The drift is modeled by a time-dependent linear drift. The used parameters are the drift direction α, the drift velocity vdrift modeling the linear drift during spectrum image acquisition as well as two parameters for the initial drift in x- and y-direction (xstart, ystart) modeling the drift occurring in the time between acquisition of the survey image and the start of spectrum image acquisition. A least-squares optimization is done in MATLAB comparing the intensities from the survey image with the signal acquired during spectrum image acquisition to calculate drift parameters. These parameters are subsequently used to compensate for the drift in the spectrum images.

For extraction of elemental maps from EDXS data the background is modeled by a Kramers-model and peak families are fitted by Gaussian models within the Gatan Microscopy Suite. For EELS analysis a fitting-based routine within the Gatan Microscopy Suite is used. The background is modeled by a power-law and the Ag M-edge as well as the C K-edge, which is overlapping with the Ag M-edge are modelled by Hartree-Slater ionization cross-section models. The low-loss spectrum is used for convolution to compensate for plural-scattering and for modeling of the near-edge structure.

Tilt Series Acquisition

Tilt series were acquired over a tilt range of −72° to +70° with a linear tilt step of 5° from −70° to +70° and 2 additional projections at −72° and +68°. The tilt range was limited

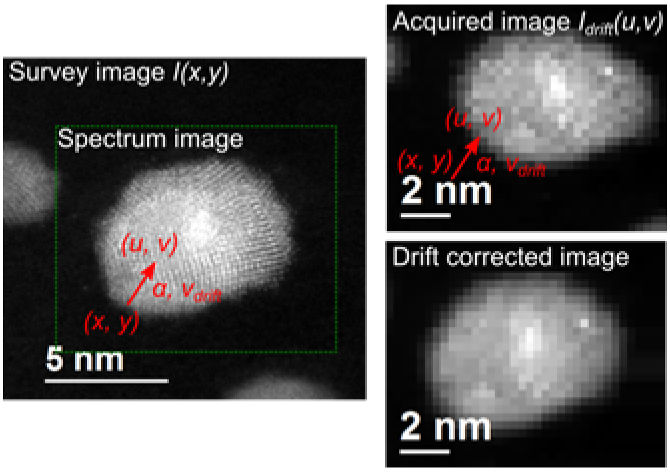

Figure 6.10: Drift correction of spectrum images: The survey image I(x,y) taken before spectrum image acquisition is taken as reference image to calculate drift parameters (drift direction α, drift velocity vdrift) in the acquired image Idrift(u,v). The calculated drift parameters are used to correct the drift in the acquired image and all associated spectroscopic signals.

by shadowing from the sample holder (Fischione 2020 Advanced Tomography Holder). Focusing at each tilt angle was done at a neighboring particle. HAADF STEM images were acquired with a convergence semi-angle of 19.6 mrad at a camera length of 91 mm. Image size was 512·512 pixels at a pixel size of 0.23 Å·0.23 Å. In order to limit the effects of sample drift at each tilt angle 15 images were acquired with a short dwell time of 2.4 μs per pixel. This was done automatically using a script in the Gatan Microscopy Suite. The 15 images were aligned and summed up using a routine in MATLAB. This alignment routine is illustrated in Fig. 6.11. The shift in x- and y-direction of each image with respect to the first image is calculated by filtered cross-correlation. These shift values are then taken as shift parameters for the central pixel of each image. Based on the total acquisition time for the 15 images the drift at each time instant is interpolated. Using the timing parameters of the image acquisition (acquisition time & dwell time) x- and y-shifts for each individual pixel can be retrieved which are then used to compensate for the drift in each image. The 15 corrected images are summed up to form the projections at each tilt angle (Fig. 6.10).

Tilt Series Alignment and Background Removal

Before tilt series alignment the background of each projection is removed. For this purpose the mean gray level in the outer regions of the image, away from the cluster is calculated for each projection and subtracted from each pixel in the projection. In this way the signal contribution of the carbon film is removed. Afterwards a mask is created around the particle using thresholding and morphological operators. All pixels outside of this mask are set to 0. For tilt series alignment center of mass methods are used. To

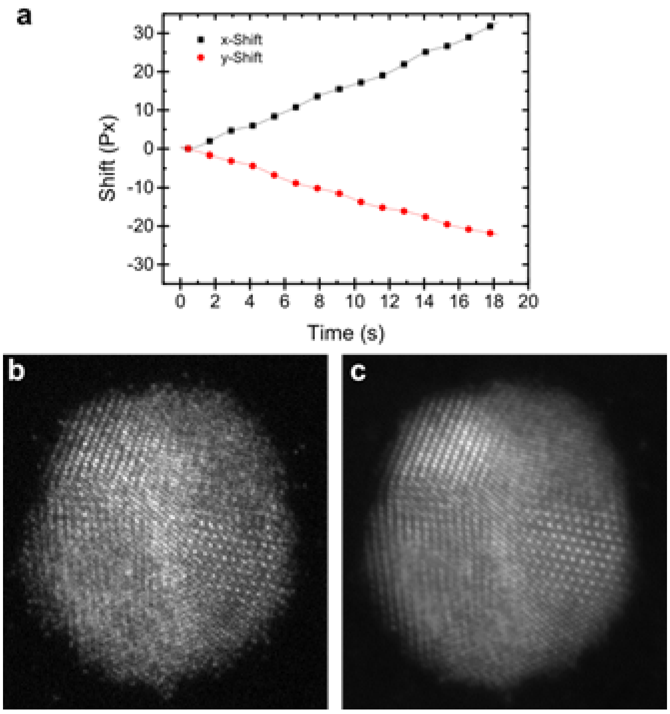

Figure 6.11: Drift correction and summing of HAADF STEM projections. (a) Drift in x- and y-direction as a function of time. Symbols denote the drift calculated for each image and used as drift parameter for the central pixel of each image. Connecting lines show the interpolation over time, which is used to estimate the drift at each time instant during image acquisition. (b) shows one HAADF STEM image and (c) shows the sum of 15 drift corrected and aligned images.

calculate the shift parameter of each projection in x- and y-direction the center of mass of each projection is calculated and used as center of the projections. To retrieve the tilt axis the centers of mass of all sinograms are calculated and a linear fit through all centers is used to calculate the position of the tilt axis.

Tomographic Reconstruction

Two different tomographic reconstructions were done. A first reconstruction was done using a multiplicative SIRT algorithm with 200 iterations and a relaxation parameter λ = 0.3, implemented in MATLAB and based on projection and re-projection operators from the ASTRA toolbox using the Graphics Processing Unit (GPU) [121]. This reconstruction provided high-resolution structural information (see Fig. 6.6a). Comparison of original projections and re-projected data is shown in Fig. 6.12a&b.

A second reconstruction was done using a 3D total-variation (TV) minimization algorithm based on the solver TVAL3 [91] and GPU-based projection and re-projection

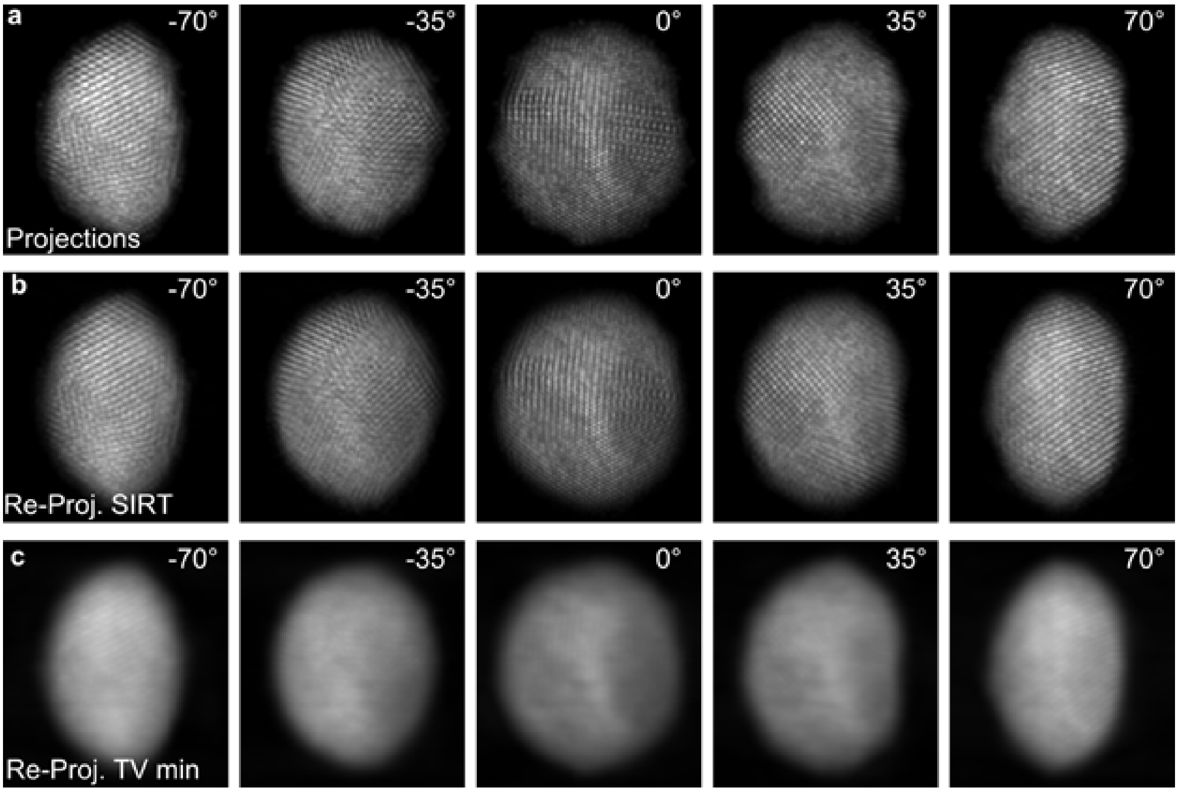

Figure 6.12: Comparison of original projections and re-projections: (a) acquired projections at 5 different tilt angles, (b) re-projections of the SIRT reconstruction (Fig. 6.6a) at the same tilt angles, (c) re-projections of the TV minimization reconstruction (Fig. 6.6b).

operators from the ASTRA toolbox. This algorithm has been described previously [58]. A small weighting parameter $\mu = 2$ was used, corresponding to a strong TV regularization of the reconstruction. This leads to large constant regions in the reconstruction, which effectively smooth out the atomic structure but do not affect contrast changes due to composition. Comparison of original projections and re-projections in Fig. 6.12 shows this effect also in the re-projections, where the atomic structure is no longer visible while contrast changes linked to composition visible in the projections are also visible in the re-projections.

Estimation of Atomic Positions

In order to be able to locate atomic positions, the SIRT reconstruction was smoothed using 3D convolution with a Gaussian kernel with a full-width at half maximum of 1.8 Å(4.2 pixel). A comparison between the original and the smoothed volume is given in Fig. 6.7a&b. Smoothing removes high frequency noise and artifacts, but the resolution remains good enough to identify the atomic structure. Within this volume a search for local maxima is performed, where each voxel is compared to its 26 neighboring voxels.

In a last step, if maxima are found, which are closer to each other than 1.4 Å, the lower maximum is removed. All the coordinates found in this way are used as atomic positions and can be displayed. In Fig. 6.7c slices through the volume with atoms represented as spheres are shown.

Chapter 7

Formation of Core-Shell Nanowires Along Vortices in Superfluid He Nanodroplets

This chapter corresponds to the publication by
Philipp Thaler, Alexander Volk, Florian Lackner, Johannes Steurer, Daniel Knez, Werner Grogger, Ferdinand Hofer and Wolfgang E. Ernst in *Physical Review B*, **90**, 155442 (2014),
which was written by the author of this thesis.

The author of this thesis was responsible for:

- performing of the nanoparticle synthesis
- interpretation of the results
- author of the publication

The contributions of the co-authors are listed below:

- A. Volk: preliminary experiments, assistance in interpreting the results
- F. Lackner: supervision, editing
- J. Steurer: assistance in the synthesis experiment
- D. Knez: performing the electron microscopic investigations, data processing, preparing the elemental mapping images
- W. Grogger, F. Hofer: supervision (microscopy)
- W.E. Ernst: supervision, editing, funding

Abstract

We report on the formation of one-dimensional Au/Ag core-shell nanostructures in superfluid helium nanodroplets (He_N) and their subsequent surface deposition under soft landing conditions. In vortex charged He_N, dopant atoms and clusters prefer to agglomerate along vortex cores, which serve as personal cryo-templates for each nanowire. A sequential pickup scheme enables the fabrication of Au/Ag structures with either Au as core and Ag as shell or vice versa. The core-shell structure is in both cases shown by energy-dispersive X-ray spectroscopy (EDX) in a scanning transmission electron microscope (STEM). The inherent spatial resolution and element sensitivity of this method allows a direct observation of the two different phases. High resolution STEM studies elucidate morphological details of the Au/Ag nanostructures and, together with the EDX analysis, indicate that the nanowires are formed in a multi-center aggregation process.

7.1 Main Article

The recent years have seen a tremendous growth of interest in one-dimensional nanostructures, accompanied with intriguing applications in various fields of research [22]. Especially carbon nanotubes and core-shell structures offer great prospects for nanophysics because of their tailorable properties, with new emerging applications ranging from nanoelectronics [93, 104] to material science [22] and catalysis [65]. Helium nanodroplets (He_N) entered the stage of one-dimensional nanoparticles only very recently with a seminal work that demonstrated the formation of elongated Ag structures along quantized vortices and their subsequent surface deposition [49]. In contrast to He_N experiments, which allow a defined formation of isolated nanowires in single droplets, experiments in bulk superfluid helium have already been used for the preparation of nanowire bundles. [52, 53, 88, 110] In this letter we show that the He_N approach can be exploited for the deliberate formation of one-dimensional core-shell nanostructures with predefined core and shell materials. The exceptional doping capabilities and high cooling rates provided by He_N suggest that this approach offers a novel route to a large variety of new material combinations which may exhibit revolutionary properties.

He_N provide a gentle, low temperature environment (0.37 K) for the preparation of tailored molecules and clusters [23, 151]. Their outstanding features enabled fascinating experiments [23, 150, 151] leading to new insights into various phenomena in physics, such as the study of superfluity on a microscopic scale [107, 130, 144], the observation of the superfluid phase in hydrogen [56] or the spectroscopic investigation of homo- and heteronuclear high-spin alkali dimers and trimers [69, 70, 117]. A new emerging branch in He_N isolation utilizes the method for the production and subsequent surface deposition of nanoclusters [20, 112], nowadays routinely done with various atomic and molecular building blocks [31, 136, 149, 150]. Their sizes can be well controlled by adjusting the pickup conditions and the mean helium droplet size, where the latter is dictated by nozzle temperature (T_0) and stagnation pressure (p_0) [23, 151]. Previously, the approach has been used for the preparation of small core-shell clusters with rare gas atoms or gas-molecules as shells [90, 98, 103]. It has been shown that clusters formed in helium droplets can be deposited on surfaces [112] under soft-landing conditions [102, 146], which allows a subsequent analysis by transmission electron microscopy (TEM) [20, 102, 155, 158]. Very recently, the existence of vortices in He_N has been demonstrated [49]. Thereby it has been exploited that dopant atoms and clusters (Ag) prefer to reside at vortex sites, which can be observed upon surface deposition in form of elongated wire structures in TEM studies. This experiment attracted strong interest and the method has recently been introduced for the vortex-assisted preparation of ultra-thin one-dimensional nanostructures [87, 140]. The production of bi-metallic core-shell clusters has been envisaged [20, 112, 158], but the actual structure of these clusters has so far not been determined unambiguously by element sensitive and spatially resolved methods. Possible configurations for bi-metallic nanoparticles are alloyed states or separated phases as for example in core-shell-particles or Janus-particles (i.e. configurations where each of the phases forms one hemisphere of the particle) [122].

In this letter we explore if a sequential pickup scheme leads to the formation of core-shell particles, as has been speculated in previous publications.[20, 112, 158] Our experiments yield bi-metallic nanowires with core-shell structures, where the center of the particle is rich in the element which is picked up first and the outer region of the particle is rich in the element which is picked up second. As materials we chose Ag and Au as they are miscible and exhibit very similar lattice parameters. With conventional techniques it would be hard to create separated phases on a nanometer length scale with these elements.

The helium droplet apparatus used in the experiments was designed for the production of very large droplets, details will be published elsewhere. In short, the setup consists of 3 vacuum chambers, separated by skimmers, with subsequently decreasing background pressure. In the first chamber He-droplets are produced via supersonic expansion of precooled high purity (99.9999%) helium into vacuum through a nozzle (diameter 5 μm) which is cooled by a closed cycle refrigerator ($T_{min} < 4$ K). In the second chamber multiple modularly designed evaporation cells, which consist of resistively heated crucibles containing the desired dopant, can be placed. The maximum crucible temperature of 2000 K allows to dope the droplets with a large variety of materials and the interchangeability of the cells enables to choose arbitrary doping sequences. Finally, the beam of doped droplets enters a UHV-chamber in which the created nanoparticles can be analyzed and deposited onto surfaces, e.g. commercial TEM substrates.

The produced samples were analyzed ex-situ with analytical HR-STEM using a probe corrected FEI Titan^3 60-300 equipped with a Super-X detector for energy-dispersive X-ray spectroscopy (EDXS) and a Gatan Quantum energy filter for electron energy loss spectroscopy (EELS). In order to avoid sample damage, a low dose condition with a beam current of 50 pA and a low dwell time were used. Furthermore, sub pixel scanning was activated during the acquisition of spectrum images (SI) in order to spread the dose over the whole pixel size.

With the experimental setup, droplets consisting of 10^3 to $>10^{10}$ He-atoms (diameter 4 nm to >1 μm) can be created. To produce clusters in He_N, large droplet sizes are required because the pickup of dopant atoms and the subsequent cluster formation results in a release of energy, which leads to the evaporation of helium atoms and consequently a shrinking of the droplet. For metal dopants, a broad size range, going from monomers up to clusters consisting of several 10^5 atoms, can be covered. Besides the helium droplet diameter, the size of the clusters obtained in an experiment strongly depends on the vapor pressure in the pickup region, which is controlled by the temperature of the evaporation cells. For experiments with Ag and Au, oven temperatures close to the respective melting points (1235 K and 1337 K) were used.

In agreement with the results presented in refs. [49] and [87] we find exclusively spherical particles at $T_0 > 7\,\mathrm{K}$ and $p_0 = 20\,\mathrm{bar}$. In the experiments presented in this letter we used $T_0 = 6\,\mathrm{K}$ and $p_0 = 20\,\mathrm{bar}$, which is slightly beyond the onset of the vortex regime [49, 87] and well suited for the production of linear one-dimensional nanoparticles with only a small number of branched structures. The tunability of the He_N allows the controlled growth of nanowires in single droplets in terms of length and composition. This is in contrast to experiments in bulk superfluid helium where always bundles of nanowires are produced and their length is determined by the physical constraints of the superfluid.[52, 88, 110] The expansion condition used here leads to an exponential droplet size distribution with an initial mean droplet size of $\bar{N} \approx 3 \cdot 10^8$ He atoms (diameter ≈ 300 nm) [48]. The temperatures of the Ag and Au evaporation cells were adjusted by measuring the dopant mass flow, which is transported by the beam, with a quartz crystal microbalance as well as by monitoring the He-beam attenuation, caused by the evaporation of He-atoms off the droplet upon pickup, with a quadrupole mass spectrometer set to 4 amu. In the experiments, the temperatures were chosen to yield an equal amount of Ag and Au atoms in each droplet and to evaporate about 50% of all He-atoms upon pickup. This doping level is a good tradeoff between creating large clusters and preserving the He_N beam.

Under this condition, STEM investigations of the produced nanoparticles show wire-structures with an average length of about 30 nm and an average diameter of approximately 7 nm. The majority of the observed nanowires exhibits a linear shape, but also kinked and branched particles were found on the substrate. High angle annular dark field (HAADF) images of some of the observed shapes are shown in Fig. 7.1. The observation of branched structures is attributed to the presence of multiple vortices in large He_N [49]. Considering the low surface coverage, it can be excluded that these structures originate from overlapping linear nanoparticles created in different droplets.

In the experiments, two different pickup sequences were applied. In the first, the Au-source was placed in the upstream- and Ag-source in the downstream-position (Au/Ag, Fig. 7.2) and in the second, the arrangement was reversed (Ag/Au, Fig. 7.3). The images in figures 7.2 and 7.3 show detailed studies of linear nanowires, including bright field (BF) and HAADF images (a and b, respectively) as well as an element sensitive EDX analysis (c-e). In both figures, the color map in (e) is based on the EDX data shown in (c) and (d) of the respective figure, with red corresponding to Au and green corresponding to Ag. To obtain the SI (c and d), each pixel was illuminated for about 2 s and the EDX data was smoothed via a spatial convolution filter with a size of 3x3 pixel [42].

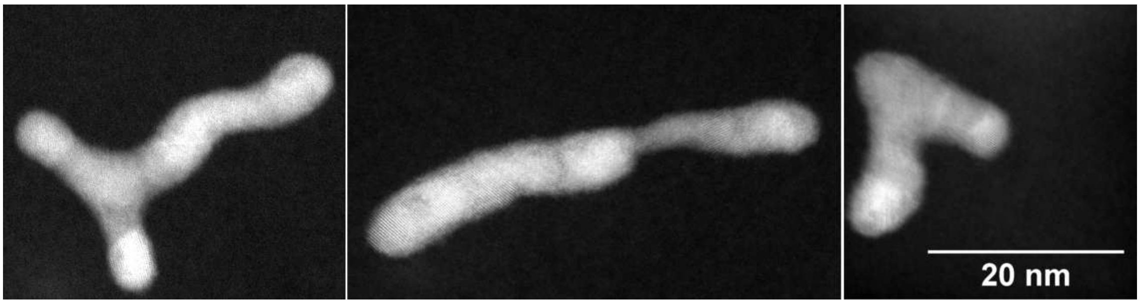

Figure 7.1: Representative STEM HAADF images of branched, straight and kinked wires with Au-core and Ag-shell on a 3 nm thick amorphous carbon substrate

In Fig. 7.2, where Au was doped first to the He_N, a Au-rich core and a Ag-rich shell region can be seen. In contrast, in Fig. 7.3, where the pickup sequence was reversed, a Ag-rich core and a Au-rich shell region are present. This demonstrates that the core-shell sequence is determined by the pickup sequence. In both cases, the cross section of the wires does not stay constant over their entire length. Constrictions between bulgy parts of the nanowires and alternations in the EDX-intensity along the wire (e) indicate that they grew in a multi-center growth process [101], starting from single spherical particles which subsequently aligned and connected along the vortices. The existence of domain boundaries between the bulgy parts of the nanowires are apparent in high resolution images (figure 7.4) and corroborate the multi center growth scenario. A possible explanation for the discontinuous cores could be that the flight time between the two pickup-cells is too short for the wire formation of the first species to be complete. The low temperature environment combined with the high cooling rate leads to a fast dissipation of the binding energy of the shell material and thus prevents the two materials from alloying. The low velocity of the He_N as well as the cushioning effect of the evaporating helium atoms in the moment of impact lead to ultra-soft landing conditions which enable the survival of the core-shell structure upon deposition.

In general, the interpretation of BF (a) and HAADF (b) images of samples with varying thickness (also in ref. [87]) is difficult. In that case, the contrast seen in these images can originate from the different thickness of the sample and not only from the different atomic number of the constituents (Z-contrast). On the contrary, the element sensitive EDX provides detailed information about the element distribution in the nanoparticles (c-e).

The interpretation of X-ray photoelectron spectroscopy (XPS) results, as presented for Au-Ni nanoparticles in ref. [20], is even more problematic in terms of characterizing their internal structure. While the absence of a pronounced core-level shift in XPS indicates that Au and Ni do not alloy in these particles, the method can not clarify the spatial distribution of different phases and thus cannot be taken as evidence for a core-shell structure. Furthermore, XPS investigations always cover relatively large areas and thereby average over a large number of nanoparticles. Only element- *and* spatially-sensitive methods give an insight into the actual distribution of the constituents in a single particle for this kind of samples.

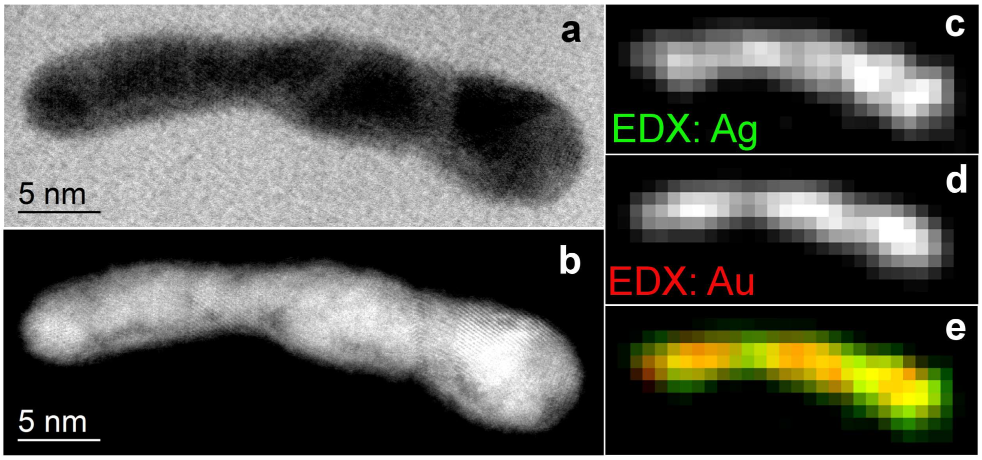

Figure 7.2: STEM-Images of a nanowire with Au as core and Ag as shell: BF-image (a), HAADF-image (b), EDX SI Ag (Ag L_α line) (c), EDX spectrum image (SI) Au (Au L_α line) (d), colored overlay image of the Ag and Au EDX SI (e).

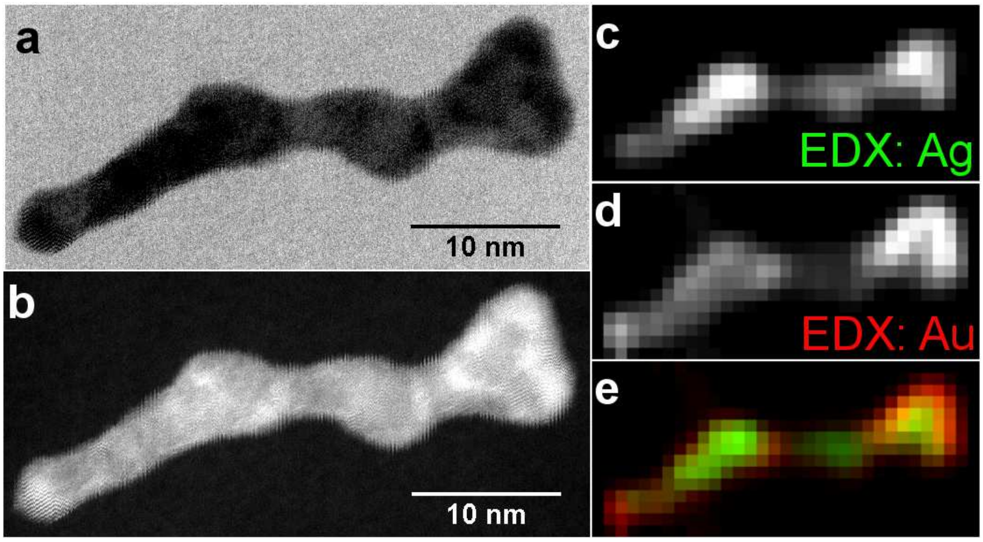

Figure 7.3: STEM-Images of a nanowire with Ag as core and Au as shell: BF-image (a), HAADF-image (b), EDX SI Ag (Ag L_α line) (c), EDX SI Au (Au M_α line) (d), colored overlay image of the Ag and Au EDX SI (e).

For the transfer from our experimental setup to the microscope, the samples were shortly exposed to ambient conditions (exposure time <5 min). Measurements with different exposure times (up to a few hours) showed no change in any of the particle characteristics. When using the low dose condition (beam current of 50 pA) in the STEM, the samples were stable under illumination by the electron beam, otherwise the EDX investigations, which usually take up to 30 min to image a single particle, would not be possible. In general, the particles seem to be very robust. Note that, in terms of long time stability, it has been reported that initially alloyed Au-Ag clusters of similar size can change their structure and form Janus-particles within a time-span of two years [18].

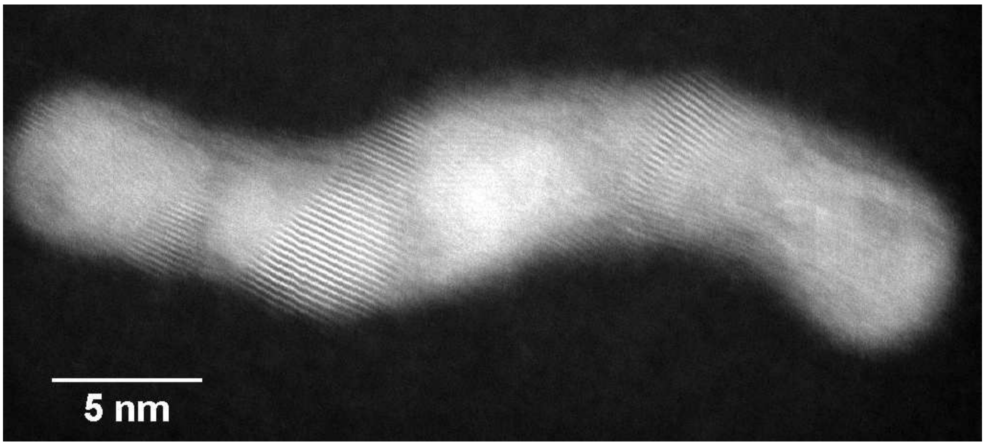

Figure 7.4: HAADF image, showing domain boundaries in a Au-core and Ag-shell nanowire

In summary, we demonstrated that core-shell Au/Ag and Ag/Au nanowires can be formed by using vortices in He_N as cryo-templates. By utilizing two pickup schemes, which differ in the sequence of the Au and Ag evaporation sources, it was shown that the resulting core and shell constituents are determined by the order of the pickup ovens and that their sequence can be reversed. Evidence for the respective structures is based on EDX, which provides element sensitive and spatially resolved images of these nanowires for the first time. Furthermore, the element distribution obtained by EDX gives insight into the formation process of the wires. Variations in the EDX-intensity of the different phases along the wires as well as the existence of domain boundaries and constrictions between the spherical sections of the wires indicate that they are formed in a multi-center growth process, starting from single spherical particles which subsequently aligned and connected along the vortices. In contrast to conventional methods, the helium droplet approach does not require chemical agents in order to dictate the shape and the sequence of the layers. Additionally, the fabricated structures can be deposited on virtually any substrate that can be implemented into a UHV apparatus. The low velocity of the He_N as well as the cushioning effect of the evaporating helium in the moment of impact ensure soft landing conditions, thus preserving the initial structure upon deposition.

Increasing the distance between the pickup cells may lead to more pronounced core-shell structures with a continuous core and may even allow the creation of a core-multi-shell system. The exceptional doping abilities of He_N allow to envisage the controlled formation of nanoparticles made from gaseous, liquid or solid building blocks. The preservation of the core-shell structure upon deposition would allow the passivation of reactive core-species by a non-reactive shell layer, in order to conserve the core for subsequent investigations [36].

The formation of tailored metal clusters inside He_N may open new prospects in helium droplet research, which could lead to a new research branch. In surface enhanced Raman scattering (SERS) experiments [77] single molecule sensitivity has been reported [119]. We propose that the enhancement of the Raman effect by nanoparticles may allow in-situ Raman spectroscopy of single molecules doped to He_N that contain a nanocluster. Tailored Au/Ag core-shell nanostructures can enable a tuning of plasmon resonances (which have been observed in Ag_n-He_N [101]), in order to increase the SERS enhancement factors, which may lead to intriguing new insights in fundamental physics, helium nanodroplet science as well as SERS and material science.

7.2 Additional Remarks

Follow-up experiments using other material combinations showed that the suggested passivation of a reactive core with an inert shell [36] is not as easily to achieve as expected. Several experiments were conduced on the Cr-Au core-shell system with the intention of protecting the Cr core against oxidation, but ended unsuccessfully. When depositing Cr-Au particles of various compositions on the QCM and subsequently introducing oxygen into the diagnostics chamber, an increase of mass due to the oxidation was detected. In the case of Cr-Au, an oxygen partial pressure of 10^{-7} mbar was sufficient to oxidize the deposited particles within seconds. The observation of Cr-Au nanowires in the TEM after exposure to ambient conditions showed that the chromium is fully oxidized and is placed around a gold core, although the pickup sequence would have forced the reversed core-shell order.

We assume that for small clusters the shell layer is either not closed, too thin, or the clusters melt upon deposition (supported by chapter 5), leading to a surface location of the chromium. For larger nanoparticles or nanowires, on the other hand, cluster-cluster aggregation obstructs the formation of a closed shell, which leaves some of the chromium unprotected, even if the structure survives the deposition unchanged. Exposure of such particles to oxygen would lead to the oxidation of the unprotected areas and the accompanying energy release would increase the temperature and enable restructuring and diffusion of chromium atoms to the surface.

In order to gain a better understanding of the Cr-Au system or reactive systems in general, the produced particles need to be investigated without prior exposure to ambient conditions. The rather small oxygen partial pressure (10^{-7} mbar) which was sufficient to start the oxidation reaction suggests that the samples should be kept under UHV conditions at all times. Such experiments might be possible in the future using the recently installed UHV-transfer system.

Chapter 8

Comparison of Mass-Spectra and Electron Microscopy Data with Simulations

This chapter corresponds to the publication
"Synthesis of Nanoparticles in Helium Droplets - a Characterization Comparing Mass-Spectra and Electron Microscopy Data"
by **Philipp Thaler**, Alexander Volk, Daniel Knez, Florian Lackner, Georg Haberfehlner, Johannes Steurer, Martin Schnedlitz and Wolfgang E. Ernst in *J. Chem. Phys*, accepted in September 2015,
which was written by the author of this thesis.

The author of this thesis was responsible for:

- performing of the nanoparticle synthesis and mass spectrometric measurements
- interpretation of the results
- author of the publication

The contributions of the co-authors are listed below:

- A. Volk: preliminary experiments
- D. Knez: performing the electron microscopic investigations
- F. Lackner: assistance in interpreting the results and editing
- G. Haberfehlner: performing the electron tomographic investigations
- J. Steurer: assistance in mass spectrometric measurements
- M. Schnedlitz: assistance in mass spectrometric measurements
- W.E. Ernst: supervision, editing, funding

Abstract

Micron sized helium droplets provide an extraordinary environment for the growth of nanoparticles. The method promises great potential for the preparation of core-shell particles as well as one-dimensional nanostructures, which agglomerate along quantum vortices, without involving solvents, ligands or additives. Using a new apparatus, which enables us to record mass spectra of heavy dopant clusters ($> 10^4$ amu) and to produce samples for transmission electron microscopy (TEM) simultaneously, we synthesize bare and bimetallic nanoparticles consisting of various materials (Au, Ni, Cr, Ag). We present a systematical study of the growth process of clusters and nanoparticles inside the helium droplets, which can be described with a simple theoretical model. Additionally, we show the spectroscopic capabilities of the new machine on the example of resonance enhanced multi-photon ionization (REMPI) spectroscopy of Au-doped helium droplets.

8.1 Introduction

During the past decades metal nanoparticles have been studied intensively. Especially small clusters, not larger than a few nanometers in diameter, are interesting because their optical,[95] magnetic,[16] catalytic[65] and other properties can differ greatly from those of the corresponding bulk materials.

Various methods for the production of nanoparticles are known, each with its own advantages and drawbacks. An outstanding method uses a beam of superfluid helium droplets (He_N) as micro-reactors for particle formation, providing confinement and ultra low temperatures ($\approx 0.4\,\mathrm{K}$).[23, 151] The unique properties of He_N have enabled fascinating experiments[56, 80, 107, 144, 150] and the helium droplet technique has matured to a standard method in spectroscopy of atoms and small molecules.[69, 85] Very recently, the method has been applied for the deposition of nanometer-sized metal clusters on surfaces [112] and later vortices inside He_N were deliberately used to create one-dimensional nano-structures.[49, 87, 145] The size of the produced clusters depends on the doping conditions as well as the mean helium droplet size. The universal doping capabilities provided by He_N allow virtually any desired species to be embedded.[134, 151] During particle formation, binding energy is released, which is efficiently dissipated by the surrounding helium matrix and the dopant particles are cooled to the droplet temperature. The cooling mechanism leads to the evaporation of helium atoms and hence a significant shrinking of the droplets. The droplet beam can be terminated on substrates, where the helium evaporates and the particles grown inside the droplets are adsorbed on the surface. Thereby, the low impact velocity of the droplet beam and the cushioning effect of the helium droplet in the moment of impact provide very gentle deposition conditions for the dopant clusters.[2, 102, 123]

Transmission electron microscopy (TEM) is a powerful tool for the characterization of deposited nanoparticles. The availability of aberration corrected microscopes, operating in a scanning mode (STEM), as well as very thin substrates enable the imaging of very small particles with atomic resolution. Using specialized detectors and additional effort

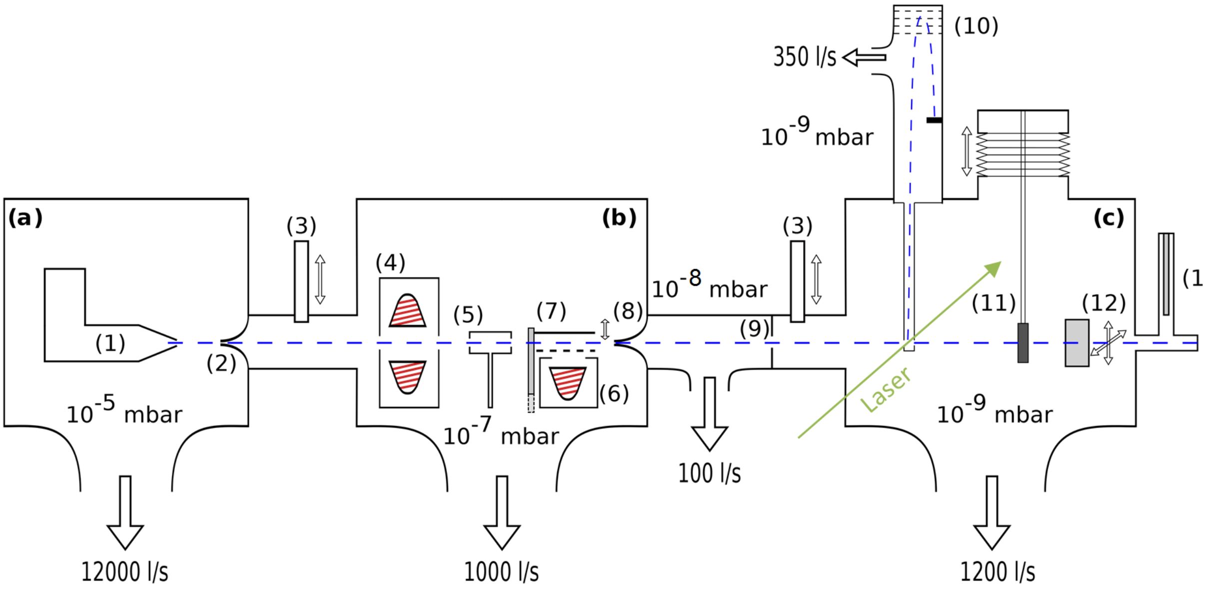

Figure 8.1: Schematics of the He_N beam machine used for the experiments in this work. The noted pressures in the 3 chambers (a, b, c) refer to the situation with open valves (3) and He-beam ($T_0 = 3 - 25\,\mathrm{K}$, $p_0 = 10 - 100\,\mathrm{bar}$) on. The droplet beam produced by the cooled nozzle (1) is shaped by the skimmers (2, 8) and an aperture (9). The droplets can be sequentially doped using different sources (4, 5, 6). As diagnostic tools a TOFMS (10), substrates for *ex-situ* TEM investigations (11) and a quartz crystal microbalance (12) are available on axis, as well as an off-axis QMS (13). The TOFMS is equipped with an electron gun for electron impact ionization (not shown) but also enables photo-ionization using an external laser.

in data acquisition and data analysis, the three dimensional structure of the imaged samples and their local chemical composition can be reconstructed, providing a detailed insight into the physical and chemical properties of the sample.[59] Nevertheless, in most cases, TEM can only be used *ex-situ*, which may be impractical if characterization is necessary prior to another experiment. Furthermore, particle analysis with TEM is a tedious task if a statistically significant number of particles needs to be characterized.

Time-of-flight (TOF) mass spectrometry enables both, studying the dopant-cluster size distributions[20, 149] *in-situ* as well as revealing information on the electronic structure of dopant molecules and clusters.[44, 63, 82, 85] With TOF mass spectrometers (TOFMS) it is possible to observe clusters in a size range (consisting of several hundred atoms)[19, 33, 132] which is also accessible with TEM, enabling a comparison of the two methods.

In contrast to electron impact ionization with its high excess energy (*cf.* section 8.3.2.1), photo-ionization provides a more gentle way to create ions either directly with a single photon or, more commonly, because of the relatively high ionization energies of metal clusters, *via* resonance enhanced multi-photon ionization (REMPI) schemes. By us-

ing photo-ionization it has been shown for the case of alkali and alkaline earth metal atoms immersed in He$_N$ that the ionized dopant-He$_N$ system can stay intact on a μs time scale, from the formation to the impact on the micro-channel plate (MCP) detector.[100, 147, 148] REMPI spectroscopy has proven to be a valuable tool for recording electronic spectra of dopant atoms, molecules and clusters in helium nanodroplets and a pulsed laser setup is already available at the machine. Mass spectra obtained by photo-ionization can complement electron impact ionization spectra and reveal additional insight in the properties of the dopant-He$_N$ system.[86, 99, 113, 115, 149]
In this work, we present mass spectra of metal-nanoparticles Me$_n$ (whereby Me stands for Au, Ni or Cr), with $n \leq 500$ atoms as well as cluster size distributions obtained by analyzing TEM-images. For a reliable comparison, the preparation of the samples for TEM-investigations and the recording of the TOF mass spectra were conducted simultaneously. In addition to the experiments, a simple theoretical model was developed to predict the produced cluster size. We show that both diagnostic methods as well as the theoretical model correspond very well for cluster sizes between $50-500$ atoms.

8.2 Experimental Setup

The experimental setup consists of three vacuum chambers with subsequently decreasing background pressure, separated by skimmers. In the first chamber, pressurized ($p_0 = 10-100$ bar) high purity He is expanded through a nozzle (diameter $d_0 \approx 5\,\mu$m), which is cooled to cryogenic temperatures ($T_0 = 3-25$ K) *via* a closed cycle refrigerator (Sumitomo RDK-408D2). Such conditions lead to the formation of a beam of helium droplets, which is collimated by the first skimmer. This process requires an enormous throughput of the vacuum system which and is realized by an oil diffusion pump (12000 l/s) in combination with a mechanical Roots pump. The collimated beam enters the second chamber, where it passes through several water-cooled pickup cells, in which the desired dopants are present in the gas phase with adjustable partial pressure. For the experiments in this article resistively heated crucibles are used to force the metal dopants into the gas phase. For dopants which need temperatures higher than 2000 K to reach the required vapor pressure, crucibles heated by electron bombardment can be employed.[124] Furthermore, gaseous or liquid dopants can be introduced along the beam *via* a specially designed pickup cell and a leak valve. Inside the pickup cells, dopant atoms colliding with droplets are confined to the volume of the He$_N$. Up to several thousand atoms can be incorporated into a single droplet along its trajectory. Inside the He$_N$, the dopants are able to move and they eventually coagulate and form clusters. During the aggregation process binding energy is released, leading to the evaporation of He-atoms off the droplet.[151] After being doped, the droplets pass a second skimmer and enter the analysis chamber where the droplet beam crosses the ionization region of the TOFMS and is terminated on a TEM-substrate. This setup allows mass spectrometric measurements and the deposition of clusters on substrates for subsequent investigations (TEM, atomic force microscopy (AFM), *etc.*) simultaneously. The mean free path of the droplets in all chambers is sufficiently large such that no other species than the dopant(s) are picked up in a significant amount, guaranteeing very clean samples. Additionally, the skimmers as well as the differential pumping scheme allow to maintain ultra high vacuum (UHV) conditions in the last chamber, guaranteeing no posterior contamination of the samples. A UHV transfer-system (Ferrovac UHV suitcase), which can maintain UHV-conditions for three days using only battery power, enables to transfer the ultra pure samples to external diagnostics.

A TOFMS with reflectron (Stefan Kaesdorf RFT50), which is specifically designed for the detection of large compounds, is used for the *in-situ* analysis of the clusters formed in the He_N and enables both, electron impact ionization and laser ionization. In this work, only the former is applied, using the built-in electron gun, which can be tuned in energy (0 - 89 eV), repetition rate (0 - 10 kHz) and duty cycle (0 - 20 μs). In all experiments presented in this work, the highest available ionization energy (89 eV) with $\approx 10\,\mu$A average electron emission current at 5 kHz repetition frequency and 20 μs duty cycle was chosen in order to get the maximum ionization cross-section for He.[32, 127]

The nanoparticles, which pass the TOFMS (*i.e.* which are not ionized), are deposited on commercial TEM substrates (Ted Pella Inc., Prod. No. 01824). The produced samples can then be analyzed *ex-situ* with TEM and high resolution STEM using a probe corrected FEI Titan3 60-300. During the transport to the microscope, the samples were exposed to ambient conditions for less than 5 min.

Complementary, a quartz crystal microbalance (QCM) and a quadrupole mass spectrometer (QMS) are used to measure the mass deposition rate and the He-intensity of the beam, respectively. The former is important in order to predetermine the surface coverage for later TEM investigations, and the latter gives information about how heavily the droplets are doped.[102]

8.3 Methods

The helium droplet approach presents a versatile tool to synthesize nanoparticles. As no chemical processes are involved in the cluster formation, new materials or material combinations can be employed easily, as long as they can be forced into the gas phase. Thereby, the synthesis conditions can be varied over a wide range with only small experimental effort (adjustment of He_N-source temperature and partial pressure of the dopants). The synthesis process can be monitored using TOFMS, simultaneously with *in-situ* experiments. This is possible because of the short duty cycle of the TOFMS: the pulsed electron beam for ionization has a maximum on-time of 20 μs and a repetition frequency of 10 kHz or less. This leaves in any case more than 80 % of the beam unaffected, which can be used for other experiments.

Especially if the nanoparticles are produced for further experiments, prior *in-situ*-characterization is advantageous, as every transfer to external diagnostics can be a source for contamination.

8.3.1 Nanoparticle Synthesis

When aiming to synthesize nanoparticles of a predefined size, one has to be aware that the maximum size of the dopant particles is restricted by the size of the helium droplets. If the droplets are too small, all the helium will be evaporated and the dopant particles will no longer be carried into the analysis chamber. On the other hand, using large helium droplets and low doping rates favors multi-center aggregation or the pinning of dopant clusters to quantized vortices which obstructs the intended growth process. From experience we know that a situation where about half of the helium in the beam is evaporated due to doping is favorable in terms of controllability. As the binding energy released upon cluster formation is the main reason for helium-evaporation, this factor determines the necessary droplet size, which defines the droplet source conditions. The relation between nozzle temperature and droplet size is taken from Ref. [48]. After setting the appropriate source condition, the temperature in the doping cells is increased until the desired doping conditions are reached (at $\approx 50\,\%$ He-loss). Finally, the nozzle temperature as well as the pickup conditions can be fine-tuned while monitoring the mass spectra recorded with the TOFMS (see Figs. 8.2 and 8.3).

The details of the particle growth mechanism change, depending on the helium droplet size compared to the velocity of the embedded particles. For small He_N ($\mathrm{N} < 5 \times 10^5$) each droplet contains a single cluster, which grows by subsequent addition of single atoms. In medium sized He_N ($5 \times 10^5 < \mathrm{N} < 1 \times 10^7$) the doping frequency exceeds the nucleation frequency, which means that clusters start to grow at different positions inside the droplet simultaneously (multi-center growth).[101] However, simulations show that the fact that atoms or small clusters move and aggregate much faster than larger compounds (conservation of momentum) leads to a situation where only one larger particle can develop during the doping process and the growth of other clusters ends at an early stage, when they collide with this major particle. Engaging the same considerations, the merging process of all picked up atoms into a single particle will be completed very soon after leaving the doping cell. Upon collision, small clusters melt completely,[50] which means that multi-center aggregation has no consequence for the final shape of particles in medium sized droplets. The situation changes for large droplets ($\mathrm{N} > 10^8$), where several bigger (slow) particles can survive for a significant amount of time. If two of these particles collide and aggregate, they no longer melt completely and do not yield a larger spherical particle. Instead, in the presence of vortices inside the droplets, which attract the dopants, the described aggregation mechanism leads to the formation of nanowires.[50] This, of course, can also be used deliberately for the synthesis of one-dimensional nanostructures.[87, 145]

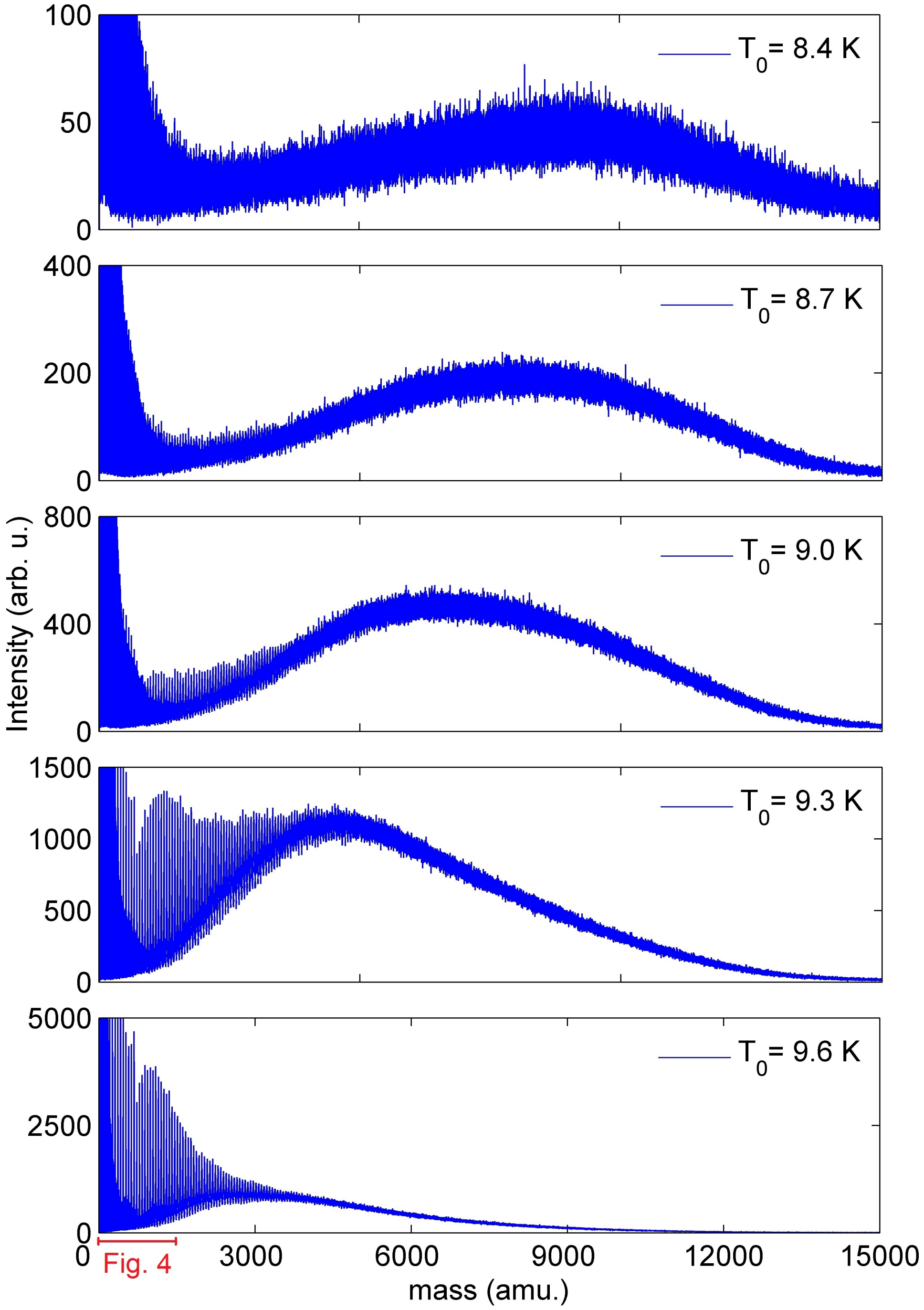

Figure 8.2: Chromium cluster size distribution for different nozzle temperatures (T_0), stagnation pressure and vapor cell temperature constant at $p_0 = 20\,bar$ and $T_{Cr} = 1375\,°\mathrm{C}$, respectively. Note the different scales on the y-axis. The mass spectra were recorded using electron impact ionization. A zoom of the section marked in red in the $T_0 = 9.6\,\mathrm{K}$ - spectrum is shown in Fig. 8.4 in order to show anomalies in the mass spectrum.

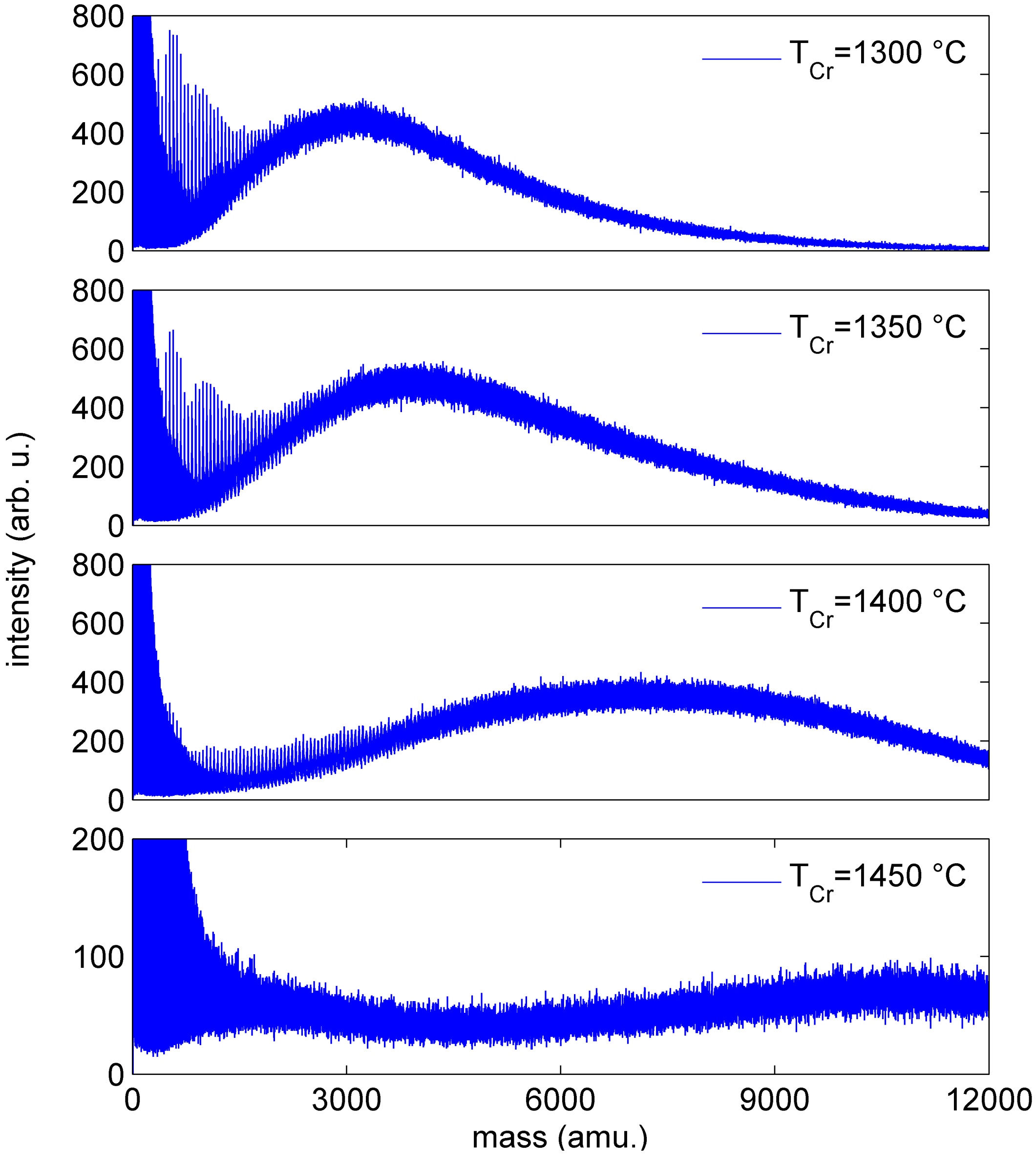

Figure 8.3: Chromium cluster size distribution for different vapor cell temperatures, stagnation conditions constant at $T_0 = 9\,K$, $p_0 = 20\,bar$. Note the different scales on the y-axis. The mass spectra were recorded using electron impact ionization.

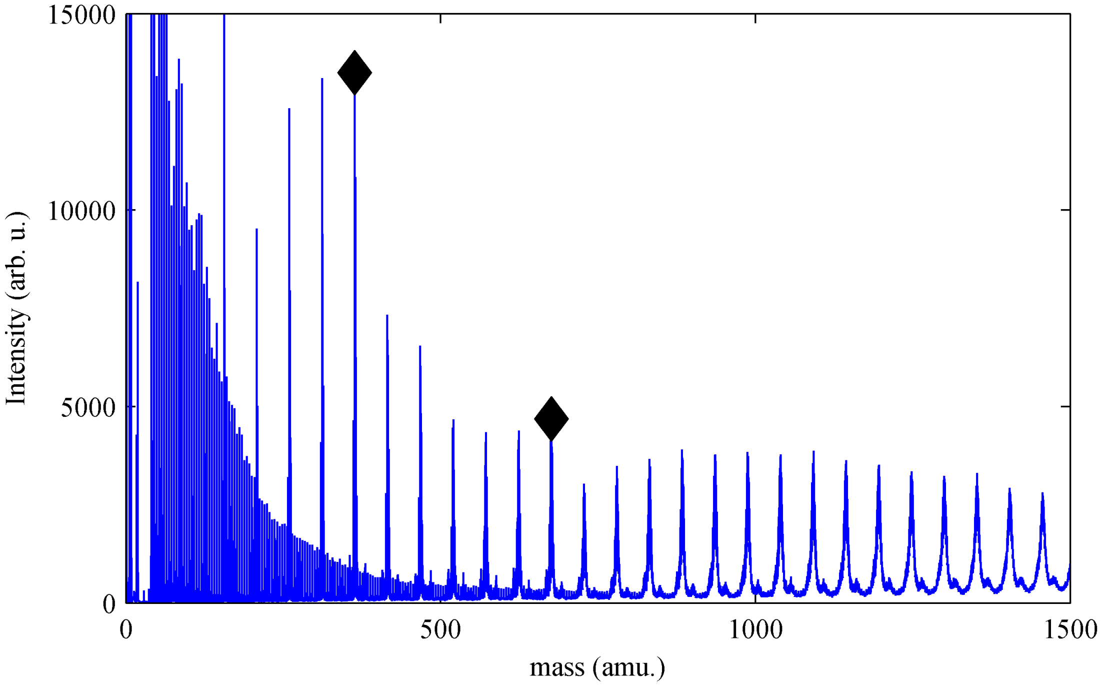

Figure 8.4: Close up on the lower masses of the $T_0 = 9.6\,\mathrm{K}$ - spectrum of Fig. 8.2. The low intensity below $\approx 50\,\mathrm{amu}$ is caused by the mass filter, which prevents saturation of the detector at low masses. The wing seen below $\approx 500\,\mathrm{amu}$ is the signal of the helium droplet fragments. The small peaks following the prominent Cr_N peaks stem from $\mathrm{Cr}_N + \mathrm{H_2O}$. The black diamonds mark the Cr_7- (pentagonal bi-pyramid) and Cr_{13}-clusters (icosahedron with a single shell around the center atom) which are more stable than the adjacent clusters because of a geometrical shell closure. The graph shows the orignal data, which means that the Cr_N peaks get wider at larger N and their height does not directly correspond to the occurrence of the respective cluster.

8.3.2 Mass Spectrometry

In this work we show that our specialized TOFMS yields reliable data for particles as large as 2 nm in diameter, which corresponds to a few hundred atoms per cluster.
When analyzing TOFMS-data, several influences have to be kept in mind, each of which may obscure the real size distribution:

8.3.2.1 Ionization:

The TOFMS in our setup enables both, electron impact ionization and laser ionization. Using the former, the short mean free path of electrons in liquid helium [43] prevents direct ionization of the dopant for He_N with $N > 10^5$. Secondary processes such as resonant charge hopping[35] or Penning ionization [30, 75] are alternative ionization pathways if the electron energy exceeds $\approx 24\,\mathrm{eV}$ or $\approx 19\,\mathrm{eV}$, respectively, but are also limited in range. This means that despite the large excess energy of the electrons, ionization and subsequent detection of embedded dopant clusters becomes increasingly difficult beyond a certain droplet size ($N \gtrsim 10^7$).

Compared to electron impact ionization, laser ionization provides a more gentle way to produce ions, because photon wavelengths in the ultra-violet, as used in many ns-laser experiments, limit the amount of excess energy introduced into the dopant-He$_N$ system. As helium is transparent in the entire spectral range from the far infrared to the vacuum ultra-violet, [23, 151] the mechanism behind laser ionization is different: photons can pass the helium droplet unhindered and directly ionize the dopant. The transparency of helium would also allow for a spectroscopic characterization of dopants using REMPI, where one laser in the ionization scheme is scanned across resonant electronic transitions and the ion yield is monitored as a function of the wavelength of the tuned laser.

For very high laser intensities, multi-photon absorption may cause fragmentation and severely alter the observed size distribution.

8.3.2.2 Ion-Extraction:

Metal clusters and nanoparticles synthesized in He$_N$ are typically located inside the droplet, while *e.g.* alkali-atoms prefer to stay on the surface.[4, 5, 6, 23] Upon ionization, the ions are extracted by a pulsed electric field. The ionization process usually leads to fragmentation of the helium - dopant-cluster complex, yielding predominantly mass spectra of pure dopant clusters, but also dopant clusters with a few helium atoms attached.

In contrast to other possible setups, where ions are extracted coaxially or at small angles with respect to the beam, our setup extracts the ions perpendicular to the beam. In this case, the low lateral velocity in the beam as well as the small ionization region ensure good resolution in the mass spectra over a wide range ($m/\Delta m = 2000$ for $0-20000$ amu). However, the forward velocity of the components of the beam must be corrected using an electric field. Thereby, the field applies the same force to all singly charged particles, which means that heavy particles are less influenced. Taking a flight-time difference of approximately $200\,\mu\mathrm{s}$ between light and heavy particles and a beam velocity of about $200\,\mathrm{m/s}$ into account, the difference in drift distance is about 4 cm, which is about the size of the MCP-detector. This estimation shows that a wide range of masses can be recorded using the same settings, but only a certain mass fraction can be guided to the detector in an optimal way, which must be considered when interpreting TOF mass spectra.

8.3.2.3 Stability:

The ionization energy as well as excitation energies of He are large compared to the ionization energy and binding energy of metal clusters. The excess energy in direct electron impact ionization or indirect ionization processes (charge hopping or Penning ionization) can lead to the emission of two electrons and to the fragmentation of larger compounds,

which is the main process leading to the increased abundance of clusters with a higher stability (experimentally observed magic numbers).[131] This stability-effect also indicates to what extent fragmentation plays a role. The effect is especially noticeable in the even-odd-oscillations at small cluster sizes (Fig. 8.5), where the peaks corresponding to an odd number of atoms in the ionized cluster (even number of electrons) have the higher intensity (higher binding energy of low-spin configurations). Besides at electronic shell closings, magic numbers can also occur at geometrically distinguished configurations, as highlighted in Fig. 8.4 where significant drops in intensity are visible after Cr_7 (pentagonal bi-pyramid) and Cr_{13} (icosahedron with a single shell around the center atom).
Additionally, not only bare dopant clusters arrive at the detector of the TOFMS, also He-droplets and their fragments (broad feature on the left side of the mass spectra in Figs. 8.2, 8.3, 8.13) and Me_nX_m can be found in the spectra (with Me corresponding to the respective metal and X corresponding to He or, if the baseline pressure is not sufficiently low, H_2O and other contamination).

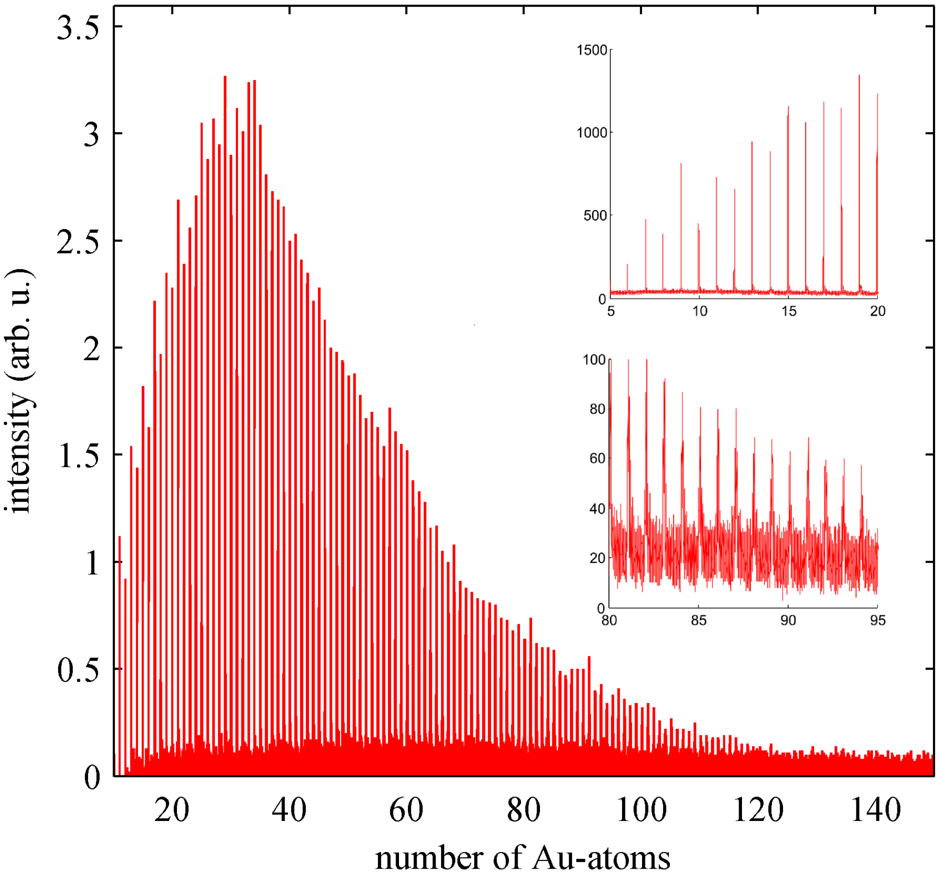

Figure 8.5: Mass spectrum of Au-doped helium droplets, recorded using electron impact ionization. The inserts show the even-odd oscillations at small cluster sizes and the resolution at higher masses.

8.3.2.4 Sensitivity of the MCP:

The sensitivity of an MCP depends on the velocity v of the impacting ions and decreases with lower velocity.[46] Consequently, larger components are harder to detect. The exact dependency of the detector response on the impact velocity is very complex and we limit ourselves to a qualitative discussion here. In order to improve the response to heavy particles in our setup, the velocity of the ions is increased ($> 10^4$ m/s for 20000 amu) by a so-called "post acceleration voltage" of 20 kV just before reaching the MCP-detector. Furthermore, a mass filter, which deflects only light ions, can be applied, preventing saturation or even damage of the detector by excessive impingement of more frequent light ions (small He_N). This enables higher operating voltages at the MCP and hence a better detection of heavy components.

8.3.2.5 Isotopes:

As gold is a mononuclidic element, a certain cluster size Au_n corresponds to a single mass, yielding a sharp peak in the mass spectrum (Fig. 8.5). In contrast, the other elements investigated in this work have several naturally occurring isotopes and therefore a certain cluster size (Me_n with fixed n) can correspond to different masses (multinomially distributed). With increasing mass, peaks start to merge because of the decreasing resolution and isolated peaks can no longer be observed for large clusters (*e.g.* Figs. 8.2 and 8.3). A clear assignment is only possible for small n, as was demonstrated for Cr clusters in Ref. [124].

8.3.3 Electron Microscopy

Although modern transmission electron microscopes are highly advanced devices, the detection of clusters containing not more than a few hundred atoms is challenging. Interactions between nanoparticle and substrate deform the clusters to an unknown extent,[67] preventing the extraction of volumetric data from two-dimensional images. Even when knowing their average shape, poor contrast caused by the smallness of the particles with respect to the substrate thickness obscures their outline and prevents an unambiguous determination of the particle diameter. A strategy to measure the cluster size distribution as unbiased as possible was developed, using the software package "Fiji ImageJ".[135] Firstly, the original TEM micrographs were processed using the built-in functions of Fiji (despeckle and fast fourier transform bandpass filter) in order to reduce noise and to highlight the clusters. Finally an intensity threshold was set manually to detect particles for a subsequent automated analysis. The process from the original image to the particle detection is depicted in Fig. 8.6. Of course, such an algorithm cannot distinguish between the particles of interest and contamination, but automation is necessary in order to collect a statistically relevant amount of data.

One has to be aware that the electron beam interacts with the particles. This interaction can lead to an increased diffusion and thereby deformation of the particles. Additionally, it can trigger oxidation of the particles or cover them with a carbonaceous layer,

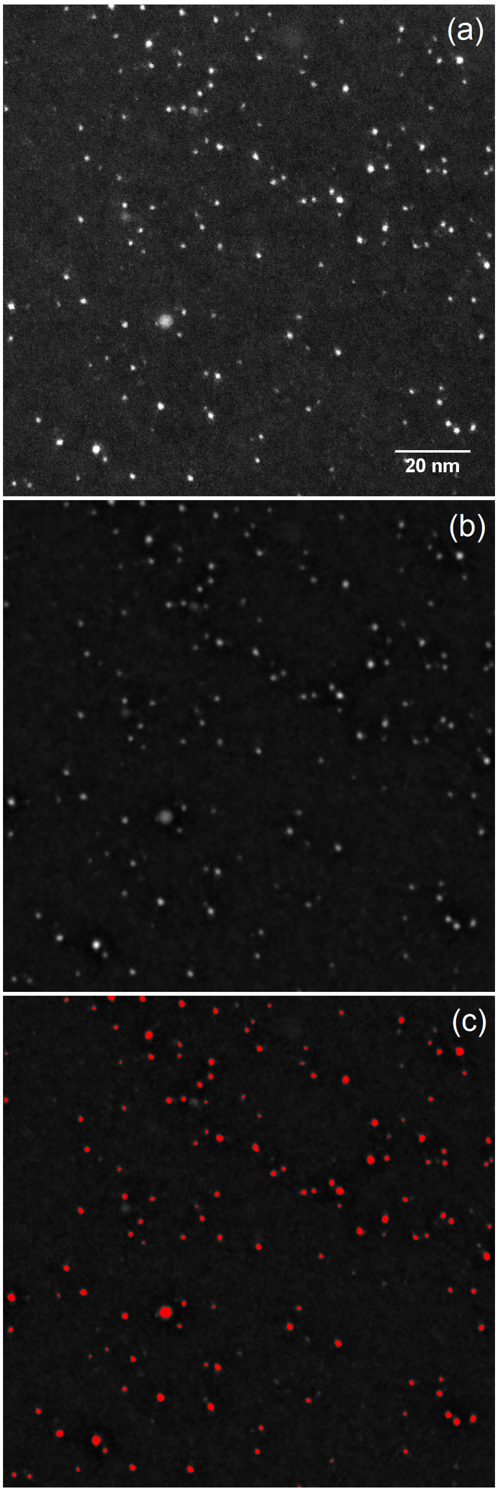

Figure 8.6: Particle analysis with the software package "Fiji ImageJ" of Au-nanoparticles, synthesized at $T_0 = 9\,\mathrm{K}$, $p_0 = 20\,\mathrm{bar}$ and a vapor cell temperature of $T_{Au} = 1100\,^\circ\mathrm{C}$. Displayed are the original image (a), the processed (see text) image (b) and the automatic particle recognition using an intensity threshold with the detected particles in red (c).

originating from hydrocarbons in the microscope vacuum.[71, 83, 125]
Primarily, TEM images yield two dimensional information, but by using advanced techniques such as tomography or quantitative high angle annular dark-field (HAADF) STEM three dimensional information can be reconstructed. The latter relies on the Z-dependency of the contrast (Z-contrast) in atomically resolved HAADF images, which can be used to count atoms column-wise. Exact knowledge of the imaging system and an appropriate orientation of the particle are, however, required for a reliable quantification result. For data analysis AbsoluteIntegrator, a freely available MATLAB-package, was used.[74]

8.3.4 Theoretical Calculation

In this section, a simple Monte Carlo simulation describing the nanoparticle growth behavior based on average pickup and nucleation rates is presented.
Using the doping cell temperature measured in the experiments and the vapor pressure curves from Ref. [92],

$$p_{vapor}\left(T\right) = a_1 + a_2 T^{-1} + a_3 log\left(T\right) + a_4 T^{-3} \tag{8.1}$$

with a_i being material dependent empirical coefficients, the temperature dependent dopant density in the pickup region can be calculated. With this and the droplet size distribution [66, 78, 150] corresponding to the experimental expansion conditions, the average pickup frequency can be determined, assuming that the pickup cross-section of helium droplets is close to the geometrical cross-section.[151] The fact that each droplet picks up hundreds of dopant atoms in our experiments justifies the usage of averages. The heavy doping of the helium droplets is connected to the release of a significant amount of binding energy during the nanoparticle growth, which can lead to the evaporation of up to 80 % of the He atoms in the droplets. The amount of binding energy and hence the loss of He-atoms through the evaporative cooling mechanism (evaporation of $\approx 1600\,\mathrm{atoms/eV}$)[23, 151] can be calculated using the formula from Ref. [114],

$$E_{binding}(N) = \varPhi + \left(\frac{1}{2}D_e - \varPhi\right)\left(\frac{2}{N}\right)^{\frac{1}{3}} \tag{8.2}$$

taking the data for the dimer binding energy D_e and bulk cohesive energy $\varPhi$ from Refs. [111] and [76] respectively. The evaporation of helium and the resulting decrease of the pickup cross-section during the doping process are included in the simulation and can be compared to the actual attenuation of the helium flux in the experiment. Within this model, the calculated dopant cluster sizes (Me_n) match the measured nanoparticle size distributions (diameters in the TEM images) very well.
Within the simulation discussed above, a second Monte Carlo algorithm models the aggregation behavior of the dopant atoms picked up by a droplet. This algorithm is based on the droplet size dependent frequency of two-particle collisions obtained from DFT-calculations by Hauser *et. al.* (Ref. [64]), and provides additional statements about the growth kinetics and not only the final nanoparticle size.[59] The aforementioned

(8.3.1) survival of several larger clusters inside a single droplet can be observed in an experiment where different materials are doped to the droplets sequentially, forming core-shell particles.[59] In the microscopy images we see that larger dopant particles exhibit two or multiple cores while smaller ones possess a single core, showing experimentally that separated clusters of the first material survive until the second pickup cell. The effect, that separated dopant clusters survive the flight-time to the second pickup cell is reproduced by this simulation.

8.4 Results and Discussion

8.4.1 Influence of the Expansion- and Doping-Conditions on the Particle Size

As already mentioned, the cluster size distribution can be controlled by varying the droplet size distribution as well as the degree of doping. The droplet size distribution depends on the nozzle diameter, the stagnation pressure and the nozzle temperature. In the experiment, only pressure and temperature can be changed easily. Assuming the expansion to be an isentropic process, different temperature-pressure couples lying on the same isentropic line yield the same result. Therefore, only one of the two parameters is independent, which means that varying the temperature is sufficient to probe different expansion conditions.

The doping intensity can be tuned by adjusting the partial pressure of the dopants in the pickup cells *via* the cell temperature. Thereby, the doping level can be observed in two ways: directly with the TOFMS and indirectly *via* the evaporation of helium due to doping. The latter is measured as a decrease in He partial pressure in the last chamber (*cf.* Ref. [102]). It should be noted that if the doping intensity is too high, the droplets are completely destroyed and the dopants are no longer carried into the last chamber.

Figs. 8.2 and 8.3 show the dependence of the particle size distribution on the nozzle temperature at constant vapor cell temperature and *vice versa*. The broad maximum observed in all the spectra shown in these two figures corresponds to the chromium cluster size distribution. By changing the experimental settings, the maximum of the Cr_N size distribution can be shifted deliberately (Figs. 8.2 and 8.3). The fact that no isolated peaks are observed beyond $\approx 4000\,$amu is a result of the different Cr-isotopes, as explained in section 8.3.2.5. Anomalies in the intensity can can be found at Cr_7 and Cr_{13} (see Fig. 8.4) which correspond to fragments in a geometrically especially stable configuration. It should be noted that Figs. 8.2 - 8.4 show unprocessed data, which means that not the height but the area below a peak corresponds to the occurrence of the respective cluster size.

It can be seen that the nozzle temperature is a very delicate parameter, while varying the vapor cell temperature provides better control over the shift of the size distribution. Nevertheless, as the droplet volume, which is important for the dopant size, grows with the third power of the droplet radius and the pickup cross-section grows with the second power of the radius, a balanced interplay between nozzle temperature and vapor cell

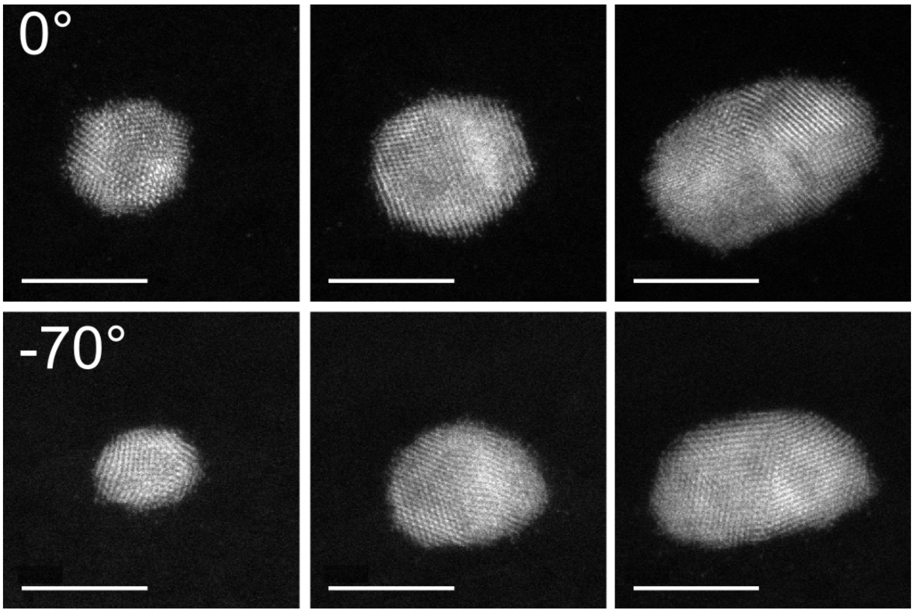

Figure 8.7: Images of three Au-Ag-nanoparticles under different tilt angles to show their flattened shape. The scale bar is 5 nm in all images. The given angles denote the tilt of the substrate's normal with respect to the electron beam.

temperature is advantageous to generate the desired dopant size distribution.

8.4.2 Particle Shape

The shape of deposited particles is mainly influenced by three aspects: the substrate and deposition conditions as well as the cluster formation process inside the droplets.

8.4.2.1 Substrate and Deposition Conditions

Simulations show that the final shape of a nanoparticle on a substrate is determined by the landing process and the binding energy to the substrate.[146] So far, most experiments were conducted using amorphous carbon as substrate. For this substrate, tomographic investigations (Fig. 8.7) as well as Z-contrast quantification (Fig. 8.8) show a lenticular shape, with the smallest dimension perpendicular to the substrate surface. The particles appear to be about half as thick as their diameter.

Tomographic reconstruction of all atomic positions in one of these clusters exemplarily showed a truncated icosahedral structure,[59] but also interference patterns in regular TEM images reveal icosahedral and decahedral structures at cluster sizes where these morphologies are no longer energetically preferred.[155] The high level of symmetry in these clusters indicates that surface diffusion also plays an important role for the final shape and structure of a particle, especially in the case of silver, which exhibits much higher diffusion coefficients than the other materials observed here. [97, 154]

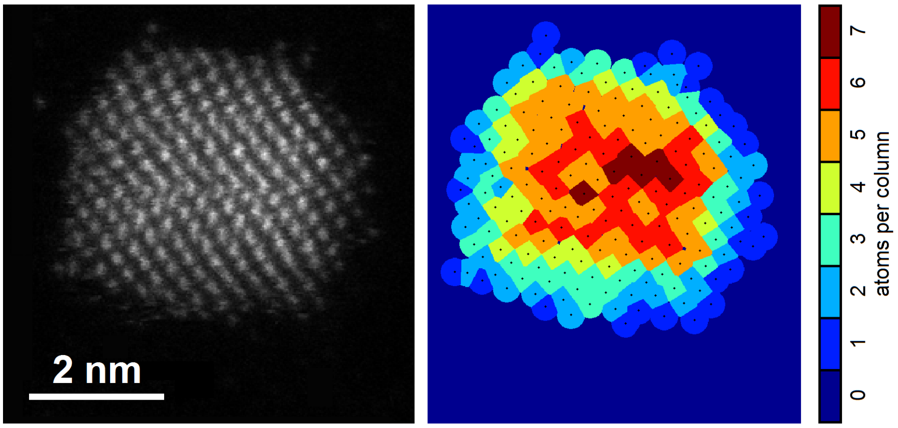

Figure 8.8: STEM-HAADF-image of a Au-cluster (left image). Z-contrast quantification indicates a flattened shape of the nanoparticles on the substrate (right image). The scale is identical in both images.

8.4.2.2 Expansion Conditions

Several experiments[47, 49, 87, 145] demonstrate the existence of vortices in helium droplets and their effect on dopants, which is the formation of one-dimensional dopant structures. In a survey using two different stagnation pressures (p_0 = 20 and 50 bar) and a series of different nozzle temperatures, we were able to localize the transition from spherical clusters to elongated particles or nanowires.

As can be seen in Fig. 8.9, we can place the transition from spherical particles to elongated structures for $p_0 = 20\,\text{bar}$ at $T_0 \approx 7.5\,\text{K}$ and for $p_0 = 50\,\text{bar}$ at $T_0 \approx 9\,\text{K}$. Both conditions lie on the same isentrope in the phase diagram [21] and yield a mean droplet size of about $\bar{N} = 10^7$ atoms.[48]

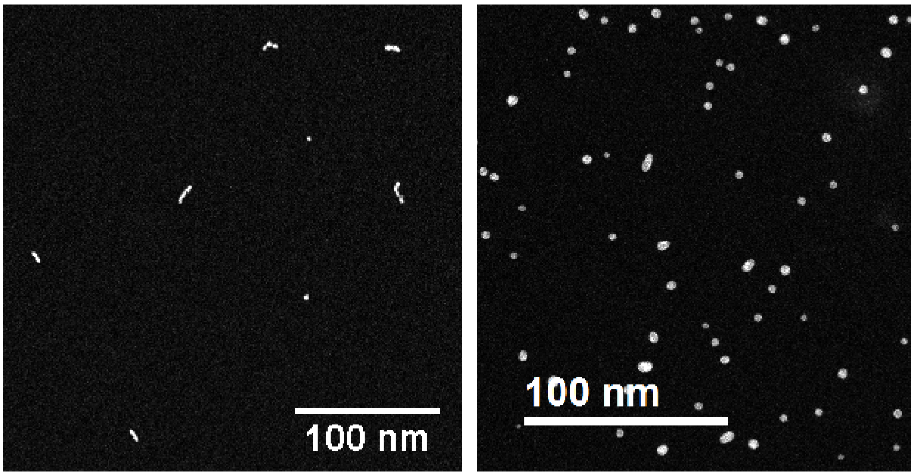

Figure 8.9: HAADF-images of spheroid (right image) and elongated (left image) Au-nanoparticles, depicting the change in particle shape between $T_0 = 8\,\text{K}$ and $T_0 = 7\,\text{K}$, respectively, at $p_0 = 20\,\text{bar}$.

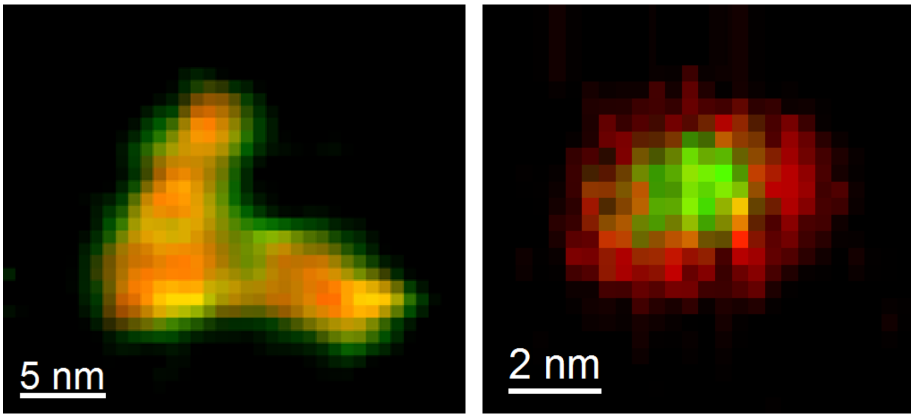

Figure 8.10: Elemental mapping of a kinked nanowire (left) and lenticular nanoparticle (right) using EDX and EELS. In both cases red corresponds to Au and green corresponds to Ag. The orange color in the left image results as an overlay of the Ag- and Au-occurrence.

8.4.3 Bimetallic Particles

It was often argued that the ultra-low temperature environment provided by the helium droplet leads inevitably to the formation of core-shell particles when two species are doped to the droplet sequentially. In recent experiments we were able to produce spherical core-shell particles[59] as well as core-shell nanowires[145] using Au and Ag as dopants, with the sequence of the materials depending on the sequence of pickup (see Fig. 8.10). Thereby, the chemically relatively inert constituents as well as the very similar lattice constants make the system experimentally easy to handle. Chemical analysis with energy dispersive x-ray spectroscopy (EDX), electron energy loss spectroscopy (EELS) as well as Z-contrast in tomographic reconstructions reveal that cluster-cluster growth obstructs ideal core-shell formation. In the case of spherical core-shell particles, multiple cores are observed in particles larger than a certain size which supports the cluster-cluster growth model (*cf.* 8.3.4 and Ref. [59]). Thereby, the transition from single- to multi-core morphologies can be predicted by a simple computer simulation.[59] In the case of core shell nanowires, the concentration of the core material varies along the wire, indicating a growth from several initially separated core-shell segments.[145]

8.4.4 Comparison Between Mass Spectrometry, Electron Microscopy and Simulations

TEM images and TOF-spectra show different aspects of the produced nanoparticles. While the latter gives information about the mass and hence the volume, the former predominantly yields the projected shape. In order to be able to compare the two techniques to each other, additional information about the third dimension of the deposited particles is necessary. This information can be extracted from Z-contrast quantification, tomographic reconstructions, QCM measurements of the total dopant mass flow or theoretical calculations and shows a lenticular shape of nanoparticles deposited on an amorphous carbon substrate. Thereby, the exact shape depends on the material of the particle, the substrate material and the size of the particles. To simplify, we assume a spherical or hemispherical shape of the deposited particles in the comparative graphs.

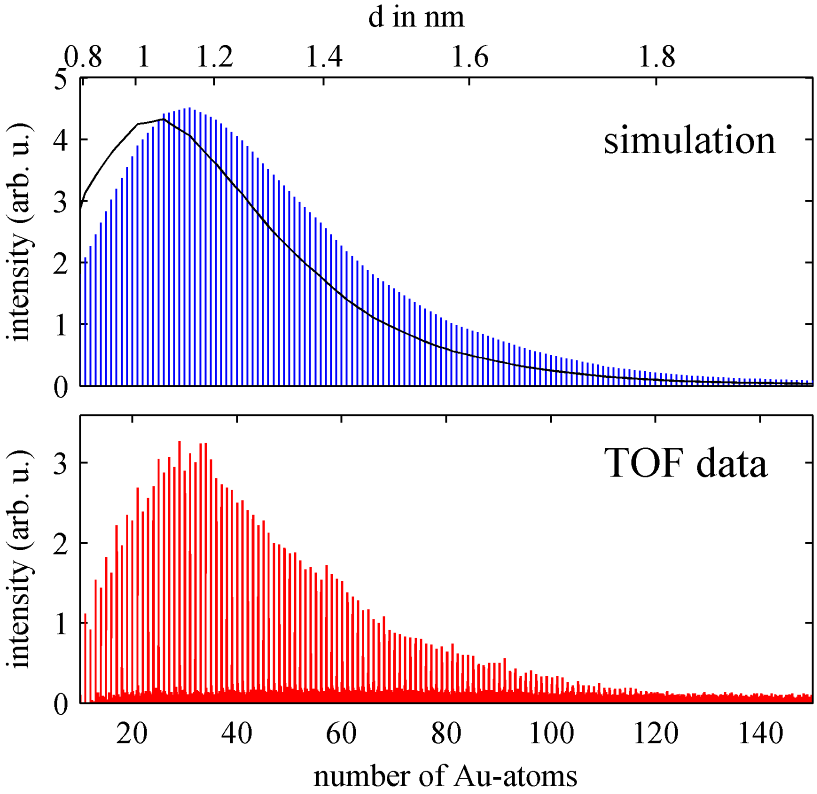

Figure 8.11: Comparison of the cluster size distribution of Au-doped helium droplets measured with TOFMS (using electron impact ionization) with the simulated cluster size distribution. The solid line in the upper graph accounts for the velocity dependent sensitivity of the MCP detector (electron emission yield $\propto v$ and accordingly $\propto 1/\sqrt{m}$). The diameter scale in the upper graph refers to hemispherical clusters. ($T_0 = 9.0\,\mathrm{K}$, $p_0 = 20\,\mathrm{bar}$)

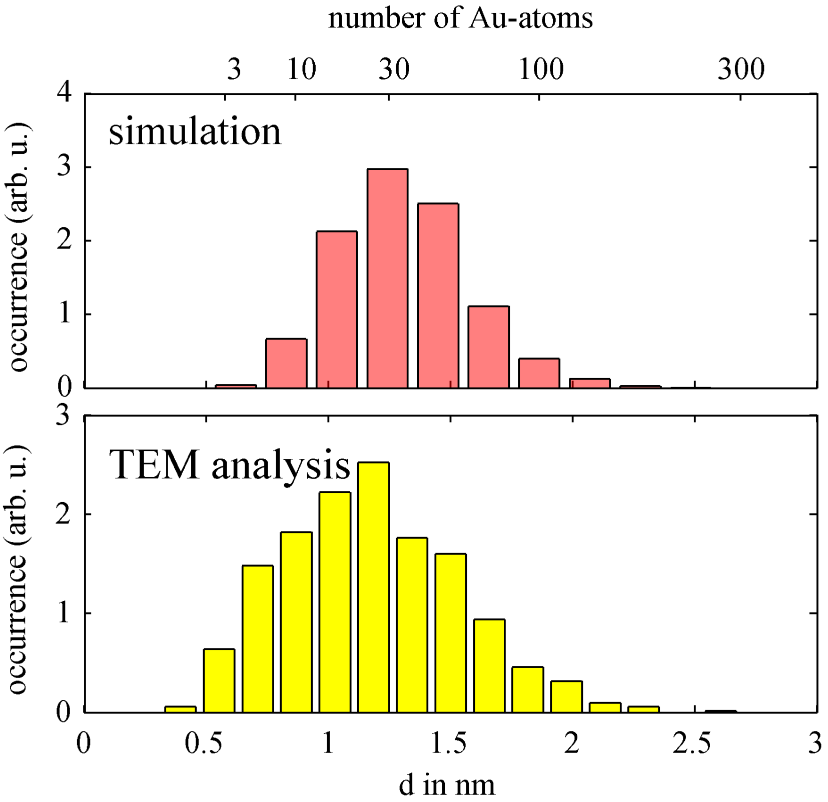

Figure 8.12: Comparison of the cluster size distribution of Au-doped helium droplets observed in TEM with the simulated cluster size distribution, assuming a hemispherical shape of the landed clusters. ($T_0 = 9.0\,\mathrm{K}$, $p_0 = 20\,\mathrm{bar}$)

In the following, the TOFMS-data (obtained with electron impact ionization), the TEM-data of simultaneously produced samples and data from computer simulations based on the experimental settings will be compared and discussed for two experiments. In order to keep the "native" scale (mass units for TOFMS and diameter for TEM) of each detection technique, the methods are compared separately to the same simulation data.

In the first experiment Au was used as dopant, which is mononuclidic and therefore yields only one sharp peak per cluster size in the mass spectrum. The decreasing detection sensitivity of the MCP for larger masses combined with the high atomic number of Au prevents the undistorted detection of Au-particles containing more than about a hundred atoms. Accordingly, the experimental conditions (stagnation conditions: $T_0 = 9.0\,\mathrm{K}$, $p_0 = 20\,\mathrm{bar}$, vapor cell: $T_{Au} = 1100\,^{\circ}\mathrm{C}$) were chosen to yield nanoparticles small enough to be detected by TOFMS but still large enough to be seen in TEM-images. Feeding the experimental conditions in our computer program, we get excellent agreement with the TOFMS data (Fig. 8.11). As discussed earlier, assumptions about the 3D-shape of the particles have to be made in order to make the TEM-data comparable.

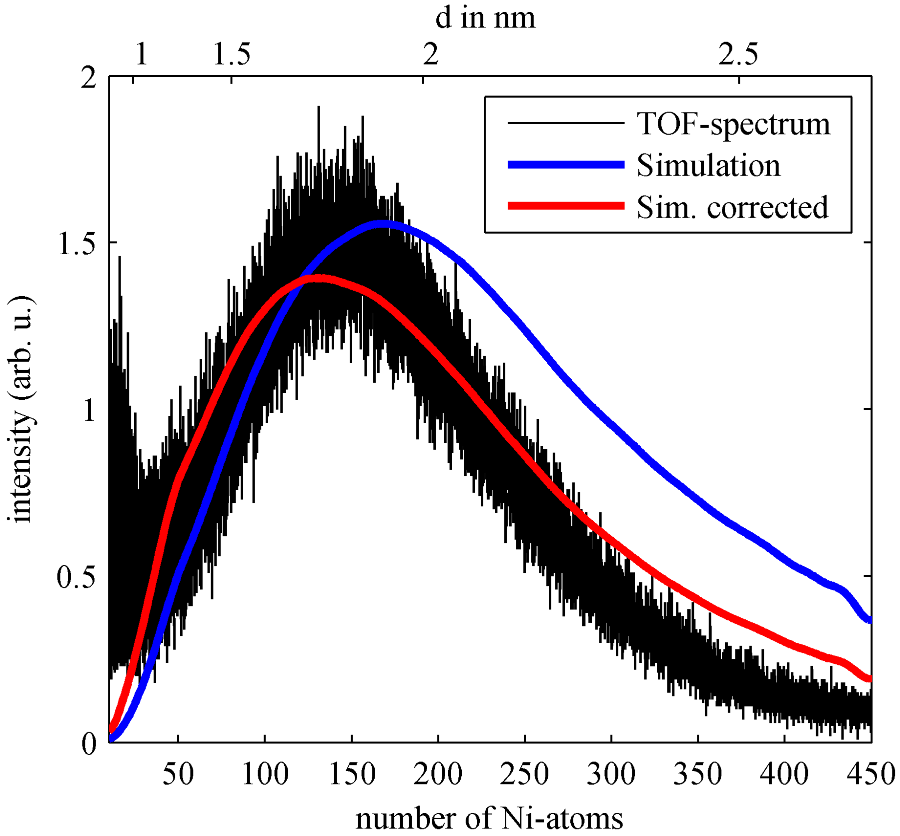

Figure 8.13: Comparison of the cluster size distribution of Ni-doped helium droplets ($T_0 = 9.0\,\mathrm{K}$) received from TOFMS measurements (using electron impact ionization) and simulations. The red curve (Sim. corrected) accounts for the velocity dependent sensitivity of the MCP detector (electron emission yield $\propto v$ and accordingly $\propto 1/\sqrt{m}$).

Fig. 8.12 shows that the simulation data (same data as in Fig. 8.11) would fit best with a particle shape between spherical and hemispherical.

The other experiment was carried out using Ni as dopant, which has a much lower atomic number than Au and hence allows to detect larger particles with the TOFMS. This fact was used to check the correspondence between the mass spectra and microscopy images for larger particles than in the Au-experiment. Using the same stagnation conditions ($T_0 = 9.0\,\mathrm{K}$, $p_0 = 20\,\mathrm{bar}$), the vapor cell temperature ($T_{Ni} = 1430\,°\mathrm{C}$) was set to yield higher doping rates and thus larger clusters. The existence of several stable Ni-isotopes leads to the merging of peaks at bigger masses, which yields a continuous mass spectrum (Fig. 8.13). The computer program again predicts the measured TOF-data very well, except for the wing on the left side of the spectrum. This feature originates from the helium droplets themselves as well as from fragmented clusters and is only visible because the overall intensity of the spectrum is low. When correcting the simula-

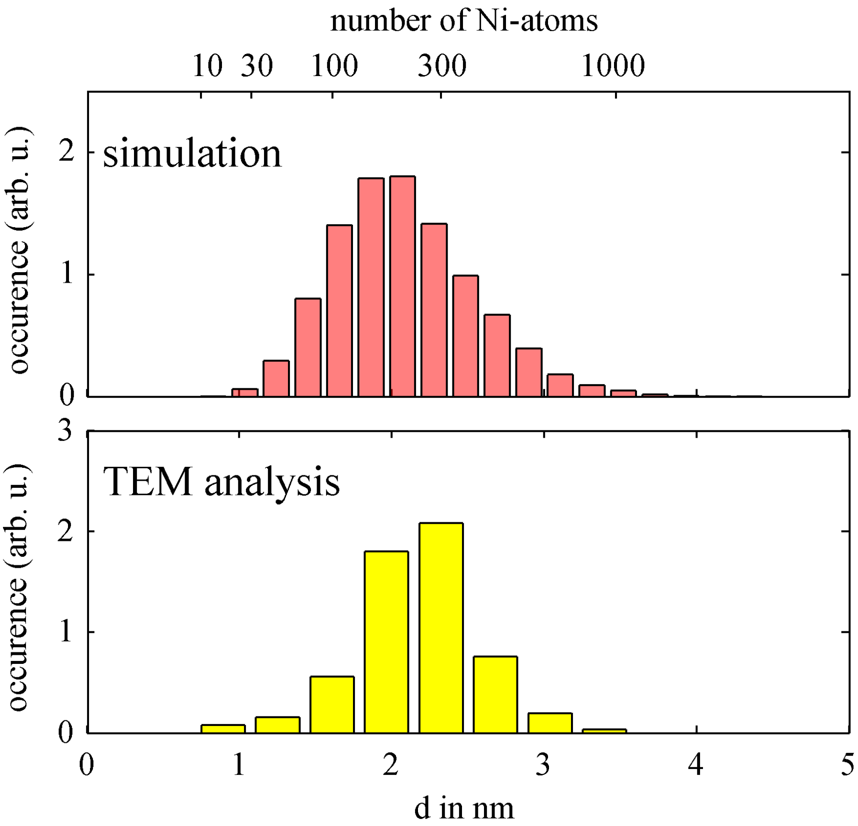

Figure 8.14: Comparison of the cluster size distribution of Ni-doped helium droplets ($T_0 = 9.0\,\mathrm{K}$) obtained from TEM-image evaluation and simulations, assuming hemispherical clusters

tion data for an MCP-sensitivity $\propto v$ and accordingly $\propto 1/\sqrt{m}$, the predicted spectrum lies even closer to the experimental data. The size distributions from TEM-image evaluation (Fig. 8.14) and the simulation (same data as in Fig. 8.13) are also in good correspondence when assuming a hemispherical particle shape.

8.5 Conclusions

We present a new helium droplet apparatus for synthesizing nanoparticles, which enables characterization of the produced particles simultaneously to other subsequent experiments. In the size range observed, the data from *in-situ* mass spectrometric measurements correspond very well with the particle sizes seen in subsequent *ex-situ* electron microscopic investigations. Furthermore, both experimental methods are in good agreement with simple theoretical considerations, which assures that our data analysis is unbiased and reliable. The possibility to characterize nanoparticles *in-situ* during the synthesis process allows to keep them under UHV-conditions at all times, which is essential when dealing with reactive samples or when inspecting the particle's catalytic properties.

In this article, the dependence of particle-size and -shape on the experimental conditions was carefully characterized and the experimental conditions for the crossover from spherical clusters to elongated structures were identified. Experiments using two different dopant species sequentially yield information on the growth process, and provide the fundamentals for generating more complex nanoparticles in a controlled way.

Chapter 9

Summary

This thesis together with the attached manual presents the development and characterization of a new apparatus for the synthesis of nanoparticles inside micron sized helium droplets. The capability of the new machine to produce bare and bimetallic (core-shell) clusters and nanowires consisting of different metals (Ag, Au, Ni, Cr) was demonstrated.

9.1 Applicability of the Helium Droplet Method

In contrast to other nanoparticle synthesis methods, the helium droplet technique distinguishes itself through the pristine, inert environment and the ultra-low temperatures provided by the He-matrix. This technique does not use any stabilizers, ligands or templates, nevertheless, the universal doping capabilities of He-droplets allow the efficient growth of clusters of arbitrary materials in a controlled way. By varying the helium droplet size and the vapor pressure of the dopants in the pickup cells, the size of the produced clusters can be controlled in a very straight forward fashion. The appliance of sequential pickup schemes was shown to result in core-shell particles which may present unusual properties in terms of catalysis and magnetism. Furthermore, by utilizing vortices inside large helium droplets, which attract dopants, one-dimensional nanostructures or nanowires can be grown. Besides *in-situ* characterization, the synthesized nanoparticles can be deposited on any ultra-high vacuum (UHV) compatible substrate for further *ex-situ* investigations. A commercial battery powered UHV transfer system enables the transport of samples to facilities all over the world without breaking the vacuum.

A limitation of the technique is the very low quantity of nanoparticles produced. Depending on the growth regime, the deposited amount of nanoparticles does not exceed 0.01 - 1 μg per hour (measured with a quartz crystal microbalance). As the properties of the synthesized nanoparticles may change if they aggregate due to migration on the surface after landing, appropriate substrates have to be chosen to immobilize the landed particles and the surface coverage has to be kept low. In many cases a single low-coverage layer of nanoparticles will not give a significant signal when using macroscopic measuring techniques. In order to be able to apply macroscopic diagnostics, several layers of nanoparticles separated by a parting layer would have to be used. Thereby, particles embedded in the separation layer may also be influenced by the matrix and show different properties than their surface deposited "naked" counterparts.

Another limitation is given by the occurrence of vortices inside the helium droplets. While these vortices can be used deliberately to create elongated structures, they set an upper limit for the maximum size of spherical nanoparticles, which lies between 5 and 10 nm diameter, depending on the dopant material.

9.2 Growth Model

By analyzing electron microscopy data of deposited nanoparticles synthesized using various experimental conditions, a model for the growth of clusters and nanoparticles inside helium droplets can be provided. Especially the investigation of bimetallic nanoparticles with element sensitive electron microscopic detection techniques, as described in chapter 6, which correspond very well with computer simulations, give insights into the growth process.

The details of the particle growth mechanism change, depending on the helium droplet size and the doping frequency compared to the velocity of the atoms or particles embedded in these droplets. The following model describes the situation where the helium droplets are doped with metal atoms and about 50% of the helium atoms in the droplets are evaporated due to doping (dissipating the binding energy during aggregation and cooling the dopants), which is a typical value for particle synthesis experiments.

Under these conditions, small helium droplets ($\mathrm{N} < 5 \times 10^5$) will contain a single cluster, which grows by subsequent addition of single atoms.

In medium sized helium droplets ($5 \times 10^5 < \mathrm{N} < 1 \times 10^7$) the doping frequency exceeds the nucleation frequency, which means that clusters start to grow at different positions inside the droplet simultaneously (multi-center growth). However, simulations show that the fact that atoms or small clusters move and aggregate much faster than larger compounds (conservation of momentum) leads to a situation where only one larger particle can develop during the doping process and the growth of other clusters ends at an early stage, when they collide with this major particle. Engaging the same considerations, the merging process of all picked up atoms into a single particle will be completed very soon after leaving the doping cell. Upon collision, small clusters melt completely, which means that multi-center aggregation has no consequence for the final shape of particles in medium sized droplets.

This situation changes for large droplets ($\mathrm{N} > 10^8$), where several bigger (slow) particles can survive for a significant amount of time. If two of these particles collide and aggregate, they no longer melt completely and do not yield a larger spherical particle. Instead, in the presence of vortices inside the droplets, which attract the dopants, the described aggregation mechanism leads to the formation of nanowires.

Bibliography

[1] D. J. Acheson. *Elementary fluid dynamics.* Oxford University Press, 1990.

[2] N. F. Aguirre, D. Mateo, A. O. Mitrushchenkov, M. Pi, and M. P. De Lara-Castells. Helium mediated deposition: Modeling the He-TiO 2(110)- (1x1) interaction potential and application to the collision of a helium droplet from density functional calculations. *J. Chem. Phys.*, 136(12):124703–1–124703–14, 2012.

[3] S. Alves, A. Vilesov, and S. Ferreira Jr. Effects of the mean free path and relaxation in a model for the aggregation of particles in superfluid media. *J. Chem. Phys.*, 130(24):244506, 2009.

[4] L. An der Lan, P. Bartl, C. Leidlmair, H. Schöbel, S. Denifl, T. D. Märk, A. M. Ellis, and P. Scheier. Submersion of potassium clusters in helium nanodroplets. *Phys. Rev. B*, 85(11):115414, 2012.

[5] L. An der Lan, P. Bartl, C. Leidlmair, H. Schöbel, R. Jochum, S. Denifl, T. D. Märk, A. M. Ellis, and P. Scheier. The submersion of sodium clusters in helium nanodroplets: Identification of the surface-interior transition. *J. Chem. Phys.*, 135(4):044309–1–044309–6, July 2011.

[6] F. Ancilotto, P. B. Lerner, and M. W. Cole. Physics of solvation. *J. Low Temp. Phys.*, 101(5-6):1123–1146, 1995.

[7] H. C. Andersen. Molecular dynamics simulations at constant pressure and/or temperature. *J. Chem. Phys.*, 72(4):2384–2393, 1980.

[8] I. Arslan, T. Yates, N. Browning, and P. Midgley. Embedded nanostructures revealed in three dimensions. *Science*, 309(5744):2195–2198, 2005.

[9] R. C. Baetzold. Calculated properties of metal aggregates: III. Carbon substrates. *Surf. Sci.*, 36(1):123 –140, 1973.

[10] B. G. Bagley. A dense packing of hard spheres with five-fold symmetry [2]. *Nature*, 208(5011):674–675, 1965.

[11] F. Baletto and R. Ferrando. Structural properties of nanoclusters: Energetic, thermodynamic, and kinetic effects. *Rev. Mod. Phys.*, 77(1):371–423, 2005.

[12] F. Baletto, R. Ferrando, A. Fortunelli, F. Montalenti, and C. Mottet. Crossover among structural motifs in transition and noble-metal clusters. *J. Chem. Phys.*, 116(9):3856–3863, 2002.

[13] F. Baletto, C. Mottet, and R. Ferrando. Reentrant morphology transition in the growth of free silver nanoclusters. *Phys. Rev. Lett.*, 84(24):5544–5547, 2000.

[14] F. Baletto, C. Mottet, and R. Ferrando. Microscopic mechanisms of the growth of metastable silver icosahedra. *Phys. Rev. B*, 63(15):155408–1–155408–10, 2001.

[15] F. Baletto, C. Mottet, and R. Ferrando. Freezing of silver nanodroplets. *Chem. Phys. Lett.*, 354(1):82–87, 2002.

[16] J. Bansmann, S. H. Baker, C. Binns, J. A. Blackman, J. P. Bucher, J. Dorantes-Dávila, V. Dupuis, L. Favre, D. Kechrakos, A. Kleibert, K.-H. Meiwes-Broer, G. M. Pastor, A. Perez, O. Toulemonde, K. N. Trohidou, J. Tuaillon, and Y. Xie. Magnetic and structural properties of isolated and assembled clusters. *Surf. Sci. Rep.*, 56(6-7):189–275, 2005.

[17] J. Barnard, J. Sharp, J. Tong, and P. Midgley. High-resolution three-dimensional imaging of dislocations. *Science*, 313(5785):319–319, 2006.

[18] D. Belić, R. L. Chantry, Z. Y. Li, and S. A. Brown. Ag - Au nanoclusters: Structure and phase segregation. *Appl. Phys. Lett.*, 99(17):171914, 2011.

[19] S. Bjørnholm, J. Borggren, O. Echt, K. Hansen, J. Pedersen, and H. Rasmussen. The influence of shells, electron thermodynamics, and evaporation on the abundance spectra of large sodium metal clusters. *Z. Phys. D*, 19:47, 1991.

[20] A. Boatwright, C. Feng, D. Spence, E. Latimer, C. Binns, A. M. Ellis, and S. Yang. Helium nanodroplets: a new route to nanoparticles. *Faraday Discuss.*, 162:113–124, 2013.

[21] H. Buchenau, E. L. Knuth, J. Northby, J. P. Toennies, and C. Winkler. Mass spectra and time-of-flight distributions of helium cluster beams. *J. Chem. Phys.*, 92(11):6875–6889, June 1990.

[22] L. Cademartiri and G. A. Ozin. Ultrathin nanowires - a materials chemistry perspective. *Adv. Mater.*, 21(9):1013–1020, 2009.

[23] C. Callegari and W. E. Ernst. Helium droplets as nanocryostats for molecular spectroscopy - from the vacuum ultraviolet to the microwave regime. In F. Merkt and M. Quack, editors, *Handbook of High Resolution Spectroscopy Vol. 3*. John Wiley & Sons, Chichester, 2011.

[24] C.-C. Chen, C. Zhu, E. R. White, C.-Y. Chiu, M. Scott, B. Regan, L. D. Marks, Y. Huang, and J. Miao. Three-dimensional imaging of dislocations in a nanoparticle at atomic resolution. *Nature*, 496(7443):74–77, 2013.

[25] H.-P. Cheng and U. Landman. Controlled deposition, soft landing, and glass formation in nanocluster-surface collisions. *Science*, 260(5112):1304–1307, 1993.

[26] Y. G. Chushak and L. S. Bartell. Melting and freezing of gold nanoclusters. *J. Phys. Chem. B*, 105(47):11605–11614, 2001.

[27] F. Cleri and V. Rosato. Tight-binding potentials for transition metals and alloys. *Phys. Rev. B*, 48(1):22–33, 1993.

[28] C. L. Cleveland and U. Landman. Dynamics of cluster-surface collisions. *Science*, 257(5068):355–361, 1992.

[29] W. A. de Heer. The physics of simple metal clusters: experimental aspects and simple models. *Rev. Mod. Phys.*, 65:611–676, Jul 1993.

[30] S. Denifl. Formation of cations and anions upon electron interaction with (doped) helium droplets. *Eur. Phys. J. ST*, 222(9):2017–2033, 2013.

[31] S. Denifl, F. Zappa, I. Mähr, J. Lecointre, M. Probst, T. D. Märk, and P. Scheier. Mass spectrometric investigation of anions formed upon free electron attachment to nucleobase molecules and clusters embedded in superfluid helium droplets. *Phys. Rev. Lett.*, 97:043201, Jul 2006.

[32] H. Deutsch, P. Scheier, K. Becker, and T. Märk. Revised high energy behavior of the Deutsch-Maerk (DM) formula for the calculation of electron impact ionization cross sections of atoms. *Int. J. Mass Spectrom.*, 233(1):13–17, 2004.

[33] T. Diederich, T. Döppner, T. Fennel, J. Tiggesbäumker, and K.-H. Meiwes-Broer. Shell structure of magnesium and other divalent metal clusters. *Phys. Rev. A*, 72(2):023203–1–023203–11, Aug. 2005.

[34] R. J. Donnelly. *Quantized vortices in helium II*, volume 2. Cambridge University Press, 1991.

[35] A. M. Ellis and S. Yang. Model for the charge-transfer probability in helium nanodroplets following electron-impact ionization. *Phys. Rev. A*, 76(3):032714, 2007.

[36] S. B. Emery, K. B. Rider, and C. M. Lindsay. Stabilized magnesium/perfluoropolyether nanocomposite films by helium droplet cluster assembly. *Propellants Explos. Pyrotech.*, 39(2):161–165, 2014.

[37] S. B. Emery, K. B. Rider, B. K. Little, and C. M. Lindsay. Helium droplet assembled nanocluster films: Cluster formation and deposition rates. *J. Phys. Chem. C*, 117(5):2358–2368, 2013.

[38] S. B. Emery, K. B. Rider, B. K. Little, A. M. Schrand, and C. M. Lindsay. Magnesium cluster film synthesis by helium nanodroplets. *J. Chem. Phys.*, 139(5):054307, 2013.

[39] Ş. Erkoç. A new class of empirical many-body potential energy functions for bulk and cluster properties. *Phys. Status Solidi B*, 171(2):317–324, 1992.

[40] D. Faken and H. Jónsson. Systematic analysis of local atomic structure combined with 3D computer graphics. *Comp. Mater. Sci.*, 2(2):279–286, 1994.

[41] R. P. Feynman. There's plenty of room at the bottom. *Engineering and Science*, 23(5):22–36, 1960.

[42] B. D. Forbes, A. J. D'Alfonso, R. E. A. Williams, R. Srinivasan, H. L. Fraser, D. W. McComb, B. Freitag, D. O. Klenov, and L. J. Allen. Contribution of thermally scattered electrons to atomic resolution elemental maps. *Phys. Rev. B*, 86:024108, Jul 2012.

[43] D. V. Fursa and I. Bray. Calculation of electron-helium scattering. *Phys.Rev. A*, 52(2):1279, 1995.

[44] C. Giese, F. Stienkemeier, M. Mudrich, A. W. Hauser, and W. E. Ernst. Homo- and heteronuclear alkali metal trimers formed on helium nanodroplets. Part II. Femtosecond spectroscopy and spectra assignments. *Phys. Chem. Chem. Phys.*, 13(42):18769–18780, 2011.

[45] P. Gilbert. Iterative methods for the three-dimensional reconstruction of an object from projections. *J. Theor. Biol.*, 36(1):105–117, 1972.

[46] I. Gilmore and M. Seah. Ion detection efficiency in SIMS: Dependencies on energy, mass and composition for microchannel plates used in mass spectrometry. *Int. J. Mass Spectrom.*, 202(1):217–229, 2000.

[47] L. F. Gomez, K. R. Ferguson, J. P. Cryan, C. Bacellar, R. M. P. Tanyag, C. Jones, S. Schorb, D. Anielski, A. Belkacem, C. Bernando, et al. Shapes and vorticities of superfluid helium nanodroplets. *Science*, 345(6199):906–909, 2014.

[48] L. F. Gomez, E. Loginov, R. Sliter, and A. F. Vilesov. Sizes of large He droplets. *J. Chem. Phys.*, 135(15):154201–1–154201–9, 2011.

[49] L. F. Gomez, E. Loginov, and A. F. Vilesov. Traces of vortices in superfluid helium droplets. *Phys. Rev. Lett.*, 108(15):155302–1–155302–5, Apr. 2012.

[50] E. Gordon, A. Karabulin, V. Matyushenko, V. Sizov, and I. Khodos. Structure of metallic nanowires and nanoclusters formed in superfluid helium. *J. Exp. Theor. Phys.*, 112(6):1061–1070, 2011.

[51] E. Gordon, A. Karabulin, V. Matyushenko, V. Sizov, and I. Khodos. The role of vortices in the process of impurity nanoparticles coalescence in liquid helium. *Chem. Phys. Lett.*, 519:64–68, 2012.

[52] E. B. Gordon, A. V. Karabulin, V. I. Matyushenko, V. D. Sizov, and I. I. Khodos. The electrical conductivity of bundles of superconducting nanowires produced by laser ablation of metals in superfluid helium. *Appl. Phys. Lett.*, 101(5), 2012.

[53] E. B. Gordon, A. V. Karabulin, A. A. Morozov, V. I. Matyushenko, V. D. Sizov, and I. I. Khodos. Structure and properties of platinum, gold and mercury nanowires grown in superfluid helium. *J. Phys. Chem. Lett.*, 5(7):1072–1076, 2014.

[54] B. Goris, S. Bals, W. Van den Broek, E. Carbó-Argibay, S. Gómez-Graña, L. M. Liz-Marzán, and G. Van Tendeloo. Atomic-scale determination of surface facets in gold nanorods. *Nat. Mater.*, 11(11):930–935, 2012.

[55] B. Goris, A. De Backer, S. Van Aert, S. Gomez-Grana, L. M. Liz-Marzan, G. Van Tendeloo, and S. Bals. Three-dimensional elemental mapping at the atomic scale in bimetallic nanocrystals. *Nano Lett.*, 13(9):4236–4241, 2013.

[56] S. Grebenev, B. Sartakov, J. P. Toennies, and A. F. Vilesov. Evidence for superfluidity in para-hydrogen clusters inside helium-4 droplets at 0.15 Kelvin. *Science*, 289(5484):1532–1535, 2000.

[57] W. Greiner and H. Stock. *Hydrodynamik: ein Lehr-und Übungsbuch; mit Beispielen und Aufgaben mit ausführlichen Lösungen.* Harri Deutsch Verlag, 1991.

[58] G. Haberfehlner, A. Orthacker, M. Albu, J. Li, and G. Kothleitner. Nanoscale voxel spectroscopy by simultaneous EELS and EDS tomography. *Nanoscale*, 6(23):14563–14569, 2014.

[59] G. Haberfehlner, P. Thaler, D. Knez, A. Volk, F. Hofer, W. Ernst, and G. Kothleitner. Formation of bimetallic clusters in superfluid helium nanodroplets analyzed by atomic resolution electron tomography. *submitted*, 2015.

[60] H. Haberland. *Clusters of atoms and molecules: theory, experiment, and clusters of atoms*, volume 52. Springer Science & Business Media, 2013.

[61] J. Harms, J. P. Toennies, and F. Dalfovo. Density of superfluid helium droplets. *Phys. Rev. B*, 58(6):3341–3350, Aug. 1998.

[62] M. Hartmann, R. E. Miller, J. P. Toennies, and A. Vilesov. Rotationally resolved spectroscopy of SF_6 in liquid helium clusters: A molecular probe of cluster temperature. *Phys. Rev. Lett.*, 75(8):1566–1569, Aug. 1995.

[63] A. W. Hauser and W. E. Ernst. Homo-and heteronuclear alkali metal trimers formed on helium nanodroplets. Part I. Vibronic spectra simulations based on ab initio calculations. *Phys. Chem. Chem. Phys.*, 13(42):18762–18768, 2011.

[64] A. W. Hauser, A. Volk, P. Thaler, and W. E. Ernst. Atomic collisions in suprafluid helium-nanodroplets: timescales for metal-cluster formation derived from He-density functional theory. *Phys. Chem. Chem. Phys.*, 17(16):10805–10812, 2015.

[65] U. Heiz and U. Landman, editors. *Nanocatalysis.* Springer-Verlag, Berlin Heidelberg, 2007.

[66] U. Henne and J. P. Toennies. Electron capture by large helium droplets. *J. Chem. Phys.*, 108(22):9327–9338, 1998.

[67] C. R. Henry. Morphology of supported nanoparticles. *Progress in surface science*, 80(3):92–116, 2005.

[68] A. Hernando, A. Masson, M. Briant, J.-M. Mestdagh, M.-A. Gaveau, and N. Halberstadt. Fluorescence emission of Ca-atom from photodissociated Ca_2 in Ar doped helium droplets. *J. Chem. Phys.*, 137(18):184311, 2012.

[69] J. Higgins, C. Callegari, J. Reho, F. Stienkemeier, W. E. Ernst, K. K. Lehmann, and G. . Gutowski, M.and Scoles. Photoinduced chemical dynamics of high-spin alkali trimers. *Science*, 273(5275):629–631, 1996.

[70] J. Higgins, W. Ernst, C. Callegari, J. Reho, K. Lehmann, G. Scoles, and M. Gutowski. Spin polarized alkali clusters: Observation of quartet states of the sodium trimer. *Phys. Rev. Lett.*, 77(22):4532, 1996.

[71] S. Horiuchi, T. Hanada, M. Ebisawa, Y. Matsuda, M. Kobayashi, and A. Takahara. Contamination-free transmission electron microscopy for high-resolution carbon elemental mapping of polymers. *ACS Nano*, 3(5):1297–1304, 2009.

[72] P. H. Hünenberger. Thermostat algorithms for molecular dynamics simulations. In C. Holm and K. Kremer, editors, *Advanced Computer Simulation*, volume 173 of *Advances in Polymer Science*, pages 105–149. Springer-Verlag, Berlin Heidelberg, 2005.

[73] S. Jalili, C. Mochani, M. Akhavan, and J. Schofield. Molecular dynamics simulation of a graphite-supported copper nanocluster: thermodynamic properties and gas adsorption. *Mol. Phys.*, 110(5):267–276, 2012.

[74] L. Jones, K. E. MacArthur, V. T. Fauske, A. T. van Helvoort, and P. D. Nellist. Rapid estimation of catalyst nanoparticle morphology and atomic-coordination by high-resolution Z-contrast electron microscopy. *Nano Lett.*, 14(11):6336–6341, 2014.

[75] D. Z. Kandula, C. Gohle, T. J. Pinkert, W. Ubachs, and K. S. Eikema. Extreme ultraviolet frequency comb metrology. *Phys. Rev. Lett.*, 105(6):063001, 2010.

[76] C. Kittel. *Introduction to Solid State Physics.* John Wiley & Sons, Hoboken, 2005.

[77] K. Kneipp, M. Moskovits, and H. Kneipp. Surface-enhanced Raman scattering. *Phys. Today*, 60(11):40, 2007.

[78] E. L. Knuth and U. Henne. Average size and size distribution of large droplets produced in a free-jet expansion of a liquid. *J. Chem. Phys.*, 110(5):2664–2668, Feb. 1999.

[79] M. Koch. *Magnetic Resonance Spectroscopy of Single Alkali-Metal Atoms Isolated in Superfluid Helium Nanodroplets.* PhD thesis, TU Graz, 2009.

[80] M. Koch, G. Auböck, C. Callegari, and W. E. Ernst. Coherent spin manipulation and ESR on superfluid helium nanodroplets. *Phys. Rev. Lett.*, 103(3):035302, 2009.

[81] K. Koga and K. Sugawara. Population statistics of gold nanoparticle morphologies: Direct determination by HREM observations. *Surf. Sci.*, 529(1-2):23–35, 2003.

[82] G. Krois, J. V. Pototschnig, F. Lackner, and W. E. Ernst. Spectroscopy of cold LiCa molecules formed on helium nanodroplets. *J. Phys. Chem. A*, 117(50):13719–13731, 2013.

[83] A. Kumao, H. Hashimoto, and K. Shiraishi. Studies on specimen contamination by transmission electron microscopy. *J. Electron Microsc.*, 30:161–170, 1981.

[84] F. Lackner. *Rydberg States of Alkali-Metal Atoms on Superfluid Helium Nanodroplets.* PhD thesis, TU Graz, 2012.

[85] F. Lackner, G. Krois, T. Buchsteiner, J. V. Pototschnig, and W. E. Ernst. Helium-droplet-assisted preparation of cold RbSr molecules. *Phys. Rev. Lett.*, 113(15):153001, 2014.

[86] F. Lackner, G. Krois, M. Koch, and W. E. Ernst. Rubidium on helium droplets: Analysis of an exotic rydberg complex for $n^* < 20$ and $0 \leq l \leq 3$. *J. Phys. Chem. Lett.*, 3(10):1404–1408, 2012.

[87] E. Latimer, D. Spence, C. Feng, A. Boatwright, A. M. Ellis, and S. Yang. Preparation of ultrathin nanowires using superfluid helium droplets. *Nano Lett.*, 14(5):2902–2906, 2014.

[88] V. Lebedev, P. Moroshkin, B. Grobety, E. Gordon, and A. Weis. Formation of metallic nanowires by laser ablation in liquid helium. *J. Low Temp. Phys.*, 165(3-4):166–176, 2011.

[89] M. Lewerenz, B. Schilling, and J. P. Toennies. A new scattering deflection method for determining and selecting the sizes of large liquid clusters of ^{4}He. *Chem. Phys. Lett.*, 206(1-4):381–387, Apr. 1993.

[90] W. K. Lewis, B. E. Applegate, J. Sztáray, B. Sztáray, T. Baer, R. J. Bemish, and R. E. Miller. Electron impact ionization in helium nanodroplets: Controlling fragmentation by active cooling of molecular ions. *J. Am. Chem. Soc.*, 126(36):11283–11292, 2004.

[91] C. Li, W. Yin, H. Jiang, and Y. Zhang. An efficient augmented lagrangian method with applications to total variation minimization. *Computational Optimization and Applications*, 56(3):507–530, 2013.

[92] D. Lide. *Handbook of Chemistry and Physics, 72nd Edition*. CRC press, 1991-1992.

[93] C. M. Lieber. Nanoscale science and technology: building a big future from small things. *MRS Bulletin*, 28(07):486–491, 2003.

[94] C. M. Lindsay and R. E. Miller. Rotational and vibrational dynamics of ethylene in helium nanodroplets. *J. Chem. Phys.*, 122(10):104306–1–104306–9, 2005.

[95] S. Link and M. A. El-Sayed. Optical properties and ultrafast dynamics of metallic nanocrystals. *Annu. Rev. Phys. Chem.*, 54:331–366, 2003.

[96] S. Link, Z. L. Wang, and M. El-Sayed. Alloy formation of gold-silver nanoparticles and the dependence of the plasmon absorption on their composition. *J. Phys. Chem. B*, 103(18):3529–3533, 1999.

[97] C. Liu, J. Cohen, J. Adams, and A. Voter. EAM study of surface self-diffusion of single adatoms of fcc metals Ni, Cu, Al, Ag, Au, Pd, and Pt. *Surf. Sci.*, 253(1):334–344, 1991.

[98] J. Liu, B. Shepperson, A. M. Ellis, and S. Yang. Core–shell effects in the ionization of doped helium nanodroplets. *Phys. Chem. Chem. Phys.*, 13(31):13920–13925, 2011.

[99] E. Loginov and M. Drabbels. Excited state dynamics of Ag atoms in helium nanodroplets. *J. Phys. Chem. A*, 111(31):7504–7515, 2007.

[100] E. Loginov and M. Drabbels. Spectroscopy and dynamics of barium-doped helium nanodroplets. *J. Chem. Phys.*, 136(15):154302, 2012.

[101] E. Loginov, L. F. Gomez, N. Chiang, A. Halder, N. Guggemos, V. V. Kresin, and A. F. Vilesov. Photoabsorption of Ag_N (N=2-6000) nanoclusters formed in helium droplets: Transition from compact to multicenter aggregation. *Phys. Rev. Lett.*, 106:233401–1–233401–4, Jun 2011.

[102] E. Loginov, L. F. Gomez, and A. F. Vilesov. Surface deposition and imaging of large Ag clusters formed in He droplets. *J. Phys. Chem. A*, 115(25):7199–7204, 2011.

[103] E. Loginov, L. F. Gomez, and A. F. Vilesov. Formation of core–shell silver–ethane clusters in He droplets. *J. Phys. Chem. A*, 117(46):11774–11782, 2013.

[104] W. Lu and C. M. Lieber. Nanoelectronics from the bottom up. *Nat. Mater.*, 6(11):841–850, 2007.

[105] A. L. Mackay. A dense non-crystallographic packing of equal spheres. *Acta Crystallogr*, 15:916–918, 1962.

[106] T. P. Martin. Shells of atoms. *Phys. Rep.*, 273(4):199 – 241, 1996.

[107] A. R. W. McKellar, Y. Xu, and W. Jäger. Spectroscopic exploration of atomic scale superfluidity in doped helium nanoclusters. *Phys. Rev. Lett.*, 97:183401, 2006.

[108] D. P. Meichle and D. P. Lathrop. Nanoparticle dispersion in superfluid helium. *Rev. Sci. Instrum.*, 85(7):073705, 2014.

[109] P. A. Midgley and J. M. Thomas. Multi-dimensional electron microscopy. *Angew. Chem. Int. Ed.*, 53(33):8614–8617, 2014.

[110] P. Moroshkin, V. Lebedev, B. Grobety, C. Neururer, E. B. Gordon, and A. Weis. Nanowire formation by gold nano-fragment coalescence on quantized vortices in He II. *Eur. Phys. Lett.*, 90(3), 2010.

[111] M. D. Morse. Clusters of transition-metal atoms. *Chem. Rev.*, 86(6):1049–1109, 1986.

[112] V. Mozhayskiy, M. N. Slipchenko, V. K. Adamchuk, and A. F. Vilesov. Use of helium nanodroplets for assembly, transport, and surface deposition of large molecular and atomic clusters. *J. Chem. Phys.*, 127(9):094701–1–094701–6, 2007.

[113] M. Mudrich and F. Stienkemeier. Photoionisaton of pure and doped helium nanodroplets. *Int. Rev. Phys. Chem.*, 33(3):301–339, 2014.

[114] H. Müller, H.-G. Fritsche, and L. Skala. Analytic cluster models and interpolation formulae for cluster properties. In H. Haberland, editor, *Clusters of Atoms and Molecules I*. Springer-Verlag, Berlin Heidelberg, 1995.

[115] S. Müller, S. Krapf, T. Koslowski, M. Mudrich, and F. Stienkemeier. Cold reactions of alkali-metal and water clusters inside helium nanodroplets. *Phys. Rev. Lett.*, 102(18):183401, 2009.

[116] B. Nacer, C. Massobrio, and C. Félix. Deposition of metallic clusters on a metallic surface at zero initial kinetic energy: Evidence for implantation and site exchanges. *Phys. Rev. B*, 56(16):10590, 1997.

[117] J. Nagl, G. Auböck, A. W. Hauser, O. Allard, C. Callegari, and W. E. Ernst. Heteronuclear and Homonuclear High-Spin Alkali Trimers on Helium Nanodroplets. *Phys. Rev. Lett.*, 100:063001, 2008.

[118] O. Nicoletti, F. de La Peña, R. K. Leary, D. J. Holland, C. Ducati, and P. A. Midgley. Three-dimensional imaging of localized surface plasmon resonances of metal nanoparticles. *Nature*, 502(7469):80–84, 2013.

[119] S. Nie and S. R. Emory. Probing single molecules and single nanoparticles by surface-enhanced Raman scattering. *Science*, 275(5303):1102–1106, 1997.

[120] F. Palacios, M. Iniguez, M. López, and J. Alonso. Molecular-dynamics study of the structural rearrangements of Cu and Au clusters softly deposited on a Cu (001) surface. *Phys. Rev. B*, 60(4):2908, 1999.

[121] W. Palenstijn, K. Batenburg, and J. Sijbers. Performance improvements for iterative electron tomography reconstruction using graphics processing units (GPUs). *J. Struct. Biol.*, 176(2):250–253, 2011.

[122] I. Parsina and F. Baletto. Tailoring the structural motif of AgCo nanoalloys: Core/shell versus Janus-like. *J. Phys. Chem. C*, 114(3):1504–1511, 2010.

[123] V. N. Popok, I. Barke, E. E. B. Campbell, and K.-H. Meiwes-Broer. Cluster-surface interaction: From soft landing to implantation. *Surf. Sci. Rep.*, 66(10):347–377, 2011.

[124] M. Ratschek, M. Koch, and W. E. Ernst. Doping helium nanodroplets with high temperature metals: Formation of chromium clusters. *J. Chem. Phys.*, 136(10):104201–1–104201–6, 2012.

[125] L. Reimer and H. Kohl. *Transmission Electron Microscopy.* Springer-Verlag New York, 2008.

[126] D. Reinhard, B. D. Hall, D. Ugarte, and R. Monot. Size-independent fcc-to-icosahedral structural transition in unsupported silver clusters: An electron diffraction study of clusters produced by inert-gas aggregation. *Phys. Rev. B*, 55(12):7868–7881, 1997.

[127] R. Rejoub, B. Lindsay, and R. Stebbings. Determination of the absolute partial and total cross sections for electron-impact ionization of the rare gases. *Phys. Rev. A*, 65(4):042713, 2002.

[128] P. Rez and M. M. Treacy. Three-dimensional imaging of dislocations. *Nature*, 503(7476), 2013.

[129] V. Rosato, M. Guillope, and B. Legrand. Thermodynamical and structural properties of f.c.c. transition metals using a simple tight-binding model. *Philos. Mag. A*, 59(2):321–336, 1989.

[130] S. Grebenev, J.P. Toennies, A.F. Vilesov. Superfluidity Within a Small Helium-4 Cluster: The Microscopic Andronikashvili Experiment. *Science*, 279:2083 – 2086, 1998.

[131] M. Sakurai, K. Watanabe, K. Sumiyama, and K. Suzuki. Magic numbers in transition metal (Fe, Ti, Zr, Nb, and Ta) clusters observed by time-of-flight mass spectrometry. *J. Chem. Phys.*, 111(1):235, 1999.

[132] K. Sattler, J. Mühlbach, and E. Recknagel. Generation of metal clusters containing from 2 to 500 atoms. *Phys. Rev. Lett.*, 45(10):821, 1980.

[133] I. Scheele, A. Conjusteau, C. Callegari, R. Schmied, K. K. Lehmann, and G. Scoles. Near-infrared spectroscopy of ethylene and ethylene dimer in superfluid helium droplets. *J. Chem. Phys.*, 122(10):104307–1–104307–4, 2005.

[134] A. Scheidemann, J. Toennies, and J. Northby. Capture of neon atoms by He 4 clusters. *Phys. Rev. Lett.*, 64(16):1899, 1990.

[135] J. Schindelin, I. Arganda-Carreras, E. Frise, V. Kaynig, M. Longair, T. Pietzsch, S. Preibisch, C. Rueden, S. Saalfeld, B. Schmid, J.-Y. Tinevez, D. J. White, V. Hartenstein, K. Eliceiri, P. Tomancak, and A. Cardona. Fiji: An open-source platform for biological-image analysis. *Nat. Methods*, 9(7):676–682, 2012.

[136] C. P. Schulz, P. Claas, D. Schumacher, and F. Stienkemeier. Formation and stability of high-spin alkali clusters. *Phys. Rev. Lett.*, 92:013401, 2004.

[137] M. Scott, C.-C. Chen, M. Mecklenburg, C. Zhu, R. Xu, P. Ercius, U. Dahmen, B. Regan, and J. Miao. Electron tomography at 2.4-Angstrom resolution. *Nature*, 483(7390):444–447, 2012.

[138] Y. A. Sergeev and C. F. Barenghi. Particles-vortex interactions and flow visualization in ^{4}He. *J. Low Temp. Phys.*, 157(5-6):429–475, 2009.

[139] X. Shao, X. Liu, and W. Cai. Structural optimization of silver clusters up to 80 atoms with Gupta and Sutton-Chen potentials. *J. Chem. Theory Comput.*, 1(4):762–768, 2005.

[140] D. Spence, E. Latimer, C. Feng, A. Boatwright, A. M. Ellis, and S. Yang. Vortex-induced aggregation in superfluid helium droplets. *Phys. Chem. Chem. Phys.*, 16(15):6903–6906, 2014.

[141] P. J. Steinhardt, D. R. Nelson, and M. Ronchetti. Bond-orientational order in liquids and glasses. *Phys. Rev. B*, 28(2):784–805, 1983.

[142] J. Steurer. Helium droplet mediated fabrication and analysis of noble metal nanoparticles. Master's thesis, TU Graz, 2014.

[143] A. P. Sutton and J. Chen. Long-range Finnis - Sinclair potentials. *Phil. Mag. Lett.*, 61(3):139–146, 1990.

[144] J. Tang, Y. Xu, A. R. W. McKellar, and W. Jäger. Quantum solvation of carbonyl sulfide with helium atoms. *Science*, 297(5589):2030–2033, 2002.

[145] P. Thaler, A. Volk, F. Lackner, J. Steurer, D. Knez, W. Grogger, F. Hofer, and W. E. Ernst. Formation of bimetallic core-shell nanowires along vortices in superfluid He nanodroplets. *Phys. Rev. B*, 90(15):155442, 2014.

[146] P. Thaler, A. Volk, M. Ratschek, M. Koch, and W. E. Ernst. Molecular dynamics simulation of the deposition process of cold Ag-clusters under different landing conditions. *J. Chem. Phys.*, 140(4):–, 2014.

[147] M. Theisen, F. Lackner, and W. E. Ernst. Forming Rb+ snowballs in the center of He nanodroplets. *Phys. Chem. Chem. Phys.*, 12(45):14861–14863, 2010.

[148] M. Theisen, F. Lackner, and W. E. Ernst. Cs atoms on helium nanodroplets and the immersion of Cs+ into the nanodroplet. *J. Chem. Phys.*, 135(7):074306, 2011.

[149] M. Theisen, F. Lackner, and W. E. Ernst. Rb and Cs oligomers in different spin configurations on helium nanodroplets. *J. Phys. Chem. A*, 115(25):7005–7009, June 2011.

[150] J. Tiggesbäumker and F. Stienkemeier. Formation and properties of metal clusters isolated in helium droplets. *Phys. Chem. Chem. Phys.*, 9(34):4748–4770, 2007.

[151] J. P. Toennies and A. F. Vilesov. Superfluid helium droplets: a uniquely cold nanomatrix for molecules and molecular complexes. *Angew. Chem. Int. Ed.*, 43(20):2622–2648, 2004.

[152] S. Van Aert, K. J. Batenburg, M. D. Rossell, R. Erni, and G. Van Tendeloo. Three-dimensional atomic imaging of crystalline nanoparticles. *Nature*, 470(7334):374–377, 2011.

[153] A. Volk. *Nanocluster and Nanowire Growth in Superfluid Helium Nanodroplets.* PhD thesis, TU-Graz, 2016.

[154] A. Volk, D. Knez, P. Thaler, A. W. Hauser, W. Grogger, F. Hofer, and W. E. Ernst. Thermal instabilities and Rayleigh breakup of ultrathin silver nanowires grown in helium nanodroplets. *Phys. Chem. Chem. Phys.*, 17:24570–24575, 2015.

[155] A. Volk, P. Thaler, M. Koch, E. Fisslthaler, W. Grogger, and W. E. Ernst. High resolution electron microscopy of Ag-clusters in crystalline and non-crystalline morphologies grown inside superfluid helium nanodroplets. *J. Chem. Phys.*, 138:214312–1–214312–7, 2013.

[156] R. Werner, M. Wanner, G. Schneider, and D. Gerthsen. Island formation and dynamics of gold clusters on amorphous carbon films. *Phys. Rev. B*, 72(4):045426, 2005.

[157] G. White. The thermal and electrical conductivity of copper at low temperatures. *Austr. J. Phys.*, 6(4):397–404, 1953.

[158] S. Yang, A. M. Ellis, D. Spence, C. Feng, A. Boatwright, E. Latimer, and C. Binns. Growing metal nanoparticles in superfluid helium. *Nanoscale*, 5:11545–11553, 2013.

Addendum: Manual

This manual was written by Alexander Volk and Philipp Thaler who designed and set up the lab infrastructure and the helium droplet beam machine in PHEG 056 (Cluster Lab III). It is addressed to future custodians of the machine. In order to serve as a general reference book, repeated explanations of the same issues in different situations are deliberately accepted.

Chapters 3, 4 and 5.3.3 were written by Alexander Volk, chapters 1, 2 and 5 - 7 were written by Philipp Thaler. Both authors were responsible for editing and obtaining the presented data and settings.

Besides instructions on how to operate and service the present machine, this manual includes explanations of the dimensioning and design of the apparatus. Furthermore, it includes typical settings for the adjustable parameters and provides experimental data as benchmark for future experiments.

The structure of the content is primarily defined by the tangible parts of the apparatus, rather than by didactics. It is not the aim of this manual to cover the theory in this field of expertise.

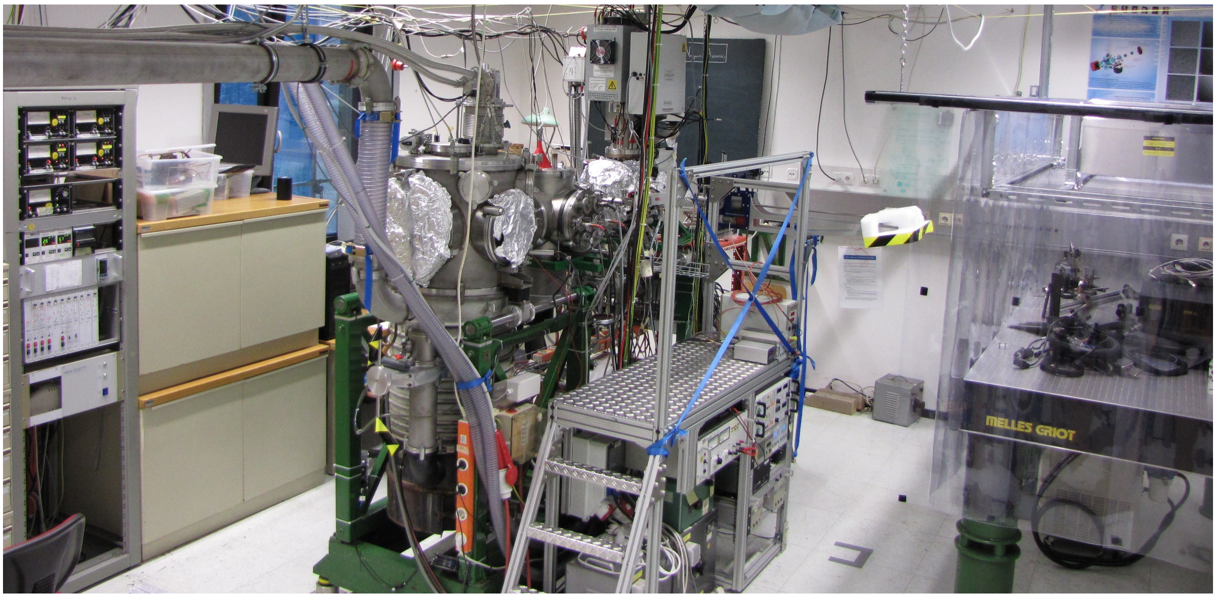

Figure 1: Foto: Cluster Lab III. Left: Control panel; Center: Helium droplet beam machine (HelENA); Right: Installation for the future laser setup.

Contents

1 History and Evolution

Helium droplet beam machines have been used at the Institute of Experimental Physics for some years. With these machines, ultra cold atoms and molecules were investigated spectroscopically on or in helium droplets. In 2011 an article reporting the formation of large silver clusters Ag_n (with n up to 6000) inside helium droplets caught the attention of the institute.[1] The decision was made to build a new machine, especially designed for the purpose of nanoparticle synthesis inside liquid helium droplets, using the knowledge emanating from the build-up and operation of the existing machines. The new apparatus was necessary, because the other machines on the institute are limited in terms of droplet size, and large helium droplets are essential for growing nanoparticles. An old helium atom beam machine, donated by Prof. Christof Wöll (Universität Bochum), was cannibalized in order to build up the new machine and was fitted with a new high-end cold head to reach the lower nozzle temperatures required for the formation of large helium droplets.

The motivation to build up this new machine was the promising prospect that the versatile doping possibilities of helium droplets combined with the cold temperatures provided by them would enable the controlled synthesis of nanoparticles with exotic material combinations exhibiting novel properties. Furthermore, for subsequent doping schemes with two different materials, the formation of core-shell structures was expected, with the low temperature preventing restructuring. Additionally, in 2012 first evidence for vortices inside liquid helium droplets was found.[2] While this phenomenon has been known in the bulk, vortices inside droplets eluded verification until that experiment, which exploits the fact that dopants prefer to reside along the vortex lines. The shape dictated by the vortices is stable upon deposition, which paves the way for a deliberate creation of one-dimensional structures with this technique.

The preparation of the infrastructure for the new laboratory started in September 2011, and the main setup was completed in September 2013 with the delivery of a time of flight mass spectrometer (TOFMS), which constitutes the main *in-situ* measuring instrument of the apparatus. In the first setup, not all of the desired specifications were met, but after some modifications a nozzle temperature of $< 3.5\,\mathrm{K}$ and a background pressure of $< 5 \cdot 10^{-10}\,\mathrm{mbar}$ in the measurement chamber were reached in April 2014. Besides the *in-situ* mass spectrometric investigations, using other (external) diagnostics, especially transmission electron microscopy (TEM), has always been part of the concept of this lab. Especially when experimenting with reactive elements, a transport of the samples to the external diagnostic facilities without breaking the vacuum is highly desired. A vacuum transfer system for sample exchange with the University of Graz was purchased and implemented in May 2015 and a system for the transport of samples to the Institute for Elecron Microscopy and Nanoanalytic was designed in fall 2015.

---

[1] Loginov, E., Gomez, L. F., Chiang, N., Halder, A., Guggemos, N., Kresin, V. V., & Vilesov, A. F. Photoabsorption of Ag_N (N $\approx$ 6-6000) Nanoclusters Formed in Helium Droplets: Transition from Compact to Multicenter Aggregation. *Physical Review Letters*, 106(23), 233401 (2011).

[2] Gomez, Luis F., Evgeny Loginov, and Andrey F. Vilesov. Traces of vortices in superfluid helium droplets.*Physical Review Letters*, 108(15), 155302 (2012).

2 Introduction & Overview

The new apparatus described here is designed to produce a beam of large helium droplets, which subsequently serve as individual reactors for nanoparticle synthesis. Once the dopant-atoms or -molecules are added to a droplet they are cooled down to droplet temperature. The superfluid matrix enables the dopants to move inside the droplet which leads to their aggregation. The binding energy released upon aggregation is dissipated by the host, which guarantees efficient nanoparticle formation. After the doping process, the droplets carry the nanoparticles into the measurement chamber, where the nanoparticles can be analyzed *in-situ* or be deposited on various substrates for *ex-situ* analysis.

The main structure of the new apparatus comprises a system of vacuum chambers with decreasing base pressure along the beam axis. In our case, there are four chambers, which can be separated into three independent regions using two gate valves (see schematics in Fig. 2.1). Helium droplets are formed if the nozzle is cooled down to temperatures lower than 20 K. Here, this low temperature can be reached using a closed cycle refrigerator whilst paying attention to a very good thermal insulation. For the doping of the helium droplets, the dopants have to be forced into the gas phase, which is realized by resistively heated ovens. In the current design, these ovens are equipped with water-cooled radiation shields and can reach a maximum temperature of 2000 K. For the analysis of the nanoparticles / the doped helium droplet beam, there are several measuring instruments installed at the measurement chamber, including a time of flight mass spectrometer (TOFMS), a quadrupole mass specrometer (QMS), a quartz crystal micro-balance (QCM) as well as a sample holder for substrates for *ex-situ* analysis.

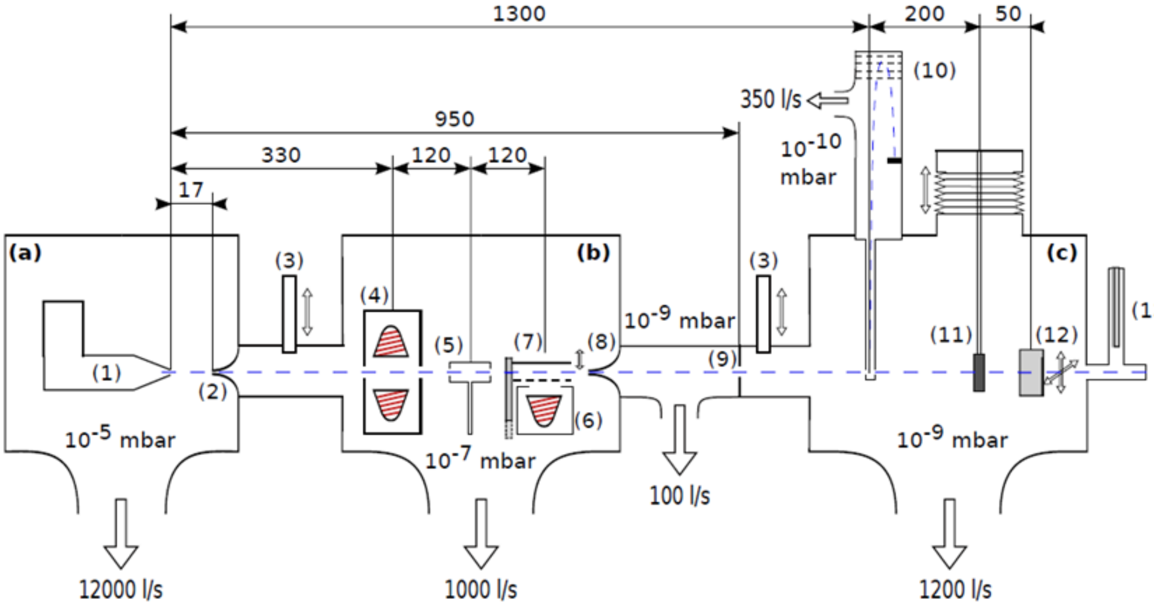

Figure 2.1: Schematic of the entire apparatus, taken from [1]

In the next chapters, the apparatus will be explained in more detail, starting with the infrastructure of the laboratory followed by a separate description of the individual vacuum chambers. Thereby, the sequence of the description matches the sequence in which the individual elements are passed by the helium droplet beam.

---

[1] Diploma thesis: Johannes Steurer

3 Laboratory Infrastructure

3.1 Layout

The whole laboratory facility consists of two rooms as depicted in Fig. 3.1. While the main laboratory comprises the helium droplet apparatus, an optical table, a working area and several storage possibilities, the fore-vacuum pumps and the coldhead compressor are located in a separate room (hereafter referred to as the pump room) for noise reduction.

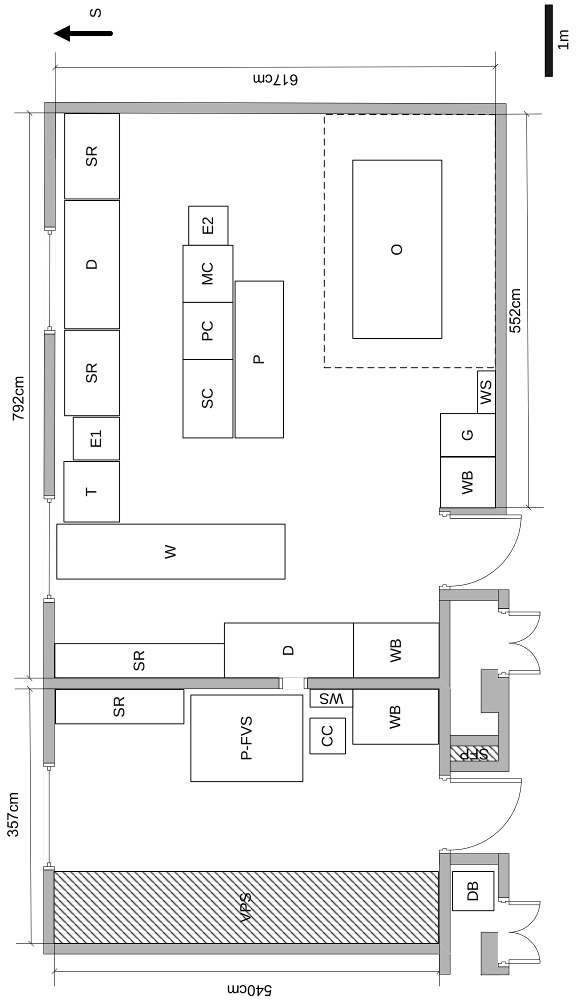

Figure 3.1: General layout of the laboratory and the pump room. CC… compressor for coldhead; D… desk; DB… distribution board; E1-2… rack for electronics; G… gas locker; MC… main chamber; O… optical table (dashed line shows borders of flow-box); P… platform; PC… pickup chamber; P-FVS… pumps of fore-vacuum system; SC… source chamber; SFP… structural fire protection; SR… storage room; T… tools; VPS… vacuum pump storage; W… working bench; WB… basin; WS… water supply (closed cooling cycle)

3.2 Electric Installations

The electrical power supply of the laboratory has been realized over an external distribution box. Every socket in the lab is labeled with an identifier distinct for the connected current circuit . Table 3.1 lists the labels of all these sockets and the corresponding fuse labels in the distribution box. The over-current protective devices are customized for the intended application of the respective current circuits (see Tab. 3.1). Some circuits are equipped with solid state relays, so that the current is switched on only if the interlock control wire with the corresponding number is connected with interlock control wire 1. This enables an efficient integration of the vacuum control system *via* relay connections. For example, the turbo vacuum pumps can only be switched on if the prevacuum pressure is below a certain threshold (see chapter 4). Fig. 3.2 shows the location of the respective sockets in the lab.

Table 3.1: Electric circuits of the laboratory. The electric circuits can be identified by their socket labels. The location of the respective sockets are depicted in Fig. 3.2. The fuses in the distribution board are labeled according to the second column. Where an interlock is available, the number of the corresponding relay control wire is given.

socket label	fuse label	$1^{\sim}$ / $3^{\sim}$	$I_{\max}$ / A	interlock control wire	assignment
CC	9Q2	$3^{\sim}$	35	10	coldhead compressor
F	9Q1	$3^{\sim}$	50	9	high current power supply
G	5F6	$3^{\sim}$	16	n.a.	for general use
H	8F7	$3^{\sim}$	16	n.a.	for general use
Laser	Laser	$3^{\sim}$	200	2	for laser with high energy consumption
M	6Q3	$1^{\sim}$	13	n.a.	computer
O/P/Q	6Q2/5Q5/5Q6	$1^{\sim}$	13/16/16	n.a.	for general electronics
P1/P2/P3	8F2/8F3/8F4	$3^{\sim}$	16/16/16	8	source chamber prevacuum pumps
P4	7Q2	$3^{\sim}$	25	7	pickup chamber prevacuum pump
P5	7Q1	$3^{\sim}$	35	6	source chamber diffusion pump
P6	6Q6	$1^{\sim}$	13	5	pickup chamber turbo pumps
P7	6Q5	$1^{\sim}$	13	4	main chamber turbo pumps
P8	6Q4	$1^{\sim}$	13	3	TOF electronics
R1/R2	5Q1/5Q2	$1^{\sim}$	16/16	n.a.	for general use
S1/S2	5Q3/5Q4	$1^{\sim}$	16/16	n.a.	for general use
T	6Q1	$1^{\sim}$	16	n.a.	main chamber prevacuum pumps

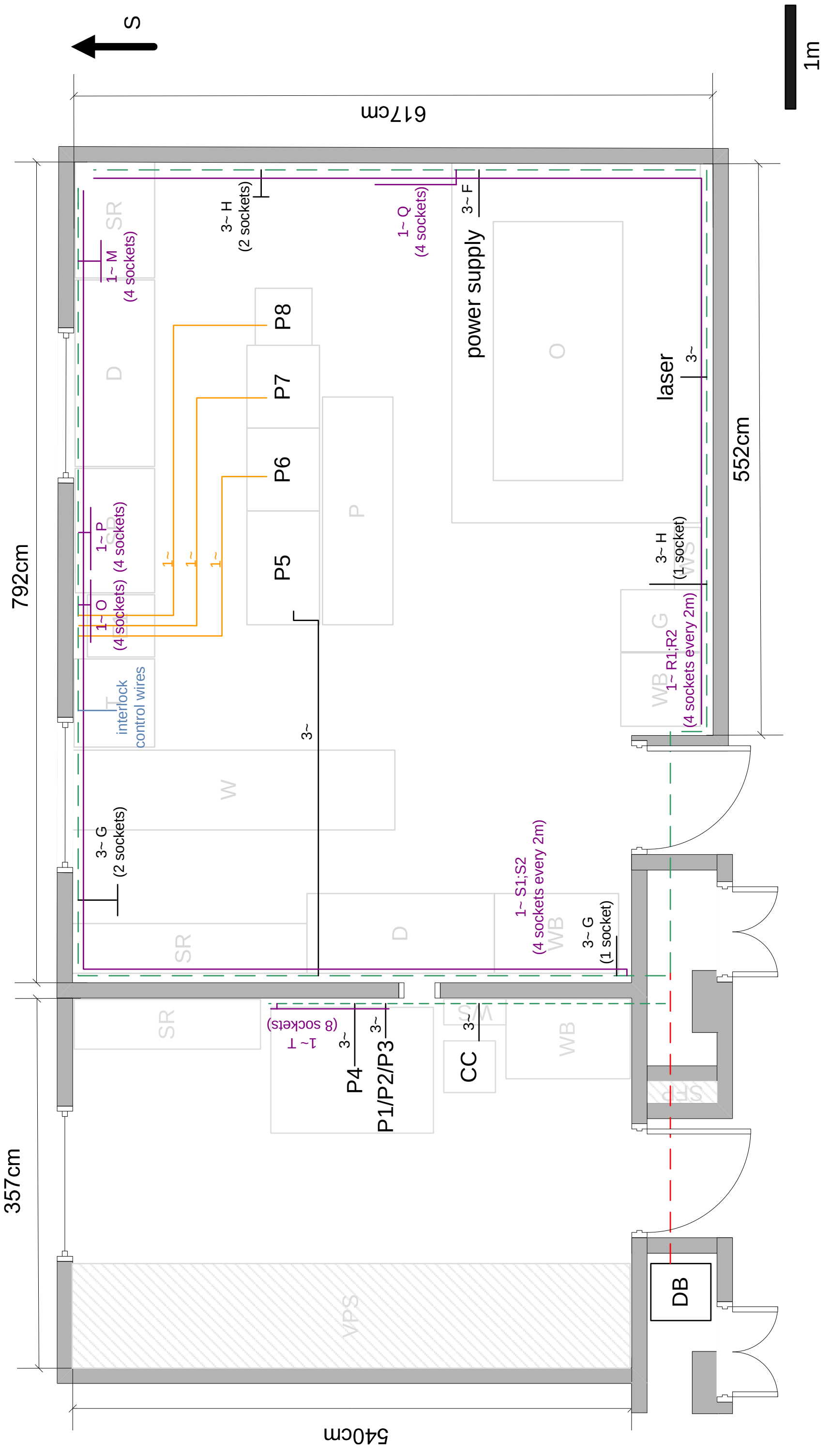

Figure 3.2: Electrical Layout of the laboratory. See Tab. 3.1 for a detailed description of the different electric circuits.

3.3 Gas Installations / Storage

The laboratory contains a fire-retarding gas locker suited for two 200 l gas bottles. In the present setup this locker contains a bottle of grade 6 helium for droplet generation, and a bottle of grade 5 N_2 for venting the vacuum chambers with dry air. The respective valves and connections for each gas line are depicted in Fig. 3.3 & 3.4. In order to prevent impurities from entering the gas system during a bottle exchange, it is possible to purge affected parts. To do so, the gate valve of the respective gas line has to be closed before the gas bottle is exchanged and the purge valve is used to flush the vented volume before re-opening the gate valve.

Gas controls for daily operations are located outside the gas locker for the purpose of easier monitoring. The pressure of the He gas can be regulated by a pressure regulator. All tubes of the He gas system are made of stainless steel and the setup has been tested to bear a pressure of 100 bar applied to the nozzle. There should always be a He flow through the 5 μm nozzle orifice to prevent clogging, which means that the applied pressure should not fall below 10 bars, even if the nozzle is not in operation.

For the N_2 system fluorpolymer gas lines are used. When venting the vacuum chambers with N_2 one should act with caution in order to prevent the chambers from getting over pressurized. While the source chamber and the pickup chamber are equipped with pressure relief valves (releasing at $\approx$ 0.4 bar overpressure), a burst disc (releasing at $\approx 0.6 - 0.8$ bar overpressure) is attached to the main chamber. Further, an additional pressure relief valve is attached to the gas line right after the N_2 pressure regulator.

Although not in use, there are additional pressure regulators for H_2 available in the gas locker as well as outside. Bottles for other gases interesting for doping the He droplets may be directly placed and secured at the frame of the apparatus.

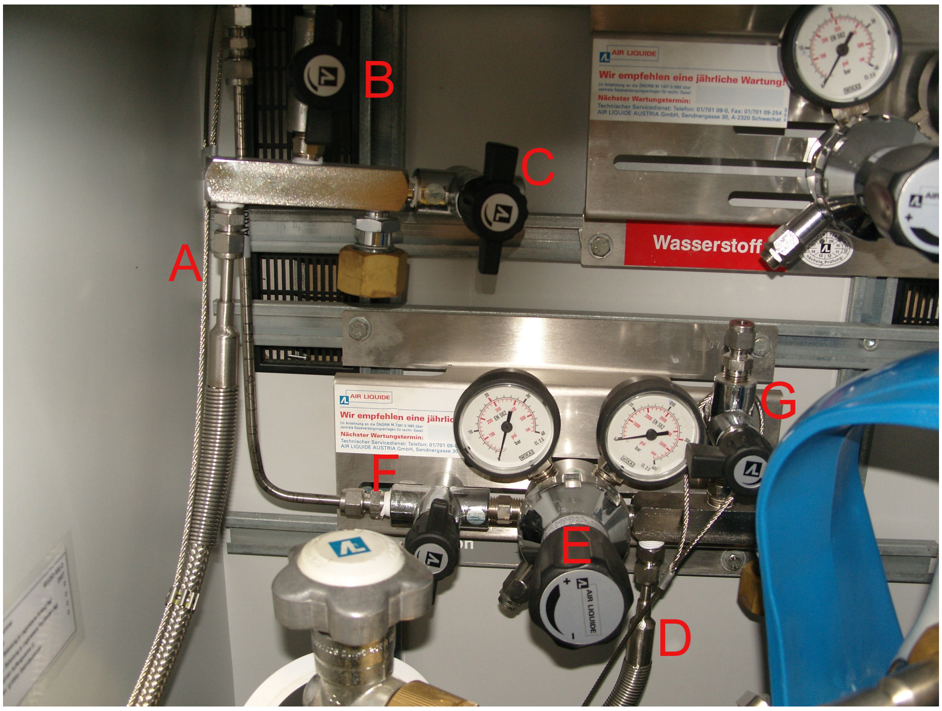

Figure 3.3: Connections and valves inside the gas locker. **A** He–gas connection; **B** He gate valve; **C** He purge valve; **D** N_2–gas connection; **E** N_2 pressure regulator; **F** N_2 gate valve; **G** N_2 purge valve.

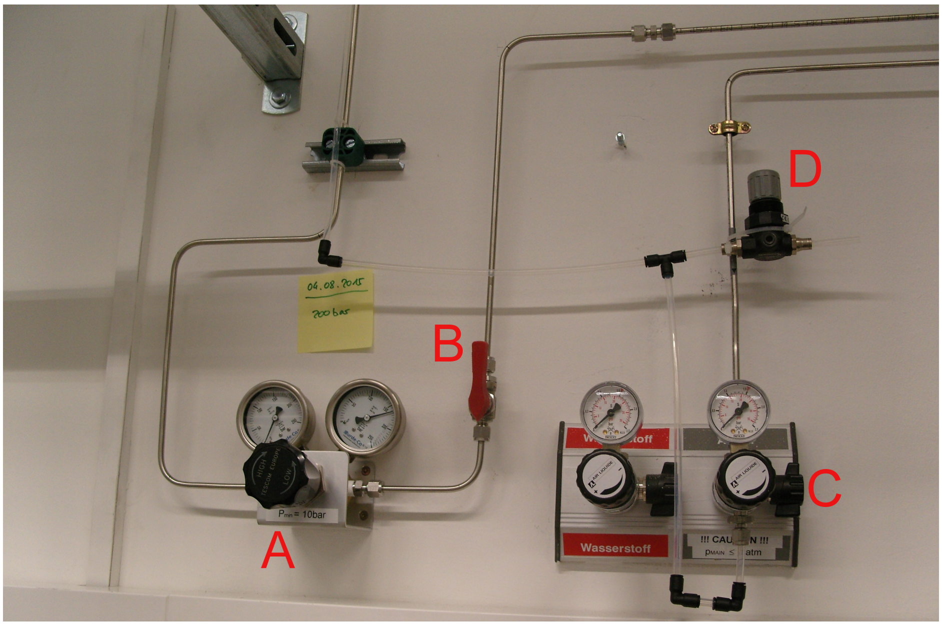

Figure 3.4: Gas controls for daily operation. **A** He pressure regulator; **B** He gate valve; **C** N_2 pressure regulator with included gate valve; **D** pressure relief valve for N_2 system.

3.4 Air Conditioning

The air conditioning system comprises two convector fans in the main laboratory and one convector fan in the pump room. Each of these air conditioners (Daikin, FWL10DATN6V3) has a maximum cooling capacity of 8 kW. The cooling agent is cooled *via* the heat exchanger of the building's central air conditioning system. While the system proved to be effective in cooling the laboratory, the temperature stability is non-satisfying as exemplary depicted in Fig. 3.5 for a preset temperature of 19°C. It can bee seen that the room temperature (black line) in Fig. 3.5 oscillates around the preset value by more than ±1°C in a time interval of $\approx$ 10 min. This behavior is the result of a simultaneous switching of the fan (see red line in Fig. 3.5) and of the cooling-solvent flow regulating valve (see blue line in Fig. 3.5).

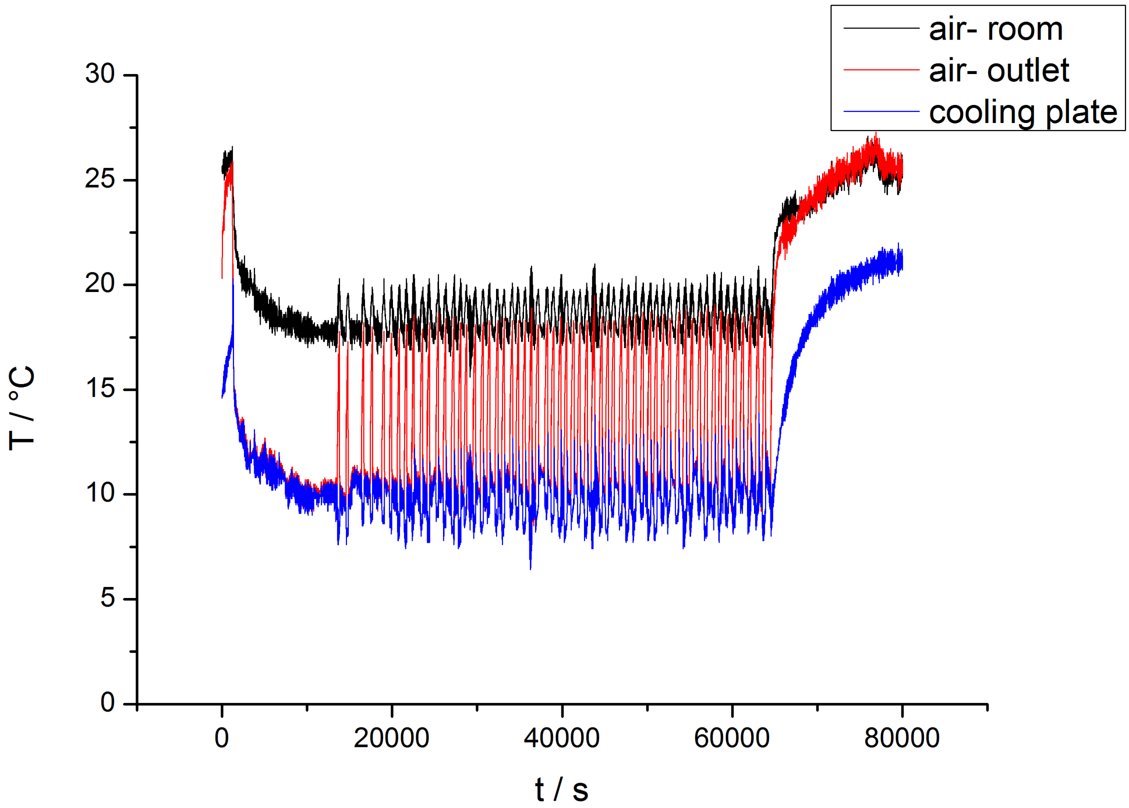

Figure 3.5: Temperature oscillation due to air conditioning. The temperature was measured at a representative position in the room (black), at the outlet of the air conditioning unit (red) and on the cooling plate of the convector fan unit. The temperature was preset to 19°C

It has to be noted that some measurement devices in the laboratory are sensitive to temperature oscillations. This is especially the case for the quartz oscillator, so that extensive housing and thermal insulation of the respective device have been necessary. Another possibility to reduce the influence of the air conditioning on measurement results lies in the adaption of its regulation process. In preliminary tests the desired temperature has been preset to a very low value (*e.g.* 10°C) and the rotational speed of the fan has been regulated by implementing a variable resistor. This setup allows to eliminate the influence of the cooling-solvent flow regulating valve, as the respective valve is opened all times and the preset temperature is never reached. On the other hand, the fan speed is maintained on a constant level. The tests showed good results as fast temperature oscillations were reduced, however long-term shifts in the temperature occurred due to changes in heat loads during full day operation. It would therefore be recommendable to imply a phase controlled modulator for the regulation of fan speed.

3.5 Aspiration System

In order to prevent the emission of oil mist into the lab room, the pump exhausts of all rotary vane vacuum pumps are connected to the central aspiration system. A suitable pipe is installed between the pump room and the laboratory, where it is connected to the aspiration system of the gas locker. It has to be noted that in case of a fire alarm the central aspiration system is shut down automatically. However, the volume of the pipes connecting the gas locker with the aspiration unit on the roof of the building is large, while the amount of air emitted by the pumps is small, so that proper functioning of the pumping system is still given.

4 Vacuum and Water control system

For safety reasons as well as for easier monitoring and better handling, all vacuum pumps and coolant supplies are operated through a home-made central control system. This enables the linkage of the pressure monitoring system and the monitoring system for coolant flows in order to assure proper operating conditions for the vacuum pumps. Further, all pumps and solenoid valves can be switched on and off through a single control panel. Other devices which need a certain grade of vacuum during operation (*e.g.* the TOFMS) are directly linked to this system. The control panel is directly connected to the relay control wires of the respective current circuit (see Tab. 3.1), *i.e.* the power supply of the connected devices is directly switched through the control panel. More detailed descriptions of single parts of the control system can be found in the following sections.

4.1 Control panel

The control panel (Fig. 4.1) is the heart of the system. The state of every parameter monitored for proper operation of a certain device is indicated by LEDs. Devices can be switched between 3 different modes: "OFF", "Auto", or "Manual". The manual-mode is intended for the start up procedure and is restricted by a timer, so that after 10 min in manual-mode the device is automatically switched off. If all monitored parameters meet the preset requirements (indicated by green LEDs) it is possible to switch the respective device to the auto-mode for continuous operation.

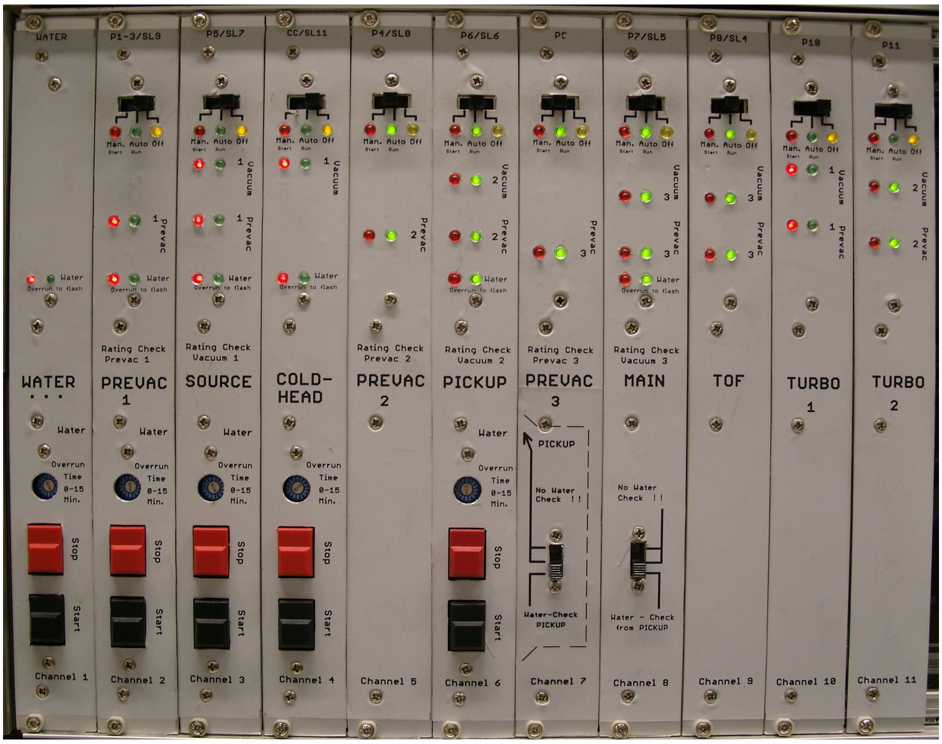

Figure 4.1: Vacuum and water control panel. Single segments control (from left to right): cooling of the pickup cells, prevacuum system of source chamber, source chamber oil diffusion pump, coldhead compressor, prevacuum system of pickup chamber, turbo pumps of pickup chamber, prevacuum system of main chamber, turbo pumps of main chamber, power supply of TOFMS. The two last panels are currently out of use.

Below, a description of the function of the control panel is given on the example of the pickup chamber turbo pump (marked as "PICKUP" in Fig. 4.1). In the case of this turbo pump, 3 parameters are monitored, namely base pressure in the pickup chamber ("vacuum 2"), the fore-pressure of the turbo pump ("prevac 2") and the coolant flow ("water"). While the coolant flow and the fore-pressure are monitored to check if the requirements for the operation of the turbo pump are met, the vacuum in the pickup chamber is monitored additionally in order to detect potential problems (*e.g.* an ingress of air) at an early stage. In case any of these parameters exceeds the specified threshold, an emergency shutdown is triggered.

Before starting the turbo pump, the respective fore-pump ("PREVAC 2"-panel) and the coolant flow (back start-button) have to be switched on. As soon as the specified fore-pressure is reached, the green "prevac 2"-LED turns on. When switching on the coolant flow, it might be necessary to hold the start-button for a few seconds until sufficient flow is detected and the corresponding green LED turns on. Then, with the "vacuum 2"-LED still red, the turbo pump is started by setting the switch on top of the panel to "Man.". With the turbo pump running, the pressure in the pickup chamber will decrease rapidly and after a few minutes, the pressure threshold in the pickup chamber will be reached ("vacuum 2"-LED turns green). With all 3 parameters within the specified limits, the start-up procedure can be finished by setting the switch on top of the panel to "Auto".

As some devices need to be cooled for some time after switching them off, all water circuits are equipped with a programmable overrun, whose time can be set through the blue potentiometer from zero to a maximum of 15 min.

For the turbo pumps of the pickup chamber and the main chamber it is possible to switch off the monitoring of the coolant flow because these pumps are sufficiently air cooled in normal operation (not during bake-out of the chamber!). However, the lifetime of the bearings increases with better cooling so that in the coolant flow should be switched on.

4.2 Pressure monitoring

Several different vacuum gauges are used to monitor the pressures in the vacuum system. All vacuum gauges are connected to individual monitors which are mounted in the same electronic rack as the control panel (see Fig. 4.2). These monitors usually feature a relay-output, and allow to define a pressure threshold. When the measured pressure falls below this threshold the output is switched from an open to a closed state or vice versa. These outputs are directly connected to the control panel.

Fore-vacuum pressures are measured with Pirani vacuum gauges (Leybold-Heraeus TR201) and corresponding monitors (L-H Thermovac TM 220 S 2). The pressure threshold can be adjusted *via* the potentiometer ("Threshold"), while pressing the "Test" button (Fig. 4.2). For the source and the pickup chamber full range gauges (Pfeiffer PKR251; combination of pirani element and cold cathode) are used in combination with single gauge monitors (Pfeiffer TPG261). The main chamber is equipped with an ionization vacuum meter (L-H Ionivac IM220 / monitor: L-H IE220). Please consult the manual for questions on threshold settings in case of monitors with digital display.

The roots pumps are switched on only after a certain fore-vacuum pressure has been reached. The corresponding switch is directly connected to the pressure monitor labeled (PREVAC ROOTS) and can not be separately controlled *via* the control panel. Further, although not connected to the vacuum control system, there are also pressure gauges attached to the TOFMS (L-H IM210 / monitor: L-H IE211) and the differential pumping station (Pfeiffer PKR251 / monitor: TPG261).

4.3 Cooling circuit

For for the operation of some devices water cooling is necessary. The lab is connected to the central closed cooling circuit of the building. Several separated circuits are used in the lab and in the pump room. Every circuit is equipped with a solenoid valve (Buerkert 138034) and a calorimetric flow monitor (IFM ST 1600) as depicted in Fig. 4.3. The solenoid valves can be switched *via* the control panel. The flow monitors are installed in the backflow-part of the system and connected to the control panel. For correct operation it is necessary to adjust the coolant flow as needed for the respective device by using the rotary ball valve, which is installed in front of the solenoid valve. The threshold of the flow monitor can then be adapted *via* a potentiometer. In the current setup over-cooling of a device is impossible and as no water is lost in the

Figure 4.2: Vacuum pressure monitors. Although the TM 220 S 2 model can control 2 pirani gauges, there is one separate monitor for every single prevacuum- line. Every monitor is labeled with respect to the position of its associated measurement gauge.

closed cooling circuit the flow is set to higher values than needed. In case of a leak in the cooling circuit, the flow is stopped by closing the respective solenoid valve and the affected part of the vacuum system is shut down.

Figure 4.3: Connections of the cooling circuit. The black solenoid valves can be controlled *via* the control panel. The orange flow monitors in the return are adjustable *via* a potentiometer.

In case of a power blackout the functioning of the cooling is ensured by an uninterruptible power supply (UPS) for $\approx 10 - 20\,\mathrm{min}$. This is especially important for the oil diffusion pump.

4.3.1 Maintenance

The function of the flow monitors has to be tested once a month by closing the lever valves mounted in front of the solenoid valves during operation. The solenoid valves should be tested by switching the flow on **and off** *via* the control panel. All connections should be checked on leak-tightness.

5 Helium Droplet Source (Source Chamber)

5.1 Abstract: Helium Droplet Beam Formation

Helium droplets can be created by expanding helium gas through a nozzle, cooled to cryogenic temperatures ($< 20\,\mathrm{K}$) by a closed cycle refrigerator (Sumitomo RDK-408D2). There are three basic formation mechanisms: Condensation of droplets out of the gas phase, fragmentation of the liquid phase and break-up of the liquid jet (illustration see Fig. 5.1). Once droplets are formed, they cool themselves down to about 0.4 K by evaporative cooling. All three formation mechanisms can be realized with this machine, depending on the experimental conditions (*i.e.* nozzle-temperature and -pressure); the transition between the regimes is smooth. This apparatus uses an electron microscope aperture with $d_0 = 5\,\mu\mathrm{m}$ diameter as nozzle (Günther Frey GmbH) and operates at nozzle temperatures between $T_0 = 4$ and $25\,\mathrm{K}$, and at pressures between $p_0 = 10$ and $100\,\mathrm{bar}$. Tuning these parameters allows to control the droplet size distribution (dependency is shown below, in Fig. 5.1) and, to some extent, the amount of He flux. The actual beam is formed by a skimmer (0.4 mm diameter), placed a few millimeters from the nozzle, which cuts out the center part of the emission profile of the nozzle. Details about the fluid mechanics involved in the beam-formation process as well as examples for dimensioning the nozzle-skimmer setup can be found in the literature.[1] [2] However, the calculations in these references do not target the situation where phase transitions become important, as in our case. Nevertheless, many of the concepts presented in these references still hold true and were used for the layout of this machine.

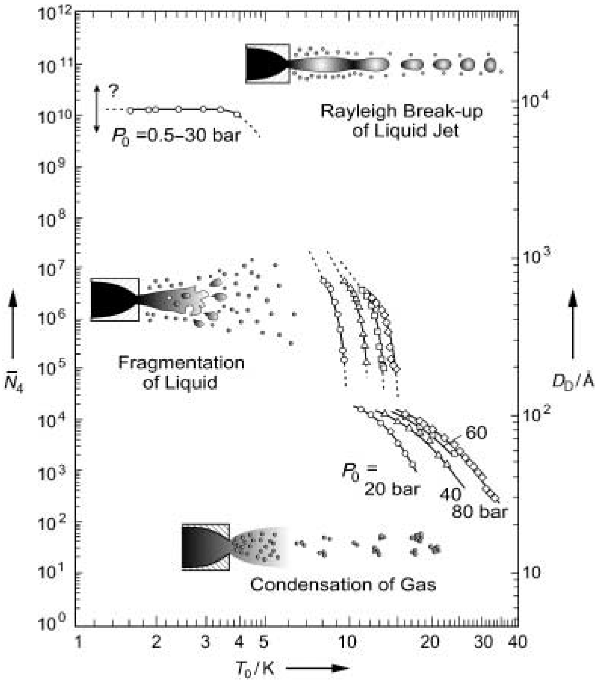

Figure 5.1: Dependency of the mean droplet size on the stagnation conditions. This graph is reprinted with permission from [3], Copyright (c) 2004 Wiley-VCH Verlag GmbH & CO. KGaA.

---

[1] Pauly, H.: Atom, Molecule and Cluster Beams I: Basic Theory, Production and Detection of Thermal Energy Beams. Springer Series on Atomic, Optical and Plasma Physics. Springer, Berlin, 2000.

[2] Scoles, G.: Atomic and molecular beam methods. Vol. 1. New York: Oxford university press, 1988.

[3] J. Peter Toennies and Andrey F. Vilesov, *Angew. Chem. Int. Ed.*, 43, 2622-2648 (2004)

5.2 Vacuum System

5.2.1 Setup

The vacuum system of the source chamber is a 4-stage system: a large oil diffusion pump (Leybold DI12000, 12.000 l/s) is backed by 2 Roots-boosters (Edwards EH1200 and EH250, in series), which are backed by a rotary vane pump (Edwards E2M80). The exhaust port of the rotary vane pump is connected to the buildings aspiration system.

5.2.2 Dimensioning

The reason for this huge pumping system is the high He flux through the nozzle. At room temperature and ambient pressure the flow rate was measured by capturing the gas bubbled into a liquid.[3] At some point, the original nozzle plate clogged and was replaced by a new plate with same nominal diameter.[4] The bubble measurement was repeated and the results corresponded reasonably well to the previous series.[5] Theoretical calculations [6] yield a flow rate which is about twice as high as measured. Even with the theoretically predicted higher flow rate our large pumping system (12.000 l/s) should be able to reach a pressure in the range of 10^{-5} mbar in the source chamber with the nozzle at room temperature and 20 bar stagnation pressure. This corresponds very well to the pressure measured in the experiments. As the nozzle is cooled down, theory predicts an increased He flow rate, but it seems as if the used equations are no longer valid at the cryogenic temperatures (< 20 K) that are present in our experiments. The observed chamber pressure with the nozzle at 10 K and 20 bar still lies in the 10^{-5} mbar range and only increases to a few times 10^{-4} mbar at the lowest nozzle temperature, in contrary to the theory, which predicts much higher values. This means that the provided base pressure is sufficiently low to ensure good beam characteristics and vanishing thermal conductivity of the residual gas in the chamber for all experimental settings.

5.2.3 Operating Instructions

While the other vacuum pumps used in this laboratory are usually working 24/7, the pumps of the source chamber are only switched on for the experiments. The diffusion pump needs some lead time until it starts working properly (heat up time $\approx$ 20 min), which is shorter than the cool-down time of the nozzle. The control system ensures that the diffusion pump can only be operated if the necessary fore-vacuum conditions are present and the pump is switched off in case of a malfunction. For special purposes (start-up, tests) the system can be overruled when switching to "manual", but the system will shut down automatically after 10 min in manual mode. The diffusion pump produces a large amount of heat; despite the water cooling, the air-conditioning of the laboratory should always running when operating the pump. Since 2014, the water-cooling is realized *via* a closed cycle system, therefore there is no need for saving cooling-water and the water cooling should be used generously (long overrun time). Further the cooling water is treated so that no problems with calcification or formation of algae should occur. Nevertheless, the magnetic valves should be switched at least once a month to check their function (necessary in case of a pipe burst).

Start-up Procedure

Before turning on the fore-vacuum pumps, check if the valve between the rotary vane pump and the Roots-boosters, as well as the gate valve in the vacuum line just before the diffusion pump are opened. It may be necessary to vent both sides of the gate valve (chamber and vacuum line) before opening it, as the valve should not be opened if there is a pressure difference between the two sides.

Check that the venting valves (chamber and pre-vacuum line) as well as the connecting gate valve between source-chamber and pickup-chamber are closed. Turn on the water-cooling of the Roots-pumps. Check that the nozzle pressure is set to 10 bar.

Set the "PREVAC 1" switch on the control panel to "manual" (auto is just for regular operation, not for the start-up) to start the rotary vane pump. In order to treat the Pirani-gauges gently, it is best practice to turn them on 2 min after starting the rotary vane pump. The employed control system turns

---

[3] measurements from 10 to 50 bar in 10 bar steps, 2 measurements at every step (flow rate of 0.35 ml/s at 20 bar)

[4] electron microscope images revealed diameters from 5 μm to 6.3 μm for nozzle plates with 5 μm nominal diameter

[5] measurements for 20 and 50 bar, only, flow rate of 0.29 ml/s at 20 bar

[6] Scoles, G.: Atomic and molecular beam methods. Vol. 1. New York: Oxford university press, 1988. p. 20, eq. 2.10

on the Roots-boosters as soon as the lower pressure threshold of the first Pirani-gauge is reached. As the Roots-boosters start, it might happen that this pressure rises above the upper pressure threshold and the Roots-boosters are switched off again (possible on-off-oscillations). Very shortly after the Roots boosters are running constantly, the required fore-vacuum pressure (second Pirani-gauge) will be reached (all control lights on the "PREVAC 1" panel should be green) and the "PREVAC 1" switch can be set to "auto". If there are many on-off-oscillations as the control unit starts the Roots boosters, the pressure threshold should be adjusted.

Turn on the water-cooling of the oil diffusion pump and switch on the full range vacuum gauge "Source" which monitors the pressure in the chamber (now all control lights on the "SOURCE" panel should be green). Setting the "SOURCE" switch to "auto" turns on the diffusion pump (red light at the diffusion pump fuse box is on). Turn on the fan on the right hand side of the frame of the apparatus, next to the viewing glass of the diffusion pump. This helps to reduce the heat-up of the chamber walls. The diffusion pump takes a while ($\approx 20\,\mathrm{min}$) to reach its final pressure. During this time the pressure in the camber might rise and fall again a few times (*cf.* Fig. 5.2). Final pressure with the nozzle at room temperature and 20 bar stagnation pressure should be $\leq 10^{-5}\,\mathrm{mbar}$. At the lowest nozzle temperatures it might rise up to a few $10^{-4}\,\mathrm{mbar}$.

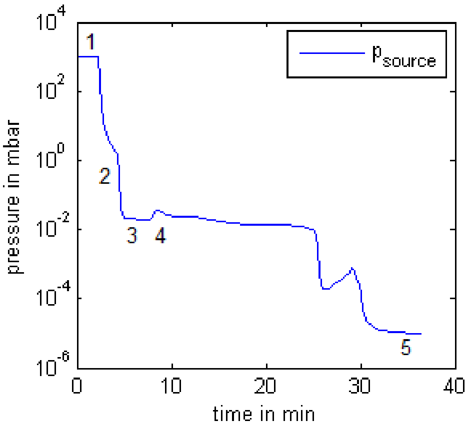

Figure 5.2: Pressure development during the start-up of the vacuum-system in the source-chamber. (1) pressure sensor in overrange, actual pressure decreasing; (2) pumping with rotary vane pump only; (3) auxiliary pumping with the Roots-boosters, plateau at $2 \cdot 10^{-2}\,\mathrm{mbar}$; (4) pressure variations during start-up phase of the oil diffusion pump; (5) oil diffusion pump in normal operation, final pressure $\approx 1 \cdot 10^{-5}\,\mathrm{mbar}$ at 12 bar nozzle pressure

Shut-down Procedure

Make sure that the cryo-cooler (cold-head) is turned off, the valve between the pickup- and the source-chamber is closed and the nozzle pressure is set back to $\approx 10\,\mathrm{bar}$.

Set the "SOURCE" switch to "off" (red light at the diffusion pump fuse box switches off). Turn on the second fan. Wait for $15 - 30$ minutes before turning off the water cooling (the timer on the panel allows a maximum water overrun time of 15 minutes, but the water overrun should be $\geq 30\,\mathrm{min}$). The fore-vacuum pumps must be running and the gate valve in the fore vacuum line must not be closed as long as the diffusion pump is hot.

After the cool down of the diffusion pump and the warm up of the nozzle (otherwise danger of clogging the nozzle), the valves in the fore vacuum line can be closed and the fore-pumps can be turned off (switch "PREVAC 1").

5.2.4 Maintenance

Cooling-Water System

Since 2014, the water-cooling is realized *via* a closed cycle system where the cooling water is treated so that no problems with calcification or formation of algae should occur. Nevertheless, the function of the valves and flow-meters should be checked monthly to ensure the system is working in case of an emergency.

Fore-Vacuum System

Depending on the operating hours of this system, the oil in the rotary vane pump as well as in the Roots boosters needs to be changed (aging process, leaks). Recommended oil-change intervals:
rotary vane pumps - semiannually (also clean the sieve filter at the filling inlet as well as the gas ballast valve and replace the oil filter; new blades are recommended after 3 years)
Roots boosters - annually
In our system the maintenance intervals maybe longer due to the short on-time of the source-chamber vacuum system.

Oil Diffusion Pump

If the oil-level drops below the threshold mark at the view-port, the reservoir needs to be filled up. In case the oil changes its color, it needs to be replaced and the pump needs to be cleaned. The oil diffusion pump is protected against overheating by an external bimetal-temperature switch connected to the fuse box. In case of an unexpected switch-off of the pump, a malfunction of this switch might be the reason.

5.3 Cooling System

5.3.1 Setup

In the current setup, the nozzle is directly connected to the second stage of the refrigerator (*via* a 40 mm diameter oxygen free copper block) and the whole assembly is placed onto a homemade manipulator (tripod consisting of three thread shafts separating the two flanges of a bellow) in order to be able to adjust the position of the nozzle relative to the skimmer (technical drawings for the whole setup: see appendix A). Further, a radiation shield is connected to the first stage of the refrigerator (cold-head), which completely surrounds the inner stage with the nozzle but is designed in a way that guarantees efficient pumping, *i.e.* good vacuum between the nozzle and the shield. The shield consists of just a single part of soldered copper tubes, is wrapped in highly reflective multi-layer foil and reaches a final temperature of 44 K in normal operation. The helium pipe (copper) coming from the vacuum feed-through (steel pipe for thermal isolation) is wrapped around and soldered to the radiation shield to pre-cool the helium gas. After the pre-cooling section, the gas is filtered by a sintered metal filter with 2 μm pore size and continues to flow through a long and thin steel capillary tube (thermal insulation) before it enters the another copper pipe wrapped around the second stage of the refrigerator for the final cooling. The already cool helium gas then moves on to the nozzle, where it expands through the clamped nozzle plate.
The temperature of the nozzle is measured by a temperature sensing diode (silicon diode, DT-670, Lakeshore Cryogenics), especially suited for this temperature range (steep characteristics between 0 K and 20 K). As the cold-head operates with constant cooling power, the temperature of the nozzle is controlled by a heating resistor (Arcol HS15), which is connected to a control-unit built on the institute. This control unit comprises a commercial PID-controller (Eurotherm 3500), a homemade constant current source (10 μA) to operate the diode and a pulse width modulated current source for the heater. The pin assignment can be found in the following figure (Fig. 5.3).

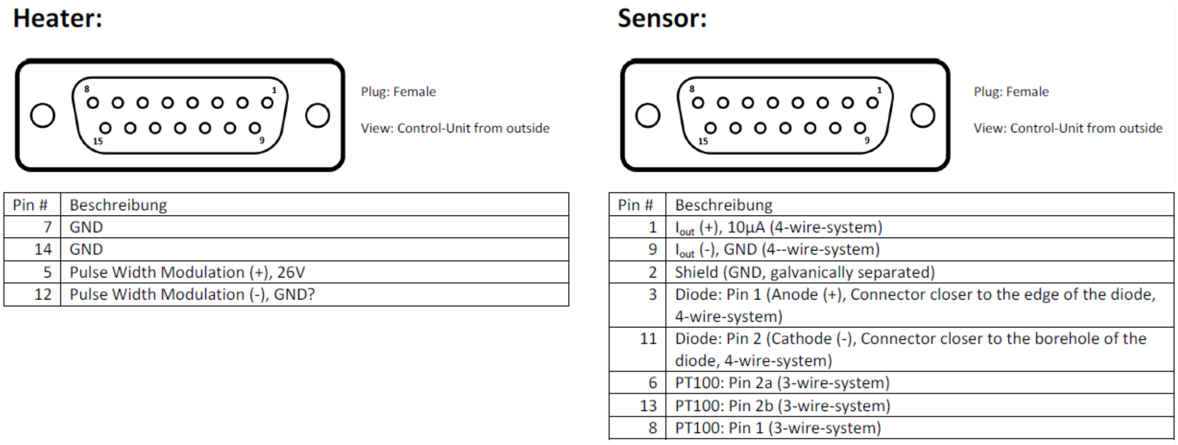

Pin #	Beschreibung
7	GND
14	GND
5	Pulse Width Modulation (+), 26V
12	Pulse Width Modulation (-), GND?

Pin #	Beschreibung
1	I_{out} (+), 10µA (4-wire-system)
9	I_{out} (-), GND (4--wire-system)
2	Shield (GND, galvanically separated)
3	Diode: Pin 1 (Anode (+), Connector closer to the edge of the diode, 4-wire-system)
11	Diode: Pin 2 (Cathode (-), Connector closer to the borehole of the diode, 4-wire-system)
6	PT100: Pin 2a (3-wire-system)
13	PT100: Pin 2b (3-wire-system)
8	PT100: Pin 1 (3-wire-system)

Figure 5.3: The pin assignment of the electrical feed-through

In order to minimize the heat flow from the electrical feed-through to the parts at cryogenic temperatures, Manganin wires were used for the electrical connection of the heater and the diode. Furthermore, the wires coming from the electrical feed-through are thermally connected to the end plate of the cold-head before continuing to the heater and the diode ("thermal anchoring") in order to reduce the heat flow from the nozzle to the refrigerator (which leads to a temperature difference between the nozzle and the end plate of the cold-head).

5.3.2 Dimensioning

In order to produce big droplets (He_N with $N \gg 10^7$) it is important to get to very low temperatures ($T \leq 6\,\mathrm{K}$). The cryo-cooler (Sumitomo RDK-408D2) used to get these low temperatures has the following specifications:

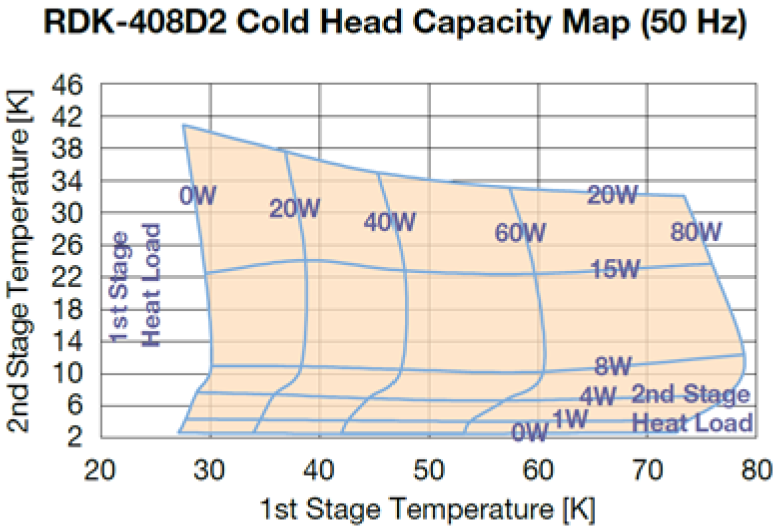

Figure 5.4: Cooling capacities of the 1st and 2nd stage of the refrigerator, depending on the stage temperature

The heat load applied to the first stage (shield) can be estimated by calculating the thermal radiation:

$$\dot{Q} = A_{\mathrm{shield}} \cdot \sigma \cdot \epsilon \cdot \left(T^4_{\mathrm{chamber}} - T^4_{\mathrm{shield}}\right) \tag{5.1}$$

Where $A_{\mathrm{shield}} \approx 0.2\,\mathrm{m}^2$ is the surface area of the radiation shield, σ is the Stefan Boltzmann constant $\epsilon = 0.4$ (estimated) is the emission coefficient and T_{x} are the temperature of the wall of the vacuum chamber ($\approx 300\,\mathrm{K}$) and the temperature of the radiation shield ($\approx 45\,\mathrm{K}$). With these parameters the heat load yields about 40 W.

The same calculation can be applied to the 2nd stage:

$$\dot{Q} = A_{\mathrm{nozzle}} \cdot \sigma \cdot \left(T^4_{\mathrm{shield}} - T^4_{\mathrm{nozzle}}\right) \tag{5.2}$$

Where $A_{\mathrm{nozzle}} \approx 0.03\,\mathrm{m}^2$, $T_{\mathrm{shield}} \approx 45\,\mathrm{K}$ and $T_{\mathrm{nozzle}} \approx 4\,\mathrm{K}$ yields a heat load of 0.007 W. Clearly, the radiation can be neglected here and the heat flow through the wires of diode and heating resistor contributes the main part of the heat load. As the thermal conductivity of copper increases dramatically at temperatures around 25 K and can reach up to 15 times the value it has at room temperature, Manganin wires were used instead of copper. Manganin has a low thermal conductivity $\left(< 25\,\frac{\mathrm{W}}{\mathrm{m\,K}}\right)$ over the whole range from room temperature until cryogenic temperatures. (compare to copper: $400\,\frac{\mathrm{W}}{\mathrm{m\,K}}$ at room temperature and much higher at 25 K).

In this setup, temperatures as low as 3.7 K at 20 bar or 4.0 K at 50 bar were reached without additional alterations. Without gas flow (clogged nozzle) a minimum temperature of 2.5 K was reached. The cool down time from room temperature to temperatures below 10 K is $\approx 100\,\mathrm{min}$.

5.3.3 Beam Dimensions

Sometimes it is important to know the approximate beam dimensions of the droplet beam at a specific location of the beam path, *e.g.* to prevent an unwanted simultaneous illumination of two seperated substrates. Therefore we estimated the beam dimension by geometric considerations.

Fig. 5.5 shows a compilation of possible beam limiting elements along the beam path. It turns out that the skimmer at the exit of the pickup chamber is the actual limiting element. From its relative position to the nozzle and its diameter one obtains a beam divergence of $\approx 0.271°$. However, we note that in some cases the helium nozzle is operated under conditions where the emerging beam is supposed to be even narrower. This will be the case especially when liquid helium is streaming out of the nozzle, *i.e.* at very cold nozzle temperatures (see Fig. 5.1). On the quarz crystal of the microbalance one can see the area of pronounced deposition by naked eye. The diameter of this area is ≈ 6 mm which would correspond to a smaller beam divergence of $\approx 0.223°$ (indicated by red lines in Fig. 5.5).

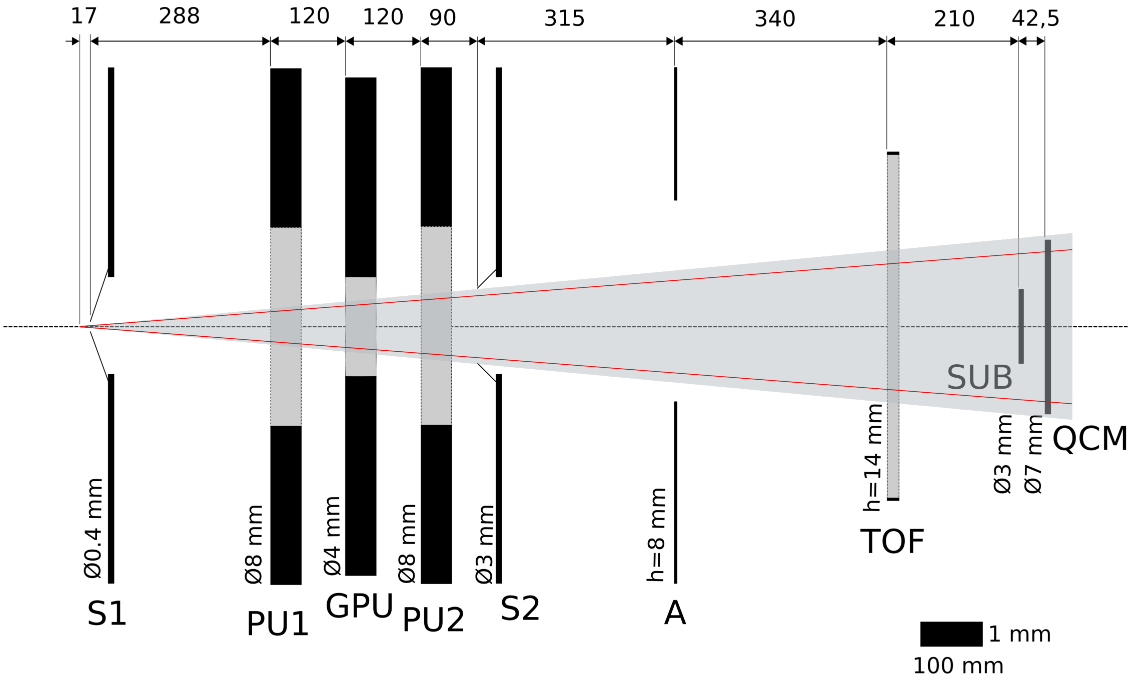

Figure 5.5: Dimensions of the droplet beam. **S1** skimmer in source chamber; **PU1/PU2** resistively heated pickup cells (length= 50 mm); **GPU** gas-pickup cell (lenght= 50 mm); **S2** skimmer at pickup chamber exit; **A** aperture seperating differential pumping stage and main chamber (width= 3 mm); **TOF** time of flight mass spectrometer ionisation zone (width= 20 mm, length= 20 mm); **SUB** substrate for cluster deposition; **QCM** quarz crystal monitor. The diameters/heights of the elements are indicated. Beam dimensions are plotted as obtained by geometrical considerations (grey area) and as visually determined (red lines). See text for further explanations. Scale is 1:10 in horizontal direction and 4:1 in vertical direction.

5.3.4 Operating Instructions

Following the code of best practice, there must always be a certain flow through the nozzle to avoid clogging. This is realized by keeping the nozzle pressure at $\approx 10\,\mathrm{bar}$ at all times. Once the nozzle is clogged (by a droplet of diffusion pump oil, dust, ect.) there is hardly any chance to get it working again - so far, clogged nozzles always had to be replaced.

Start-up Procedure

As it takes about 100 min for the cold-head to cool down the nozzle, which is much longer than the diffusion pump needs to get started, one can begin with start-up procedure of the cold-head right after switching on the diffusion pump. To start the cold-head, turn on the water-cooling on the respective control panel and set the "COLD-HEAD" switch to "auto" (typical pumping noise of the cold-head). After a few minutes the nozzle temperature should start to decrease (monitor at the display of the temperature control unit or with iTools software on the computer). After about 100 min a temperature below 10 K should be reached. When the desired temperature is reached, the nozzle pressure can be increased to the required value.

Shut-down Procedure

Set the nozzle temperature to $T_0 = 0\,\mathrm{K}$ and close iTools. Set the "COLD-HEAD" switch to "off" and turn off the water-cooling. After that, the cooling water will continue to run for another couple of minutes (as set on the panel), which is indicated by the flashing green light. The nozzle pressure can be reduced to the base-pressure of $\approx 10\,\mathrm{bar}$ which prevents the nozzle from clogging. As long as the nozzle-structure is colder than $\approx 0\,^{\circ}\mathrm{C}$ the chamber should not be vented, otherwise the humidity in the air will immediately freeze on the cold parts, thereby possibly clogging the nozzle.

5.3.5 Maintenance, Troubleshooting

Compressor-Cold-Head Unit (Sumitomo RDK-408D2)

Maintenance work that can be done by the user:

- Since 2014, the water-cooling is realized *via* a closed cycle system where the cooling water is treated so that no problems with calcification or formation of algae should occur. Nevertheless, the function of the valves and flow-meters should be checked monthly to ensure the system is working in case of an emergency.
- Replacement of the Compressor Adsorber (every 30.000 hrs → with the short runtime of our system, this will probably not apply here), for instructions see manual of the compressor unit
- Recharging helium gas (as required → see pressure gauges on the compressor unit) , for instructions see manual of the cryocooler

Maintenance work that cannot be done by the user:

- Replacement of the cold-head mechanical parts (every 10.000 hrs), cold-head has to be shipped to the manufacturer

Adjusting the Nozzle-Setup

Due to the cooling cycles of the nozzle-setup and the heating cycles of the oil diffusion pump it might happen that the position of the nozzle and/or the chamber gets distorted. If this is the case, the helium pressure in the source chamber does not change, but the helium flow through the skimmers is significantly reduced. If the droplet beam cannot pass the skimmers any longer, there will still be He-gas in the measurement chamber, but no droplets (distinguishable in the mass spectrum → no signal at the multiples of He_4). If the nozzle is clogged, on the other hand, not only the helium pressure in the down-stream chambers, but also in the source chamber is reduced. Once the nozzle is clogged (by a droplet of diffusion pump oil, dust, ect.) there is hardly any chance to get it working again - so far, clogged nozzle plates (electron microscope apertures, Günther Frey GmbH) always had to be replaced.

After replacing the nozzle or whenever the beam is poorly aligned, the alignment can be checked with a telescope, looking along the beam axis from the downstream end of the machine. In order to find the right position for the nozzle, the flange with the skimmer has to be removed from the source chamber. After this, the nozzle is visible in the telescope and the position as well as the tilt can be adjusted using the 3 screw nuts on the tripod (gray in Fig. 5.6). Keep in mind that the nozzle axis must be horizontal (check with a mason's level). The tilt around the vertical axis can be checked by controlling whether the nozzle and the flange-plane are parallel, using an indicating caliper. The tilt around the beam axis is used to change the nozzle position horizontally (left image in Fig. 5.6). When putting the flange with the skimmer back on, its position must also be adjusted using the telescope (illuminate the skimmer from inside the source chamber). In the aligned setup, only minimal adjustments (less than a half turn on each of the 3 screw nuts of the tripod) are needed to optimize the helium flow through the chambers. If bigger adjustments are necessary, there is most likely something wrong with the nozzle plate. A more detailed description of the alignment procedure for the whole machine follows in section 8.1.

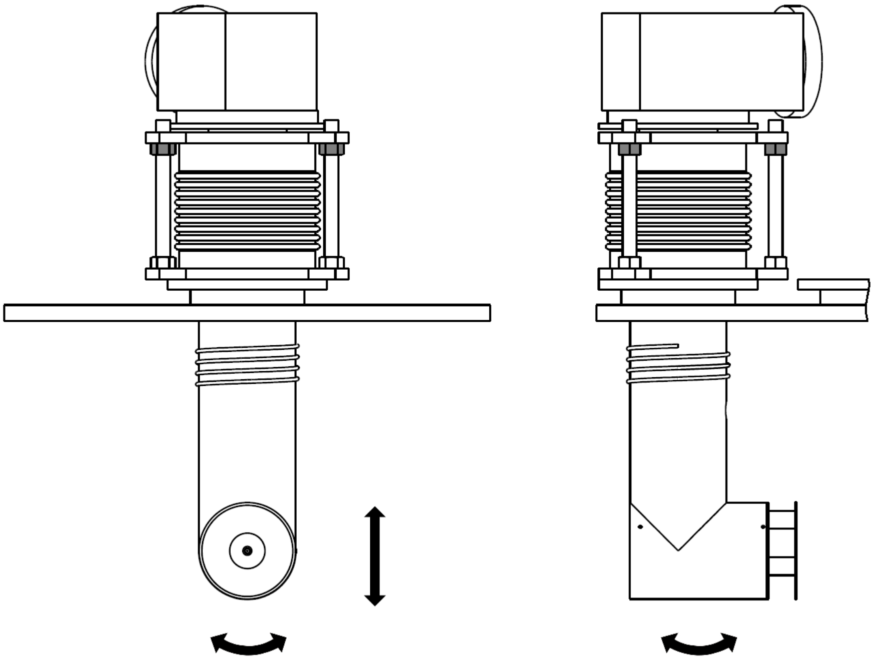

Figure 5.6: Schematics illustrating the adjustment of the nozzle. The left image shows the adjustment of the nozzle position. The tilt shown in the right image must be zero, *i.e.* the beam axis must be horizontal.

6 Droplet Doping (Pickup Chamber)

6.1 Abstract: Pickup and Cluster Formation Inside Helium Droplets

When a helium droplet collides with an atom or molecule, the probability that the particle gets picked up by the droplet is close to unity (for all dopant species). Therefore, the interaction cross section can be approximated by the geometrical cross section of the droplet. The amount residual gas pickup is defined by the droplet size and the base pressure in the pickup chamber. In order to keep the ratio between parasitic pickup of residual gas and the pickup of the desired dopant species low, base pressures lower than $\approx 1 \cdot 10^{-6}$ mbar have to be provided. Consequently, a certain pickup rate of a desired dopant can be adjusted by controlling its abundance (*i.e.* partial pressure / vapor pressure) along the beam line. For gaseous species, this is realized by dosing the dopant gas into a hollow cylinder through which the beam is guided. This way, the partial pressure of the dopant is elevated inside the pickup cell, while a low base pressure is maintained in the chamber (outside the cell). In order to pick up solid species, they have to be forced into the gas phase first, usually by heating the desired dopant to a temperature, at which the vapor pressure is sufficient to yield the necessary amount of collisions with helium droplets. For the synthesis of nanoparticles (*i.e.* the pickup of several thousand atoms) this temperature usually lies in the region of the melting point of the dopant material. The metal pickup cells used in this machine utilize resistively heated crucibles in a water-cooled housing, through which the beam is passed.

Once a dopant hits the droplet, it gets cooled down (slowed down), but afterwards the interactions with the superfluid environment are very weak and the dopant is able to move inside the droplet. If additional dopants are added to the same droplet, they will eventually meet and coagulate. Thereby, binding energy is released, which causes the evaporation of helium atoms from the droplet. Especially when producing larger clusters, this leads to a significant shrinking of the droplet. As a rule of thumb, about 1600 helium atoms are evaporated to dissipate 1 eV of binding energy. For most metals this means that each atom added to the droplet eventually leads to the evaporation of ≈ 5000 helium atoms.

The introduction of sequential pickup schemes as well as the low temperature of the droplet lead to interesting possibilities for cluster production in terms of exotic material combinations and core-shell systems.

6.2 Vacuum System

6.2.1 Setup

The vacuum system of the pickup chamber is a 2-stage system: a large turbo pump (Oerlikon Turbovac 1000C, nominal throughput = 1000 l/s) is backed by a rotary vane pump (Leybold Trivac D40B). The exhaust port of the rotary vane pump is connected to the buildings aspiration system. In order to reduce the noise level in the lab, the fore-pump is located in the adjacent room. During experiments, the vacuum in the pickup chamber can be improved by operating the installed liquid nitrogen cooling trap. At the end of the pickup chamber, there is a second skimmer ($3\,mm$ diameter), which shapes the beam before it runs through the differential pumping stage, which is pumped by a small turbo pump (Pfeiffer TPU 062, nominal throughput = 50 l/s). This turbo is backed by the same rotary vane pump as the pickup chamber. There are two valves in the fore-vacuum line, one right after the rotary vane pump and one just before the turbo pumps. The pickup chamber is sealed using rubber gaskets, which means that a minimum base pressure of high 10^{-8} mbar or low 10^{-7} mbar can ultimately be reached. The differential pumping stage (sealed with copper gaskets) is necessary in order to maintain the very low pressures in the measurement chamber during operation ($\mathrm{He_N}$-beam on). The copper gasket between the differential pumping stage and the measurement chamber is not ring-shaped as usual, but circular with a slit (height = 8 mm, width = 3 mm), which acts as another aperture for the beam, in order to increase the pressure gradient.

6.2.2 Dimensioning

Ideally, the helium beam created by the skimmer in the source chamber enters the pickup chamber on the front end and leaves it at the back end without any helium losses, as long as there is no doping. In practice, there will be losses due to self cooling and possibly the beam spread angle (skimmer at the exit of the pickup chamber). As soon as there is pickup, there will be additional evaporation losses. Furthermore, when heating up the crucibles, absorbed and adsorbed substances will desorb and add gas to the chamber. When dosing gas into the gas pickup chamber, only a fraction of the introduced atoms or molecules will be picked up, the rest has to be removed. In order to keep the base pressure in the pickup chamber low, especially when the pickup cells are turned on, the high throughput of the turbo pump is needed. Otherwise, there would be uncontrolled pickup of all residual gas species along the beam. In the current setup, only parasitic pickup of water molecules can be observed in the mass spectra, the abundance of all other gases is too low in order for them to be detected.

After the beam passes through the second skimmer (3 mm diameter) at the exit of the pickup chamber, the beam enters the differential pumping stage with another aperture (rectangular, height = 8 mm, width = 3 mm), in order to get a larger pressure gradient between the pickup chamber and the last chamber. In a previous design, there were three apertures in the differential pumping stage, but it turned out that one is sufficient, which makes the alignment procedure (section 8.1) much easier. The rectangular shape of the aperture in the current setup was chosen in order to allow the beam to pass, even if it is deflected downwards by gravity (significant gravity effect can only occur at the lowest possible nozzle temperatures, where the beam velocity is low) or upwards by extensive doping.

6.2.3 Operating Instructions

Be aware that the vacuum systems of the pickup-chamber and the differential pumping stage are not separated and can only be operated together. Usually, the vacuum System of these 2 chambers is working 24/7 and maintains a base pressure in the low 10^{-7} mbar range in the pickup-chamber and a base pressure in the high 10^{-9} mbar range in the differential pumping stage.

Shut-down Procedure

Before shutting down the system, make sure that the gate valves to the source- and measurement-chamber are closed and the crucibles are at room temperature. Close the valve in the fore-vacuum line and turn off the pumps at the control panel (switches "PREVAC 2" and "PICKUP" in position "off"). As a rule of best practice, one waits until the large turbo pump has slowed down to half its nominal speed (only half of the LEDs in the LED-bar on the controller Leybold TD20 are illuminated) before opening the venting valve. While opening the venting valve, monitor the chamber pressure. As soon as the pressure has risen by an order of magnitude, close the valve again and wait a minute for the turbo pump to slow down, then repeat the procedure. The chambers can either be vented with an inert gas (dry nitrogen or argon, which is recommended if the side flanges remain closed or are opened for only a few minutes) or with ambient air. Venting with an inert gas reduces the introduction of moisture to a minimum, therefore, good vacuum conditions can be reached very shortly after restarting the pumps. After venting with air or longer maintenance work, a bake-out of the chambers is needed in order to reach the before mentioned base pressures. When venting with inert gas, be aware that overpressure in the vacuum chamber should be avoided (may harm the gate valves, feedthroughs and windows). Unfortunately, the standard vacuum pressure gauges are very inaccurate above $\approx 10\,\mathrm{mbar}$ and cannot be used as indicators for reaching ambient pressure. Instead, the opening of the pressure relieve valve on the side flange can be taken as indicator to immediately close the venting valve (escaping of the gas can be heard and the button of the relieve valve can be moved). As long as the system is at ambient pressure, the pressure gauges should be switched off.

Start-up Procedure

Before starting the vacuum system, make sure that the gate valves to the source- and measurement-chamber are closed and the valves in the fore-vacuum line are opened. Start the fore-vacuum pump by setting the "PREVAC 2" switch on the control panel to "manual" and, after one minute, turn on the pressure gauge "PREVAC PICKUP". As soon as the backing pressure is sufficiently low, the "prevac" LED turns green and the "PREVAC 2" switch must be set to "auto" (otherwise, the system shuts down automatically after 10 min in "manual"-mode). Then, the "PICKUP" switch can be set to "manual". Turn on the cooling water (black button on the control panel) and the pressure gauge "PICKUP". As soon as $1 \cdot 10^{-3}\,\mathrm{mbar}$ are reached in the pickup chamber all LEDs (prevac, vacuum, water) on the PICKUP control panel should be green and the PICKUP switch must be set to "auto". If the $10^{-5}\,\mathrm{mbar}$ range is not reached within a short time, there will likely be a leak [1] [2]. When searching for a leak, start with the flanges that were open during the shutdown and control the Swagelok connections inside the chamber as well, if they were opened.

6.2.4 Maintenance

Since 2014, the water-cooling is realized *via* a closed cycle system where the cooling water is treated so that no problems with calcification or formation of algae should occur. Nevertheless, the function of the valves and flowmeters should be checked monthly to ensure the system is working in case of an emergency.

The oil in the rotary vane pump is recommended to be changed (aging process, leaks) semiannually (also clean the sieve filter at the filling inlet as well as the gas ballast valve and replace the oil filter), new blades are recommended after 3 years. The rotor of the Oerlikon turbo pump should be replaced after 9 years. The operating fluid of the Pfeiffer turbo pump should be changed every 4 years. Check manuals for further information.

6.3 Feed-Throughs

In order to operate the components inside the pickup chamber, serveral feed-throughs are required. Most importantly, for the two metal vapor pickup cells two high current (up to 185 A and 8 kV) 2-pole electrical feed-throughs (Vacom, W-HC8-CE-CV64) are installed. Be aware that these feed-throughs may become hot during operation (up to 200°C). Besides the power supply, these vapor cells need water-cooling, whereby the pipes are internally connected *via* Swagelok-connectors. The temperature inside the chamber can be monitored on several positions using a triple-feed-through of type K thermocouples (Vacom, W-TC3-CE-K) as well as a double-feed-through of type C thermocouples (Vacom W-TC2-CE-C). Furthermore, a gas-feed-though with a dosing valve on the outside of the chamber is installed in order to operate the gas-pickup cell. For the operation of a chopper (as in other machines on the institute) a 15 pin SubD-feedthrough (Vacom, W-SUBD-15-DE-CE-SSG, max. 500 V, 5 A/pin) is provided, however, was not used so far.

Other small loads can be connected *via* a multi-pole feed-through (Vacom, W-MPC2-19-SE-CE-SSG, max.

---

[1] In case of a leak: shutdown, find and seal the leak, start again

[2] Exception: if the chamber has been opened for a day or longer, there will be a lot of water adsorbed, which takes some time to desorb and keeps the pressure in the $10^{-4}\,\mathrm{mbar}$ range

1 kV, 3 A/pin) which is connected to a box with electrical sockets outside the chamber to enable fast and secure plugging. By the time this manual was written, only the light bulbs for the internal bakeout were connected, using sockets D and K (denomination adopted from the feed-through). In earlier experiments other pairs of sockets were used to operate lifting solenoids for blocking the droplet beam or blocking the dopant-atom beam (crossed beam setup).

6.4 Pickup Cells

6.4.1 Gas Pickup Cell

Using a regular gas dosing valve (Duniway VLVE-1000) gaseous (and some liquid substances) can be introduced into a vacuum chamber in finely adjustable amounts. Without any further action, the substance dosed into the vacuum chamber would spread in the whole chamber. In order to dope the helium droplets, a spatially confined pickup-region is desired. Only then, the sequence in which the different species are added to the droplet can be controlled by the position of the respective pickup-cells. The spatial confinement is realized by dosing the desired substance(s) into a tube with a hollow cylinder at the end, through which the beam is passed. Thereby, the gas volume inside the cylinder (12 mm diameter, 50 mm length) is larger than the interaction region with the beam, which enters and leaves the cylinder through a 4 mm borehole (see Fig. 6.1).

Figure 6.1: Gas pickup cell

The option of dosing *e.g.* oxygen into the droplets opens the way to investigate chemical reactions inside the droplet. Furthermore, it allows a comparison between situation where *e.g.* oxygen is present already during cluster formation or not until after cluster formation.

6.4.2 Metal Pickup Cells

For the experiments conducted with this machine so far, magnetic fields inside the pickup chamber were not critical. Therefore, the simplest solution for evaporating the dopants are resistively heated crucibles (Ted Pella Aluminia Coated Tungsten Wire Basket, Style 6), which need high electrical currents (up to 40 A per crucible). With these, a maximum temperature of about 2000 K can be reached, which yields sufficient pickup conditions (vapor pressure) for a broad range of metals (so far, silver, gold, copper, chromium and nickel have been evaporated with this design). In order to avoid damage or excessive heating of other elements in the same chamber, the hot crucibles have to be housed in water-cooled radiation shields. Following, two different designs of the evaporation sources are described, technical drawings can be found in appendix A.

Crossed Beam Setup

In this design the crucible is covered by a tantalum sheet with a 3 by 25 mm slit (see Fig. 6.2a) in order to minimize the loss of Ag atoms and the heat flow to the cooling shield. The shield itself also has a slit, which is placed just below the helium beam (see Fig. 6.2b). This way, the passing He droplet beam is hit by evaporated atoms from underneath, under an angle of about 90°. The main advantage of this design is the possibility to introduce a shutter (depicted in Fig. 6.2 c), which allows to switch the source on and off within seconds, while in other designs, the crucibles need to be heated up or cooled down in order to turn the pickup on and off. A disadvantage of this concept is the unidirectional doping, which deflects the helium droplet beam at high doping rates. Furthermore, this source requires frequent maintenance because the dopant material tends to condensate at the slits, making them narrower over time until they plug up completely.

(a) (b) (c)

Figure 6.2: Crossed beam setup. (a) crucible with tantalum cover (1), Cu colums as electrical contactors (2) and water-cooled base-plate (3); (b) assembly with water-cooled housing; (c) assembly with electromagnetic shutter.

Vapor Cell Setup

Here, two crucibles are mounted on top of each other (mirrored) and the beam passes between the crucibles (see Fig. 6.3). They are connected in parallel and consequently will have about the same temperature. The crucible at the bottom is filled with the metal to evaporate. Atoms that are evaporated at the bottom are either picked up by the He droplet beam or they arrive at the top crucible, where they will be reflected and thus can hit the droplet from the opposite direction. With this design the droplet beam is not deflected as in a crossed beam setup, which is crucial for experiments where heavy doping is desired.[3] Unlike the previous design, this setup does not allow turning the pickup on and off fast. Different pickup rates can only be adjusted by changing the temperature, which takes time.

---

[3] Diploma thesis: Johannes Steurer

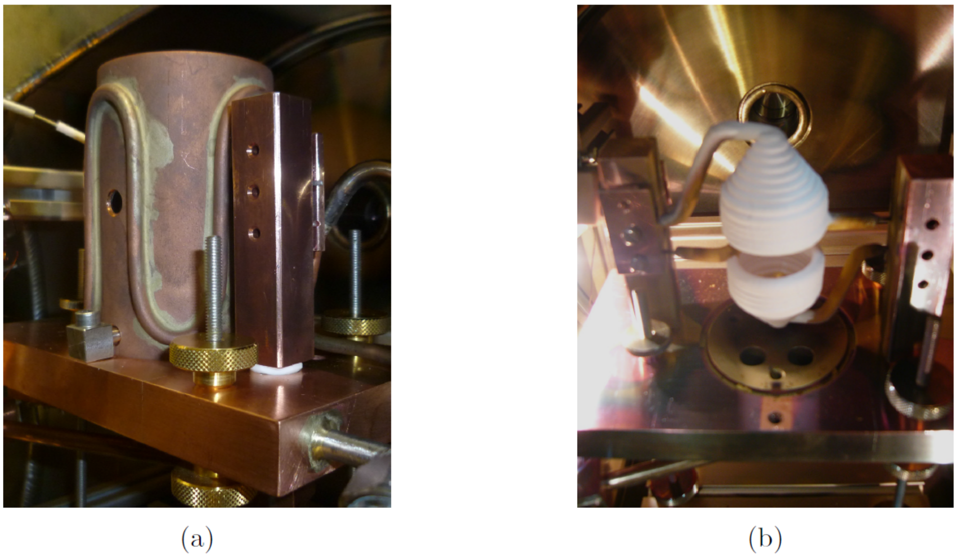

(a) (b)

Figure 6.3: Vapor cell setup with (a) and without (b) Cu cooling shield.

Temperature Measurement

Earlier designs were equipped with a Type C thermocouple, housed in a ceramic husk, which was placed inside the metal melt. During the first experiments it turned out, that it is practically impossible to avoid thermal contact of the husk with the cooling shield. Consequently, there is a significant heat-flow over the ceramic husk, which changes during melting and solidifying. Besides the varying heat flow, which leads to significantly different temperatures of the heated metals at identical heating power, also the temperature measurement itself is affected by the thermal contact to the shield. With this measuring principle, it was impossible to reproduce the same conditions in subsequent experiments. In order to get information about the dopant temperature after removing the thermocouple and husk, the electrical resistance of the wire basket was recorded and used as temperature sensor. Through this measure, reproducibility was guaranteed, however, this way of determining the dopant temperature is not accurate.

Computer Program: Temperature Control

During the cluster synthesis process it is important that the vapor density in the pickup cells can be held at a constant level. As the vapor pressure depends exponentially on the temperature, temperature differences of 20 K or less do make a difference. Hence, setting a constant heating current and waiting for the temperature to stabilize is not a good strategy. An automated temperature control is needed.
After an attempt to realize the temperature control using LABVIEW, which always had stability issues, a MATLAB code was developed to communicate with the power supplies (EA-PS 9080-100). The communication with the power supplies (*via* UTA12-interface) is done with telegrams in hexadecimal form. A command cycle typically consists of a command transfer and a reply transfer. Hence, the interface works as a slave and waits for commands. Instructions on how to program the communication can be found as an attachment to the manual of the power supplies. For the communication to work it is important that the USB-Serial Ports are correctly configured in the hardware manager. Furthermore the ports have to be opened and closed properly in the computer program. If the power supplies are not responding to the MATLAB program, this is most likely related to a problem with the ports and can be resolved by restarting the MATLAB program. The control program itself reads the voltage and current provided by the power supply and by calculating the resistance of the crucible gives a calculated temperature (eqn. 6.1).

$$T = \frac{\frac{R_T}{R_{20}} - 1}{\alpha} + 20^\circ\mathrm{C} \qquad \text{with} \qquad \alpha = 0.0044\,^\circ\mathrm{C}^{-1} \tag{6.1}$$

As the different crucibles do not have exactly the same resistance, the resistance at room temperature is tested by the program by sending a short current pulse of twice the specified minimum current through the crucible while measuring the voltage drop, before the actual control program starts. The control program can operate in two modes, "ramp" and "constant". In the ramp-mode the temperature is increased or decreased with a specified rate, which is important for the lifetime of the crucibles. If they are heated or cooled down too fast, they might break (rates $< 150\,\mathrm{K/h}$ are advised by the manufacturer at absolute temperatures below $600\,\mathrm{K}$). If the desired temperature is reached, the program automatically switches to constant-mode, which holds the temperature in a window of about $\pm 2\,\mathrm{K}$ around the specified value. It should be noted that this way of determining the temperature is not very accurate and uncertainties of $10 - 15\,\%$ of the absolute temperature value have to be expected, however, the reproducibility and the stability are very good. Besides live-control, the program also can save log-files containing all measured and calculated values with a time-stamp.

6.4.3 Operating Instructions

Before switching on the power supplies for the crucibles (EA-PS 9080-100), check that the water-cooling of the cooling shields is on and that the vacuum conditions are sufficient (pressure below 10^{-6} mbar, otherwise, the beam won't reach the measurement chamber; at ambient conditions the crucibles might be damaged if they are heated). As described above, the current setup is not equipped with temperature sensors, instead the electrical resistance of the setup is taken as a measure for the temperature. The resistance (temperature) readout as well as the control of the heating power can be carried out by a self-made MATLAB program, exploiting the very linear temperature dependence of the resistance of tungsten.

Below a temperature of $\approx 300°\mathrm{C}$, the crucibles should not be heated up or cooled down at a rate higher than $150°\mathrm{C/h}$, at high temperatures rates of up to $5000°\mathrm{C/h}$ are no problem. With the ramp-function of the Matlab-program, an adequate heating rate can be set and after reaching the desired temperature, the program maintains a stable temperature (typically within $\pm 2°\mathrm{C}$). For safety reasons, a maximum current as well as a maximum voltage can be set. For the 2-crucibles setup, the resistance of the system at room temperature lies around $0.03\,\Omega$ to which the tungsten wires of the crucibles contribute the largest part. When heating up, not only the resistance of the crucible, but also the resistance of the copper wires changes, leading to a systematic error in the temperature measurement. The resistance at a known temperature (*e.g.* room temperature) can be measured by the Matlab program, when checking the respective option (needed *e.g.* after changing the setup), but may also result in a bias. With this method, the absolute error in the temperature measurement might be as high as 15%, but the settings are reproducible (a certain heating power yields the same resistance/temperature).

Every time the temperature is increased, gases start to desorb from the crucible, especially when heating the first time after venting the chamber. In normal operation, pressures below 10^{-6} mbar (which are necessary for good experiments) can be reached without using the liquid nitrogen trap. Nevertheless, the liquid nitrogen trap can be used to improve the vacuum conditions at any time.

If the water-cooling is not switched on for any reason while the crucibles are hot, immediately turn off the power supplies. Do **NOT** turn on the water-cooling - the water will boil and the steam will melt the rubber hoses. Furthermore, the temperature shock might break the pipes inside the vacuum with potentially catastrophic consequences. With the water-cooling off, the crucibles will cool down slowly and likely there won't be any damage. If the crucible temperature without cooling exceeded 400°C, some components of the solder on the cooling shield will evaporate and the chamber needs to be cleaned.

In order to dope the droplets heavily, temperatures corresponding to a vapor pressure of $10^{-4} - 10^{-2}$ mbar of the respective material are needed. If these temperatures are not / no longer sufficient, there is either not enough material left in the crucible or there is another problem. Do not push the temperatures to extremes. When experimenting, always check the un-doped droplet signal first with the TOFMS (helium-comb) as well as with the QMS to determine the He-partial pressure as a reference for the later measurements with doped droplets. If there is no He-signal, control the pressures in all chambers and check the beam-line with the telescope for obstacles and correct alignment.

6.4.4 Maintenance

Depending on the intensity of use, the crucibles will have to be refilled after a certain time. When using small pellets of the material to evaporate, a straw can be plugged through one of the holes for the beam (vapor cell setup) or through the slit at the top (crossed beam setup) into the crucible. The pellets have to be put into the straw with tweezers and slide down into the crucible. The filling level can be checked using an endoscope. This method has the big advantage, that neither the electrical contacts nor the water-cooling have to be disconnected and the alignment is not obstructed.

If the method above cannot be applied, or a different material should be placed in the oven, the simplest method is to disconnect the water-cooling (after turning off the water and dry-blowing the tubes) and the copper-rods (such that the columns on each side of the crucible remain clamped to the base plate) and to remove the whole setup from the rails (by opening the 2 knurled nuts). Once the setup is outside the vacuum chamber, it is much easier to service. When changing the materials, it is best practice to also switch the crucibles (each crucible is only used for one material). To do so, remove the cooling shield and open the clamps on the columns. Remove the old crucibles (be careful, the alumina as well as the tungsten wires are brittle!) and clean the shield as well as the base plate. Collect the material scraped off the shield and the base plate in case it is valuable (*e.g.* gold or silver). Mount the new and filled crucibles and assemble the oven again. If all tasks have been carried out very carefully, the alignment might still be alright, but the alignment has to be checked in any case.

When using the crossed beam setup, keep track of the cell temperature needed for a certain beam attenuation. The material condensing at the slit reduces the slit's cross-section, such that higher temperatures are required to get the same doping load. Higher temperatures lead to a faster clogging of the slit, which means that after a while the excess material has to be scraped off.

7 Droplet and Cluster Analysis (Measurement Chamber)

7.1 Abstract: Beam and Cluster Analysis

The nanoparticles assembled in the pickup chamber are carried into the measurement chamber by the droplet beam. There, they can be analyzed *in-situ* or deposited for subsequent *ex-situ* diagnostics. In-flight diagnostics offer the advantage of very cold (ground state) particles which are only very weakly influenced by their surrounding. Measurements on deposited particles have the advantage that the particle density on the substrate can be chosen by adjusting the time span for deposition and instead of measuring averages, single particles can be addressed on the surface. However, during the landing process on a certain substrate, the helium surrounding the nanoparticle will evaporate and the particle will warm up. Additionally, the adsorption of the particles on the substrate may change their shape and morphology and may alter their properties.

The most important detection / analysis techniques at the moment are time-of-flight mass spectrometry (TOFMS) (in flight) and *ex-situ* transmission electron microscopy (TEM) of the deposited clusters. The TOFMS yields data about the composition, abundance and stability of different cluster sizes in the produced cluster collective. The TEM, especially with the element-sensitive detectors, can provide information about single clusters (size, element distribution, morphology). If the samples are exposed to ambient conditions during the transport to external diagnostics, the high reactivity of nanoparticles can become an issue. In order to be able to investigate pre-reactive nanoparticles, a UHV-transfer system was purchased (see section 7.6). This permits the use of more reactive materials as well as other detection techniques, which are available at *e.g.* the University of Graz. For the protected transfer of samples to the electron microscopes, a specialized TEM-holder, already purchased by the Institute for Electron Microscopy and Nanoanalysis, might be used in the future. A suitable docking port for this holder on our machine is currently under construction.

In addition to the main investigation methods, *in-situ* microbalance measurements provide information about the absolute cluster mass-flow and helium partial pressure measurements show the influence of the doping on the droplet beam (evaporation).

7.2 Vacuum System

7.2.1 Setup

The vacuum system of the main chamber is a 3-stage system: there are 3 turbo-molecular pumps directly connected to the chamber (Pfeiffer HiPace 700 + Pfeiffer TPU 520 on the bottom and Pfeiffer HiPace 300 on the TOFMS). The compression ratio provided by these pumps is not sufficient to reach UHV conditions ($< 10^{-9}$ mbar) given the rather poor fore-vacuum pressure provided by the oil free multi-Roots primary pump system (Adixen ACP40, $3 \cdot 10^{-2}$ mbar ultimate pressure at the flange of the fore pump which means $1 \cdot 10^{-1}$ mbar at the connection to the turbo pumps, due to the long fore-vacuum line). Therefore a third stage, which is a small turbo pump between primary pump and the turbo pumps on the chamber, was introduced. If this turbo pump is placed between the fore vacuum line and the pumps on the chamber, the fore-pressure provided by the fore-turbo is so low (10^{-6} mbar) that the lubricant of the bearings of the regular 3 turbo pumps might evaporate. To avoid this, the fore-turbo was placed between the primary pump and the fore vacuum line. Because of the length of the line this only leads to an improvement of about an order of magnitude in the fore-pressure compared to the system without the fore-turbo pump. Nevertheless, this is sufficient to reach the 10^{-10} mbar regime, which was one of the objectives of the machine. All the pumps used here are usually working 24/7. In order to reach the lowest possible pressure in the main chamber, bake-out at $\approx 120°$C for at least one day is necessary. For the purpose of noise reduction in the lab, the primary pump and the later installed fore turbo pump are located next door.

7.2.2 Operating Instructions

Start-up Procedure

Before starting the fore-vacuum system, check that the gate-valve to the differential pumping stage is closed and that the fore-vacuum valve is opened! This is very important because opening the fore-vacuum valve when the fore-turbo pump is at full speed might damage the pump! The two fore-vacuum pumps (multi-Roots + turbo) are connected to the same control line and can be started *via* the control panel "PREVAC 3" (start with "manual" and switch to "auto" as soon as the pressure falls below the threshold).
The 3 turbo pumps directly mounted to the chamber are linked to the same control line and can be switched on *via* the control panel "MAIN" (start with "manual"). Check that all 3 pumps are starting up regularly! It might be the case that the pumps were turned off manually (at the respective controllers) because one of the controllers is needed to switch the venting valve of the chamber and during the venting process the other controllers must be switched off. Usually the 3 turbo pumps are water-cooled in series with the pickup turbo pumps, but air-cooling is also possible ("no water check " - switch on the control panel). If the air-cooling mode is chosen and the water-cooling is turned off, the pumps will eventually become hot if no cooling fans are installed. When going through a bake-out procedure, water-cooling is absolutely necessary!
Since no copper sealed Pirani-manometer was available, only 2 hot cathode manometers are used to monitor the pressure in the TOF- and MAIN-chamber. These manometers may only be turned on below a certain pressure in the chamber. To be safe, wait until all 3 turbo pumps have reached their full speed before turning on the pressure gauges. Very shortly after that, the pressure threshold should be reached and the "MAIN" switch must be set to "auto". Note that the manual mode only works for 10 min, afterwards, the power is switched off (like in the "off" state).

Shut-down Procedure

Before shutting down the vacuum system, make sure that the gate-valve to the differential pumping stage is closed and close the valve in the fore vacuum line. Turn off the primary pump and the fore-turbo ("PREVAC 3"-panel), turn off the 3 turbo pumps ("MAIN"-panel) and turn off the pressure gauges! For venting the chamber with dry nitrogen, open the valve at the gas bottle and the valves along the gas line. Check if the electromagnetic valve on the turbo pump "MAIN 1" is connected. Turn off the turbo controllers "TOF" and "MAIN 2". Set the switch on "MAIN" control-panel to manual. Turn off the motor and the pumping station at the turbo-controller "MAIN 1" (options 023 and 010 in the menu), enable the venting valve (option 012) and set venting mode to 2 (option 030). Do not enable the valve as long as the turbo pumps are above 50% of their nominal speed (to go easy on the bearings).

The main chamber is not equipped with an over-pressure valve. The installed safety feature is a burst disk (breaks at 0.6-0.8 bar overpressure), which only works once and is expensive (keep the overpressure below 0.4 bar!). Therefore, listen carefully to a clicking noise stemming from the burst disk as the pressure in the champer rises above 1 atm. As soon as you hear the noise, the nitrogen valve must be closed and the valve options (012 and 030) must be set back to their original values.

7.3 Time-of-Flight Mass Spectrometer (TOFMS)

The apparatus is equipped with a Stefan Kaesdorf RFT50 time-of-flight mass spectrometer with electron impact ionization and 20 kV post-acceleration, which is especially suited for the measurement of large masses ($m > 10^4$ amu). The ionization region of the spectrometer is located on the beam axis and the ions are extracted perpendicular to the beam, allowing mass spectrometric measurements simultaneously to other experiments further downstream. The setup is designed such that the initial ionization can be conducted *via* electron impact (built-in electron beam) or *via* laser ionization (external). Data acquisition and the control of the device are executed by the computer underneath the high voltage control units (TOF-PC). In order to avoid software problems, the TOF-PC should not be connected to the internet and no other programs should be installed. The TOF-PC can be operated from the regular laboratory computer using a remote-desktop connection.

For the start-up and shut-down procedure, the checklist in appendix D should be used. Voltage settings for different extraction conditions can be found in the manual of the spectrometer. Typical settings can be found in section 8.2.

When changing the voltage settings or the region of interest, the grid potentials as well as the deflection potentials have to be fine-tuned in order to maximize the signal in the region of interest. Especially when going form small to large masses, the deflection potentials have to be adjusted.

If there is no signal, its most likely due to a software-bug: when switching between the software modes, the ionization current is switched off (check electrometer current). To switch the current back on, change any of the puls-generator settings (*e.g.* pulse duration). Another reason for a very low ionization current could be a flat battery (9 V battery in wire #1). When replacing the battery, be sure to connect the battery in the right way!

In order for the discriminator to work correctly, the offset at the preamplifier has to be small. As there is a natural drift, the offset at the preamplifier should be checked and corrected monthly. To do so, turn down the MCP-voltage and disconnect the output of the preamplifier (green cable). Connect a voltmeter to the output of the preamplifier and set the offset to zero, using the potentiometer inside the preamplifier box.

After a long time of operation or if the heating current was set to high, the filament emitting the electron beam might break. Suitable filaments are on stock in the laboratory and can be replaced by the user. When replacing tungsten filaments, always wear goggles as the filaments are brittle and chips are hard to remove, even for an eye-doctor.

7.4 Quadrupole Mass Spectrometer (QMS)

The QMS installed on the apparatus is a Balzers (Pfeiffer) Prisma QME 200. The hardware of the QMS consists of two parts, the analyzer (mounted on the chamber) and the control unit (containing the electronics). These two parts are connected *via* a plug, whose pins are delicate to handle. Ideally, the connection should not be separated. The QMS can be operated with the software package QUADSTAR 7.0.3, which is an old software and only the main program ("Measure") works under Windows 7. This mass spectrometer can analyze masses between 0 and 200 amu and is therefore mainly suited to analyze the residual gas as well as the amount of He in the beam. The software can display the whole mass spectrum or the time-dependent intensity of one or more constituents. Suitable templates for both purposes are predefined and can be loaded by the program. In the current setup the main use is to record the decrease of He in the beam due to doping. In order to work stable, the SEM (secondary electron multiplier) and the filament should be running about half an hour. Note that blocking the beam with the microbalance or the TEM-sample-holder significantly changes the partial pressure measured by the QMS. Comparable measurements can only be recorded if these two elements are in the same position and if the SEM voltage is set at the same value. Before venting the chamber, the QMS has to be switched off!

7.5 Microbalance

The measurement principle of the quartz crystal microbalance is based on the measurement of the resonance frequency of the shear-oscillations of a piezo-quartz. As mass is deposited on the quartz crystal, the resonance frequency f of the oscillation system changes by $\varDelta f$ and allows a very precise measurement of the deposited mass m using the Sauerbrey-equation:

$$\varDelta f \approx -\frac{2f^2}{Z}m \tag{7.1}$$

with Z being a constant, depending on the density and shear modulus of the quartz.
In operation, it is striking that the measured frequency does not only depend on the deposited mass, but also on the temperature of the crystal and the electronics. In fact, the resonance frequency is very sensitive to temperature changes and for the most accurate measurements (accuracy: few $10^{-6}\,\frac{\mu\mathrm{g}}{\mathrm{cm^2 s}}$) a temperature stabilization to ±0.02°C is necessary. This was achieved by heating the microbalance to 50°C and compensating the heat flux to the colder chamber wall by regulating the heating. Furthermore, the electronics of the microbalance and the temperature stabilization have to be in a temperature-controlled environment as well. Without these measures, the most prominent signal would stem from the room temperature oscillations due to the cooling cycles of the air conditioning. In order to reach a constant temperature, the stabilization needs to work for a couple of hours. Especially after a bake-out cycle, several hours are required until the system is ready for measurements.

The software to operate the microbalance is not compatible with Windows 7 or higher and therefore runs on a virtual machine. The built-in live visualization of the deposition rate does not work very well, especially with the very low deposition rates present in typical experiments on this machine. To overcome this limitation, a MATLAB-code copies the live-stored measurement data and computes and displays the deposited mass as well as the deposition rate.
When conducting measurements, care has to be taken that the microbalance is correctly positioned (xyz-manipulator). The correct position can be checked by using the telescope on the beam axis: the borehole in the center of the back side of the microbalance should lie on the cross hairs. For the alignment procedure of the rest of the apparatus, the microbalance has to be moved out of the beam line (see section 8.1).

Metal nanoparticles deposited on the crystal do not desorb, limiting the life-time of a crystal. If the software indicates that the life-time of the crystal comes to its end or a clean surface is desired, the crystal can be changed (see manual of the microbalance).

7.6 Vacuum Transfer System

When dealing with reactive samples and in order to guarantee clean surfaces, exposure to ambient air must be avoided. Ideally, the samples which are produced under UHV-conditions in our machine, should be kept in UHV during the transport from our lab to the diagnostics (*e.g.* scanning probe microscope on the University of Graz). For this task, a commercially available system was purchased from Ferrovac, consisting of a chamber fitted with the pumping system, a wobblestick with pincers, a storage shelf for samples and a suitable gate valve at the connecting flange.
For the transport, a pumping system with low energy consumption is required in order to be able to run the system on battery power. Furthermore, a system without moveable parts (in case of mechanical shocks) is beneficial. Both of these key points are satisfied using a non-evaporable getter (NEG) in combination with an ion getter pump. Thereby, the NEG, which simply adsorbs gas-atoms and -molecules, does not need electrical power. The fact that the NEG is only suitable for certain gas species (especially H_2O, N_2, O_2 and H_2) and cannot adsorb other species (*e.g.* rare gases, CH_4) makes the battery powered ion getter pump necessary. In principle, an ion getter pump alone would also be possible, but in combination with the NEG,

the size and energy consumption of the ion getter pump can be drastically reduced which is essential for this purpose. In the purchased configuration, the pumping system can operate for 3 days using only battery power.

In order to reduce the gas load for the pumping system the linear movements of wobblestick and sample storage shelf are realized without feedthroughs, using magnetic coupling between a ring on the outside and a piston on the inside which guarantees leak-tight sealing. Additionally, an evacuated buffer volume is connected to the the atmosphere-side of the gate valve during transport, which reduces the permeation through the rubber-sealed gate valve to a minimum.

For the transfer of samples from the respective apparatus into the UHV-suitcase, a third chamber (lock chamber (LC)) is needed. While the apparatus and the suitcase are maintained under UHV all the time, the LC is installed between them and will be pumped down or vented in order to connect or disconnect the suitcase to or from the apparatus. For the pumping of the LC a HiPace80 turbo-pump backed by an ACP15 multi-Roots fore pump is used. This system reaches a background pressure in the 10^{-10} mbar regime, which is sufficient for all purposes this system is designed for.

A summary of the operating instructions, including all the information needed for regular operation of the device, is attached in appendix F. For extra information consult the manual of the suitcase or the manual of the pumping system.

8 Settings and Typical Readings

8.1 Beam Alignment

A proper alignment of all components of the apparatus along the beam axis is crucial for the success of any experiment. Thereby, the position of the beam is given by the position of the first skimmer, which defines the placement of all other components. For the first alignment of all chambers, a piece of string was connected to the center of the flange-plate on which the skimmer is mounted (reference flange). Using a water level and an engineer's square the string was oriented horizontally, orthogonally to the reference flange. With the string as guidance, the two following vacuum chambers as well as a telescope for optical control of the beam path were installed. Once the telescope was set up, the cross hairs of the telescope could be used to control the position of all further components.

The telescope is shared with other labs and therefore has to be repositioned every now and then. Assuming that the positions of both skimmers in the apparatus do not change, the position of the telescope can be restored by adjusting its tilt as well as its position orthogonal to the beam such, that the cross hairs can be pointed at the center of both skimmers when only changing the focal plane. If this is the case, the optical axis of the telescope coincides with the beam axis defined by the skimmers.

If the telescope is correctly aligned, the flange-plate with the first skimmer mounted on it can be removed in order to see and position the nozzle. Besides positioning the nozzle opening on the beam axis, the nozzle plate has to be oriented parallel to the skimmer-flange and the nozzle axis has to be horizontal. Once the nozzle is positioned, the flange-plate with skimmer can be mounted again, using the cross-hairs to find the correct position.

While the parts described so far do not move under normal circumstances, the pickup cells along the beam are changed regularly to switch dopants, to refill them or for maintenance. Therefore, these elements have to be aligned much more often. To do so, at first the position of the telescope is controlled by focussing on both skimmers. Then, reinstall the pickup cell, including the electrical wiring and the cooling water pipes (connecting these afterwards may displace the cell again). Using the adjusting screws, the beam-entry and -exit opening of the pickup cell can be positioned on the beam axis.

Without additional lighting the apertures for the beam are hard to recognize and distinguish when looking through the telescope. The method of choice is to illuminate the respective apertures with different colored LEDs while adjusting. This way the contour lines of the orifices should be clearly visible and the color indicates to which orifice the focal plane is set.

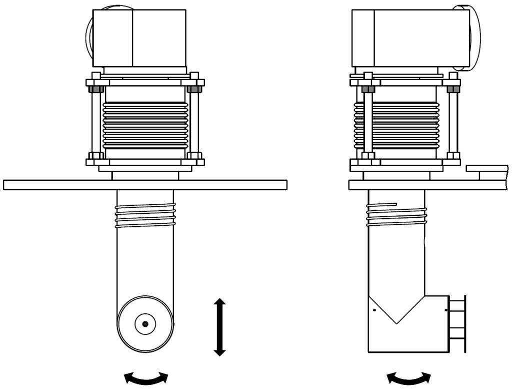

Figure 8.1: Schematics illustrating the adjustment of the nozzle. The left image shows the adjustment of the nozzle position. The tilt shown in the right image must be zero, *i.e.* the beam axis must be horizontal.

8.2 Typical Settings of the Time of Flight Mass Spectrometer

The following tables contain optimized settings for the TOFMS, determined by Johannes Steurer within the course of his master's thesis.

Table 8.1: TOFMS settings used in this thesis to obtain mass spectra of doped or bare He droplets up to a mass $< 7000\,\mathrm{u}$. The given values, especially the ones for the deflection unit, correspond to the ones set directly at the TOFMS power supply, not the ones read in by the analog-to-digital converter (ADC).

Ion source	
Filament current	2.1 - 2.2 A
electron energy	89 eV
resulting electrometer current	in the range of 1 ¯A
Voltage settings	
HV settings	#3 (see TOF-manual) → last- and central grid alternately adjusted for best resolution
repeller offset	0
mass filter	off
deflect-x	5.5
deflect-y	5.5
MCP	2.3 - 2.5 kV depending on the mass of interest
Post acceleration	20 kV
Pulse generator	
repetition frequency	10 kHz
duration e-beam	1 ¯s
delay ion extraction / ionisation	0 ¯s
duration ion extraction	2.4 ¯s
duration mass filter	no influence if the mass filter is off
Fast Multiscaler	
number of sweeps	$2 \cdot 10^4$ - several millions
range	$2.8 \cdot 10^5$ (for a bin width of 1)
bin width	1 - 2
Start/Stop Disc.	0.3/-0.15

8.3 Settings / Operating Instructions for the QMS

The quadrupole mass spectrometer installed on this machine is a Balzers Prisma QME 200, controlled by the Quadstar 7.0.3-Software. This software is old and only the "Measure" program, which operates the QMS and displays the signals, works under Windows 7 without problems. Usually, this device is used to gain qualitative data (*i.e.* if there is a signal at a specific mass or not), quantitative statement can be made in terms of ratios (*e.g.* helium signal with and without doping). The comparison of different QMS-measurements is difficult due to their dependance on the vacuum conditions and the position of beam blocking elements such as the microbalance and the TEM-substrate holder.

The QMS can be switched on by the I/O - switch on the power supply cable. After that, the software ("QMS Measure"-icon on the desktop) can connect with the detector. Setup → SEM / Emission Control opens a window with two check-boxes which switch on the emission current and the secondary electron multiplier (SEM). The SEM voltage is normally set to **2000 V**. Usually, a drift of the signal intensity occurs during the first half hour of operation, afterwards, the signals are stable. There are two typical modes for measurements: "Analog" and "Versus Time". The former shows a mass spectrum and the latter the evolution of the signal of a specific mass with time. For both modes there are templates available (Scan → Analog → test.sap and MID → Versus Time → he4.mip). After loading one of these templates, the settings can be changed by Parameters → Setup and more importantly Parameters → Channel. In both cases, the changes made in the new windows are saved to the template (!) and activated after closing

Table 8.2: TOFMS settings used in this thesis to obtain mass spectra of doped or bare He droplets for big masses up to about 25000 u. The given values, especially the ones for the deflection unit, correspond to the ones set directly at the TOFMS power supply, not the ones read in by the ADC.

Ion source	
Filament current	2.3 - 2.4 A
electron energy	89 eV
resulting electrometer current	15 - 20 ¯A
Voltage settings	
HV settings	#1 (see TOF-manual) → last- and central grid alternately adjusted for best resolution ($U_{\text{centralgrid}} = 2.25\,\text{kV}$, $U_{\text{lastgrid}} = 1.08\,\text{kV}$)
repeller offset	5.2
mass filter	250 V
deflect-x	5.75
deflect-y	5.6
MCP	2.7 kV
Post acceleration	20 kV
1^{st} aperture	2.7
Pulse generator	
repetition frequency	4 kHz
duration e-beam	20 ¯s
delay ion extraction / ionisation	0 ¯s
duration ion extraction	6 ¯s
delay mass filter / ion extraction	1 ¯s
duration mass filter	3 ¯s
Fast Multiscaler	
number of sweeps	$5 \cdot 10^5$ - 10^7
range	$2 \cdot 10^5$
bin width	4
Start/Stop Disc.	0.3/-0.15

the windows.

Before switching off the device (I/O - switch on the power supply cable) the SEM voltage and emission current should be turned off by the software (Setup → SEM / Emission Control).

Extensive information on Quadstar can be found in the printed manual (white folder) as well as in the help file "Quadstar 32-bit.chm".

A Engineering Drawings

The following pages contain engineering drawings of the most important home-made parts needed for the buildup of the apparatus, which are:

The new nozzle,

the resistive pickup cells,

the modifications on the measurement chamber in order to enable laser ionization for the TOFMS

Besides the drawings here, 3D-CAD constructions for the whole apparatus are available on the laboratory computer. These CAD-constructions were conducted using ProEngineer Wildfire, for which the university has a license.

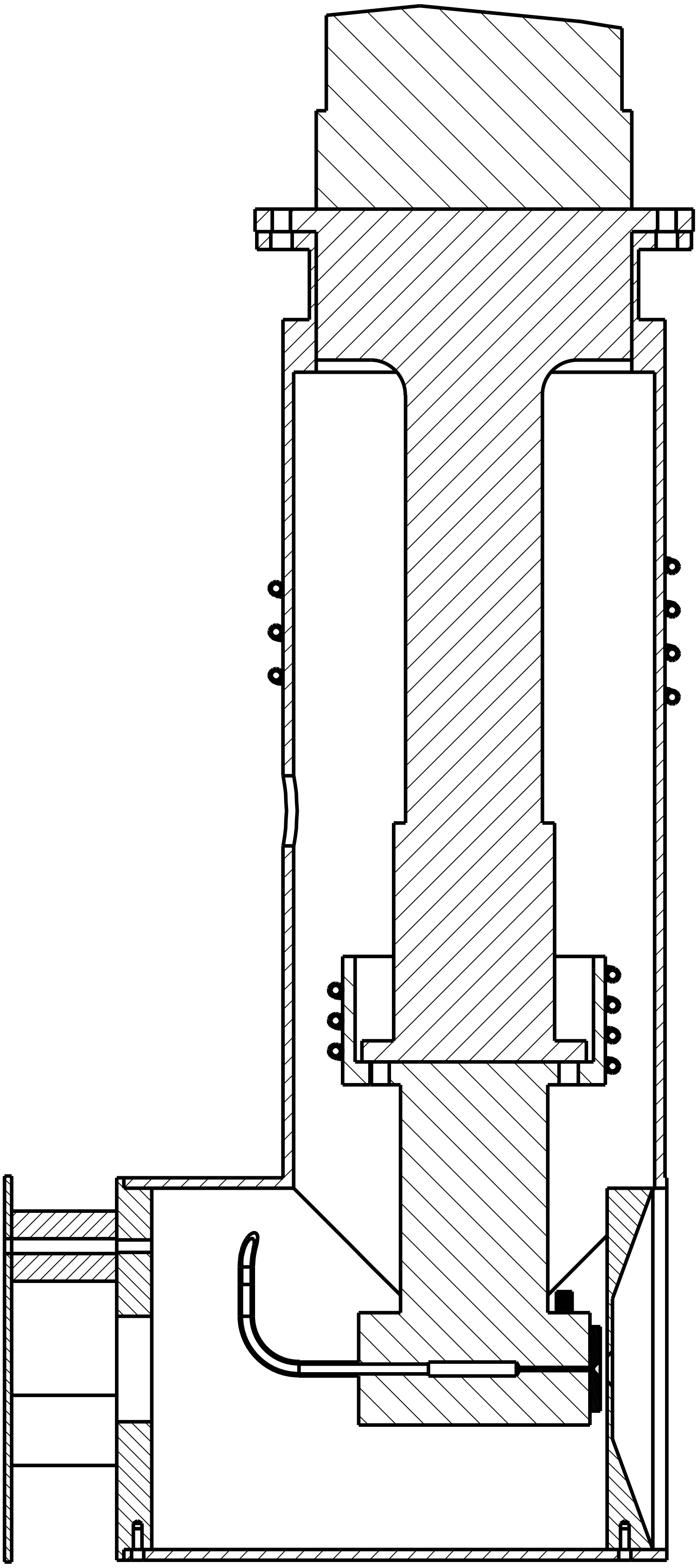

Bemerkung :		Name	Datum	Werkstoff:
	Gez.	Thaler	28-Aug-15	Rohmass:
	Gepr.	–	–	Gewicht: Kg

Zust.	Aenderung	Datum	Name

TUG

Benennung

Nozzle Setup

Dateiname : ASSEMBLY.QUELLKAMMER

Masstab: 1:2

Blatt: 1 von 2

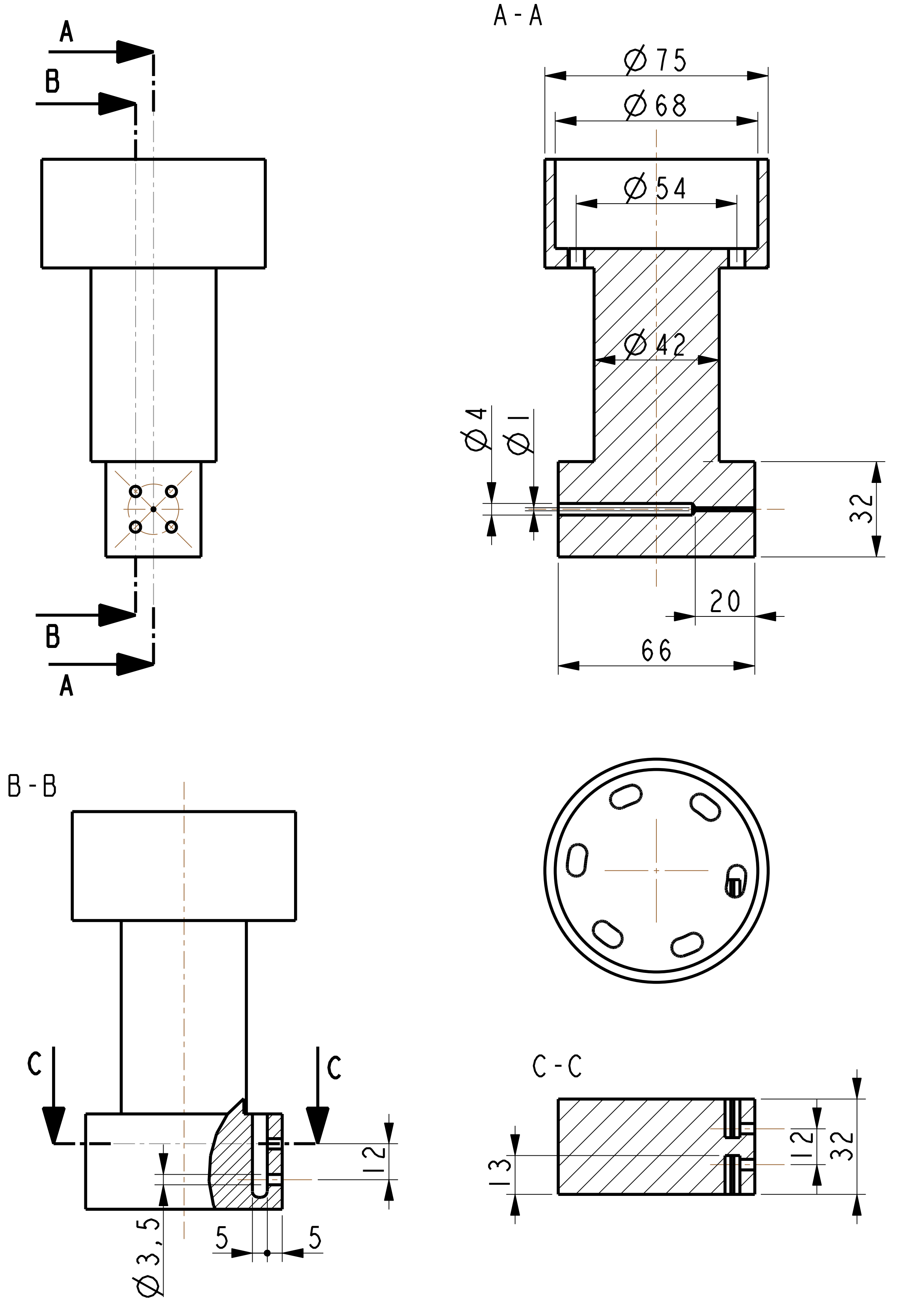

Bemerkung :		Name	Datum	Werkstoff:	Kupfer
	Gez.	Thaler	26-Feb-14	Rohmass:	**Durchm. 80mm**
	Gepr.	-	-	Gewicht:	Kg

Zust.	Aenderung	Datum	Name

TUG

Benennung

Duese

Dateiname : CONNECTION.FUER.ZEICHNUNG

Masstab: **1:2**

Blatt: **1** von **1**

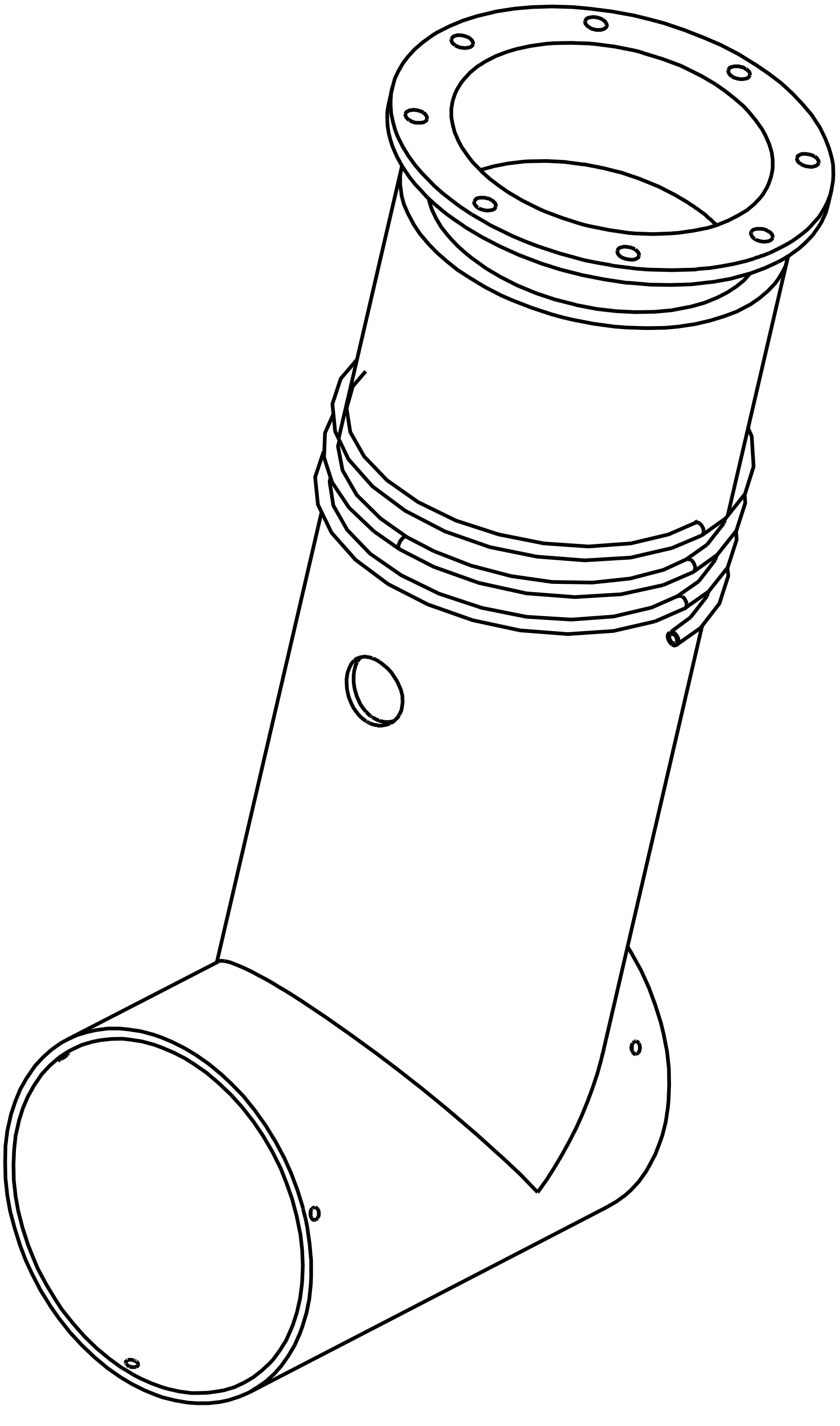

Bemerkung :		Name	Datum	Werkstoff:	**Kupfer**
	Gez.	Thaler	27-Feb-14	Rohmass:	
	Gepr.	-	-	Gewicht:	Kg

					Benennung	
				TUG	**T-Shield**	
					Dateiname :	Masstab: **1:2**
Zust.	Aenderung	Datum	Name		**T_SHIELD**	Blatt: **1** von **1**

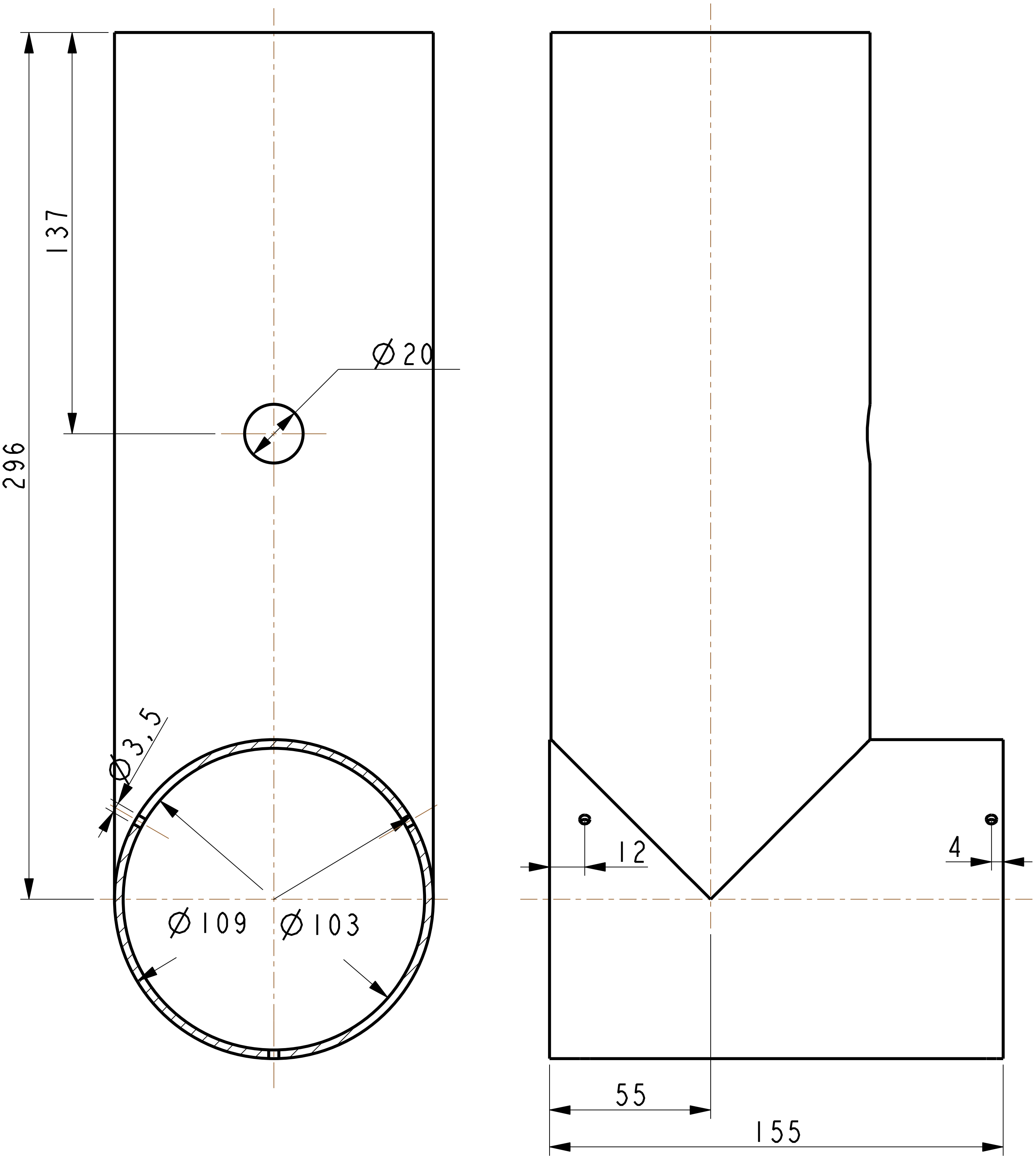

		Name	Datum	Werkstoff:	**Kupfer**
Bemerkung :	Gez.	Thaler	26-Feb-14	Rohmass:	**Rohr, D_innen : 103mm**
	Gepr.	-	-	Gewicht:	Kg

Zust.	Aenderung	Datum	Name

TUG

Benennung

Shield-Tubes

Dateiname :

SHIELD_TUBES

Masstab **0,200**

Blatt: **1** von **1**

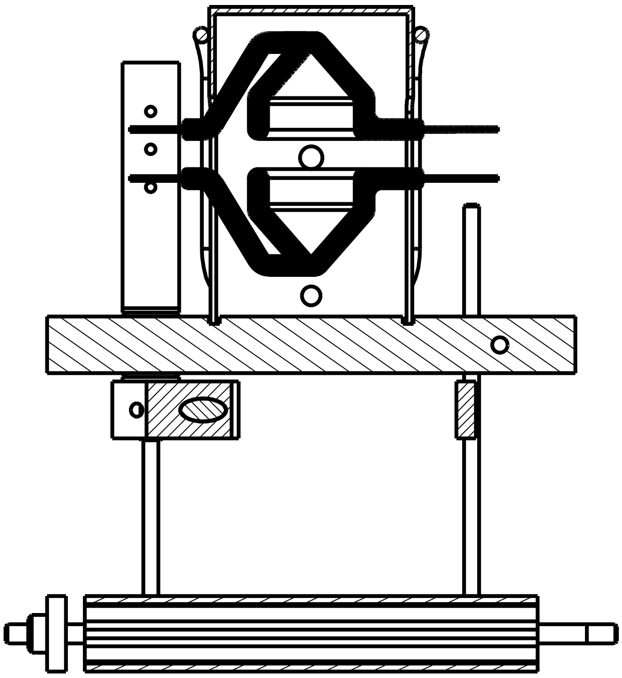

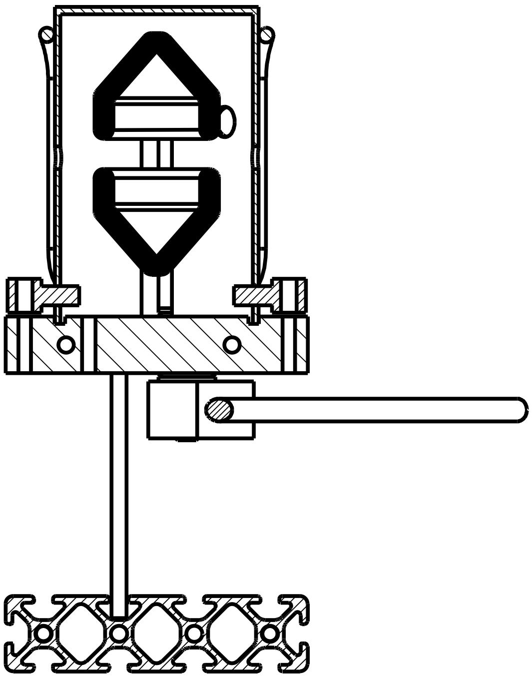

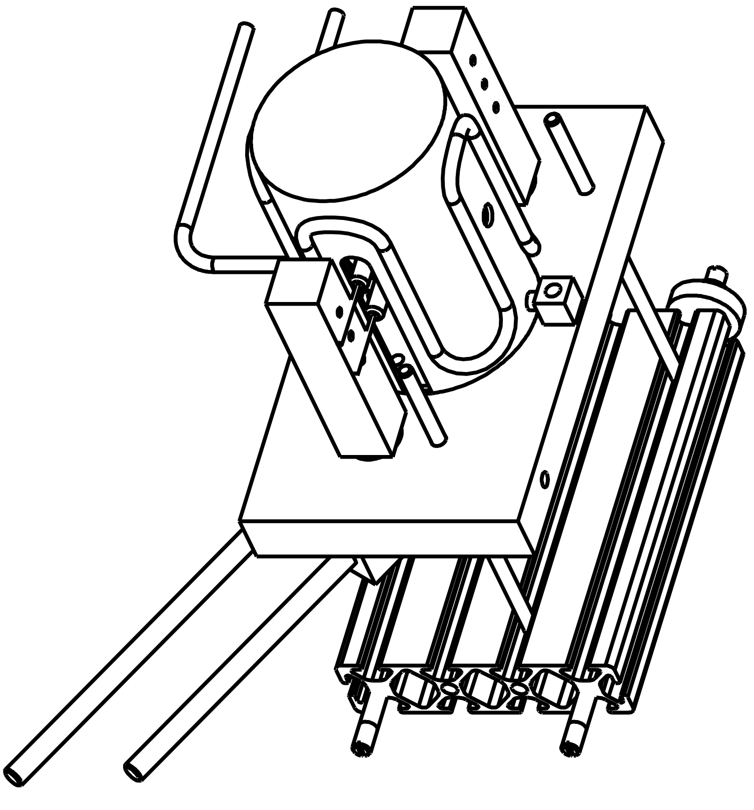

		Name	Datum	
Bemerkung :		Name	Datum	Werkstoff:
	Gez.	Thaler	28-Aug-15	Rohmass:
	Gepr.	–	–	Gewicht: Kg

				TUG	Benennung **resistive Quelle**
					Dateiname : **RESISTIVE_QUELLE_PUC5**
Zust.	Aenderung	Datum	Name		Masstab: **1:2** Blatt: **1** von **1**

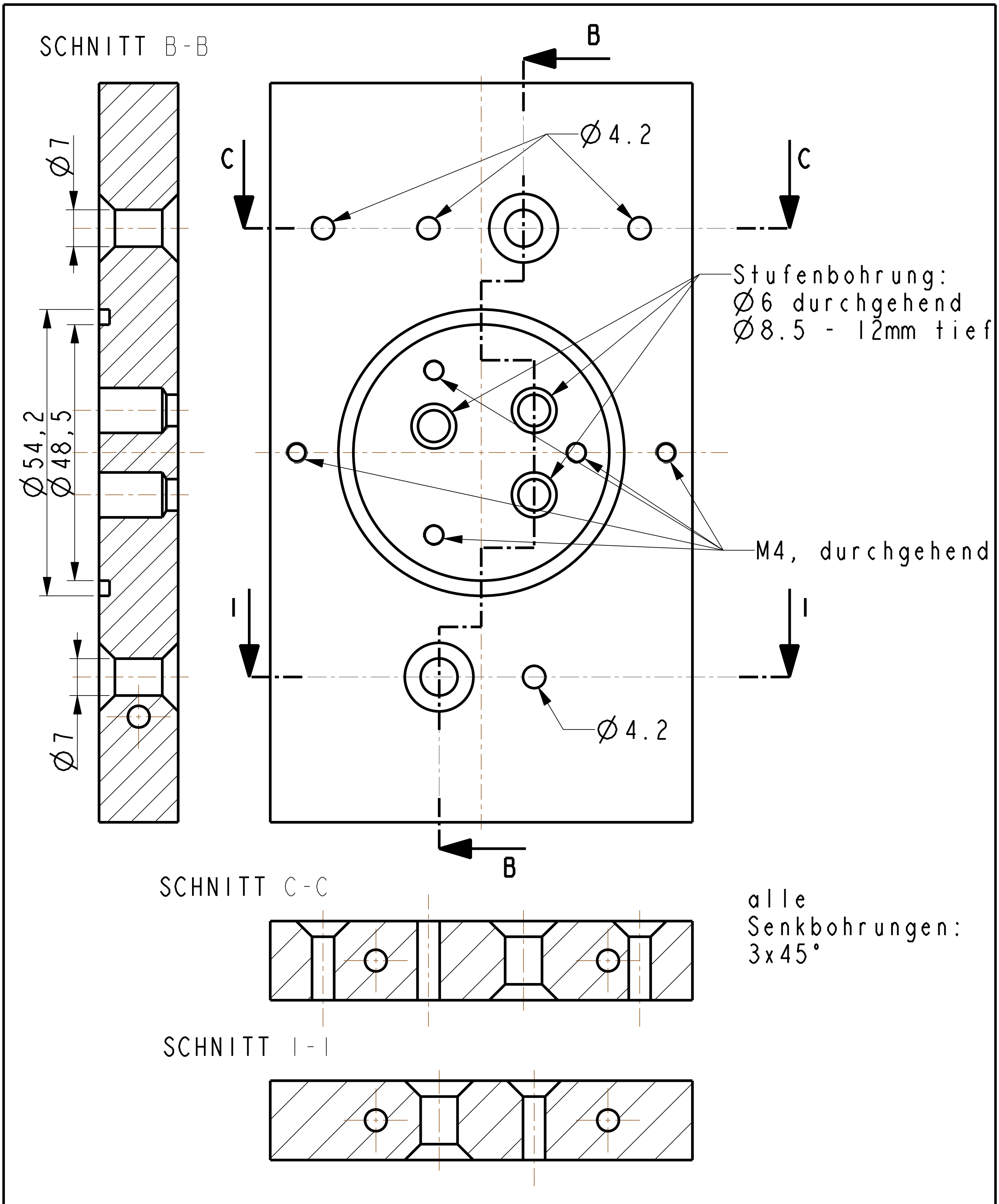

Bemerkung :		Name	Datum	Werkstoff:	**Kupfer**
	Gez.	Thaler	29-Jun-12	Rohmass:	
	Gepr.	–	–	Gewicht:	Kg

				TUG	Benennung **Baseplate**
					Dateiname : **HQ_BASEPLATE**
Zust.	Aenderung	Datum	Name		Masstab: **1 : 1** Blatt: **1** von **1**

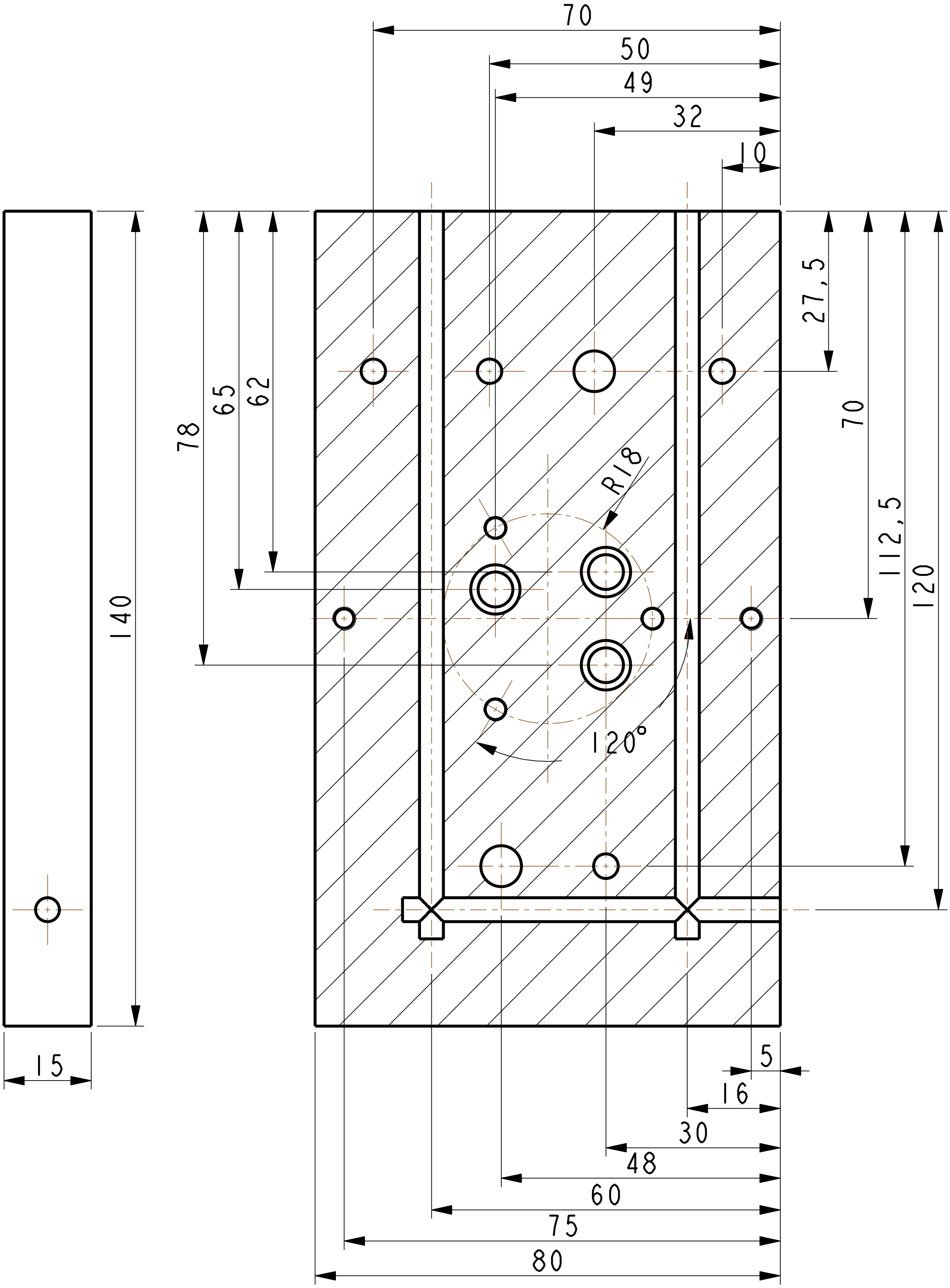

		Name	Datum	Werkstoff:	**Kupfer**
Bemerkung :	Gez.	Thaler	29-Jun-12	Rohmass:	
	Gepr.	-	-	Gewicht:	Kg

Zust.	Aenderung	Datum	Name

TUG

Benennung

Grundplatte Verdampferquellen

Dateiname :
HQ_BASEPLATE

Masstab: **1 : 1**

Blatt: **1** von **1**

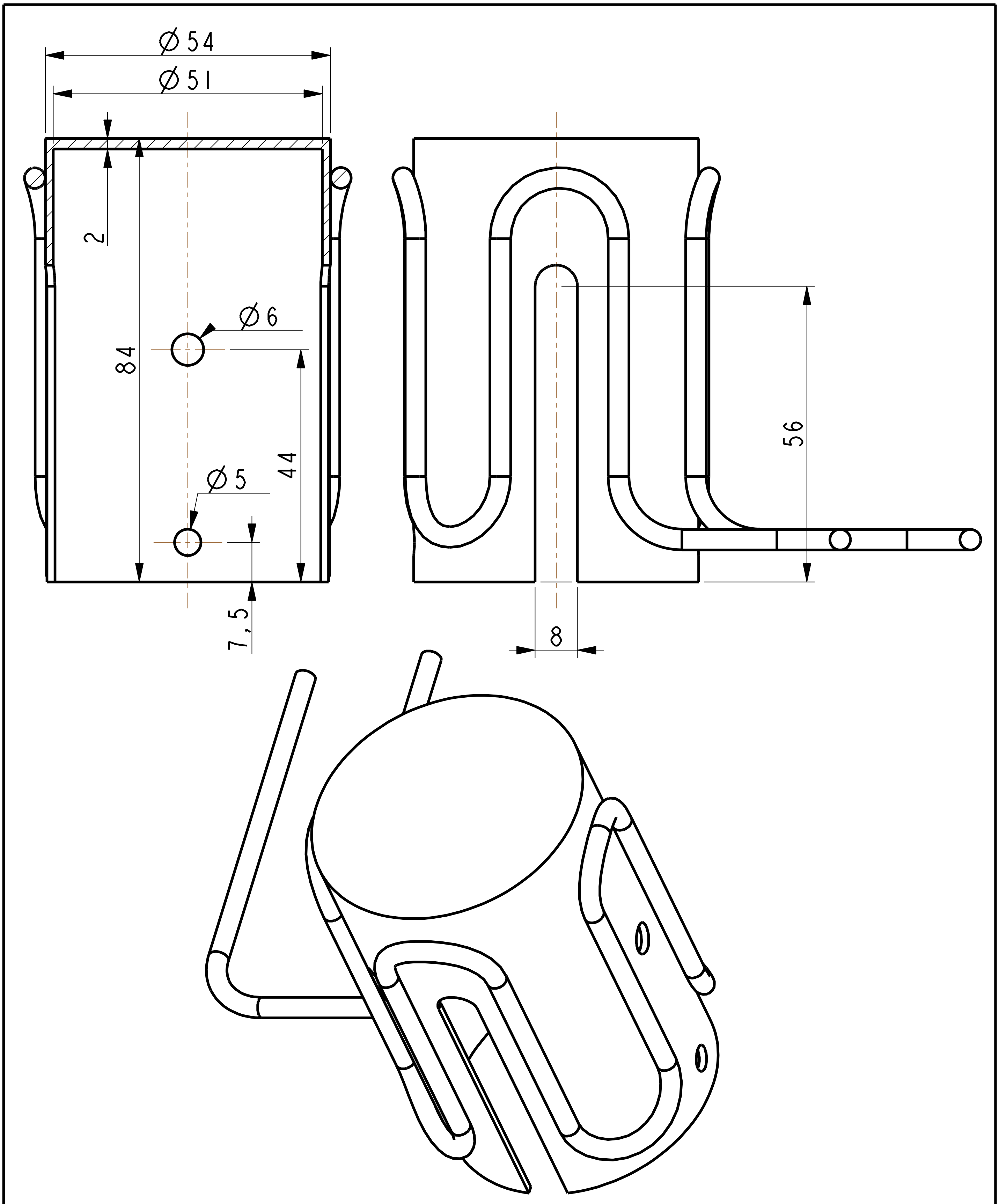

Bemerkung :		Name	Datum	Werkstoff:	**Kupfer**
	Gez.	Thaler	28-Aug-15	Rohmass:	
	Gepr.	-	-	Gewicht:	Kg

Zust.	Aenderung	Datum	Name

TUG

Benennung

Kühlschild hoch

Dateiname : RESISTIVE.SOURCE.SHIELD.PUC5

Masstab: 1:1

Blatt: 1 von 1

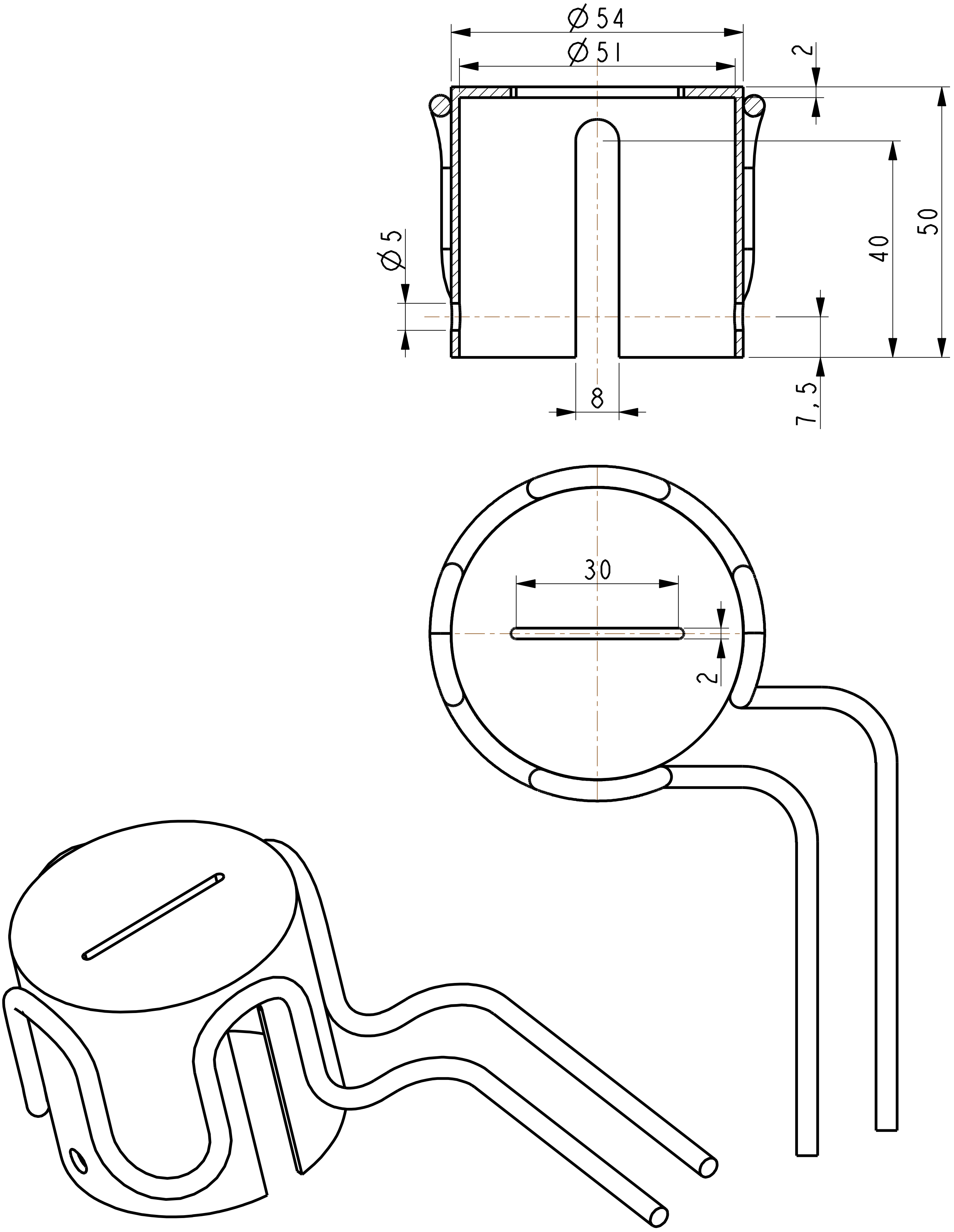

Bemerkung :		Name	Datum	Werkstoff:	**Kupfer**
	Gez.	Thaler	29-Jun-12	Rohmass:	
	Gepr.	–	–	Gewicht:	Kg

TUG

Benennung

Kühlschild

Zust.	Aenderung	Datum	Name

Dateiname : **HQ_SHIELD_2**

Masstab: **1 : 1**

Blatt: **1** von **1**

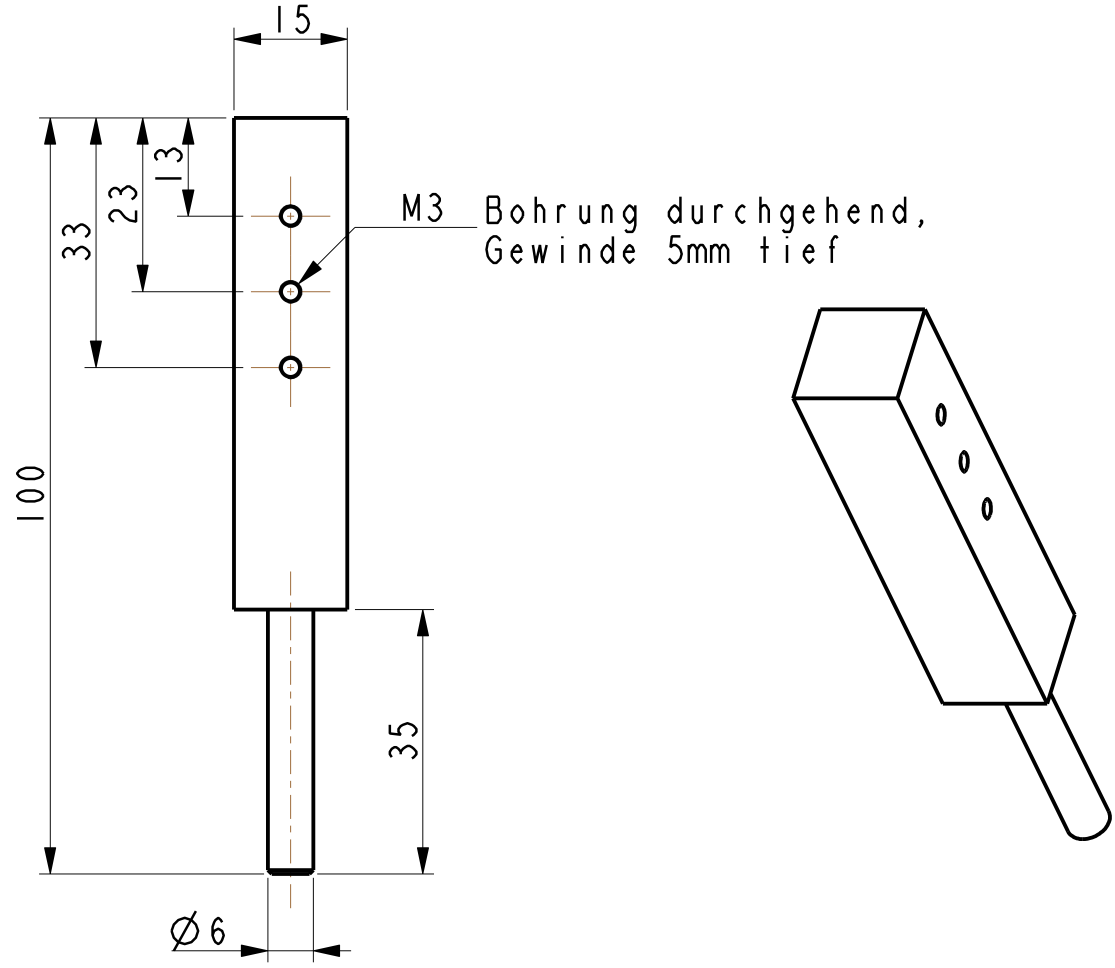

Bemerkung :		Name	Datum	Werkstoff:	**Kupfer**
	Gez.	Thaler	29-Jun-12	Rohmass:	
	Gepr.	-	-	Gewicht:	Kg

				TUG	Benennung **Säule RS**
					Dateiname : **SAEULE**
Zust.	Aenderung	Datum	Name		Masstab: **1 : 1** Blatt: **1** von **1**

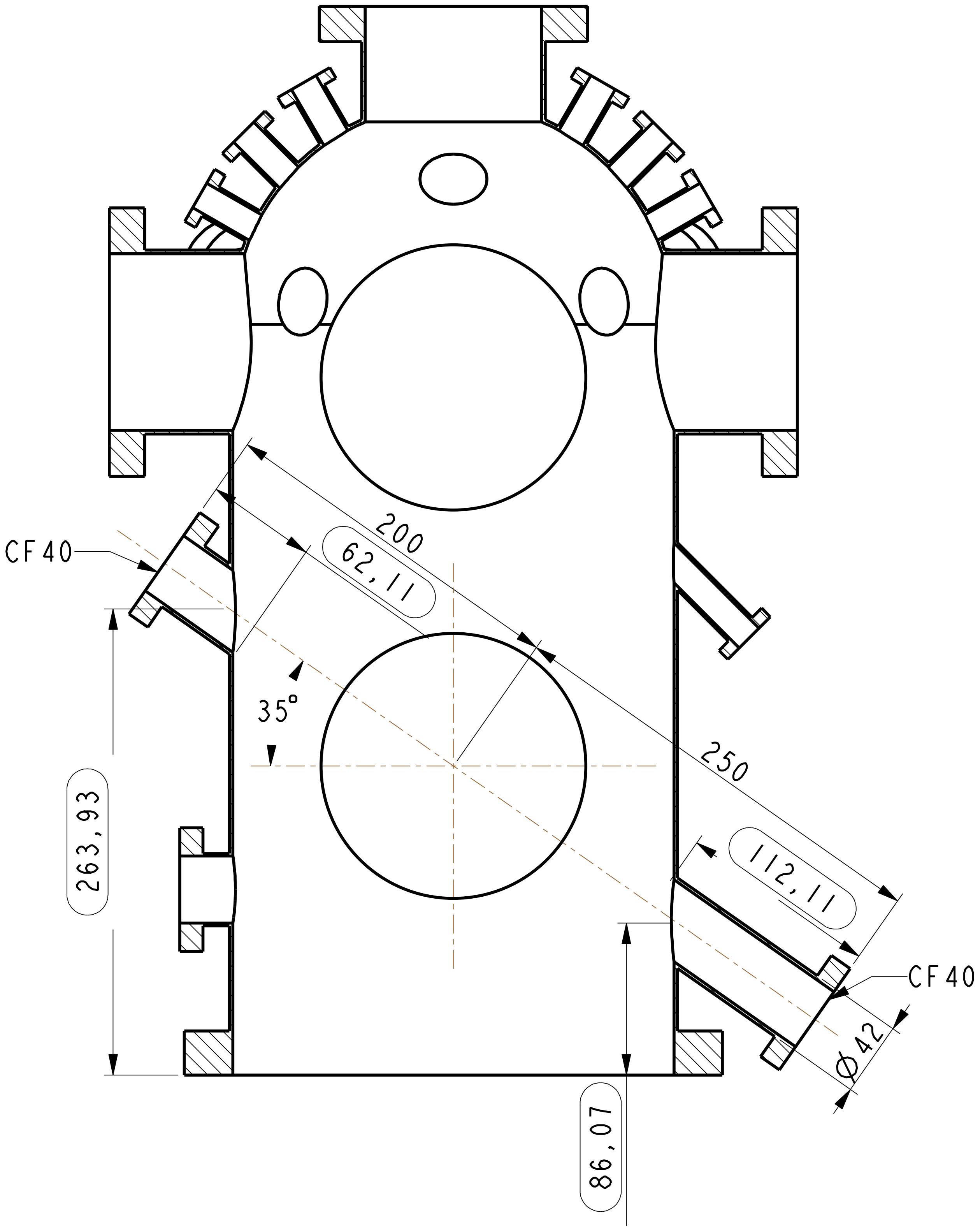

Bemerkung :

	Name	Datum
Gez.	Thaler	08-Jan-13
Gepr.	-	-

Werkstoff:

Rohmass:

Gewicht: Kg

Zust.	Aenderung	Datum	Name

TUG

Benennung

Umbau: Messkammer

Dateiname :

MESSKAMMER.UMBAU

Masstab: **1 : 3**

Blatt: **1** von **1**

B Helium Flux and Droplet Size

For the production of clusters/nanoparticles with a desired size distribution, it is essential to set the adequate droplet size distribution. This is accomplished by setting the expansion conditions accordingly, following the table below, which is reprinted with permission from Gomez, L.F. *et. al.*, "Sizes of large He droplets" JCP 135.15 (2011): 154201. Copyright 2011, AIP Publishing LLC.

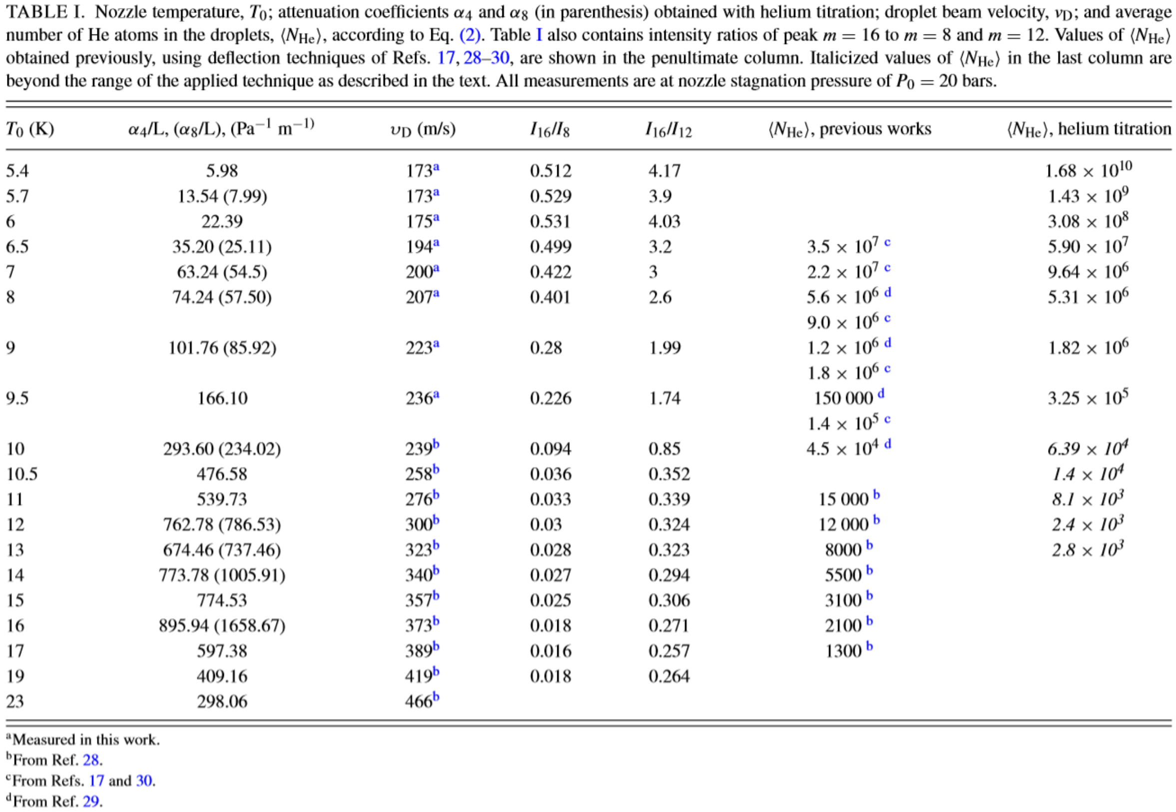

TABLE I. Nozzle temperature, T_0; attenuation coefficients α_4 and α_8 (in parenthesis) obtained with helium titration; droplet beam velocity, v_D; and average number of He atoms in the droplets, $\langle N_{He} \rangle$, according to Eq. (2). Table I also contains intensity ratios of peak $m = 16$ to $m = 8$ and $m = 12$. Values of $\langle N_{He} \rangle$ obtained previously, using deflection techniques of Refs. 17, 28–30, are shown in the penultimate column. Italicized values of $\langle N_{He} \rangle$ in the last column are beyond the range of the applied technique as described in the text. All measurements are at nozzle stagnation pressure of $P_0 = 20$ bars.

T_0 (K)	α_4/L, (α_8/L), (Pa^{-1} m$^{-1)}$	υ_D (m/s)	I_{16}/I_8	I_{16}/I_{12}	$\langle N_{He} \rangle$, previous works	$\langle N_{He} \rangle$, helium titration
5.4	5.98	173[a]	0.512	4.17		1.68×10^{10}
5.7	13.54 (7.99)	173[a]	0.529	3.9		1.43×10^{9}
6	22.39	175[a]	0.531	4.03		3.08×10^{8}
6.5	35.20 (25.11)	194[a]	0.499	3.2	3.5×10^{7} [c]	5.90×10^{7}
7	63.24 (54.5)	200[a]	0.422	3	2.2×10^{7} [c]	9.64×10^{6}
8	74.24 (57.50)	207[a]	0.401	2.6	5.6×10^{6} [d] 9.0×10^{6} [c]	5.31×10^{6}
9	101.76 (85.92)	223[a]	0.28	1.99	1.2×10^{6} [d] 1.8×10^{6} [c]	1.82×10^{6}
9.5	166.10	236[a]	0.226	1.74	150 000 [d] 1.4×10^{5} [c]	3.25×10^{5}
10	293.60 (234.02)	239[b]	0.094	0.85	4.5×10^{4} [d]	$\mathit{6.39 \times 10^{4}}$
10.5	476.58	258[b]	0.036	0.352		$\mathit{1.4 \times 10^{4}}$
11	539.73	276[b]	0.033	0.339	15 000 [b]	$\mathit{8.1 \times 10^{3}}$
12	762.78 (786.53)	300[b]	0.03	0.324	12 000 [b]	$\mathit{2.4 \times 10^{3}}$
13	674.46 (737.46)	323[b]	0.028	0.323	8000 [b]	$\mathit{2.8 \times 10^{3}}$
14	773.78 (1005.91)	340[b]	0.027	0.294	5500 [b]	
15	774.53	357[b]	0.025	0.306	3100 [b]	
16	895.94 (1658.67)	373[b]	0.018	0.271	2100 [b]	
17	597.38	389[b]	0.016	0.257	1300 [b]	
19	409.16	419[b]	0.018	0.264		
23	298.06	466[b]				

[a] Measured in this work.
[b] From Ref. 28.
[c] From Refs. 17 and 30.
[d] From Ref. 29.

Besides the droplet size also the total He-flux changes with the nozzle temperature, which can be seen in the following graph.

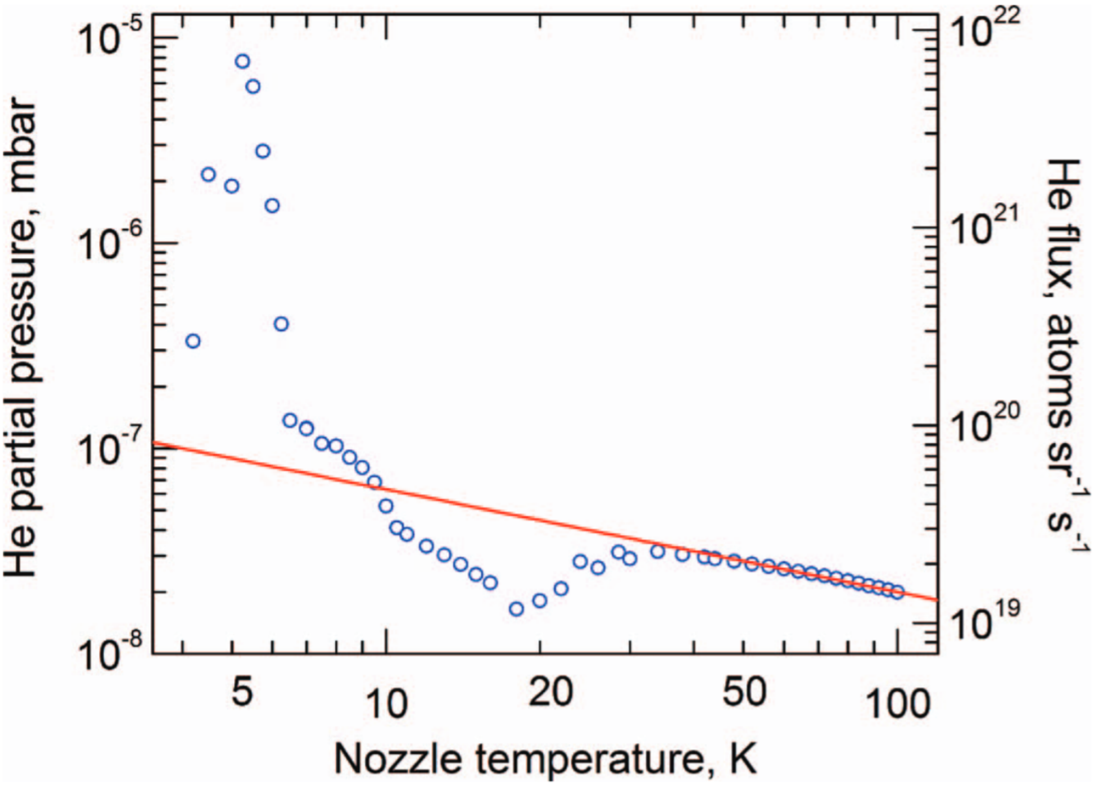

Figure B.1: Temperature dependent He flux through a cooled nozzle (5 μm diameter) at 20 bar stagnation pressure. The red line symbolizes the theory for free jet expansion, which is no longer valid below $\approx$ 30 K. This graph is reprinted with permission from Gomez, L.F. *et. al.*, "Sizes of large He droplets" JCP 135.15 (2011): 154201. Copyright 2011, AIP Publishing LLC.

C Vapor Pressure Diagrams

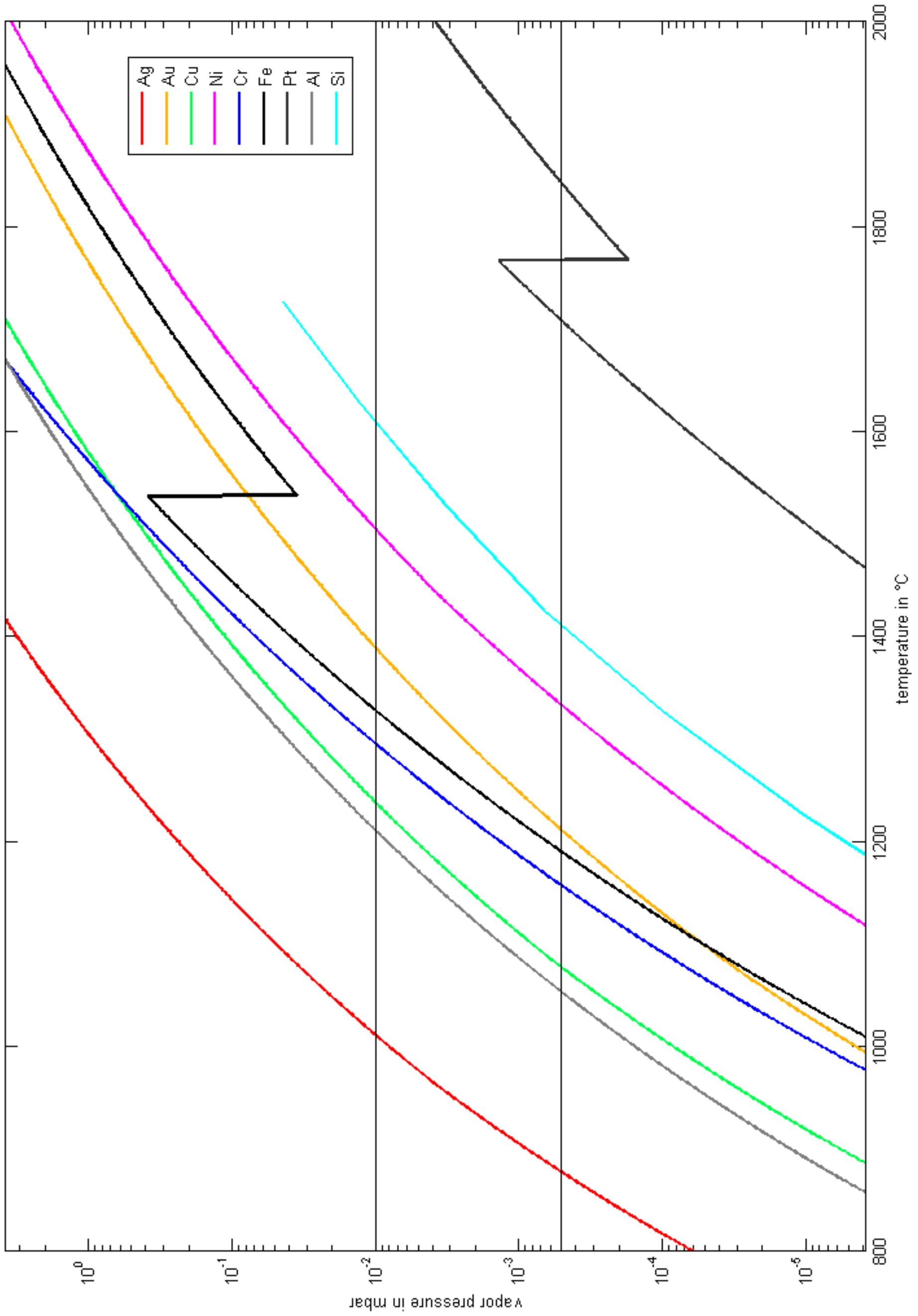

Figure C.1: Temperature dependent vapor pressures for various materials (data taken from [1])

---

[1] D.R. Lide, Handbook of Chemistry and Physics

D Time of Flight - Checklist

Updated: May 2015

Checklist TOF

Start Up:

- Set the TOF-switch on the control-panel to “auto” (power supply) ☐
- Check pressure in TOF (≤ $5 \cdot 10^{-6}$mbar for 3 hours) and turn off the gauge ☐
- Check if preamplifier is disconnected ☐
- Turn the PC on, start the software ☐
- Check if the HV control knobs for MCP, post acc., liner and lens are at min. ☐
- Turn on the HV control units ☐
- Heat up the filament (-70eV and 2.2A as starting values), turn on the pulse generator, check the electrometer current (≥ µA) ☐
- Slowly increase the HV to operating conditions (values see table in manual) ☐
- Connect preamplifier ☐
- Optimize e.g. the OH peak (adjust central grid, deflection) ☐
- Calibrate / check calibration (are the residual gas peaks at the right positions?) ☐
- Measure ☐

Shut Down:

- Stop measurement, turn off pulse generator, turn off filament ☐
- Turn down HV for MCP, post acc., liner, lens, repeller and extraction ☐
- Turn off the HV control units, shut down the PC ☐
- Disconnect preamplifier ☐
- Turn on the pressure gauge ☐
- Set the TOF-switch on the control-panel to “off” (power supply) ☐

E Reference: TOF Mass Spectra

The following pages contain exemplary spectra obtained on this machine in different experiments, each followed by a page listing the corresponding TOFMS settings.

The first spectrum shows a measurement of Xe-gas ($1.5 \cdot 10^{-6}$ mbar). Both singly and doubly ionized species are visible in the spectrum.

The second spectrum shows a measurement of undoped helium droplets at 8.0 K nozzle temperature and 20 bar stagnation pressure. In this measurement, the He_N-comb is visible until ≈ 500 amu. The missing signal below ≈ 40 amu is caused by the mass filter, which kicks out the frequently occurring light ions in order to avoid saturation of the detector. The zoomed spectrum nicely shows that there is no other significant signal except for the He_N.

The third spectrum shows a measurement of silver doped helium droplets at 9.5 K nozzle temperature and 20 bar stagnation pressure. In this measurement not only bare silver clusters (Ag_n) but also silver clusters with 1-3 H_2O molecules attached ($Ag_n(H_2O)_m$) can be seen, as well as the typical multinomial peak distribution at a specific Ag_n, which is caused by the different naturally occurring silver isotopes.

The fourth spectrum shows a measurement of gold doped helium droplets at 9.0 K nozzle temperature and 20 bar stagnation pressure. In contrast to many other elements, gold possesses only a single stable isotope and hence, a specific Au_n only yields a single peak in the mass spectrum. The small peaks in the zoomed spectrum belong to bare He_N. Additionally, a very small signal can be seen at (Au_3He_m with m = [1, 2, 3]).

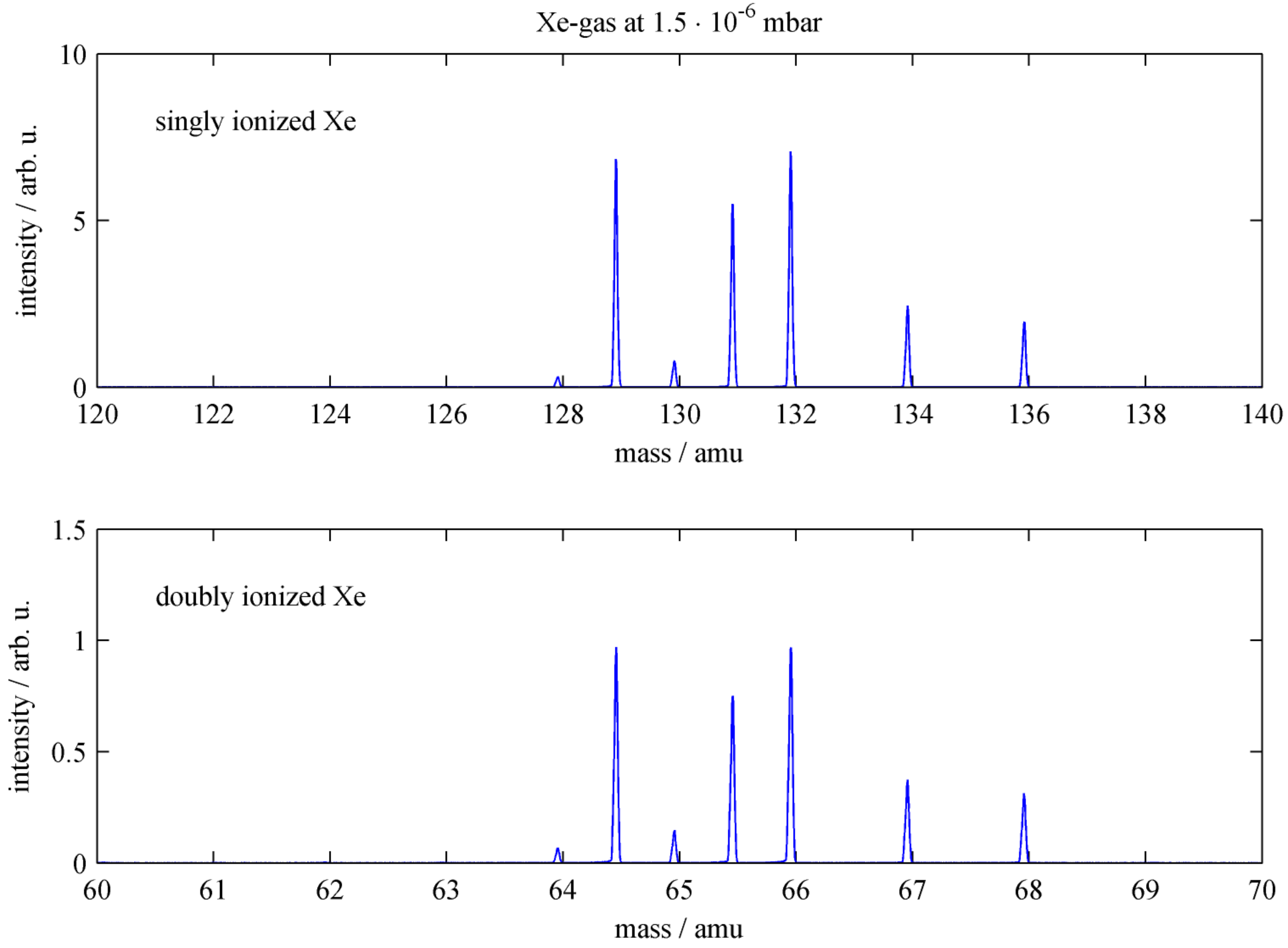
Xe-gas at 1.5 · 10^-6 mbar
singly ionized Xe
intensity / arb. u.
10
5
0
120
122
124
126
128
130
132
134
136
138
140
mass / amu
doubly ionized Xe
intensity / arb. u.
1.5
1
0.5
0
60
61
62
63
64
65
66
67
68
69
70
mass / amu

Xe - spectrum

bin width=1,000000

sweeps=2000000,000000

time resolution (ps)=250,000000

electron energy (eV)=70,00

frequency (Hz)=10000

duration electron beaml[µs]= 1,000

delay ion extraction / ionisation[µs]= 0,000

duration ion extraction[µs]= 2,000

heating current=2,011450

electrometer current=0,319989

emission current=0,151001

repeller=2,831053

extraction=2,817410

postacceleration=19,911194

MCP=2,204163

last_grid=0,337158

central_grid=0,890808

lens=2,968750

liner=3,015137

deflect_X(+)=2,962036

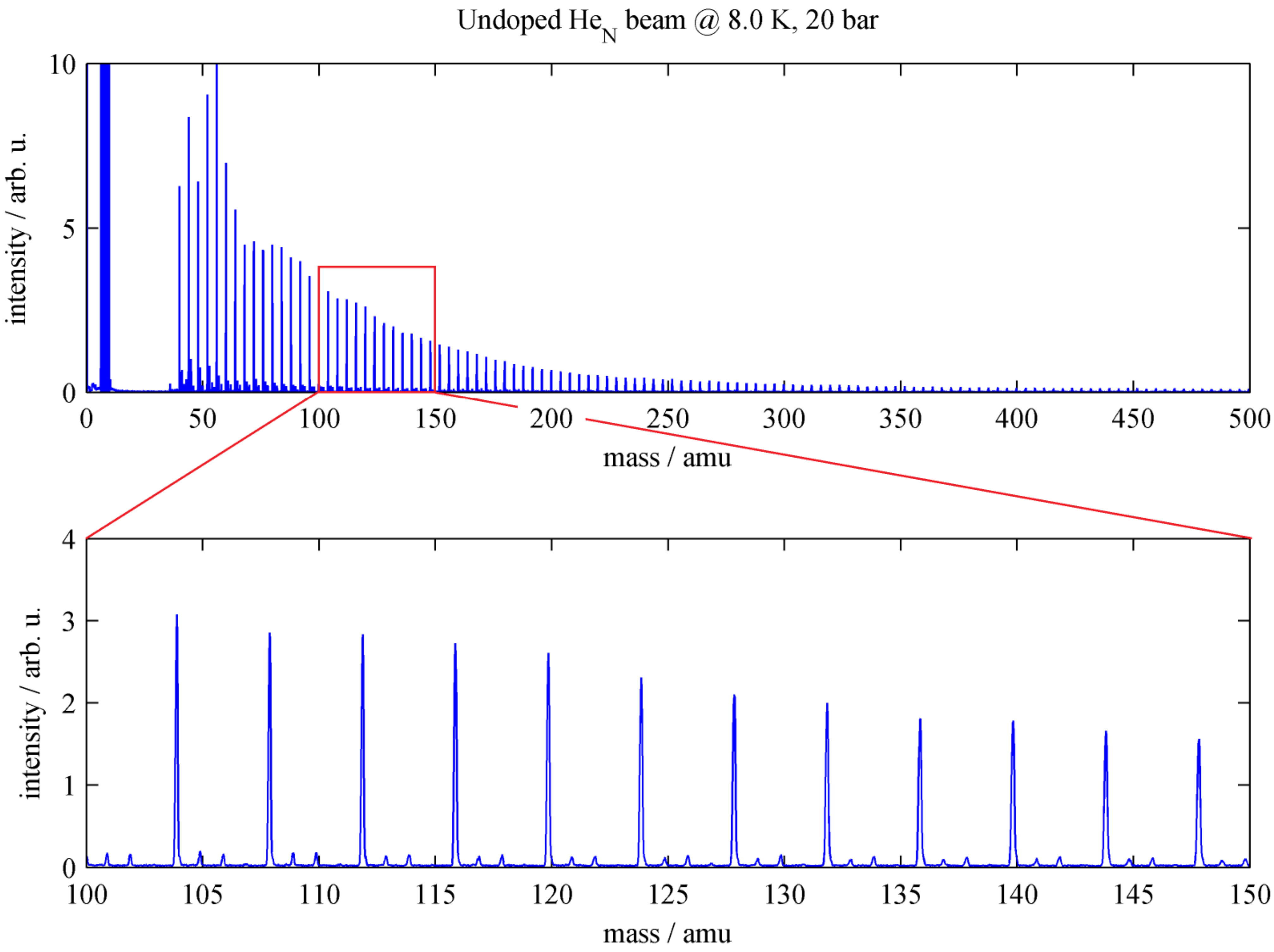
Undoped He_N beam @ 8.0 K, 20 bar
intensity / arb. u.
10
5
0
0
50
100
150
200
250
300
350
400
450
500
mass / amu
intensity / arb. u.
4
3
2
1
0
100
105
110
115
120
125
130
135
140
145
150
mass / amu

He$_N$ - spectrum

bin width=4,000000

sweeps=1000000,000000

time resolution (ps)=250,000000

electron energy (eV)=89,00

frequency (Hz)=4000

duration electron beaml[µs]= 20,000

delay ion extraction / ionisation[µs]= 0,000

duration ion extraction[µs]= 3,000

delay mass filter / ion extraction[µs]= 0,000

duration mass filter[µs]= 3,000

heating current=2,274829

electrometer current=4,075931

emission current=0,612427

repeller=4,511014

extraction=4,481299

postacceleration=19,868469

MCP=2,805618

last_grid=1,114624

central_grid=2,256775

lens=8,021851

liner=8,019409

mass_filter=0,498779

deflect_X(+)=8,247681

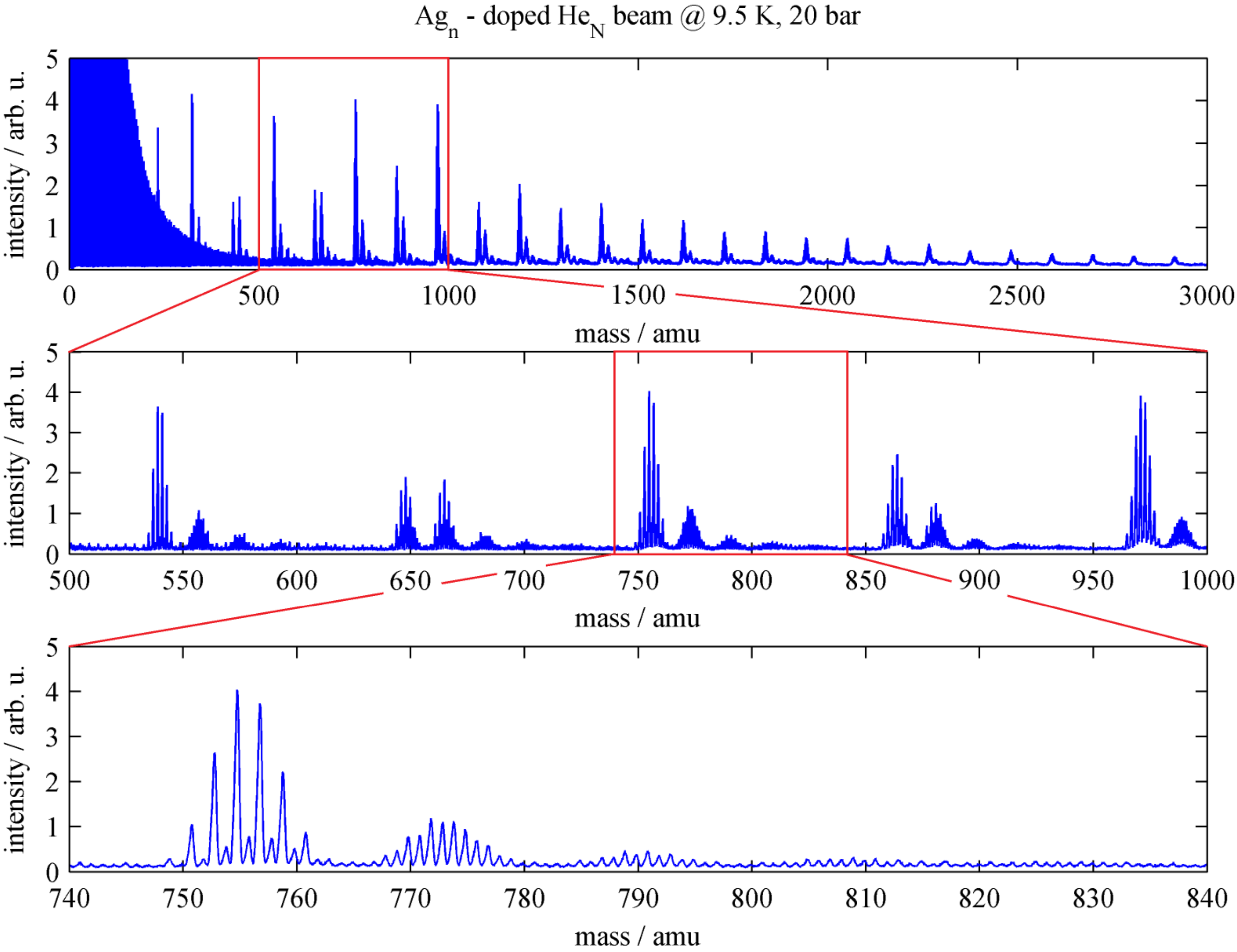
Ag_n - doped He_N beam @ 9.5 K, 20 bar
intensity / arb. u.
0
1
2
3
4
5
0
500
1000
1500
2000
2500
3000
mass / amu
intensity / arb. u.
0
1
2
3
4
5
500
550
600
650
700
750
800
850
900
950
1000
mass / amu
intensity / arb. u.
0
1
2
3
4
5
740
750
760
770
780
790
800
810
820
830
840
mass / amu

Ag_n - spectrum

bin width=2,000000

sweeps=10000000,000000

time resolution (ps)=250,000000

electron energy (eV)=89,00

frequency (Hz)=7000

duration electron beaml[µs]= 1,000

delay ion extraction / ionisation[µs]= 0,000

duration ion extraction[µs]= 3,000

heating current=2,143848

electrometer current=0,608231

emission current=0,398560

repeller=2,832413

extraction=2,794830

postacceleration=19,861603

MCP=2,502380

last_grid=1,385254

central_grid=2,115784

lens=8,013916

liner=8,024902

deflect_X(+)=8,043213

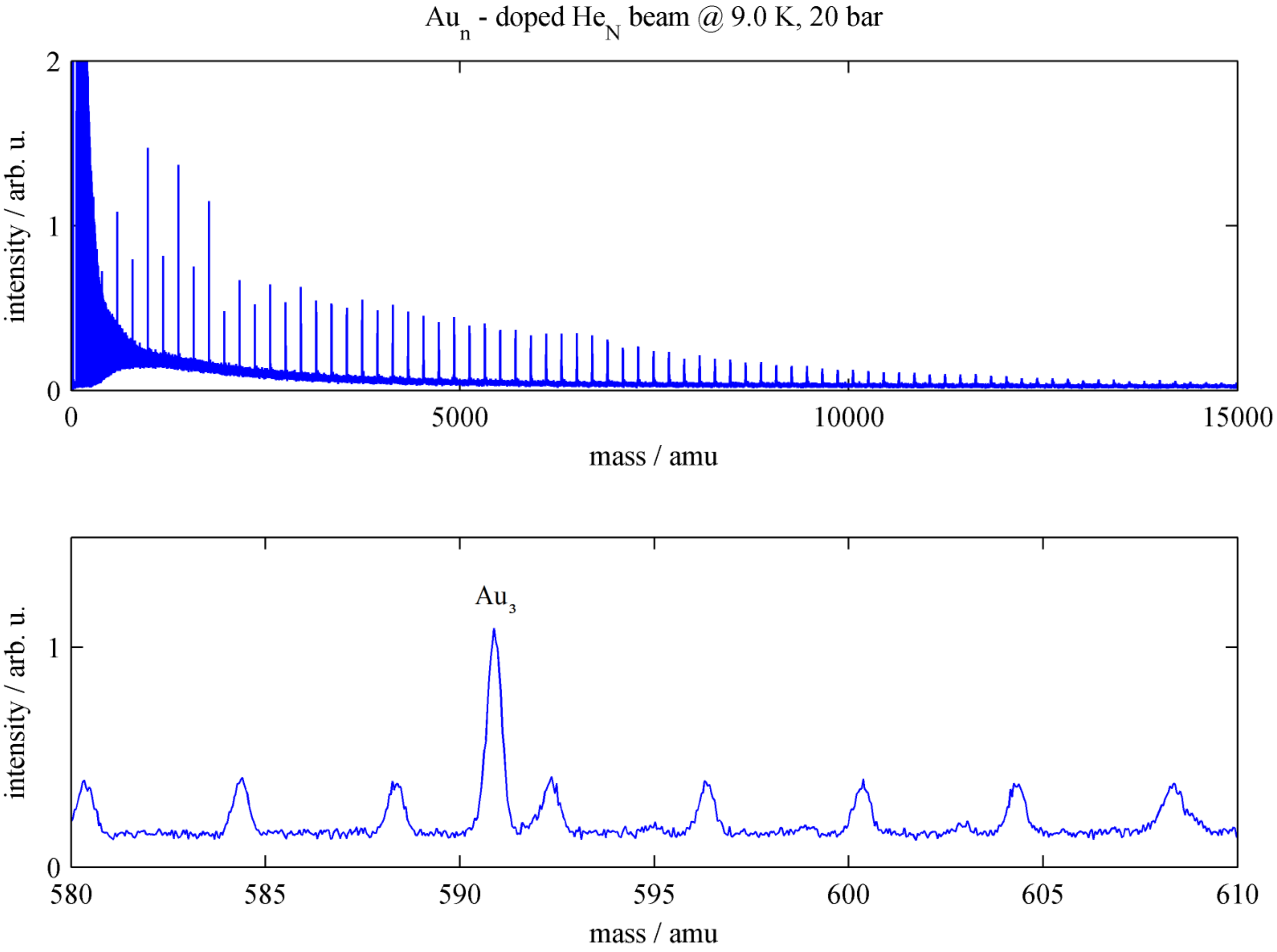

Au$_n$ - doped He$_N$ beam @ 9.0 K, 20 bar

Au_n - spectrum

bin width=4,000000

sweeps=2000000,000000

time resolution (ps)=250,000000

electron energy (eV)=89,00

ramp voltage (V)= 9,99

frequency (Hz)=5000

duration electron beaml[µs]= 20,000

delay ion extraction / ionisation[µs]= 0,000

duration ion extraction[µs]= 5,000

delay mass filter / ion extraction[µs]= 0,000

duration mass filter[µs]= 4,000

heating current=2,491745

electrometer current=3,096161

emission current=0,823486

repeller=4,507388

extraction=4,488626

postacceleration=19,857788

MCP=2,710770

last_grid=1,113647

central_grid=2,283691

lens=8,023682

liner=8,019409

mass_filter=0,499603

deflect_X(+)=8,211670

F UHV-Suitcase Operating Instructions

UHV – Suitcase: Operating Instructions

1. Controller:

Check if the ion-pump is connected before starting the controller. In order to start the controller, press the start-button (red) for 5 seconds.

The display on the ion-getter-pump controller reads the ion-current in µA. An ion-current of 1 µA corresponds to about 10^{-8} mbar. A display reading of ".000" indicates underrange (< 10^{-11} mbar), a reading of "1." indicates overrange.

If the pressure is higher than 10^{-9} mbar check for the cause! NEG-activation and bakeout might be necessary.

If the display signals overrange ("1."), ***turn off the controller*** - press the off-button (black) for 5 seconds (wait 1 minute before disconnecting any cables) and consult the manual!

2. Standby mode:

When not in use, the UHV-Suitcase should always be kept under vacuum conditions, the lower the baseline pressure, the better. In order to remain UHV conditions in the suitcase:

- ***Keep the ion-getter-pump running*** → the manufacturer guarantees 50.000 hours of operation at 10^{-7} mbar → as the vacuum in the suitcase in standby will be much better, the ion-pump will last forever.
- ***Ensure that there is fore-vacuum pressure (5 mbar or better) at the atmospheric side of the gate-valve*** in order to reduce air diffusion through the rubber sealing of the valve. When using the buffer container provided by the manufacturer, renew the vacuum in the buffer every now and then.

Check the vacuum conditions regularly → the ion-current of the ion-pump is proportional to the pressure inside the suitcase

3. Battery mode:

Before switching to battery mode:

- ***Check the pressure in the suitcase*** → low pressure/ion current necessary for battery runtime and reliable pumping
- ***Ensure that there is fore-vacuum pressure (5 mbar or better) at the atmospheric side of the gate-valve*** in order to reduce air diffusion through the rubber sealing of the valve. When using a buffer container → renew the vacuum in the buffer
- **Ensure that the battery was charged for 8 hours**

In order to switch to battery operation, simply pull the power plug. Battery specifications are 55 hours operation @ 5 µA, battery life span is 1000 cycles. The battery should not be operated outside a 0°C to 40°C window. About 3 hours before the battery runs out of power, the controller will start beeping and the red led turns on.

UHV – Suitcase: Operating Instructions

4. Connecting to and disconnecting from a host UHV system:

Install a turbo-pumped T-piece (lock chamber) between the valve of the host system and the valve of the UHV-suitcase. ***Ensure that the UHV-suitcase is properly aligned and supported by a suitable structure***.

Before opening any valves, pump down the lock chamber to sufficiently low vacuum level (depending on the sensitivity of the samples).

Open the gate valve to the lock chamber and recheck the reading of the ion-pump controller. If the reading is as expected, the valve to the host system can be opened and the sample transfer can be started.

Always retract the wobble-stick after use and close both gate valves.

Check that both valves are firmly closed before starting the disconnection procedure. Then, switch off the vacuum system of the lock chamber, vent the chamber and open the CF40 connection.

Reattach the buffer volume at the atmospheric side of the gate-valve and evacuate the buffer volume to fore-vacuum pressure (5 mbar or better) in order to reduce air diffusion through the rubber sealing of the valve.

5. NEG activation and bakeout:

Activation is necessary after venting or if the pumping speed falls below acceptable limits.

Establish a connection to a turbo-pump, e.g. by using the lock chamber and pump down to vacuum conditions better than $1{\cdot}10^{-6}$ mbar; the ***pressure must be better than*** $5{\cdot}10^{-5}$ ***mbar at all times*** during the activation and bakeout. Make sure that the gate valve is open and the ion-pump is turned off during activation and bakeout.

Connect the silicone cable (banana plugs → use a standard lab power supply) for activation of the NEG.

(Re-)activate the NEG before starting the bakeout: 4.8 A for 60 minutes. ***Maximum current: 5 A***

Follow a typical bakeout procedure (heating cords, etc.) but do not exceed 150°C (magnetic manipulators).

Flash the NEG during the cooldown (@ ≈ 80°C) → 3.6 V | 2.5 A for 30 minutes.

Turn the ion-pump back on and close the gate valve, but keep the turbo connected and running until the ultimate pressure is reached (24 h).

6. Venting / pumpdown after venting

If not absolutely necessary, avoid venting the UHV-suitcase. Especially contact with oxygen and humidity is harmful for the NEG. However, the manufacturer guarantees 100 regeneration cycles of the NEG when venting with dry nitrogen. For the venting- and pumpdown-procedures consult the manual!